INFORMATION TO USERS

This manuscript has been reproduced from the microfilm master. UMI films the text directly from the original or copy submitted. Thus, some thesis and dissertation copies are in typewriter face, while others may be from any type of computer printer.

The quality of this reproduction is dependent upon the quality of the copy submitted. Broken or indistinct print, colored or poor quality illustrations and photographs, print bleedthrough, substandard margins, and improper alignment can adversely affect reproduction.

In the unlikely event that the author did not send UMI a complete manuscript and there are missing pages, these will be noted. Also, if unauthorized copyright material had to be removed, a note will indicate the deletion.

Oversize materials (e.g., maps, drawings, charts) are reproduced by sectioning the original, beginning at the upper left-hand corner and continuing from left to right in equal sections with small overlaps. Each original is also photographed in one exposure and is included in reduced form at the back of the book.

Photographs included in the original manuscript have been reproduced xerographically in this copy. Higher quality 6" x 9" black and white photographic prints are available for any photographs or illustrations appearing in this copy for an additional charge. Contact UMI directly to order.

UMI

A Bell & Howell Information Company
300 North Zeeb Road, Ann Arbor MI 48106-1346 USA
313/761-4700 800/521-0600

Interactions of the Northern and Southern Branches of the Thermohaline Circulation

by

David A. McDermott

A dissertation submitted in partial fulfillment
of the requirements for the degree of

Doctor of Philosophy

University of Washington

1996

Approved by Edward S. Sarachik
(Chairperson of Supervisory Committee)

Program Authorized
to Offer Degree Atmospheric Sciences

Date 22 April 1996

UMI Number: 9637987

UMI
300 North Zeeb Road
Ann Arbor, MI 48103

Doctoral Dissertation

In presenting this dissertation in partial fulfillment of the requirements for the Doctoral Degree at the University of Washington, I agree that the Library shall make its copies freely available for inspection. I further agree that extensive coping of this dissertation is allowable only for scholarly purposes, consistent with "fair use" as prescribed in the U.S. Copyright Law. Requests for copying or reproduction of this dissertation may be referred to University Microfilms, 1490 Eisenhower Place, P.O. Box 975, Ann Arbor, MI 48106, to whom the author has granted "the right to reproduce and sell (a) copies of the manuscript in microform and/or (b) printed copies of the manuscript made from microform."

Signature____________________

Date 22 April 1996

University of Washington

Abstract

Interactions of the Northern and Southern Branches of the Thermohaline Circulation

by David A. McDermott

Chairperson of the Supervisory Committee: Professor E. S. Sarachik
Department of Atmospheric Sciences

Coarse resolution models are used to investigate the influence of Southern Hemisphere processes on the Northern branch of the thermohaline circulation. The link between the zonal wind stress at the latitude of Drake Passage and the production of deep water in the Northern Hemisphere is explored. A nearly linear response to wind stress at the tip of South America is seen in northern deep water production rates in both one- and two-basin configurations. Transient studies are conducted that illustrate the transmission of the wind generated signal from the Southern Hemisphere to the northern sinking region.

Mixed-boundary condition experiments are conducted in a number of model configurations. Deep-decoupling oscillations are produced in a one-hemisphere configuration, but can be suppressed by representing the influence of AABW by restoring the bottom temperatures to appropriate values. In two-hemisphere numerical experiments, the continuous production of AABW is seen to prevent the destabilization of the high northern latitudes, and deep-decoupling oscillations do not occur. In a two-basin configuration, the export of fresh water from the Atlantic basin during a colder climate allows century-scale deep-decoupling oscillations.

The results of the OGCM mixed boundary condition experiments are investigated using simple box models. One-hemisphere circulations are generated that are consistent with the 3-D model, and the influence of deep restoring is explored. Deep-decoupling oscillations can only be produced in a two-hemisphere box model if boundary and initial conditions do not allow AABW production. Multiple equilibria are found in the overturning circulation.

Two scenarios are presented to produce oscillations that are similar to deep-decoupling oscillations in the presence of continued AABW production. First, the high northern latitudes are subjected to a melt pulse/ retreat pattern of freshening. These perturbations can cause transitions from one stable mode to another, as well as overturning flushes that are followed by a return to the original stable overturning mode. Second, stochastic forcing is applied to the high northern latitude surface fresh water flux. The variations in surface forcing are capable of producing transitions between overturning states that are similar to deep-decoupling oscillations. The stochastic forcing acts to overcome the stabilizing effect of the AABW. In two-basin mixed boundary condition experiments, cooling the climate is seen to result in deep-decoupling type oscillations under stochastic forcing that produced no such variability in a warmer climate.

TABLE OF CONTENTS

LIST OF FIGURES

LIST OF TABLES

ACKNOWLEDGEMENTS

I would like to thank my advisor, Dr. E. S. Sarachik, for his guidance during my tenure at the University of Washington. I thank the members of my reading committee for their careful reading of this dissertation, and for their thoughtful questions and helpful suggestions. Thanks also to my fellow students and JISAO denizens, and especially to Paul Goodman for his thoughtful discussions, patience, and sharp editing pencil. Most importantly, I would like to thank my wife Marian for her patience and support in seeing me through my graduate school years.

The majority of the figures in this dissertation were generated using FERRET, a product of NOAA's Pacific Marine Environment Laboratory.

Chapter 1 Introduction

The earth's low latitudes receive more energy from the sun than they radiate to space. The atmosphere and ocean act as heat pumps to deliver the excess heat from low latitudes to high latitudes, where the radiative balance is opposite that of the tropics. Within the ocean, the wind and buoyancy driven circulations both contribute to this redistribution of heat. The delivery of heat to high latitudes by the circulation of the Atlantic ocean is responsible for the much milder climate experienced by Europe compared to locations at similar latitudes in North America. While the importance of the large-scale buoyancy-driven overturning is well known, difficulties in measuring vertical motion and the deep circulation require us to infer much about the present overturning circulation from tracer measurements. The surface fluxes of both heat and fresh water, the important buoyancy forcings for the global oceans, are poorly documented, further complicating our efforts to understand the behavior of the large-scale overturning.

The conveyor belt picture of the thermohaline circulation (THC) popularized by Broecker (1987) is designed to give a first approximation of the large scale overturning in the world's oceans (see Figure 1.1). In this scenario, warm saline water flows northward in the North Atlantic where it cools and sinks to form deep water. Runoff, ice melt, and the excess of precipitation over evaporation all act to freshen the high-latitude North Atlantic surface water, but this freshening is insufficient to prevent deep water formation in our present climate. The deep water flows south toward the Southern Ocean as a deep western boundary current. There it contributes to circumpolar deep water (CDW) in the

Antarctic Circumpolar Current (ACC). CDW flows northward into the Pacific and Indian basins where it upwells, conforming to a Stommel-Arons-like balance; downward diffusion of heat is balanced by upward advection of cold water (Stommel, 1958, Stommel and Arons, 1960a,b). Warm surface waters then return to the Atlantic via the Aghulas Current to complete Broecker's conveyor belt circulation.

However, this picture of the THC is contradicted by some observations. Radiocarbon data has been used to derive a residence time for each of the ocean basins (Toggweiler et al., 1989). If the upwelling implied by the radiocarbon-derived residence times is balanced by the vertical diffusion of heat, a value for the vertical diffusivity (K_v) of 1 cm^2/sec is required. Estimates from representative experiments and observations (Ledwell et al., 1993) suggest that a value of approximately 0.11 - 0.15 cm^2/sec would be more appropriate. As a result, wind mixing near the surface and mixing at boundaries become better candidates than Stommel-Arons for achieving the necessary heat balance while remaining consistent with the residence time.

In addition, it may be misleading to consider the production of North Atlantic Deep Water (NADW) without considering the influence of the Southern Ocean. Observations indicate that all of the deep water in the ocean is produced in either the North Atlantic or the seas around Antarctica. The interaction of the deep water produced in the northern and southern high latitudes is not well understood. Evidence from sediment cores suggests that during the last glacial maximum (LGM) the North Atlantic ceased to serve as a source of deep water (Charles and Fairbanks 1992), and high-nutrient water, presumably of southern origin, took its place. Boyle (1990) argues that sediment core records indicate that the North Atlantic formed intermediate rather than deep water at this time. This shift is generally thought to be the result of changes in the local forcing in the northern hemisphere, with the increased intrusion of Antarctic Bottom Water (AABW) occurring as a response. The possibility that the southern oceans influence the production of NADW has only recently been considered seriously.

Deacon (1937) raised the possibility of deep water being upwelled to the surface in the Southern Ocean, an idea later promoted by Stommel (1957). Stommel noted that a good approximation of the Atlantic circulation could be generated by superimposing a western boundary current that joins upwelling in the Southern Ocean to downwelling in the North Atlantic on the wind driven surface flow. He did not, however, specify the mechanisms which produced the deep water in the North Atlantic that was then upwelled in the Southern Ocean. The connection between North Atlantic sinking and upwelling in the Southern Ocean was incorporated into the work of Gordon (1986) and Broecker (1991) who identified the circumpolar ocean to be the primary location for upwelling of deep water.

The hydrography of the Southern Ocean and the resulting outcropping of the deep water are strongly influenced by a unique dynamical constraint that exists within the latitude band of Drake Passage (Stommel, 1957, Gill and Bryan 1971). This latitude band is notable as the only continuous zonal band of ocean outside of the Arctic Ocean. Above the height of various topographic features in this latitude band (ridges, plateaus, etc.) there can be no zonally averaged east-west pressure gradient, and hence no net geostrophically balanced meridional flow. The equatorward surface Ekman flow is not bound by geostrophy, nor is the upwelling which supplies it. Mass continuity requires a poleward return flow to compensate for the Ekman drift, yet this flow can only exist in geostrophic balance below the tops of any topographical features. Warren (1990) identifies the water at a depth which could provide the geostrophically balanced return as North Atlantic Deep Water (NADW).

This dynamical constraint serves to isolate the ocean south of Drake Passage from the upper ocean north of Drake Passage, and may also serve to link the strength of the winds in the latitude of Drake Passage to the production of deep water in the North Atlantic. However, the relationship between the wind stress over the Southern Ocean and NADW production has not been well-explored. Toggweiler and Samuels (1993) (TS93 hereafter) conducted numerical experiments in which they found that NADW production, as measured by both North Atlantic overturning and deep outflow from the Atlantic basin, increased as the zonal wind stress in the southern ocean increased. Thus the wind-driven upwelling in the Southern Ocean served to regulate NADW production, rather than serving only as a fortuitous return route to the upper ocean. In a modelling study, England (1992) saw an increase in the deep outflow from the Atlantic basin in response to an increase in the northward wind driven flow at the latitude of Cape Horn. The net overturning in the North Atlantic was unchanged, however, because the increase in outflow was accompanied by a decrease in local upwelling. The results of these experiments raise the interesting possibility of an indirect link between the atmosphere in the southern hemisphere (through wind stress on the ocean) and the atmosphere in the northern hemisphere (through heat exchange with the ocean) via the deep ocean.

Paleorecords indicate that southern hemisphere winds have, at times, been stronger in the past than at present. Petit et al. (1981) analyzed aerosols trapped in Antarctic ice cores and determined that during the last glacial maximum (18,000 years before present), winds in the circumpolar region were approximately 50% stronger than those observed at present. Attempts to model the atmosphere at the last glacial maximum using CLIMAP (1981) and other data generally produce at least some increase in the subantarctic winds over those at present (Manabe and Broccoli 1985a,b, Broccoli and Manabe, 1987, Rind, 1987). In their simulation of the atmosphere during the last glacial maximum, Kutzbach and Guetter (1986) saw a southward shift in the westerlies in the southern hemisphere, primarily in the Southern Hemisphere winter, but they did not specify a magnitude at the surface. Lautenschlager and Herterich (1990) produced an increase of greater than 60% at 50°S, though this increase tapered to zero by 63°S.

Some of the attempts to use coupled ocean-atmosphere models to represent the climate with altered atmospheric CO_2 concentrations also produce changes in the winds in the southern hemisphere. Manabe et al. (1991) conducted coupled model experiments in which the atmospheric CO_2 concentration was gradually increased and gradually decreased. In both cases the largest change in the surface wind stress occurred over the Southern Ocean. Similarly, in the coupled model experiments of Manabe et al. (1990), a doubling of the atmospheric CO_2 concentration produced the largest changes over the circumpolar region.

Relatively large temperature variations in the northern hemisphere climate of the last ice age are apparent in the Greenland ice core record (Johnson et al., 1992, Dansgaard et al., 1993). Many of these oscillations show the same shape as that introduced by Broecker (1991) in a schematic interpretation of temperature variability around the North Atlantic region during the last deglaciation. The Greenland ice core ^{18}O records during the last glaciation are characterized by rapid (decadal-scale) warmings followed by gradual cooling (several-century-scale) and then a rapid (decadal-scale) transition to a cool state. Because of its proximity to the NADW formation regions, the Greenland ice sheet is believed to record heat loss associated with NADW formation. Further support for this hypothesis is offered by North Atlantic sediment records. Bond et al., (1993) find a strong correlation between the Greenland ice core ^{18}O record and sea surface temperatures as recorded by foraminifera in North Atlantic sediments.

Evidence for changes in the NADW production during the glacial period has been seen in a number of sediment records. Charles and Fairbanks (1992) interpret ^{13}C from benthic foraminifera in a core from the Southern Ocean. They see evidence of an abrupt increase in NADW immediately preceding the melting of Northen Hemisphere ice sheets. Using Cd/Ca ratios to identify the nutrient-depleted signal of water formed in the North Atlantic, Duplessey et al. (1988) found that during the LGM, the North Atlantic formed intermediate rather than deep water. Boyle and Keigwin (1987) saw a reduction in the low nutrient signal of NADW during the Younger Dryas, which is believed to have been a period in which the earth's climate briefly returned to conditions more like those at the LGM.

Several possible mechanism to explain the rapid climate fluctuations indicated in the ice-core record have been proposed. Broecker (1991) infers that the export of fresh water from the Atlantic basin, in the form of atmospheric water vapor transport, could drive a 'salt-oscillator' that would turn on and shut off the North Atlantic overturning circulation. Broecker speculates that oscillations characterized by a build-up and release of salt in the Atlantic basin could result in rapid transitions in climate similar to those inferred from the $\delta^{18}O$ record. Broecker suggests that the excess of evaporation over precipitation and runoff in the Atlantic basin that we see in today's Atlantic would result in increasing basin-averaged salinity in a glacial climate in which North Atlantic Deep water production is reduced or eliminated. The increase in salinity eventually allows the destabilization of the northern halocline, and a rapid return to an overturning circulation in the North. The reduction in basin-averaged salinity is accomplished by export of high-salinity deep water leaving the basin, accompanied by increased glacial melting resulting from the heat released during the periods of rapid overturning.

Another explanation for the rapid climate changes is the deep-decoupling oscillation described by Winton (1993), Sarachik et al. (1996), and Winton (1996). These studies use numerical models forced with steady mixed boundary conditions to produce free-evolving oscillations in ocean heat transport with timescales of centuries to millennia.

Winton described these oscillations as rapid shifts between an ocean circulation in which vigorous overturning cooled the deep ocean ('coupled') and a circulation in which the deep overturning was interrupted and heat from the low-latitudes diffusively warmed the interior. Most importantly, the model oscillations produced time series of high-latitude heat fluxes with rapid transitions and gradual cooling like that in the ice core temperature record.

The deep-decoupling oscillations produced in Winton (1993) were produced in a single-hemisphere sector model, those in Sarachik et al. (1996) were produced in a two-hemisphere sector model, and those in Winton (1996) were produced in a two-dimensional viscous ocean model. The two-dimensional ocean model of Winton (1996) represented both the Northern and Southern Hemisphere, and was coupled to a simple atmosphere model. Because of the geometry and surface forcing of the Sarachik et al. (1996) two-hemisphere model, there was no southern source of deep water formation. In contrast, sediment records (Duplessy et al., 1988, Charles and Fairbanks, 1992) indicate that AABW production continued throughout the LGM. Neither Sarachik et al. (1996) nor Winton (1996) produce deep-decoupling oscillations with the continued production of AABW.

Numerical simulations that included more complete representations of a possible southern deep water source (e.g. Rahmstorf, 1994, Weaver & Hughes, 1994) tend to generate circulations with multiple equilibria rather than clear examples of internal modes of temporal variability. In a coupled ocean-atmosphere general circulation model, Manabe and Stouffer (1988) found two stable equilibria; one that included NADW production and one that did not. In both the coupled general circulation model of Manabe and Stouffer (1988) and the simpler coupled model of Rahmstorf (1994), reduced NADW production was associated with cooler sea surface and air temperatures in the North Atlantic region.

While multiple-equilibria type solutions suggest an important role for the ocean in determining climate, they are generally solutions that require an external impulse (e.g. a meltwater pulse) to toggle the ocean circulation from one state to another. Oppo and Lehman (1995) present evidence that many of the major fluctuations in the rate of production of NADW during isotope stage 3 occur *without* evidence of major meltwater pulses preceding the cool periods. This finding suggests that other mechanisms, such as deep-decoupling modes of variability, may also be at work. The extent to which the presence of a more realistic southern source of deep water plays a decisive role in producing steady equilibria rather than internal oscillations will determine the extent to which such internal oscillations are applicable conceptual models for the real ocean.

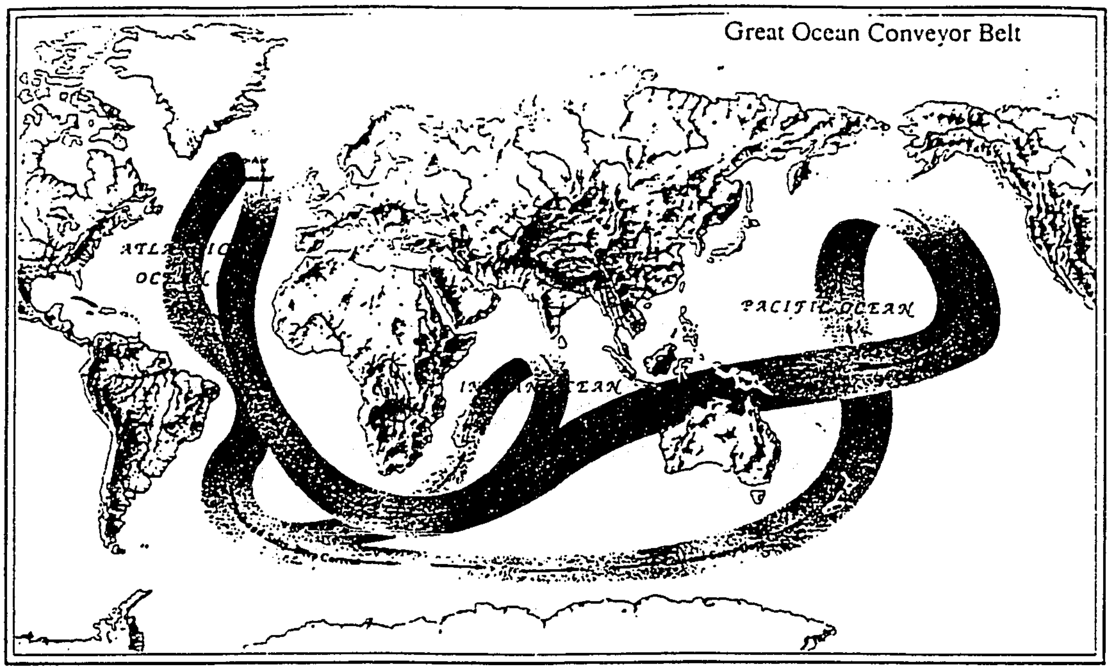

FIGURE 1.1 Overturning conveyor belt of Broecker (1991).

Chapter 2 Investigative Approach

In this thesis, I use simplified but relevant ocean general circulation models (OGCMs) to explore the influence of the southern oceans on the production of deep water in the North Atlantic. The model used for all of the OGCM experiments in this thesis is the Geophysical Fluid Dynamics Laboratory's Modular Ocean Model (MOM) described by Pacanowski et al. (1991). The model is a primitive equation, coarse resolution ocean-only model. Using coarse resolution and the simplified geometries presented here allows rapid computation, while still capturing the essential features of a global ocean model. In particular, a two-hemisphere sector model can be configured that produces some of the most important water masses of the world's oceans: Antarctic Bottom Water (AABW), North Atlantic Deep Water (NADW), and Antarctic Intermediate Water (AAIW). Expanding to a two-basin configuration improves the representation of the global overturning circulation. Several basin configurations are used in the thesis; they are discussed in the chapters in which they appear. Likewise, the surface forcing and model parameters (e.g. mixing, viscosity) are also discussed in each chapter.

In Chapter 3, I discuss the connection between the wind stress in the latitude of Drake Passage and the rate of overturning in the North Atlantic. The first experiments find changes in the steady-state solutions that result from altering the strength of the Southern Hemisphere westerlies. The northern overturning is found to increase as the magnitude of the zonal wind stress in the Subantarctic increases.

In the next set of experiments, I modify the geometry of the two-basin configuration to find the geometry's role in determining the link between northern overturning and Southern Hemisphere winds. First I extend the Pacific basin by adding a representation of the Indian Ocean, in order to test the importance of the model's longitudinal extent. Increasing the extent of the Southern Ocean increases the influence of Southern Hemisphere winds on northern deep sinking. I also modify the Drake Passage configuration to assess the importance of its representation in the model to the response of northern overturning to Southern Hemisphere winds. Modifications of the idealized Drake Passage include changes in width, depth, and in the alignment of South America and the Antarctic Peninsula. The configuration of the model's Drake Passage determines the extent to which the response to changes in wind stress in the Southern Hemisphere westerlies effects northern overturning, and the extent to which the changes are local.

The final set of experiments in Chapter 3 illustrate the mechanism linking the Drake Passage region and the northern Sinking region. The transient response to changes in the strength of Southern Hemisphere westerlies is observed for both one- and two-basin model configurations. Changes in the wind stress in the Southern Hemisphere westerlies excite boundary modes that produce changes in the circulation similar to the spin-up process described by Kawase (1987).

In Chapter 4, I use similar OGCMs to look at variability of the THC under mixed boundary conditions, focusing on the influence of the southern ocean. These numerical modeling experiments are presented in order of increasing complexity. The first mixed-boundary condition experiments are performed in a one-hemisphere basin model, and deep-decoupling oscillations are produced. The influence of Antarctic Bottom Water is simulated in this simple configuration by restoring the temperature and salinity of the deep ocean near the southern wall to AABW values. When the bottom water is strongly restored toward the cold AABW value, deep-decoupling oscillations are suppressed. The basin is then extended to include a region where AABW can form, and the salinity flux is modified to maintain a continuous supply of AABW. Under surface forcing that results in continuous production of AABW, no deep-decoupling oscillations are produced in the two-hemisphere configuration. Finally, mixed-boundary condition experiments are conducted in a two-basin sector model. The two-basin model allows continuous AABW production, and includes a freshwater export from the North Atlantic to the Pacific basin. When the surface restoring temperatures are reduced, deep-decoupling oscillations occur in the North Atlantic as long as sufficient interbasin freshwater transport is maintained.

In Chapter 5, a series of box models are used to illustrate the behavior of the circulation under mixed boundary conditions. Box models allow a more thorough explorations of boundary- and initial-conditions, and offer the possibility of simplified analysis. The first box model used is a three-box model of a single hemisphere basin, and like the one-hemisphere sector model of Chapter 4, it produces deep-decoupling oscillations. The deep-restoring experiments of Chapter 4 are reproduced here by adding a fourth box representing the influence of AABW. Analysis of the system of equations for the four-box model predicts the range of salinity forcing over which deep-decoupling oscillations occur, as a function of the influence of AABW. The results are in agreement with the results from the deep-restoring experiments of Chapter 3. Finally, a twelve-box model of a two-hemisphere basin is described, and is used to find the conditions under which a two-hemisphere basin will produce deep-decoupling oscillations. In the twelve-box model, it is necessary to prevent deep sinking in both the Antarctic and Subantarctic to generate deep-decoupling oscillations.

Because deep-decoupling oscillations are not seen to occur spontaneously in any of the two-hemisphere configurations of Chapter 4 that did produce AABW, a series of OGCM experiments were conducted in which time-dependant surface fluxes were applied. These mixed-boundary condition experiments are presented in Chapter 6. Steady state equilibrium solutions from the two-hemisphere boundary condition experiments of Chapter 4 are used as initial states for ocean basins subjected to a simulated melt pulse followed by a retreat of glacial melting. Both the two-hemisphere single-basin and the two-basin configurations are then subjected to stochastic forcing in the high-latitude freshening region. By introducing time-varying surface forcing in the North, oscillations can be induced despite the influence of southern-source deep water.

A summary and conclusions are presented in Chapter 7.

Chapter 3 Drake Passage Effect Experiments

3.1 Introduction

In this chapter, I seek to explore the effects of the strength of the wind stress at the latitude of Drake Passage on the outflow of NADW from the Atlantic basin. The model configurations, forcings, and parameterizations used in this chapter are discussed in Section 3.2. The steady state response of the ocean to changes in the strength of the wind stress is discussed in Section 3.3.

The importance of the geometry in determining the Drake Passage effect is explored in section 3.4. The two-basin geometry is modified by extending the latitudinal extent of the Pacific basin, varying the height and width of the reentrant channel, and by offsetting the Antarctic Peninsula from the tip of South America. To elucidate the processes through which the southern winds influence northern deep sinking, a series of experiments was conducted in which the transient response of the circulation to wind forcing in the southern hemisphere was examined. In Section 3.5, the transient response to changes in Southern Hemisphere wind forcing is reported. First, the spin-up of an otherwise unforced ocean under wind stress in the high southern latitudes is described. Then an ocean at equilibrium with weak southern wind forcing (see Section 3.3) is subjected to strong southern wind forcing, and the transient solution is compared to the transient solution of the spin up problem.

3.2 Model Description

The model used is the MOM version of the GFDL ocean model described by Pacanowski et al. (1991). The horizontal resolution of the model is 3.75° in longitude and 4.0° in latitude. There are 20 levels in the vertical, defining a total depth of 5000m. The thickness of the layers increases from 50m at the surface to 449m in the bottom layer. Two basic geometries are used: a single basin with a reentrant channel and a two-basin configuration with a similar reentrant channel. The one-basin model was first used in McDermott and Sarachik (1996), and the two-basin configuration was first used in McDermott (1996). Additional modifications to the geometry are used for the steady state experiments of Section 3.4.2, and are detailed in that section. The geometry of the single basin configuration is shown in Figure 3.1a, and the geometry of the two-basin configuration is shown in Figure 3.1b. Note that while the basins appear rectangular in these figures, they are bounded by meridians that converge in the higher latitudes. The single basin extends from 72°N to 72°S, and is 56.25° wide. In the two-basin configuration, the smaller of the two basins has the same dimensions as the single basin. The second basin is 120° wide, and only extends to 64° N. The depth slopes from 2500m within the channel to the full depth of 5000m in a few grid spaces on either side of the channel. The reentrant channel has a width of 3.75° longitude (bringing the total widths to 60° and 180°) and extends four tracer grid points, from 48°S to 64°S. This is considerably larger than the actual latitudinal extent of Drake Passage. At this resolution, the actual width of Drake Passage would be represented by only two tracer points and one velocity point. As discussed by Toggweiler et al. (1989), the horizontal viscosity required to resolve boundary

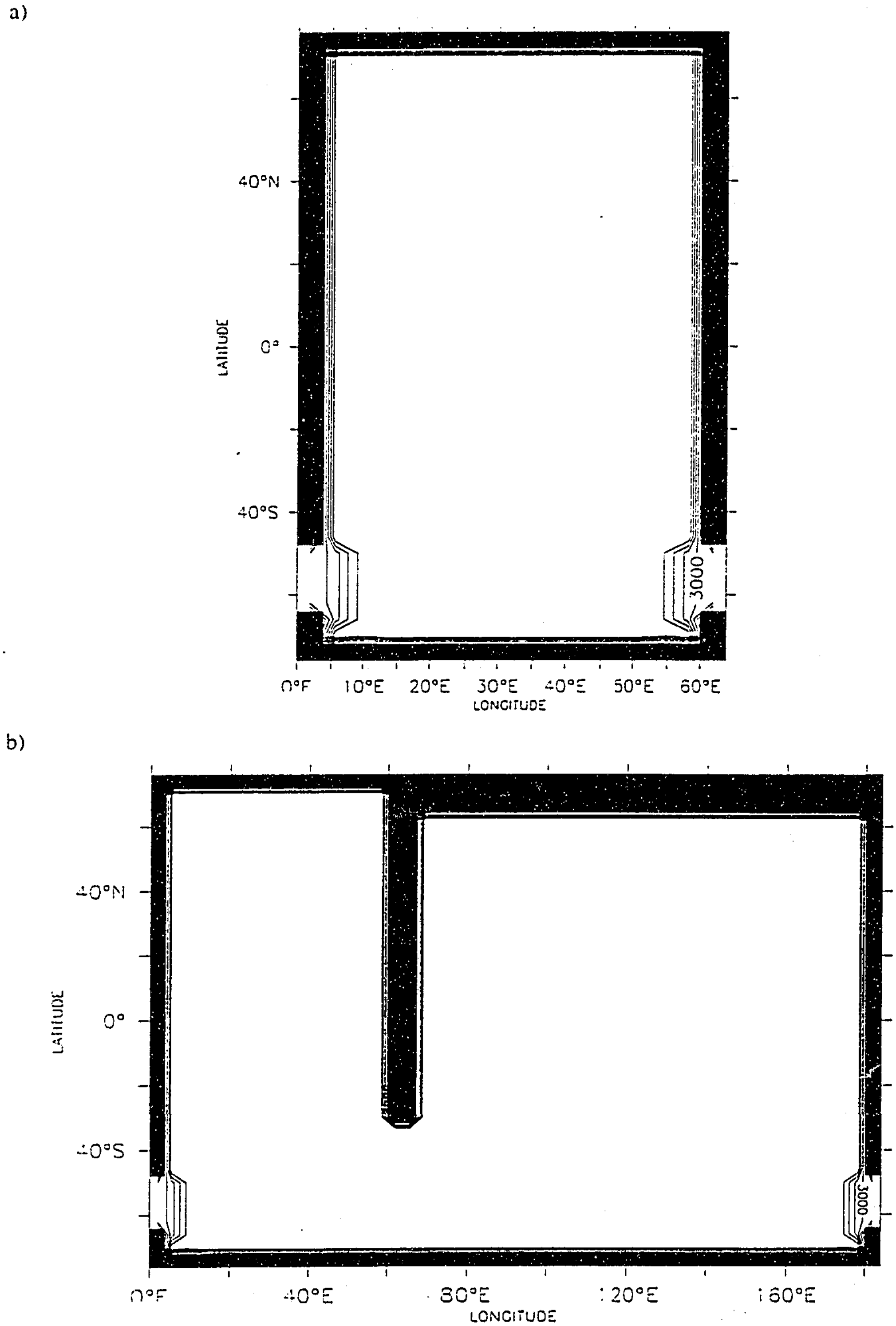

FIGURE 3.1 Basin configurations, a) one basin, and b) two-basin. Contours show depth, contour interval is 500m, sill depth is 2500m.

currents prevents realistic flows through a channel with only one velocity point. The channel in this model is therefore expanded to include four tracer points and three velocity points.

The geometric configuration of the channel is of great importance because of the dynamic constraints it imposes on geostrophic flow. Sensitivity to the width of the channel is explored in England (1992), and to depth in Cox (1989). The significance of the location of the northern boundary of the channel with respect to the maximum in the zonal wind stress curl is discussed in Toggweiler and Samuels (1993a, TS93a hereafter). The location of the channel in relation to the southern wall is also important. Locating the reentrant channel at the southern wall (e.g. Marotzke and Willebrand 1991) does not allow geostrophically balanced poleward flow below the surface Ekman drift. Consequently, northward Ekman flow extends all the way to the southern wall, and implies upwelling at the southern wall and deep sinking in the latitude of their reentrant channel. This problem is corrected in the two basin study by Hughes and Weaver (1994) by the addition of a representation of the Antarctic Peninsula. The peninsula allows for geostrophically balanced poleward flow south of their Drake Passage. This flow supplies the formation of Antarctic Bottom Water (AABW) in their model. In the current model. the configuration of the Antarctic Peninsula extends two grid boxes north of the Antarctic continent. This provides the support for poleward geostrophic flow, and extends the southern boundary slightly farther south without shifting the reentrant channel farther away from the actual location of Drake Passage. It also allows for both upwelling and downwelling to occur south of the circumpolar region.

At the surface, temperature and salinity are restored to zonally averaged Levitus (1982) climatological mean ocean values. For the single basin experiments, the world zonal mean values are used. For the two-basin experiments, the zonally averaged Atlantic and Pacific values are used north of the southern tip of "Africa" in the respective model ocean basins, and zonally averaged world values are used in the southern ocean. The restoring time constant for both temperature and salinity is 50 days. The use of restoring boundary conditions for both temperature and salinity avoids the question of multiple equilibria seen in mixed boundary condition (restoring in temperature with a prescribed salinity flux) ocean models (i.e. Hughes and Weaver 1994, Rahmstorf 1994). The relatively short Haney (1971) restoring time scale limits the response of the sea surface temperatures (SST's), a larger response might be seen with a larger time constant, or using a different thermal boundary condition (i.e. Zhang et al. 1993, Rahmstorf and Willebrand 1995)

Only the zonal component of the wind stress is applied. The nominal value for wind stress is the world zonal mean climatology from Hellerman and Rosenstein (1983). In Experiments I and VII, the nominal values for zonal wind stress are used everywhere. In other experiments, "strong" and "weak" winds, following TS93a and TS95, are defined as wind stress of 1.5 and 0.5 times the nominal value in the region of westerly wind stress in the Southern Ocean. Figure 3.2 shows the weak, nominal, and

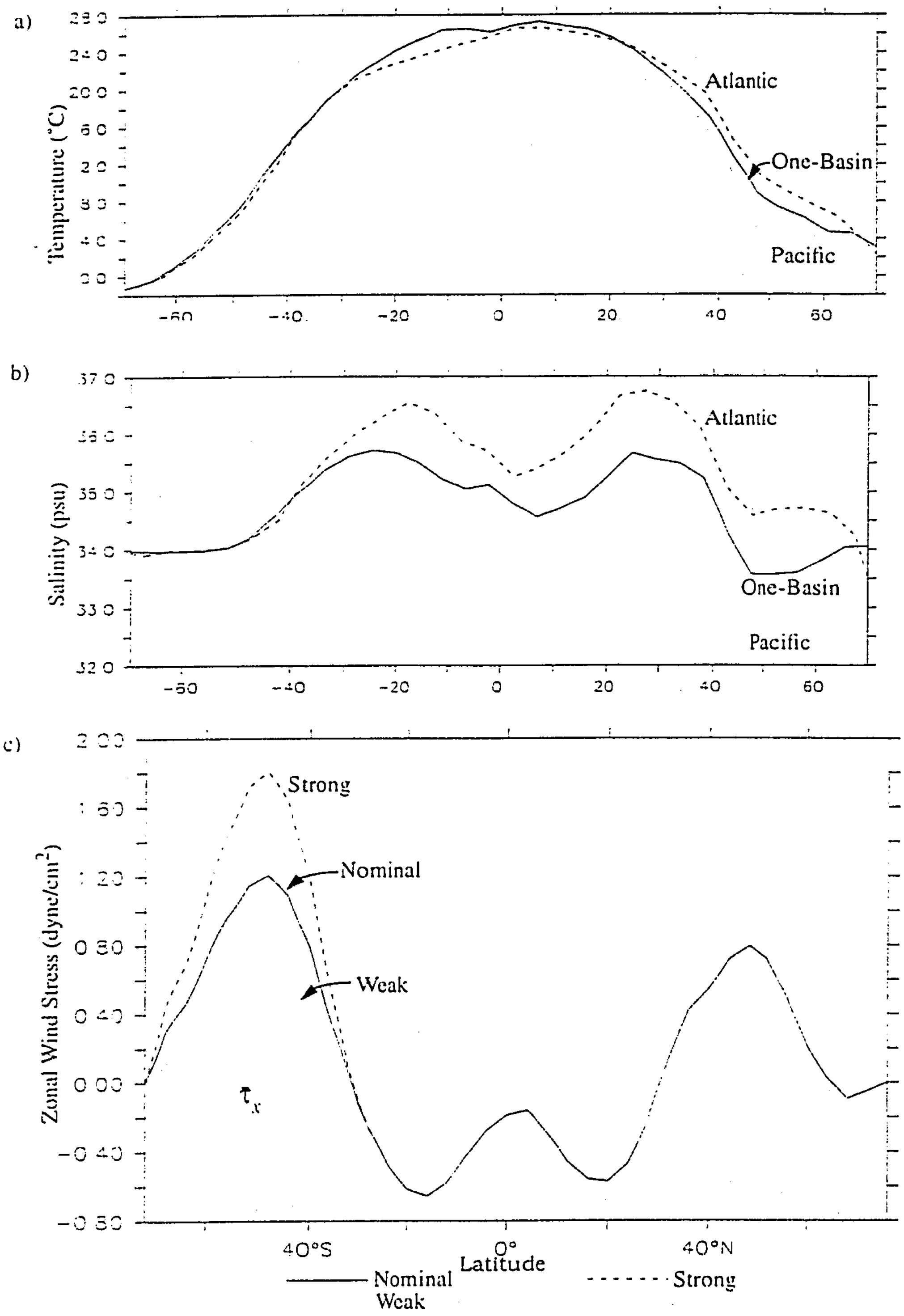

FIGURE 3.2 Surface boundary conditions for Chapter 3. a) Surface restoring temperature (°C), b) Surface restoring salinity (psu), and c) zonal wind stress (dyn/cm^2)

strong wind stress. Note that the maxima occurring at 48°S are located at the northern wall of the reentrant channel.

For steady state solutions, the asynchronous integration technique of Bryan (1984) is used without vertical acceleration. The tracer calculations use a two day time step, while the momentum calculations use a time step of one-half hour. In the transient case experiments, synchronous time-stepping is used with time steps of one hour. The horizontal diffusivity has a value of 1.0×10^7 cm^2/sec for all depths. Horizontal viscosity is 6.0 $\times 10^9$ cm^2/sec, and both the vertical diffusivity and viscosity are 1.0 cm^2/sec. Model results for single basin experiments are summarized in Table 3.1, and results for the standard two-basin experiments are summarized in Table 3.1. The results for the extended two-basin experiments are summarized in Table 3.1. The results from the changed Drake Passage configuration experiments are contrasted with the results for the nominal configuration in Table 3.1 and Table 3.7.

TABLE 3.1 Summary of standard single basin experiments.

	τ_x max (dyne/ cm^2)	Deacon Cell Strength (Sv)	Circumpolar current (Sv) (in Drake Passage)	Northward Heat Transport (max) (10^{15} W)	Northern Sinking (Sv)
Exp. I	1.2	3.87	174.8	0.4402	10.3
Exp. II	1.8	5.89	193.3	0.4718	11.2
Exp. III	0.6	1.84	155.5	0.4018	9.4

TABLE 3.2 Summary of standard two-basin experiments.

	τ_x max (dyne/ cm^2)	Deacon Cell Strength (Sv)	Circumpolar current (Sv) (in Drake Passage)	Northward Heat Transport (max) (10^{15} W)	North Atlantic Sinking (Sv)	Deep Atlantic Outflow (Sv)
Exp. IV	1.2	12.95	265.1	0.5911	18.9	9.1
Exp. V	1.8	19.90	306.2	0.6152	20.5	10.4
Exp. VI	0.6	5.97	215.7	0.5594	17.1	7.6

Notes for Tables 3.1, 3.2, 3.5, 3.6, and 3.7:

τ_x max: Maximum wind stress in Southern Hemisphere westerlies, ~48°S. For Table 3.7, the values given for the offset Drake configuration represent wind stress at the north of that configuration's Drake Passage, 56°S

Deacon Cell Strength: Maximum value of meridional stream function at 48°S.

Circumpolar Current: Eastward transport through Drake Passage.

Northward Heat transport: Maximum northward heat transport in Northern Hemisphere. In two-basin experiments, value is heat transport in the Atlantic basin only.

Northern (North Atlantic) Sinking: Maximum value of the meridional stream function in the North, at ~50°N. In the two-basin experiments, value is for Atlantic overturning only.

Deep Atlantic Outflow: Maximum value of meridional stream function at 30°S.

Ekman theory predicts the magnitude of the northward wind drift as:

$$\text{northward Ekman volume transport} = -\tau_x / (\rho_o f)$$

where τ_x is the zonal wind stress, ρ_o a reference density, and f the coriolis parameter. Multiplying by the latitudinal extent, the integrated northward transport can be found and compared to the Deacon Cell Strength determined by the model runs (see Table 3.3). The Deacon Cell here refers to the meridional overturning cell in the Southern Ocean associated with wind driven upwelling in the latitude of Drake Passage (Deacon, 1937, K. Bryan, 1991). The modeled value of the northward Ekman wind drift is smaller than the predicted Ekman drift in all cases, though it does vary linearly with wind stress. Further study will be required to establish the physical processes responsible for the discrepancy.

TABLE 3.3 Predicted and observed northward wind drift at 48°S.

	one-basin		two-basin	
$-\tau_x$ (dyne/cm^2)	**observed (Sv)**	**predicted (Sv)**	**observed (Sv)**	**predicted (Sv)**
1.2	3.87	5.98	12.95	14.9
1.8	5.89	7.47	19.9	22.4
0.6	1.84	2.49	5.97	7.47

The circumpolar current also scales nearly linearly with τ_x for each configuration, with the magnitude of the change decreasing slightly as the current increases. A brief discussion of changes in ACC that occur within each configuration in response to changes in wind forcing is included in section 3.3. The difference in the ACC between the one- and two-basin cases is a product of a number of things, including the different prescribed density forcing and changes in latitudinal extent. A full exploration of the influences determining the changes in the ACC strength from one- to two-basins is outside the scope of this thesis.

The experiments presented in Chapter 3 are summarized in Table 3.4.

TABLE 3.4 Description of Chapter 3 Experiments

Experiment	Basins	Description	Remarks
Exp. I	1	Normal winds	
Exp. II	1	Strong winds	
Exp. III	1	Weak winds	
Exp. Ic	1	Normal winds, no gap	
Exp. IIc	1	Strong winds, no gap	
Exp. IIIc	1	Weak winds, no gap	
Exp. IV	2	Normal winds	
Exp. V	2	Strong winds	
Exp. VI	2	Weak winds	
Exp. VII	1	Strong westerlies applied in south to uniformly stratified approximation of Exp.III	transient, no restoring of T or S
Exp. VIII	1	Strong winds applied to Exp. III equilibrium	transient
Exp. IX	2	Strong westerlies applied in south to uniformly stratified as in Exp.VII	transient, no restoring of T or S
Exp. X	2	Strong winds applied to Exp. VI equilibrium	transient
Exp. B1	2	Normal winds, Pacific Basin extended 60°	
Exp. B2	2	Strong winds, Pacific Basin extended 60°	
Exp. B3	2	Weak winds, Pacific basin extended 60°	
Exp. H1	2	Normal winds, High sill	
Exp. H2	2	Strong winds, High sill	
Exp. L1	2	Normal winds, Low sill	
Exp. L2	2	Strong winds, low sill	
Exp. S1	2	Normal winds, shifted Drake Passage	
Exp. S2	2	Strong winds, shifted Drake Passage	

3.3 Steady State Responses

3.3.1 One Basin

The single-basin configuration of the model is the simplest geometry containing all the elements necessary to test the Drake Passage effect. There are deep-sinking regions in both the north and south. and a reentrant channel providing a latitude band with no mean east-west pressure gradient above the sill. The overturning stream function for Experiment I, the one-basin, nominal winds case. is shown in Figure 3.3a. Deep sinking of 10.3 Sv occurs in the north of the basin. The northern overturning is weaker than estimates of North Atlantic overturning in part because the deep water is required to upwell within the single basin. In the two-basin experiments that follow (see section 3.3.3), NADW can leave the basin at depth, and northern overturning increases. This sinking extends to approximately 3000m. An overturning cell with 11.6 Sv of deep sinking exists in the southern hemisphere. Only about 6 Sv of this water flows north of 50°S to fill the basin as bottom water.

In addition, a Deacon Cell of 3.87 Sv is seen in the southern hemisphere. The positive 2 Sv. contour seen at about 50°S in Figure 3.3a shows the location of the Deacon Cell. In the zonal average presented by the overturning stream function, the equatorward surface transport driven by the westerlies is seen to downwell north of the wind stress maximum. This downwelling extends below the thermocline depth, and appears to supply the upwelling south of the wind stress maximum. Döös and Webb (1994) suggest that this overturning can be accomplished by recirculations along stacked and sloping isopycnal

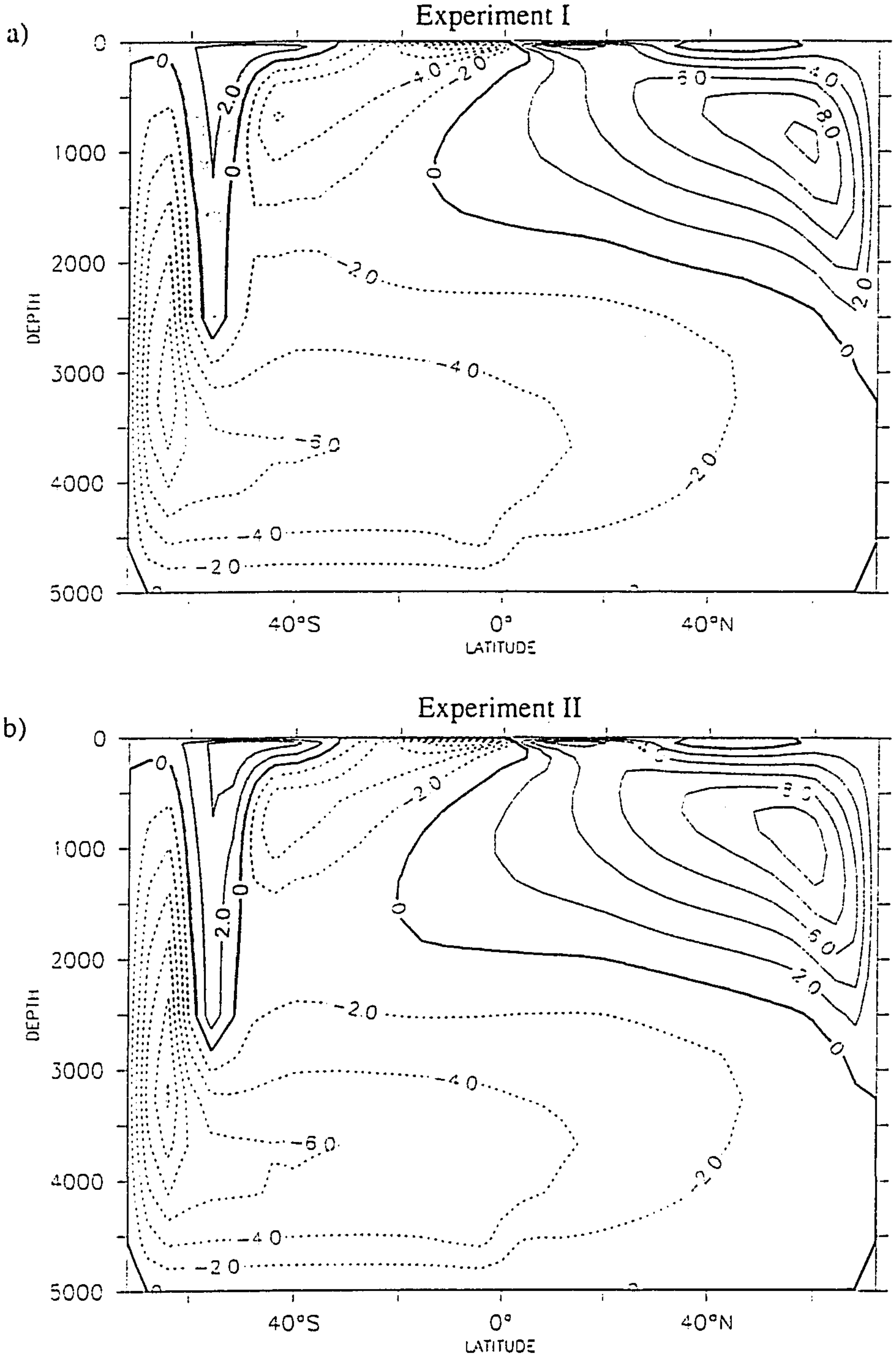

FIGURE 3.3 Overturning stream function for a) Experiment I (normal winds), b) Experiment II (strong winds), c) Experiment III (weak winds). Contour interval is 2 Sv.

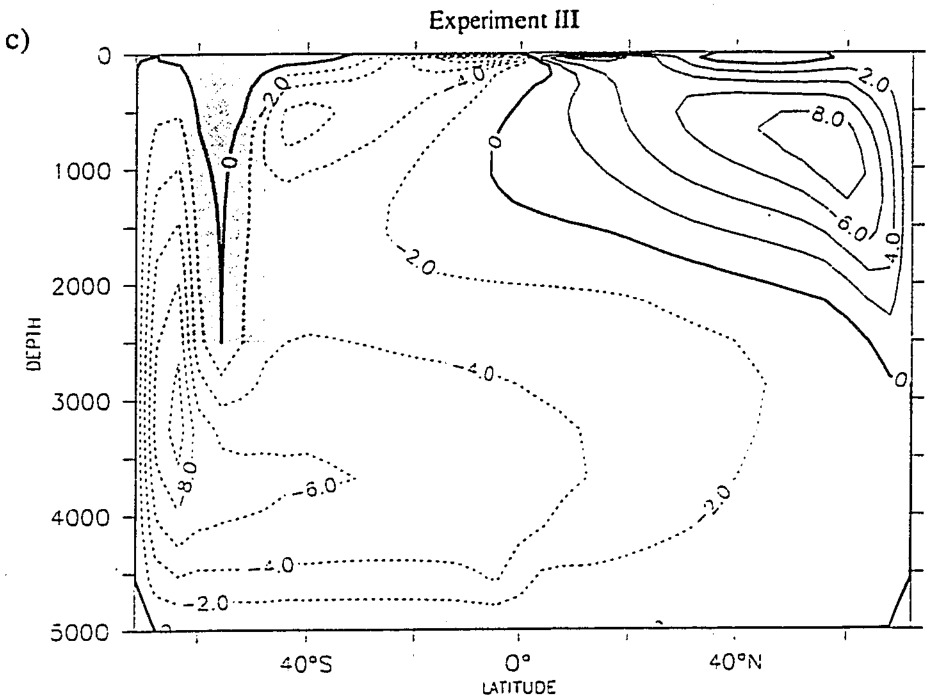

FIGURE 3.3 (Continued)

surfaces. This is true north of Drake Passage, where meridional boundaries allow isopycnal surfaces to reside at different depths across the basin. Within the latitude band of the Drake Passage, however, there can be no net zonal slope to isopycnal surfaces, and the circulation indicated by the Deacon Cell in this model cannot be accomplished without crossing isopycnals.

Note that the Deacon Cell in coarse resolution models such as this one is not the same as the Deacon Cell in the eddy resolving model of Döös and Webb (1994). They identify only the recirculation along stacked and sloping isopycnal surfaces *north* of Drake Passage as the Deacon Cell. An additional overturning cell, identified by Döös and Webb as the subpolar cell, upwells water from depths between 1600m and 3000m that does cross isopycnals. That newly upwelled water subsequently moves equatorward as near-surface flow. The density of the water mass being upwelled in Döös and Webb's subpolar cell is consistent with that of North Atlantic Deep Water. Toggweiler and Samuels (1995) suggest that the subpolar cell demonstrates the Drake Passage effect.

Experiments II and III involved increasing and decreasing magnitude of the southern hemisphere *westerlies* by 50%, respectively. The overturning stream functions for these two experiments are shown in Figure 3.3b and Figure 3.3c. The strength of the Deacon Cell varies linearly with τ_x, as discussed above. The strength of the circumpolar current also follows the changes in wind stress in a linear fashion, although the buoyancy forcing alone would maintain some circumpolar flow in the absence of wind forcing.

It can be seen that the northern sinking increases slightly as the wind forcing increases. A better view of where the changes occur is shown in Figure 3.4, where the differences in the velocities between Experiment II (strong winds) and Experiment I (nominal winds) are shown. The near surface velocity differences (Figure 3.4a) show an increase in northward flow all along the western boundary north of the southern hemisphere westerlies. This flow extends northward to the north end of the basin, where it turns eastward and sinks in the northeast corner; it can be seen as extra outflow from that corner in Figure 3.4b. The flow at depth shows that the anomalous southward return also occurs in the western boundary current. The change in barotropic stream function (not shown) reveals very little change away from the region where wind forcing has been altered. It is interesting to note that Stommel (1957) proposed achieving a more accurate representation of the observed circulation in the Atlantic by superposing a similar internal mode with the surface wind gyres.

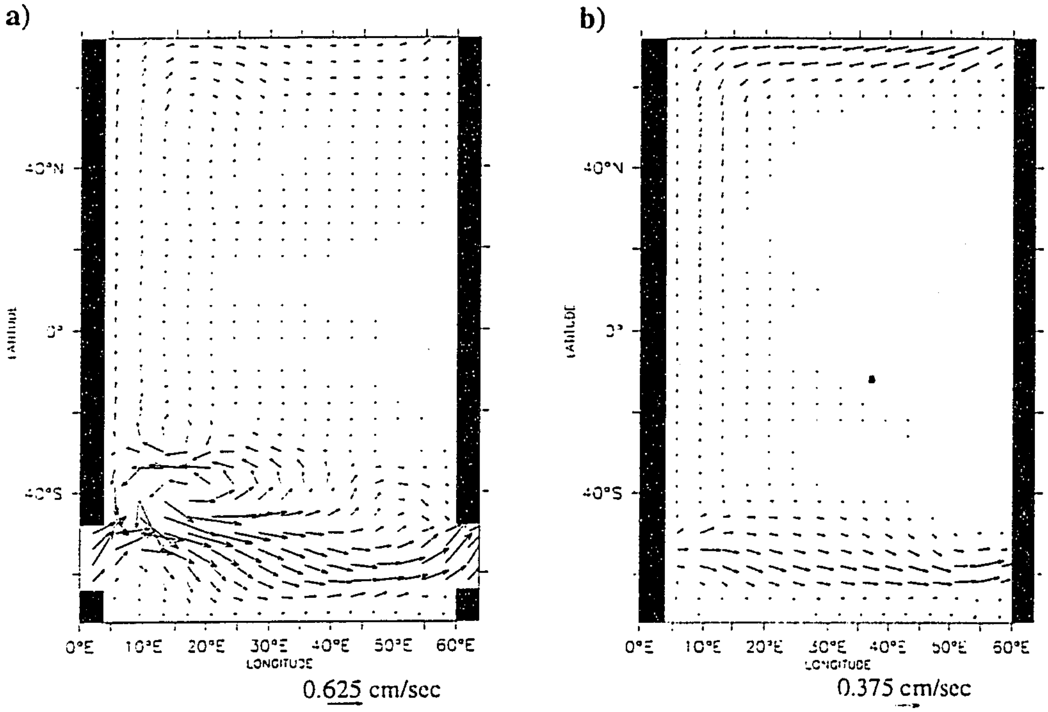

FIGURE 3.4 Difference in velocities, Experiment II - Experiment I, at a) 81m, b) 2687m. Note change of vector length scales.

As a result of increasing the southern hemisphere westerlies to 1.5 times their nominal value, the basin averaged temperature rises by 0.16° C. The zonal mean of this temperature change is shown in Figure 3.5. Sea surface temperatures (SST's), because of the strong restoring boundary condition in temperature, show little change away from the region where wind forcing has been changed. In the region where the wind stress has been strengthened, increased equatorward Ekman drift reduces the SST through advection. This, in turn, reduces the temperature of the convecting columns extending down from the surface, which can be seen as the negative values of temperature difference

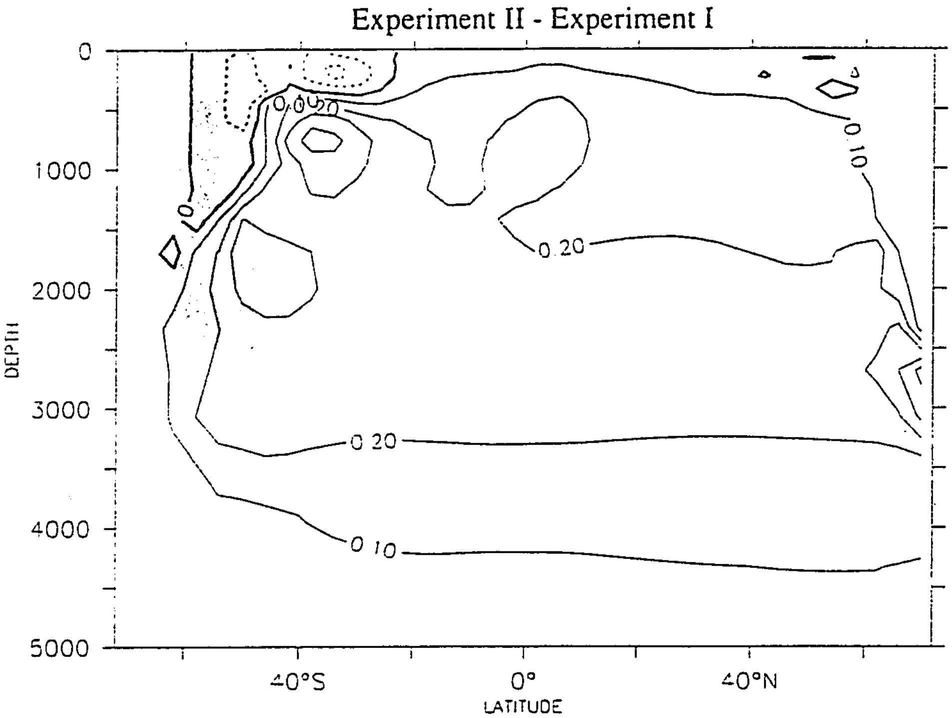

FIGURE 3.5 Zonal mean, difference in temperature, Experiment II - Experiment I (one-basin strong winds - weak winds).

in Figure 3.5. While this surface water is cooler, the water below it becomes warmer as a result of the changed THC associated with the increase in wind stress. Figure 3.5 shows that this increase in temperature at mid-depth is not limited to the region immediately adjacent to the changed wind forcing, but extends to the northern boundary. The local maximum seen near 40°S at about 1000m results from an increase in poleward flow at that depth to supply the ageostrophic "leak" discussed in Section 3.5. The warming at the northern wall occurs as a result of the greater northern overturning, which introduces more water of northern origin at the expense of AABW. As it proceeds southward, the northern-source deep water warms the entire mid-depth basin.

The warming that occurs north of the gap at around 800 m acts to increase the thermal gradient across the latitude band of the Drake Passage. This increases the baroclinicity across the ACC and, through the JEBAR term in the depth averaged vorticity equation (e.g. Mertz and Wright (1992)), produces an increase in barotropic transport approximately ten times larger than that for similar changes in wind stress in an ocean with fixed density structure (see Appendix B).

3.3.2 One Basin, Closed-gap Experiments

The effect of closing Drake Passage on ocean circulation has been explored in other studies (Gill and Bryan 1971, Cox 1989). The role of the gap in the Drake Passage effect hypothesis can be tested by reproducing experiments I - III in a closed basin. Experiments Ic - IIIc repeat the first three experiments without the reentrant channel.

The overturning stream function for Experiment Ic is shown in Figure 3.6. This run is similar to Exp. I, except that the reentrant channel has been filled. All other forcing is the same. As can be seen by comparing Figure 3.6 and Figure 3.3, the circulation is qualitatively different. The colder southern boundary condition creates a southern sinking cell which clearly dominates the circulation. Northern sinking is reduced to approximately 3.5 Sv, and penetrates to only about 2000m, compared to about 3000m in Figure 3.3. It is also interesting to compare these two runs to Figure 5 in Cox (1989). In his experiments, the circulation in the no-gap configuration was similarly dominated by the southern overturning cell, while the addition of a reentrant channel reduced the southern overturning and strengthened the northern overturning.

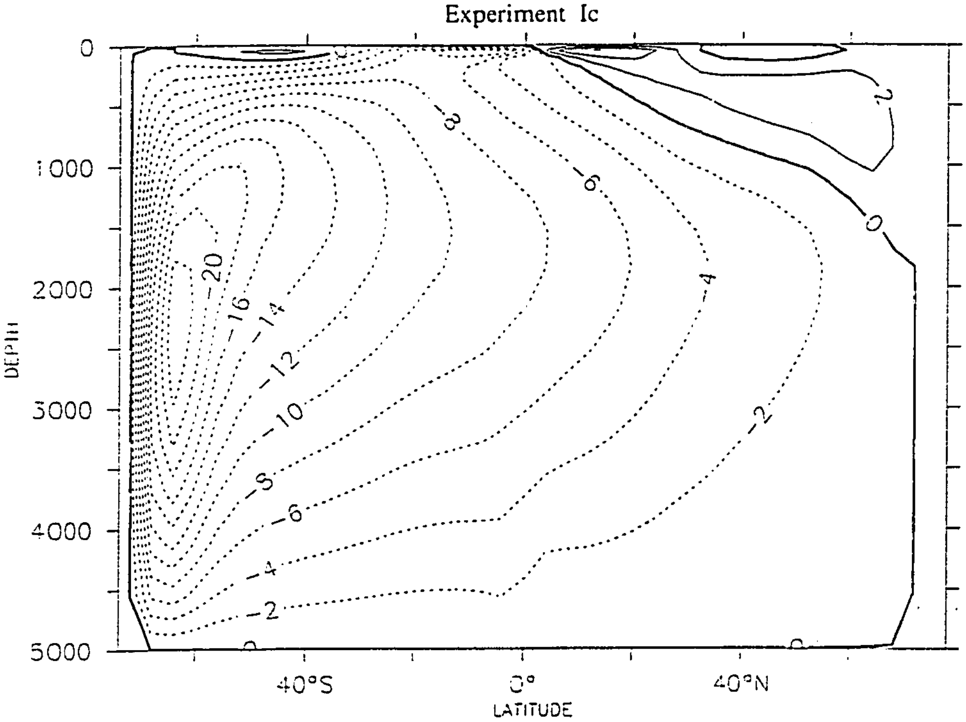

FIGURE 3.6 Overturning stream function, Experiment Ic. Units are Sv.

As discussed in Gill and Bryan (1971), abyssal waters to the north of a cyclic gap are considerably warmer than they would be with a closed basin. They attribute this to the circumpolar current which forms when the gap is open. In order for the circumpolar current to be in geostrophic balance, the density gradient across the circumpolar current must be increased relative to the closed basin case. Since the density in the southernmost latitude is very closely linked to the surface boundary conditions, the density to the north of the circumpolar current must decrease relative to the closed basin case. Figure 3.7 shows the change in zonally averaged potential density in the latitude of the circumpolar current

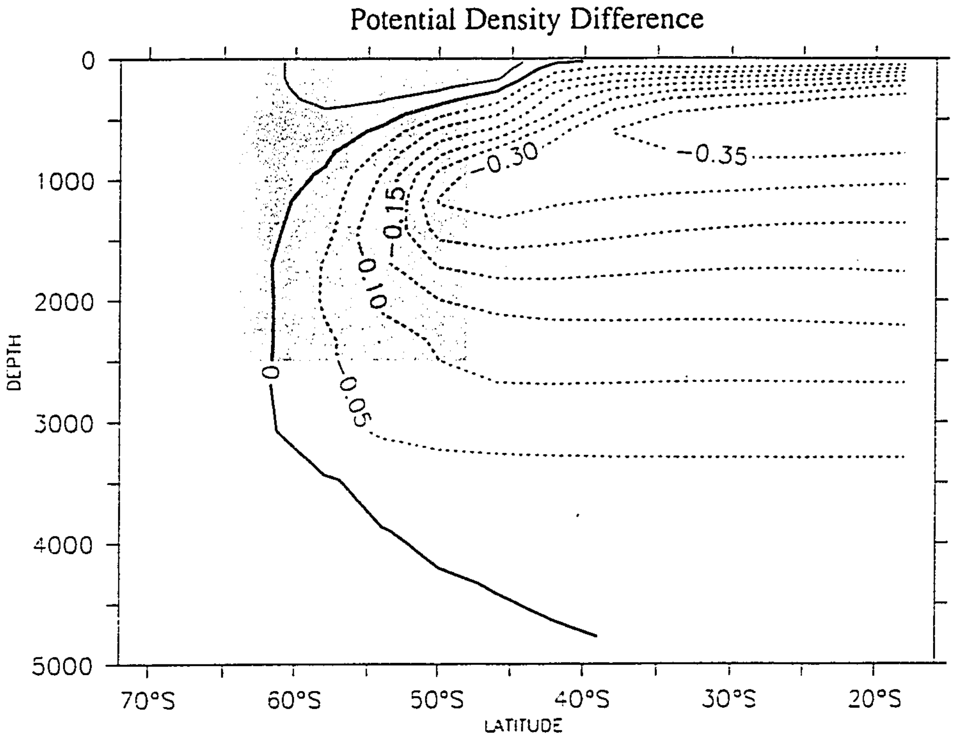

FIGURE 3.7 Difference in zonally averaged potential density, Experiment I - Experiment Ic. Units are kg/m^3, contour intervals are 0.05.

from experiment Ic to I. The circulation depicted in Figure 3.6 (Exp. Ic) produces much denser water to the north of the latitude where the gap was found in Exp. I. The greatest density difference comes from a shoaling of the thermocline, the result of the increased upwelling. The deeper thermocline in the presence of the gap is needed to satisfy geostrophy.

Experiments IIc and IIIc (not shown) repeat the changes in zonal wind stress made in Experiments II and III, respectively. The maximum values of northern sinking are 3.9 Sv and 3.6 Sv, respectively. Note that in the reentrant experiments, the range of northern sinking varied by approximately 1.8 Sv, six times the variation seen in the closed basin experiments (0.3 Sv). North of the location of increased winds, enhanced convergence and downwelling occur, as before. In a closed basin, however, geostrophically balanced southward flow can occur immediately below the surface Ekman drift. In the reentrant experiments, the change in northern overturning was between one-third and one-half of the change in wind driven surface Ekman flow, while in the no-gap experiments it is less than one-tenth as large. While the greatly reduced northern overturning in the closed basin case makes a direct comparison with the reentrant channel case difficult, it does appear that the southern hemisphere winds are less able to influence northern sinking in the absence of a cyclic gap. A greater exploration of the role of the Drake Passage configuration is conducted in Section 3.4.2.

3.3.3 Two-Basin

In a one-basin configuration, deep water of northern origin has no choice but to upwell within the single basin. In a multi-basin or global ocean model, the North Atlantic Deep Water (NADW) can become part of the circumpolar water and leave the Atlantic basin, to upwell elsewhere. In addition, the volume of near-surface water forced north by the westerlies and replaced from depth varies linearly with the longitudinal extent of open ocean. In the real ocean, the southern hemisphere westerlies act over 360°, while in the one-basin configuration the winds act over only 60° of ocean. This reduces the magnitude of the northward wind drift to one-sixth of the value it would have in a global ocean model, while the areal extent of the North Atlantic remains similar. In order to assess the role of a second basin on the Drake Passage effect, a series of two-basin experiments was conducted.

The overturning stream functions for the two-basin, nominal wind case, Experiment IV, are shown in Figure 3.8. The Atlantic basin has 18.9 Sv of sinking in the north, of which 9.1 Sv leaves the basin at 30° S as North Atlantic outflow (Figure 3.8b). In addition, over 6 Sv of Antarctic Bottom Water (AABW) enters the Atlantic basin from the south. The Pacific basin is characterized by upwelling everywhere except in the wind driven gyres and near the surface in the north (Figure 3.8c). The total ocean overturning (Figure 3.8a) reveals a Deacon cell with a larger magnitude commensurate with the increase in the ocean's width. The total overturning looks very much like an amplification of the one-basin stream function, although the partitioning of the north into two basins allows each to serve a very different function in the THC.

Experiments V and VI repeated the two-basin configuration and buoyancy forcing with winds adjusted to 1.5 and 0.5 times their nominal values in the southern hemisphere westerlies. Table 3.2 summarizes the changes that take place with the changes in wind stress. As in the one-basin experiments, the magnitudes of the Deacon cell and the circumpolar current both follow τ_x. Note that the Drake Passage configuration that produced values for the circumpolar current of around 170 Sv in the single basin experiments now produces much larger values. For comparability, however, the configuration of the channel is maintained for the two-basin experiments.

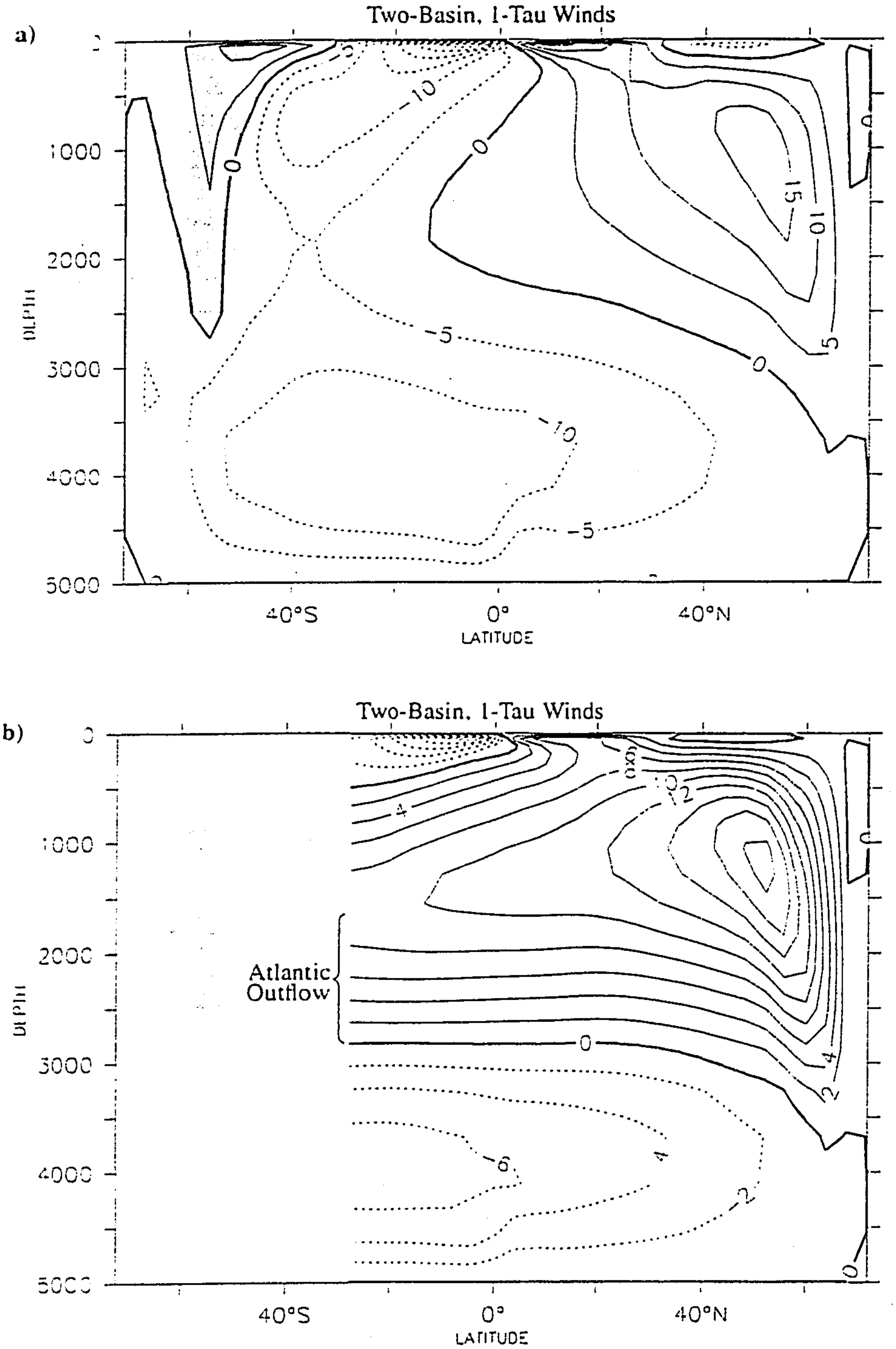

FIGURE 3.8 Overturning Stream Function, Experiment IV a) Whole Ocean, b) Atlantic, and c) Pacific. Shaded area indicates location of reentrant channel. Units are 10^6 m^3/sec.

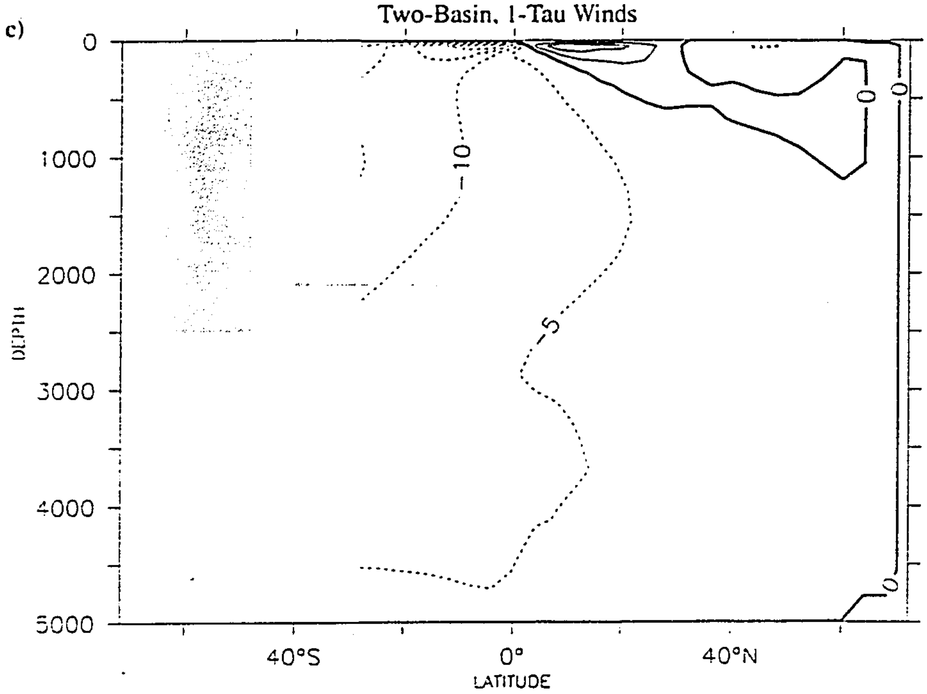

FIGURE 3.8 (Continued)

The Atlantic Outflow is shown in Figure 3.9, plotted against the northward Ekman drift at the latitude of the tip of South America. For comparison, the results of TS93a are plotted as well. Note that for equivalent wind stresses TS93a see twice as much northward Ekman drift because my simplified configuration has a longitudinal extent of only 180°. The sensitivity of Atlantic Outflow to northward Ekman drift is likely to depend on geometry, topography, and the choice of parameters for sub-grid scale processes. A full exploration of parameter space is beyond the scope of this thesis, although a broader exploration of the Drake Passage configuration is conducted in Section 3.4.2.

The change in the deep Atlantic outflow listed in Table 3.2 is nearly 3 Sv. By comparison, the change in the deep inflow in the larger Pacific basin is only 0.3 Sv. The

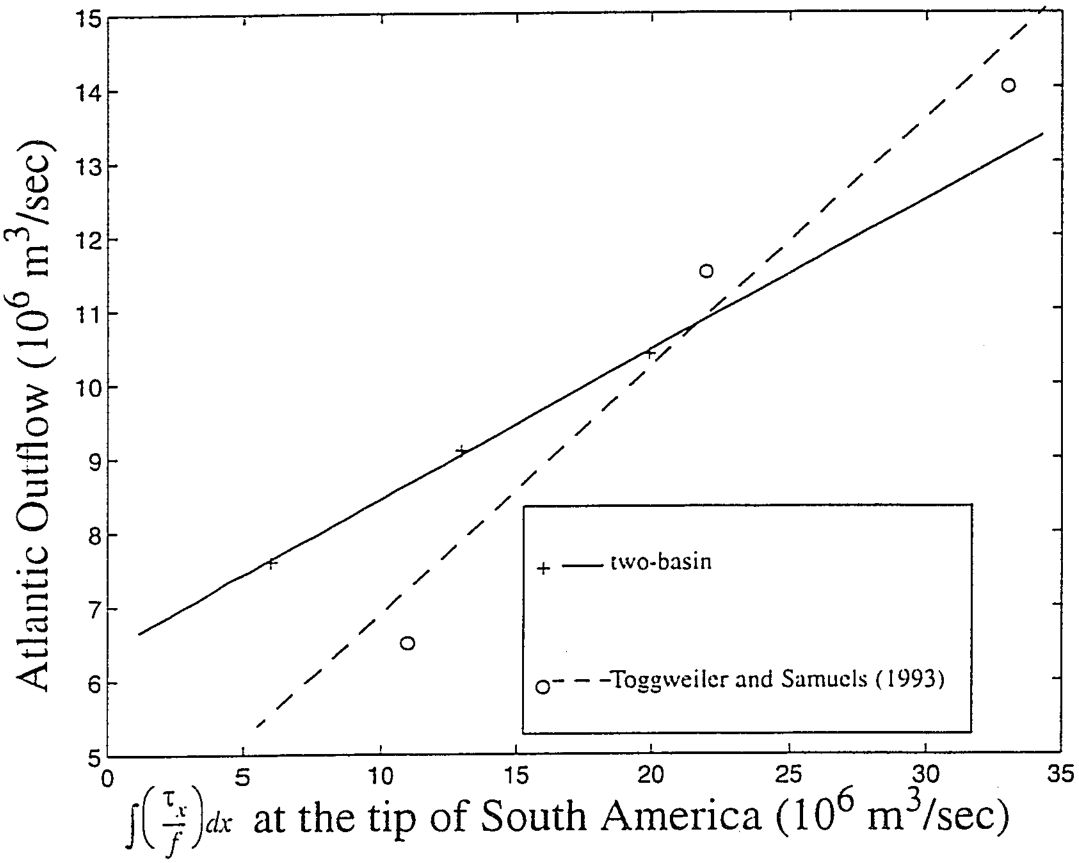

FIGURE 3.9 Atlantic outflow vs. northward Ekman drift at the tip of South America. Two basin cases are shown as (+)'s. For comparison, the results of Toggweiler and Samuels (1993) are shown as (o)'s.

changes in circulation are again concentrated in the western boundary currents, predominately that of the Atlantic basin. The changes in horizontal velocity (Experiment V minus Experiment IV) near the surface and just below the sill are shown in Figure 3.10. The increase in the supply of NADW flowing south beneath the sill is clear in Figure 3.10b. In contrast, the western boundary current flow in the south of the Pacific basin actually becomes more northward with the increase in wind stress, although the change is small.

This indicates that the Pacific basin does not serve as a significant supply for the increased wind driven upwelling.

When the wind stress in the south is increased in the two-basin configuration, the basin averaged temperature increases 0.29° C. The zonal mean of the temperature change for the two-basin case is shown in Figure 3.11. As in the one-basin case, the warming that occurs acts to increase the thermal gradient, and hence the baroclinicity, across the latitude band of the Drake Passage. As in the one-basin experiments, the JEBAR term magnifies the changes in barotropic transport that would occur in a homogeneous ocean.

3.4 The Role of Model Geometry

3.4.1 Longitudinal Extent of Southern Ocean

The two-basin configuration used in Section 3.3.3 depicts a circumpolar Southern Ocean that extends only 180°. In the real ocean, of course, the Southern Ocean extends 360°. For a given wind stress, the northward Ekman mass transport at the surface increases linearly with longitudinal extent. To test the sensitivity of the Drake Passage effect to the longitudinal extent of the Southern Ocean, the two-basin geometry described in Section 3.2 was modified by adding an extension to the Pacific basin as a representation of the Indian Ocean. The extended basin geometry is shown in Figure 3.12. The circumpolar region in this configuration is 240° wide. All surface forcing and parameterization is the same as the two-basin experiments of Section 3.3.3, and the Indian Ocean is subject to the same surface boundary conditions as the Pacific Ocean. The results for the extended two-basin experiments are presented in Table 3.5.

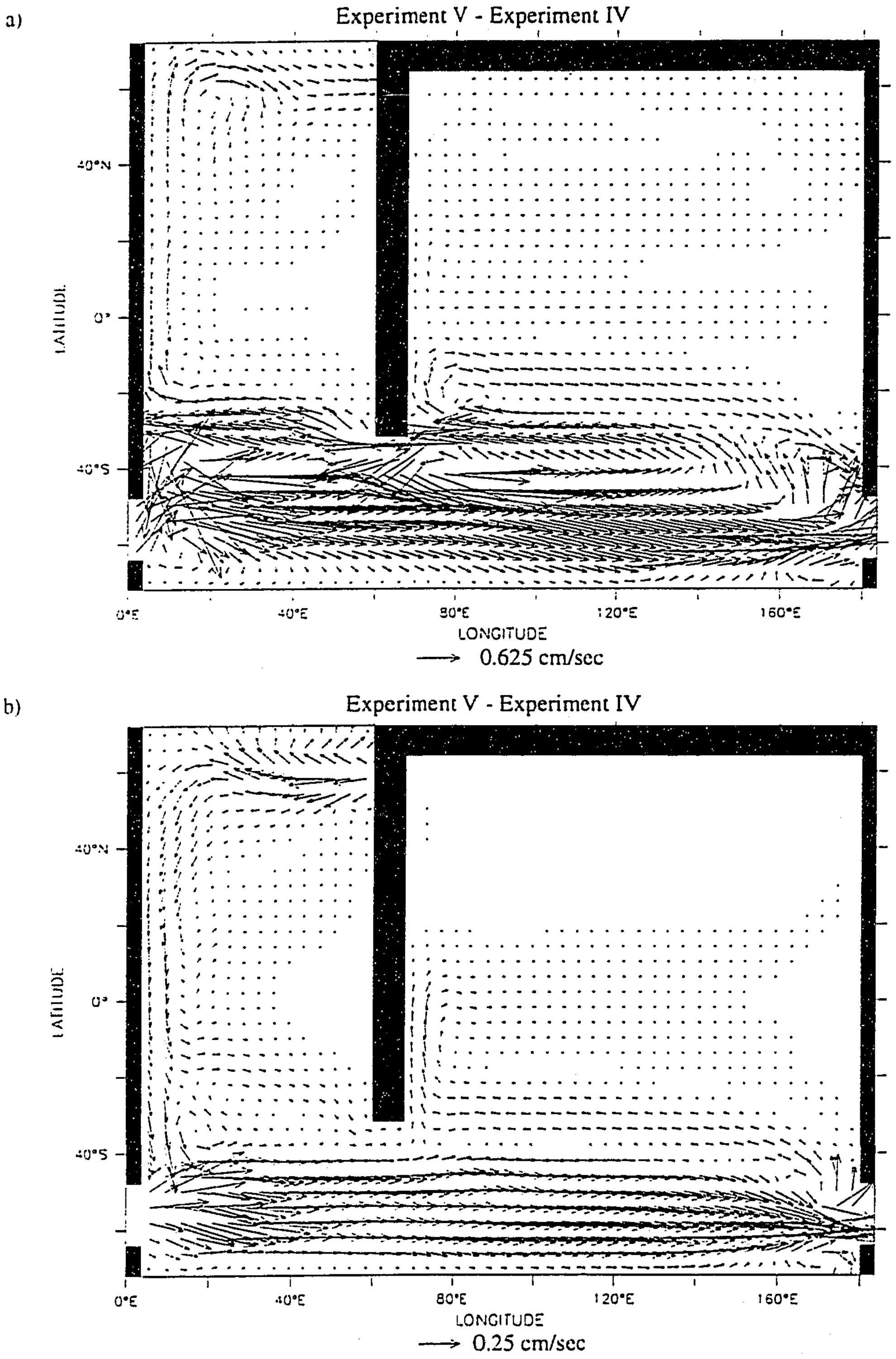

FIGURE 3.10 Velocity difference, Exp. V - Exp. IV, at a) 81m, b)2687m. Note different vector lengths.

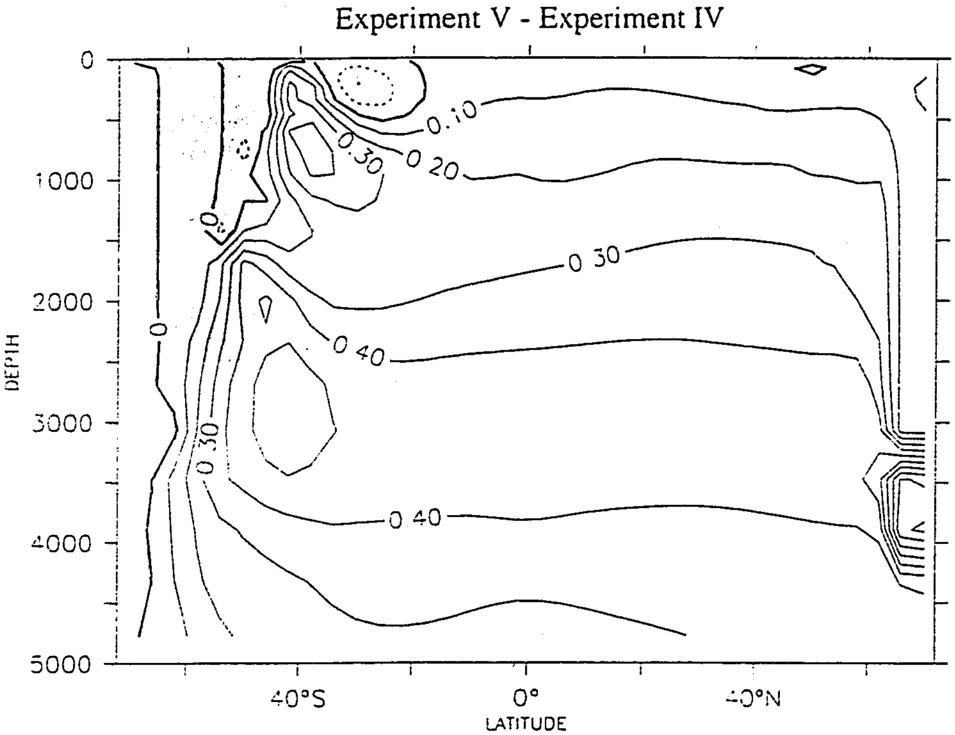

FIGURE 3.11 Zonal mean, difference in temperature, Experiment V - Experiment IV (two-basin strong winds - weak winds).

The increases in the Deacon Cell and ACC strength are the result of the increased longitudinal extent of the Southern Ocean. Note that the Atlantic overturning is larger for all wind stress strengths than in the equivalent standard two-basin experiments (cf Table 3.2). The sensitivity of the Atlantic outflow to changes in the wind stress at the latitude of Drake Passage has also increased. The Atlantic outflow for the extended basin experiments is plotted in Figure 3.13, along with the results from the standard basin configuration and those of Toggweiler and Samuels (1992). As the longitudinal extent of the Southern Ocean is increased, the slope of the Atlantic outflow vs. Northward Ekman drift curves increases. This indicates that while the simple two-basin geometry represents the

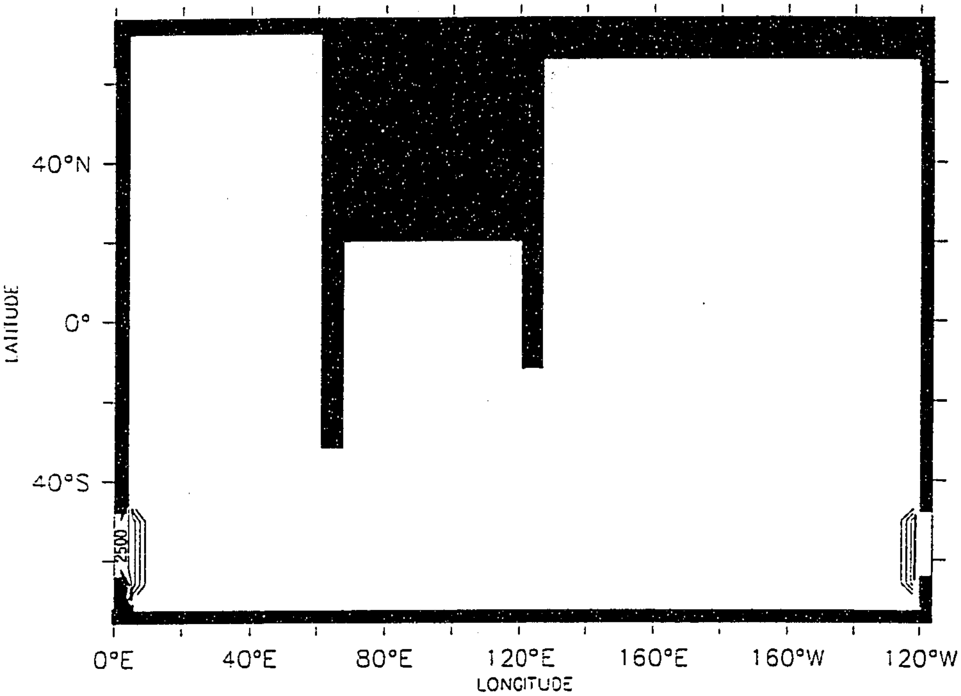

FIGURE 3.12 Basin configuration for extended two-basin experiments. Contours indicate depth, contour interval is 500m.

TABLE 3.5 Summary of extended two-basin experiments.

	τ_x max (dyne/ cm^2)	**Deacon Cell Strength (Sv)**	**Circumpolar current (Sv) (in Drake Passage)**	**Northward Heat Transport (max) (10^{15} W)**	**North Atlantic Sinking (Sv)**	**Deep Atlantic Outflow (Sv)**
Exp. B1	1.2	17.80	291.1	0.6354	21.29	11.7
Exp. B2	1.8	27.21	342.1	0.6614	23.16	13.61
Exp. B3	0.6	8.43	230.8	0.5977	18.73	9.35

Drake Passage effect, it underestimates the strength of the influence that would be seen in a global configuration.

3.4.2 Drake Passage Configuration

In Section 3.3, the wind stress acting on the ocean at the latitude of Drake Passage served to regulate the rate of deep water production in the northern sinking regions. The

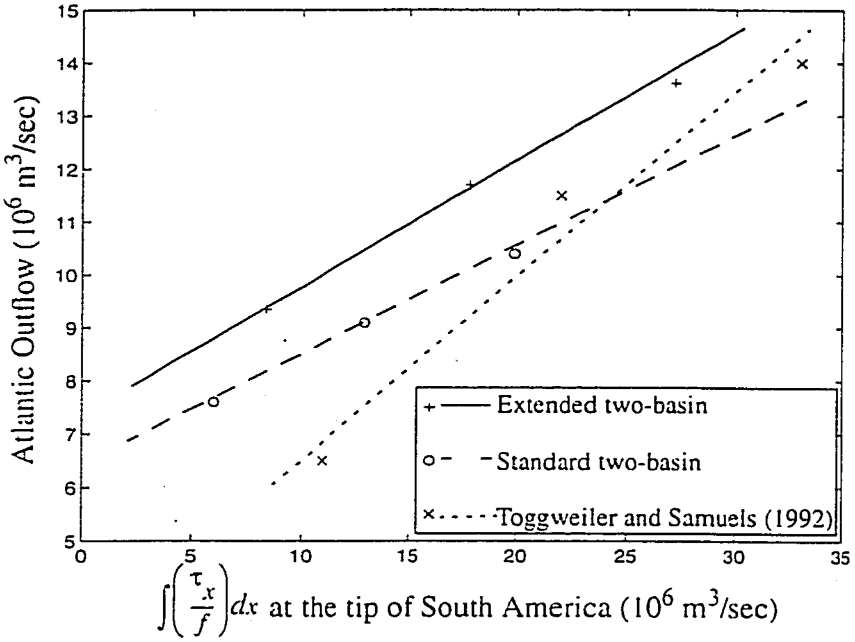

FIGURE 3.13 Atlantic Outflow vs. Northward Ekman drift at the tip of South America. (+)'s represent the extended two-basin configuration, (o)'s represent the standard configuration. For comparison, the results of Toggweiler and Samuels (1992) experiments in an idealized world ocean are plotted as (x)'s.

unstratified northern sinking region acted as a "path of least resistance" connecting the upper and lower ocean. The absence of meridional boundaries above the sill in Drake Passage determines that the equatorward surface Ekman drift cannot be compensated geostrophically above the sill depth. Some of the water transported to depth in the northern sinking region flows south of the latitude of Drake Passage, where it is available to upwell and supply the northward wind drift at the surface.

The wide Drake Passage used in the experiments of section 3.3.1-section 3.4.1 is a crude representation of the actual topography of Drake Passage. As previously noted in section 3.2, the number of grid points chosen to represent Drake Passage was motivated by the need to obtain a reasonable flow through the passage, rather than to adhere strictly to the true bathymetry. The region without meridional boundaries is essential in establishing the link between southern hemisphere winds and northern deep sinking, so it is important to understand how the representation of this region influences the meridional overturning. In this section we examine the model's sensitivity to the idealized representation of Drake Passage.

The original Drake Passage configuration for this model was selected to produce an ACC of approximately 150 Sv in the one-basin geometry of Experiments I-III. When the second basin was added for Experiments IV-VI, this wide reentrant channel produced ACC transports of over 200 Sv. The strength of the ACCs in these experiments was approximately twice as large as the observed flow through Drake Passage, estimated by Whitworth et al. (1982) to be 130 Sv ± 15 Sv. The first change in the simulated Drake Passage configuration reduces the ACC transport by extending the tip of South America southward by 4° (the narrow Drake Passage experiment). In the standard Drake Passage experiments, the tip of South America is at the latitude of the maximum wind stress. In the narrow Drake Passage experiments, the wind stress at the tip of South America is smaller, and the Drake Passage effect is also expected to be smaller.

A model with resolution of 3.75° x 4° does not represent the many islands found at the latitude of Drake Passage. When the islands at this latitude are considered, the region of the ocean without meridional boundaries at the latitude of Drake Passage is nowhere deeper than 1000 meters. A second modification of the idealized Drake Passage considers the importance of the depth of the meridionally unbounded region. Numerical simulations are conducted in which the sill depth of the standard Drake Passage is varied. In order to investigate the importance of the representation of sill depth in the model's Drake Passage effect, both nominal- and strong- wind forcing are applied.

The final modification of Drake Passage considered involves changes in the geometry of Drake Passage. Here, the latitude band over which there can be no zonal pressure gradient is reduced to one tracer point (4°) by extending South America southward by 8° and the Antarctic Peninsula northward by 4°, and by offsetting them slightly (see Figure 3.14). If the two continents were extended without being offset, a 4° gap would allow one tracer point and no velocity points, and hence no ACC. The geometry incorporated here allows for the formation of an ACC although the latitudinal band without meridional boundaries is actually narrower than that caused by the real topography. This configuration is very similar to a schematic representation of Drake Passage suggested by Stommel (1957), although he extended the two boundaries to the same latitude, so there was no longer any latitudinal band without meridional boundaries. Pressure gradients in the GFDL MOM model are calculated on the velocity grid points, so there is no latitude where velocity calculations are made without the influence of a meridional boundary.

3.4.2.1 Narrow Drake Passage

When Drake Passage is narrowed by 4° in the two-basin model, the magnitude of the ACC is reduced from 265 Sv to 182 Sv. This value is still larger than, but much closer to, estimates of the actual transport. This indicates that the wide Drake Passage configuration used to achieve reasonable throughflow in a one-basin configuration is not necessary

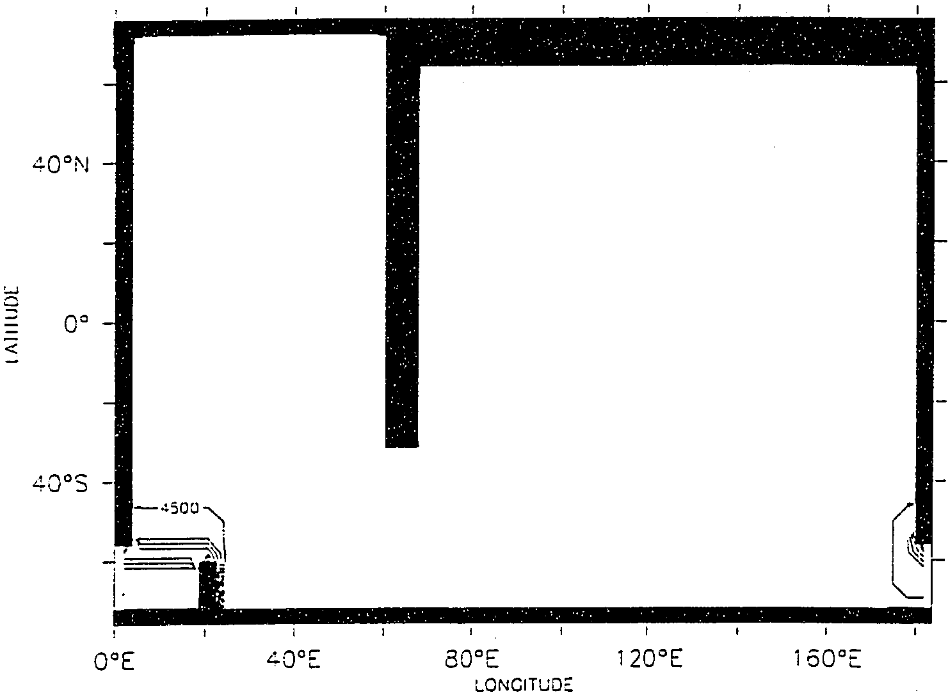

FIGURE 3.14 Basin configuration for offset-Drake Passage experiments. Contours represent depth, contour interval is 500m. Shaded walls are idealized continental boundaries.

in a two-basin configuration of this resolution. It argues that a more accurate representation of the Drake Passage geometry could be used in the two-basin model. The Atlantic basin outflow, as defined in Section 3.3, is seen to be significantly reduced. The reduction is in keeping with the idea that the northern overturning is regulated by the integrated northward Ekman drift at the latitude of the tip of South America. By extending the continent 4° farther south, the wind stress at the tip is reduced, and the northern overturning is reduced.

The Atlantic outflow for both the wide and narrow Drake Passage configuration is plotted against northward wind drift in Figure 3.15. If the reduced wind stress were the only influence exerted by the change in Drake Passage configuration, all of the points would lie on the same line. For a northward wind drift of 10.5 Sv, by this estimate, we would expect over 8 Sv of Atlantic outflow. As can be seen in Figure 3.15, however, the overturning decreases more than would be expected by extrapolating the wind stress in the wide Drake experiments down to a value that would produce the same northward Ekman drift at that more northern Drake Passage boundary.

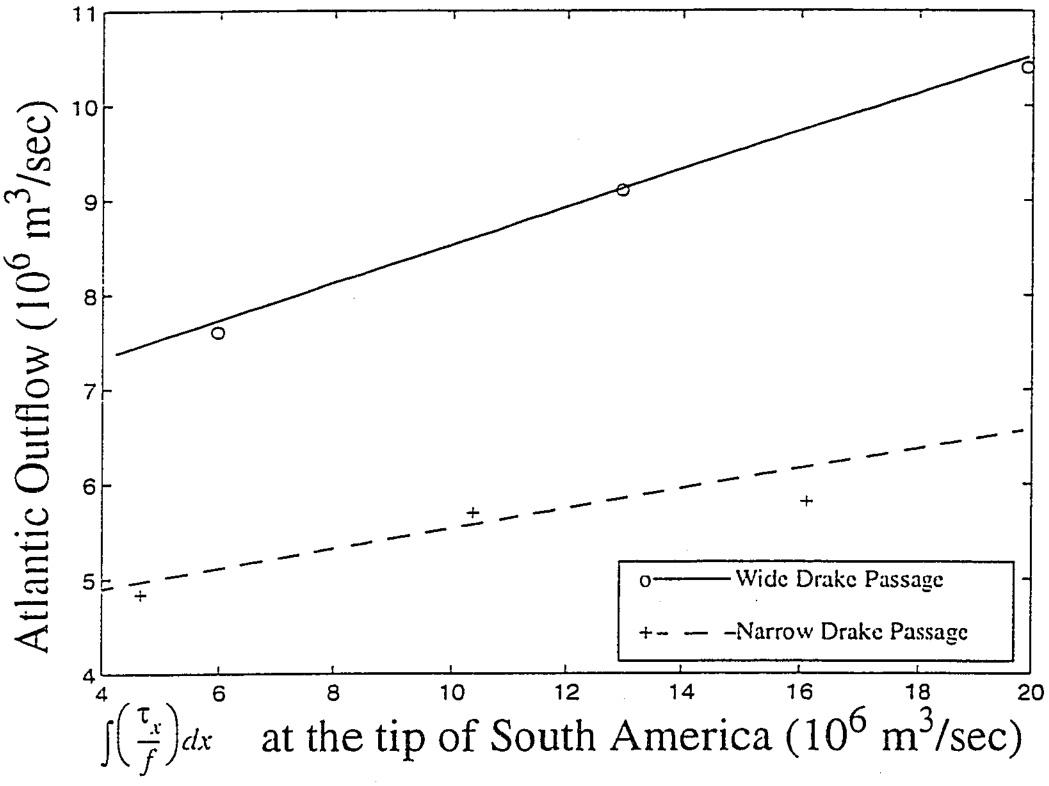

FIGURE 3.15 **Atlantic outflow vs. northward wind drift at the latitude of Drake Passage. Solid line indicates values for Drake Passage extending from 48°S to 64°S, dashed line indicates values for Drake Passage extending from 52°S to 64°S.**

In the two-basin experiments with the narrow Drake Passage, the Atlantic Outflow is smaller, and less sensitive to wind forcing than it was in the wide Drake experiments. The reduction in outflow is accompanied by a reduction in the maximum overturning when compared to the wide Drake experiments (See Table 3.2). Part of the reduced outflow can be attributed to the shift in the location of the tip of South America relative to the surface restoring temperatures. Since Drake Passage is farther south in this case, the water columns just north of the gap have a colder surface boundary condition and are less stratified. The reduced stratification makes it easier for more local downwelling to feed the deep southward flow.

3.4.2.2 Sill Depth

The choice of the depth for the idealized Drake Passage was motivated by the actual depth of Drake Passage. If one considers the other topographic features in the latitude band of Drake Passage, however, it is clear that the actual depth above which there can be no zonal pressure gradient is much shallower. In a coarse resolution model such as the one used here, resolving all of the significant topographic features in the southern ocean is untenable. Instead, I investigate the impact of sill depths on model behavior by running a few experiments that differ only in the choice of fixed sill depths.

For this investigation, the two-basin configuration was used. Experiment IV of Section 3.3.3, with the standard Drake Passage configuration (sill depth 2500m), was taken as the nominal case, and the sill depth was raised and lowered to show the sensitivity of the circulation. For the 'high-sill' experiments below, the sill was raised to 1550m, and for the 'low-sill' experiments it was lowered to 4109m. All other forcing was the same as in Experiment IV in Section 3.3.3.

Raising the sill depth allows the wind driven surface flow to be replaced more easily by intermediate water than was possible in Experiment IV. As seen in the overturning stream function in Figure 3.16a, the vertical extent of the Deacon cell is reduced. The higher sill allows water formed locally near Drake Passage to penetrate to near sill depth, increasing its ability to compensate for the northward Ekman drift within the latitude of the gap. The overturning associated with AABW has become more vigorous, and returns southward at a shallower depth. Comparing the Atlantic outflow in Figure 3.16b with that seen in Experiment IV shows that, under the same forcing, a higher sill results in less Atlantic outflow.

The overturning stream function for the low-sill experiment is shown in Figure 3.17. In contrast to Experiment IV, it is more difficult for intermediate water formed north of the gap to contribute to the southward return flow. The overturning associated with AABW, as depicted in Figure 3.17a and Figure 3.17b, is weaker than that in the nominal-sill experiment, although the magnitude of the change (approximately 2 Sv) is not well resolved by the contour interval. In response to both of these influences, the Atlantic Outflow increases. Note that convection and sinking to the bottom occurs at the southern boundary in the low-sill case, although zonal averaging clouds the fact in Figure 3.17a.

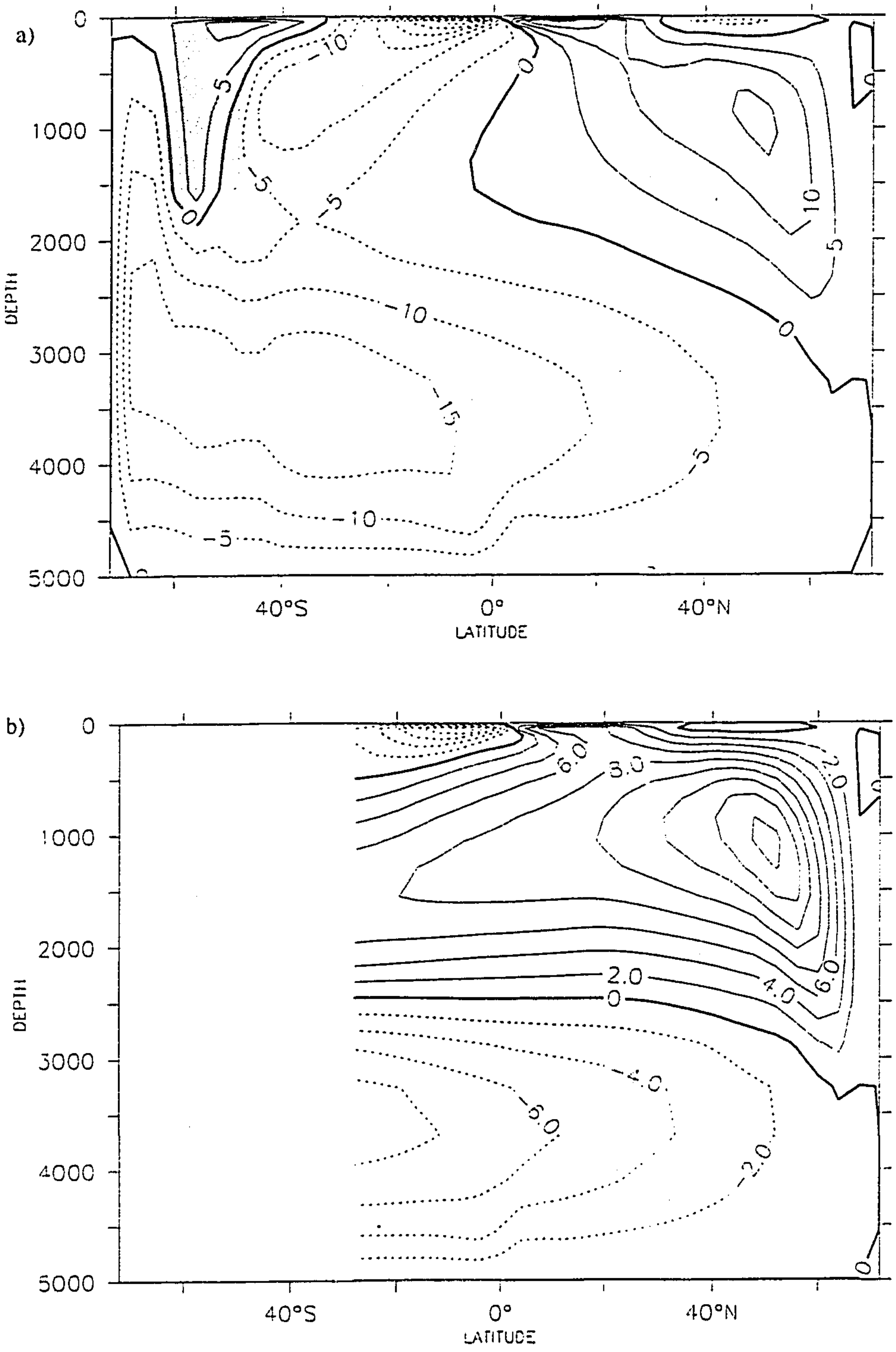

FIGURE 3.16 Overturning stream function for 'high sill' case, a) Total, b) Atlantic, and c) Pacific. Units are 10^6 m^3/sec (Sv). Shading indicates location of Drake Passage.

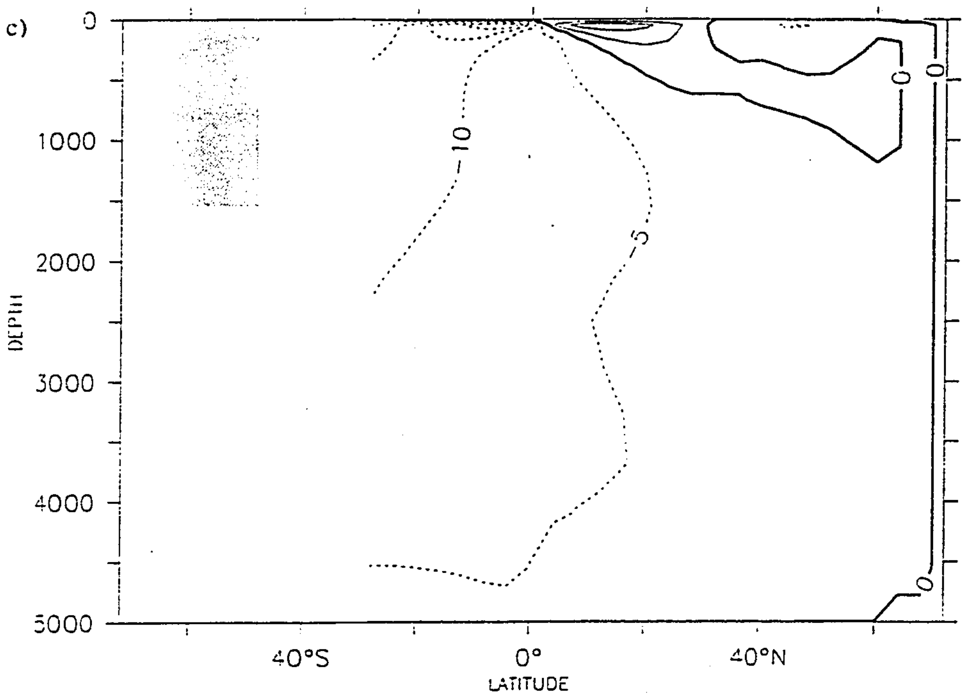

FIGURE 3.16 (Continued)

The impact on the AABW overturning cell warrants further discussion. Comparing the nominal-sill run (Experiment IV) with the low-sill and high-sill runs illustrates an additional impact of Drake Passage geometry on northern overturning in numerical models. The dynamical constraint of no net geostrophic flow above sill depth has been discussed in the context of the southward flow supplying the upwelling that feeds the Northward Ekman drift at the surface. This same constraint acts to limit the geostrophically balanced southward supply of water to the bottom water formation regions. Therefore, the southward flow across the latitude of Drake Passage that supplies these sinking regions is either ageostrophic or it occurs below the tops of the model topography. A

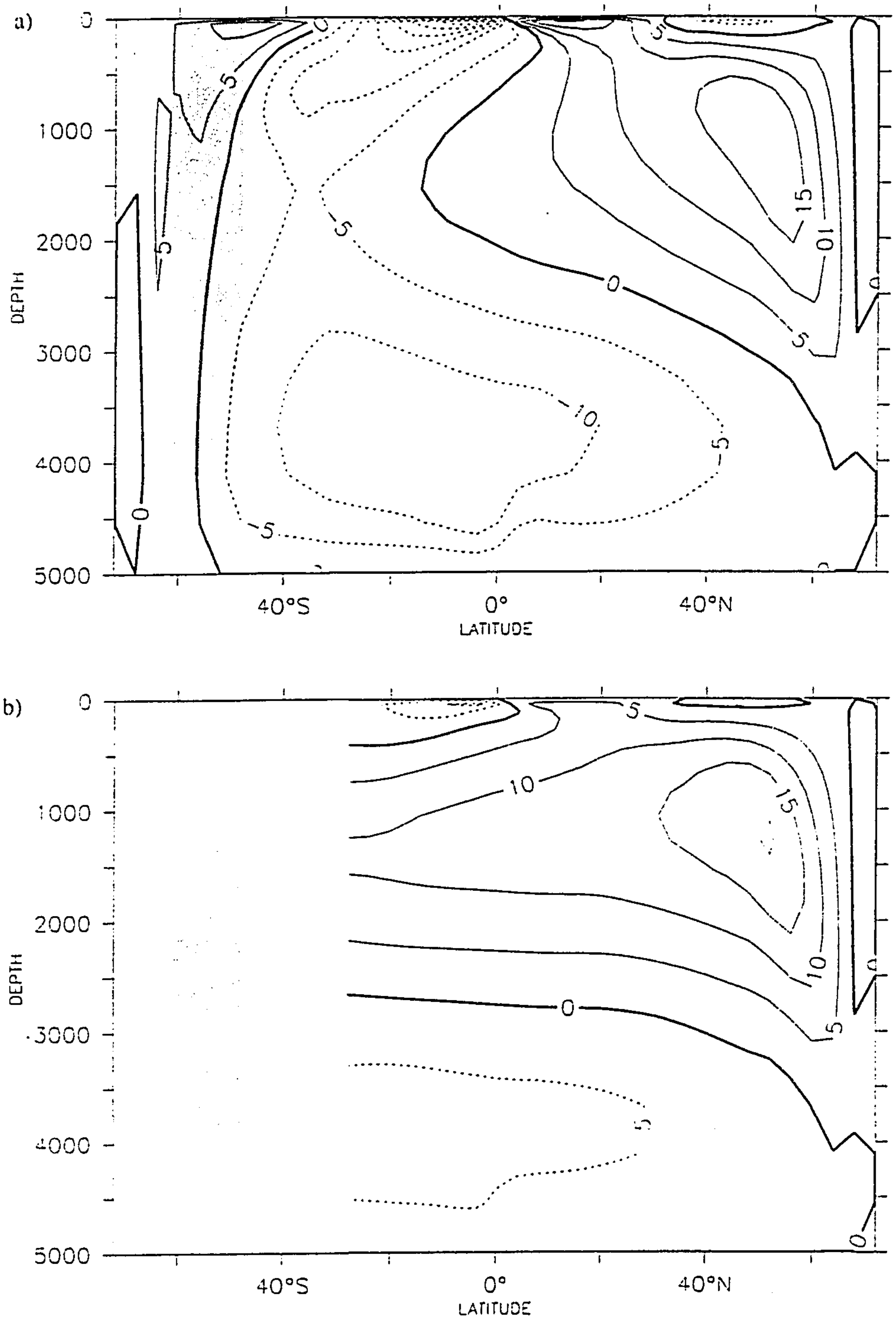

FIGURE 3.17 Overturning stream function for 'low sill' case, a) Total, b) Atlantic, and c) Pacific. Units are 10^6 m^3/sec (Sv), contour intervals are 5 Sv. Shading indicates location of Drake Passage.

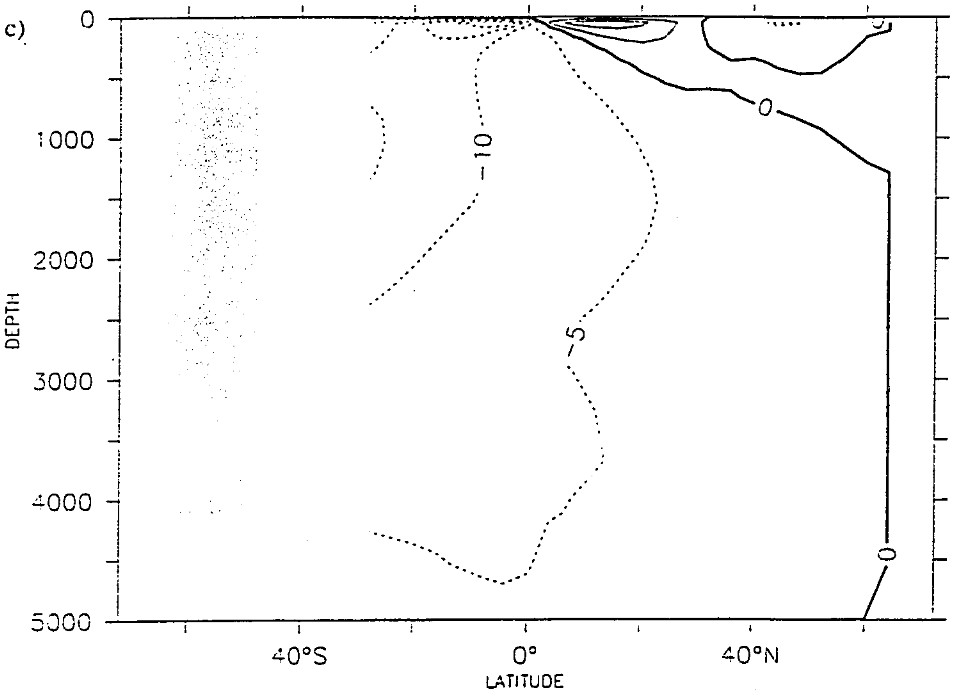

FIGURE 3.17 (Continued)

lower sill works to the disadvantage of AABW and to the advantage of NADW in the competition between the two water masses.

In order to assess the impact of the representation of sill depth on the Drake Passage effect, strong wind equilibrium solutions were found for the low- and high-sill configurations. The results of the sill-depth experiments are presented in Table 3.6. The strength of the Atlantic outflow is plotted in Figure 3.18 for nominal and strong wind forcing on all three (high-, low-, and nominal-) sill depths. The low-sill depth case is seen to have the greatest sensitivity to changes in the wind forcing, while the high-sill configuration shows a small *decrease* in Atlantic outflow with increased wind stress.

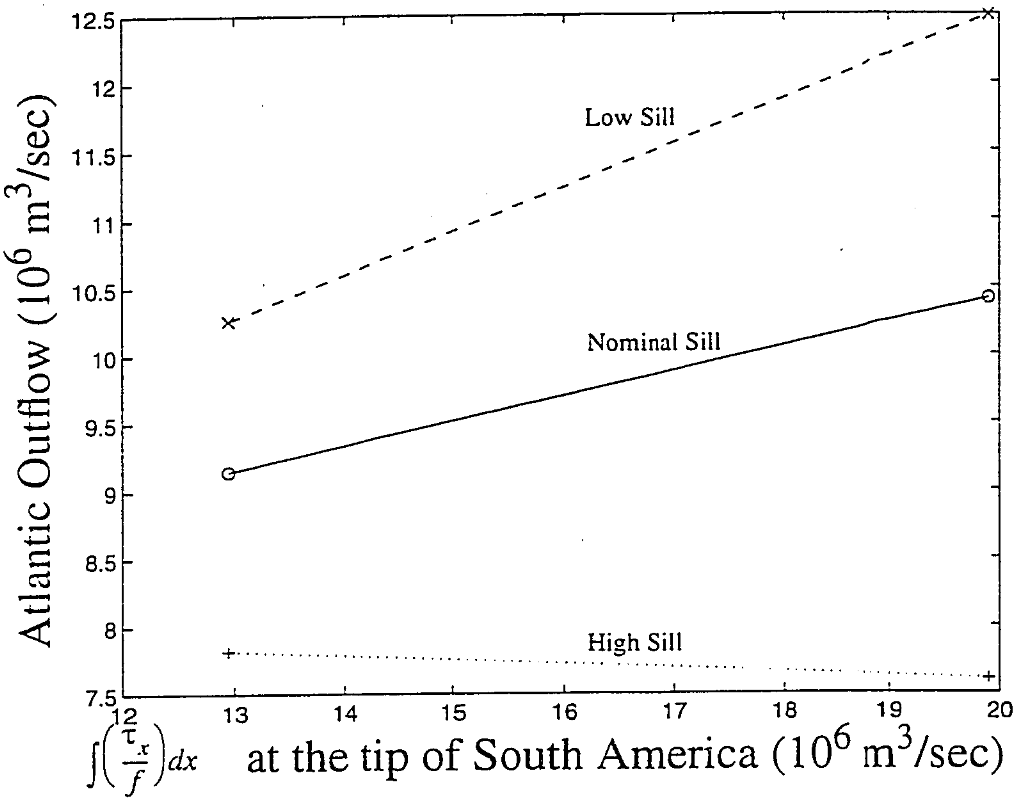

FIGURE 3.18 Atlantic outflow vs. northward wind drift at the latitude of Drake Passage. Solid line (o's) indicates nominal 2450m sill depth, dashed line (x's) indicates low 3900m sill depth, and dotted line (+'s) indicates high 1550m sill depth.

In the case of the high sill, the reduction in Atlantic outflow with increased winds runs counter to the behavior of the model in all other configurations tested. The maximum Atlantic overturning does show a modest increase (from 16.5 Sv to 17 Sv) as the winds are increased. In all of the Drake Passage configuration experiments, the water column north and upstream of Drake Passage (west coast of South America) is unstratified to approximately 1700m. In the high-sill case, the water column at that location is therefore unstratified to the depth of the sill. The increased upwelling that occurs under strong wind forcing can now draw water downwelled locally, instead of relying on NADW. An unstratified region like this one on the west coast of South America was the primary location for the production of AAIW in England (1992), although it is unlikely that downwelling in this region is a realistic representation of AAIW production. It appears that the way that the model forms intermediate water may be important in assessing the extent to which the wind response can be compensated locally. Models with sufficient resolution to represent the shallower topography in this latitude band may also do a better job of intermediate water production.

TABLE 3.6 Summary of sill depth experiments.

Drake Configuration	Wind Forcing	τ_x max (dyne/ cm^2)	Deacon Cell Strength (Sv)	Circumpolar current (Sv) (in Drake Passage)	North Atlantic Sinking (Sv)	Deep Atlantic Outflow (Sv)
Nominal Sill	Nominal	1.2	12.95	265.1	18.9	9.1
	Strong	1.8	19.90	306.2	20.5	10.4
High Sill	Nominal	1.2	12.93	173.3	16.5	7.8
	Strong	1.8	19.79	189.7	17.0	7.6
Low Sill	Nominal	1.2	12.96	306.1	20.6	10.3
	Strong	1.8	19.90	375.4	23.0	12.4

3.4.2.3 Offset Drake Passage

The surface forcings for the nominal- and strong-wind offset-Drake Passage experiments are identical to those used in experiment IV in Section 3.3.3, only the basin geometry has been changed. The basic circulation of a two-basin ocean with the offset-Drake configuration (Figure 3.14) under nominal wind forcing is shown as overturning stream functions in Figure 3.19. The offset-Drake Passage configuration is much less of a barrier to meridional flow than the nominal Drake Passage configuration was. Much of the northward wind drift from the Southern Hemisphere westerlies returns as shallow southward flow. The Antarctic sinking region is supplied more easily above the sill depth, and AABW production increases. The NADW overturning cell is shallower and less vigorous than it was under similar forcing in the standard-Drake Passage configuration, and AABW spreads upward to take its place (cf Figure 3.8). Atlantic outflow is reduced by approximately 9 Sv to less than one Sv, and the maximum Atlantic overturning is reduced by approximately 8 Sv to 11 Sv. The Atlantic overturning does not seem to be directly supplying the wind driven upwelling in the southern hemisphere; that upwelling is supplied locally. Moving the southern tip of South America poleward of the maximum westerlies reduces the magnitude of the northward wind drift at that latitude, but only by approximately 20 percent relative to the nominal configuration (see τ_x values in Table 3.7).

Increasing the wind stress in the Southern Hemisphere westerlies produces very little change in the Atlantic overturning (not shown). The Atlantic outflow increases by approximately one-half Sv, as does the maximum Atlantic overturning. In general, though, in this Drake Passage configuration, the coarse resolution model produces a greatly reduced Drake Passage effect.

TABLE 3.7 Comparison of offset-Drake experiment.

Drake Configuration	Wind Forcing	τ_x at North of Drake Passage (dyne/cm^2)	Deacon Cell Strength (Sv)	Circumpolar current (Sv) (in Drake Passage)	North Atlantic Sinking (Sv)	Deep Atlantic Outflow (Sv)
Wide Drake	Nominal	1.2	12.95	265.1	18.9	9.1
	Strong	1.8	19.90	306.2	20.5	10.4
Offset Drake	Nominal	1.0	11.90	118.6	11.2	0.5
	Strong	1.4	18.75	137.2	11.9	0.9

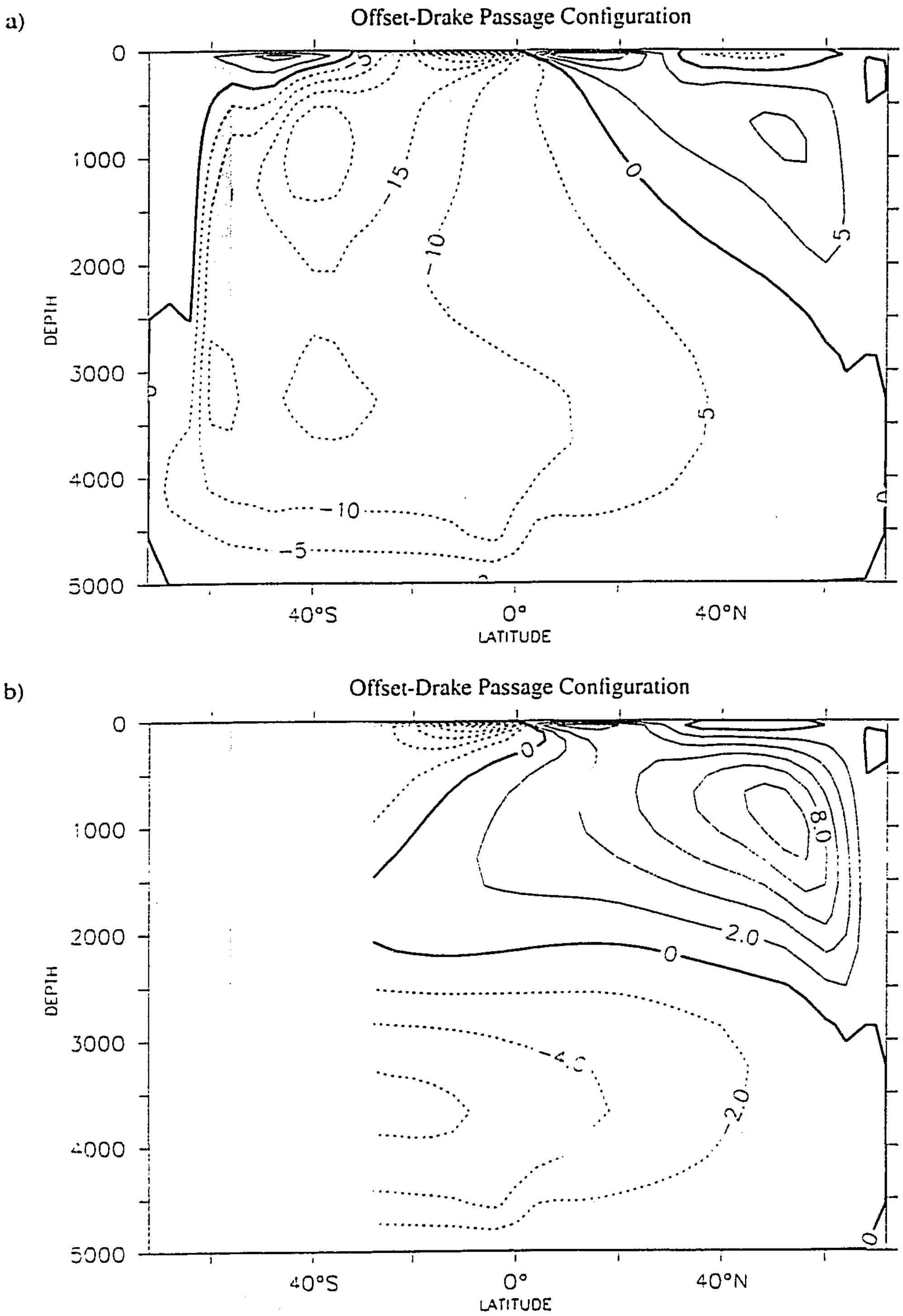

FIGURE 3.19 Overturning stream function for Offset-Drake configuration with nominal wind forcing: a) Global, b) Atlantic, c) Pacific. Units are 10^6 m^3/sec (Sv). Contour intervals are 5 Sv for Global and Pacific, 2 Sv for Atlantic. Shaded area indicates no meridional boundaries.

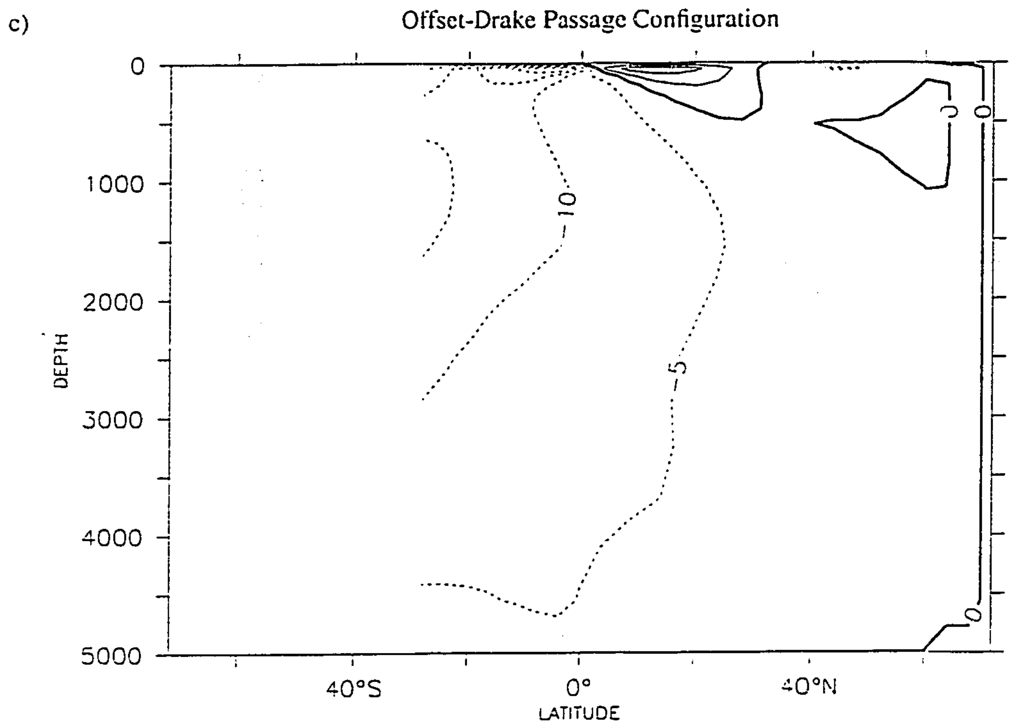

FIGURE 3.19 (Continued)

3.5 Transient Response Drake Passage Effect Experiments

3.5.1 Response to A Switch-On of Wind Forcing

3.5.1.1 One-Basin

In the simplest of the transient cases, Exp. VII, the one-basin model is initially stratified and at rest. The stratification is determined by applying the basin averaged temperature profile from Experiment III (weak winds case) and uniform 34.9 salinity. There is no thermal or haline forcing of any kind at the surface. The winds are the Experiment II (strong winds) westerlies in the southern hemisphere (see Figure 3.2, dashed curve). Winds are applied south of 28°S only; no wind, heat, or salinity forcing is applied north of

28°S. The strongest winds are used to maximize the response. The winds are ramped up to full strength over 20 days, and then maintained. By eliminating surface forcing of any kind away from the area of wind stress, the observation of effects propagating from that area is simplified. There is no surface forcing to damp out or enhance an advancing signal. Likewise, a basin that is everywhere similarly stratified will simplify the calculation of wave speeds. In the absence of surface forcing, however, the stratification is being slowly eroded by vertical diffusion and mixing.

The region of westerly wind stress in the southern hemisphere produces northward Ekman drift. This results in convergence (and hence downwelling) to the north of the wind stress maximum, and divergence (and accompanying upwelling) to the south of the wind stress maximum. The wind forcing produces a change in the barotropic stream function in the southern hemisphere, a circumpolar current, and an anticyclonic gyre roughly centered on the minimum of the wind stress curl (See Figure 3.20). In addition, it excites baroclinic Kelvin-like signals that propagate along the western boundary northward towards the equator.

Once the Kelvin-like boundary modes are excited on the western boundary, the advance of the signal can be compared very directly to the propagation of the signal in Kawase (1987). At the equator, they propagate eastward across the basin like equatorial Kelvin modes. At the eastern boundary, some of the energy is directed poleward as Kelvin-like boundary modes, while some is reflected westward as Rossby modes. The response at the eastern boundary splits evenly into the two hemispheres. In Kawase's model, the advancing signal is dissipated through a damping term in the continuity equation, and the strength of the damping dictates how much of the energy crosses as Rossby modes, and how much continues as boundary modes. In this model, the advancing signal is dissipated through viscous damping and mixing of tracer properties determining the density structure.

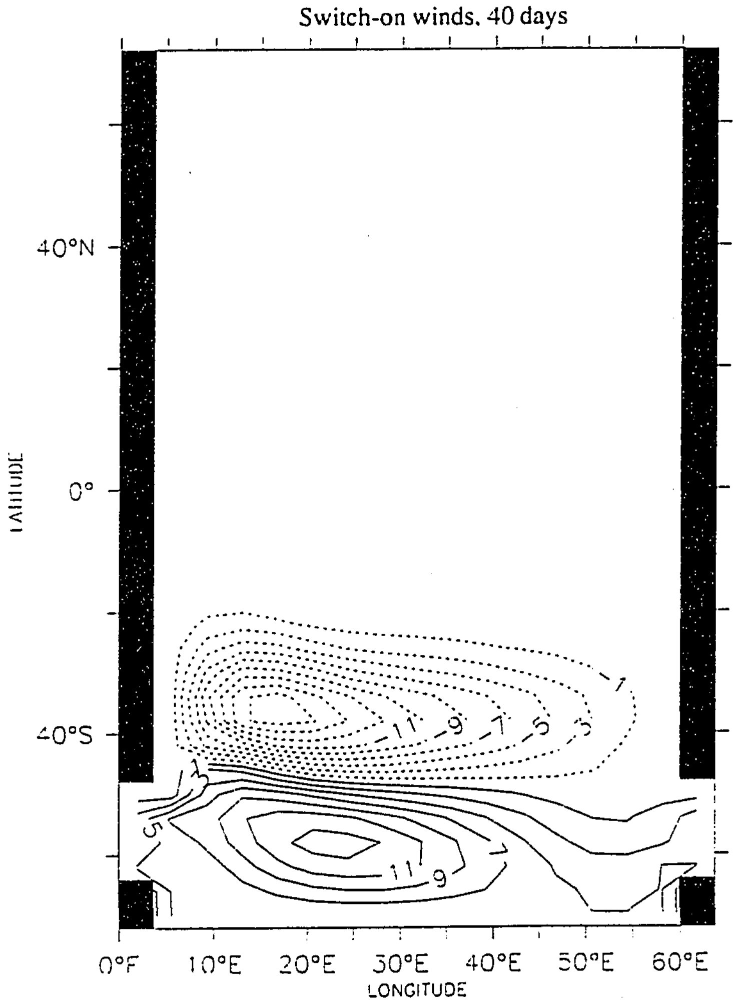
Switch-on winds, 40 days

FIGURE 3.20 Horizontal transport in Experiment VII, 40 days after switch-on of winds. Units are 10^6 m^3/sec (Sv.)

The development of the flow may be seen in Figure 3.21. Because the response in the area of wind forcing is much larger than the response in the rest of the basin, only the area north of 22°S is shown. The advance of the signal can be considered a front that passes by and sets up a circulation in its wake. The reversal of the near surface flow near the equator in Figure 3.21f compared to the earlier flow is the result of the increasing dominance of higher order modes.

Figure 3.22 shows the meridional velocity in the upper layer near the eastern boundary as a function of time. The first three baroclinic modes as determined by the density structure are shown in Figure 3.23. The speed, c, for the first baroclinic mode in Figure 3.23 is calculated to be 2.67m/sec. This speed is used to calculate the advance of the numerical boundary mode indicated by the dashed line in Figure 3.22 (see Appendix A). Note that the advance of the numerical boundary modes is dependent on the model resolution, Δx, and that increasing the resolution would increase the speed of propagation.

The propagation of the Kelvin mode across the north and south in the west can be seen in Figure 3.21c and Figure 3.21d. At the same time, Rossby modes do reach across the basin to the west where they are reflected as higher wave number Rossby modes. These are then trapped, and serve to enhance the western boundary current. The circulation shown in Figure 3.21e represents a state in which the downwelling occurs broadly north of the gap (see Figure 3.24b). The continued wind forcing gradually erodes the stratification just north of the gap. As the southern ocean becomes increasingly

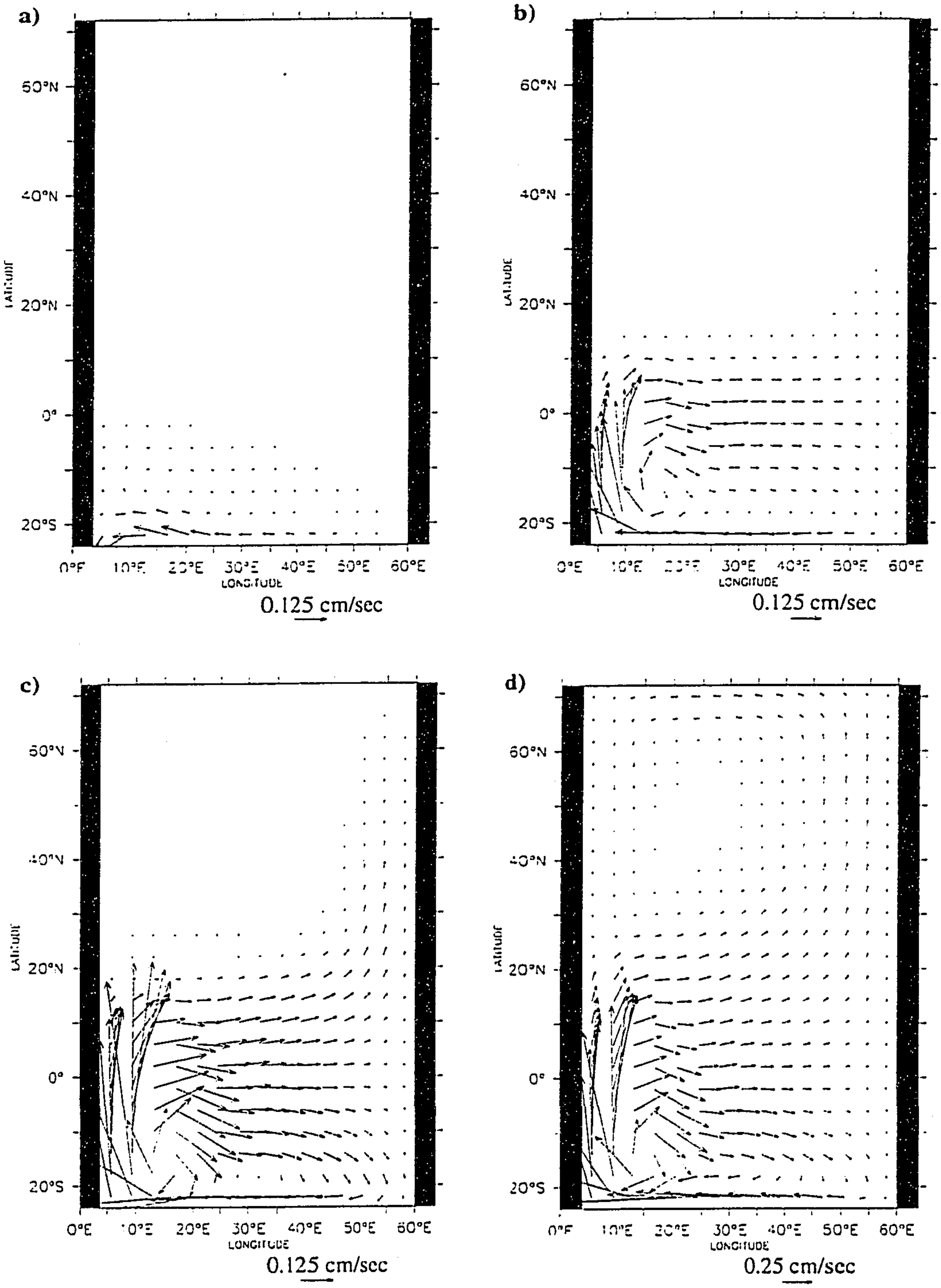

FIGURE 3.21 Horizontal velocities at 81m in Experiment VII, after a) 40 days, b)200 days, c)400 days, d)3 years, e)7 years, and f)50 years. Note different vector lengths.

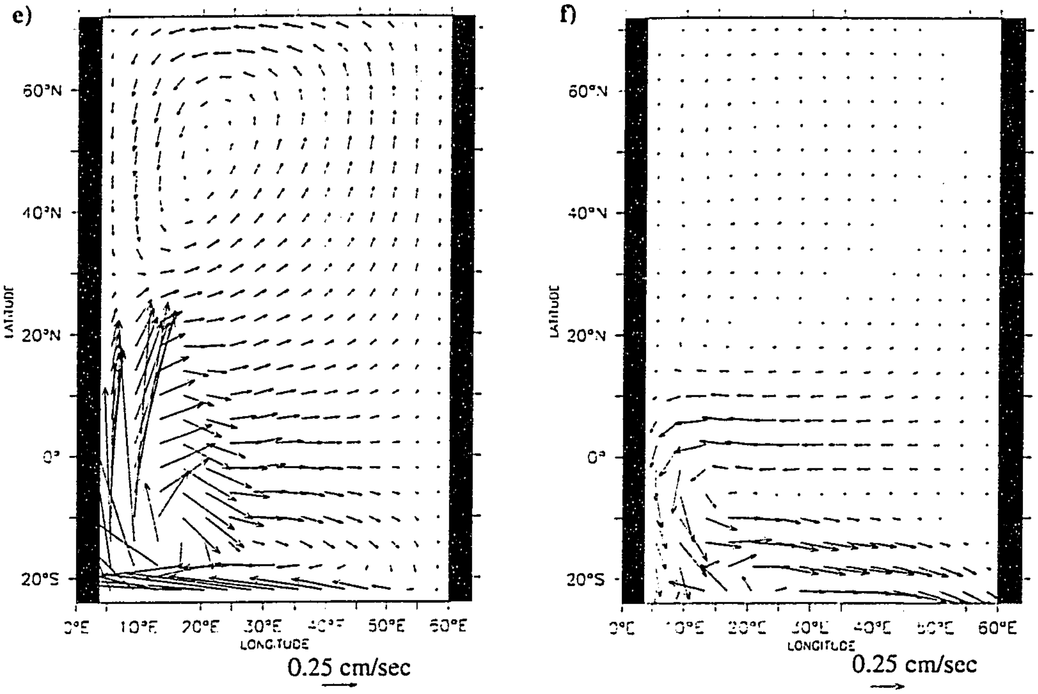

FIGURE 3.21 Horizontal velocities at 81m in Experiment VII, after a) 40 days, b)200 days, c)400 days, d)3 years, e)7 years, and f)50 years. Note different vector lengths.

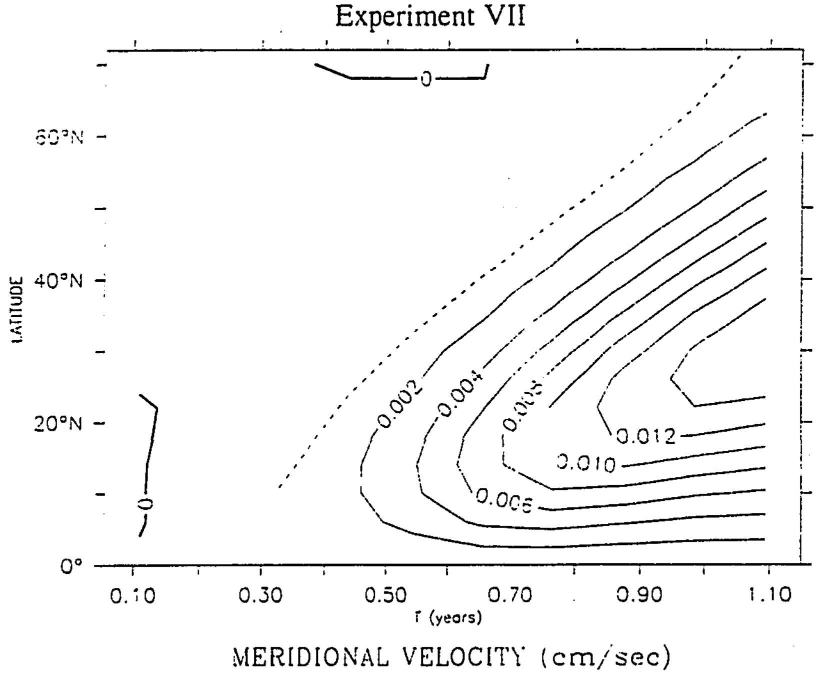

FIGURE 3.22 Meridional surface velocity at eastern boundary vs. time. Dashed line indicates the predicted advance of a wave front.

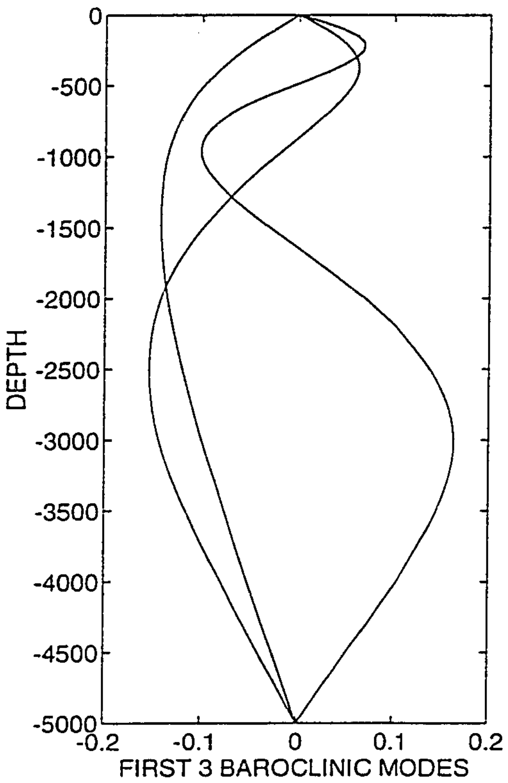

FIGURE 3.23 First three baroclinic modes of the uniformly stratified ocean for the switch-on transient cases, Experiments VII and IX.

unstratified, the sinking concentrates there. In the absence of other surface forcing, the wind driven overturning becomes surface intensified and localized in the region of forcing. Some of the subsurface flow does manage to leak southward ageostrophically above the sill, and some of it downwells and flows southward below sill depth. The shallow ageostrophic return flow occurs as a result of friction on the Antarctic Circumpolar Current (ACC) as it flow through the gap (TS93a), so as the circumpolar current spins up, this shallow return across the latitude band will also increase. This can be seen in both Figure 3.21f and Figure 3.24c. The effect of the higher modes on the overturning is also apparent in Figure 3.24c.

a) Switch-on winds, 40 days

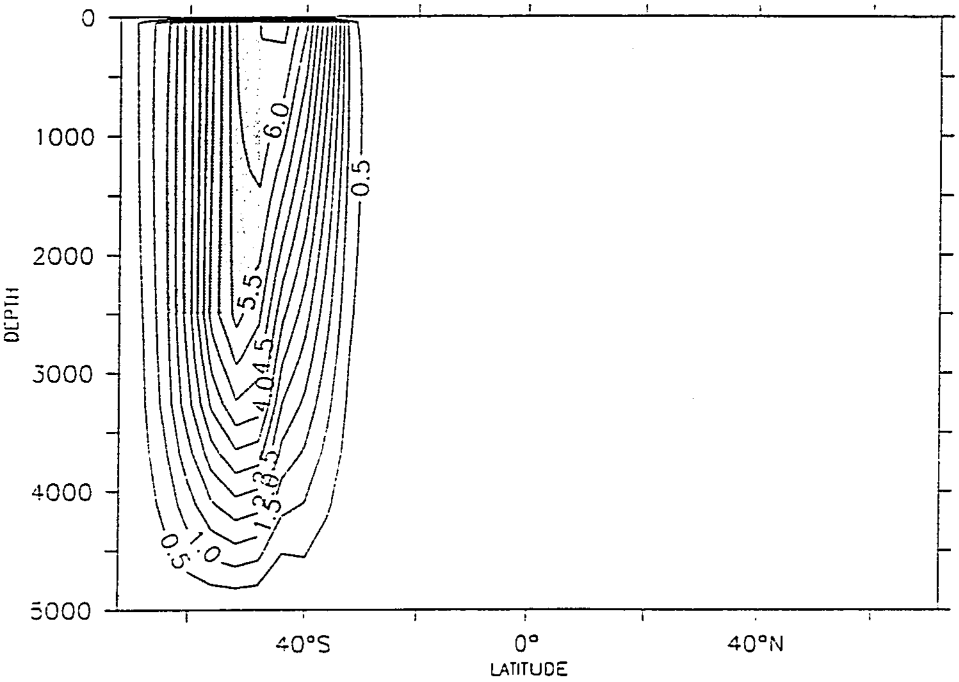

c) Switch-on winds, 7 years

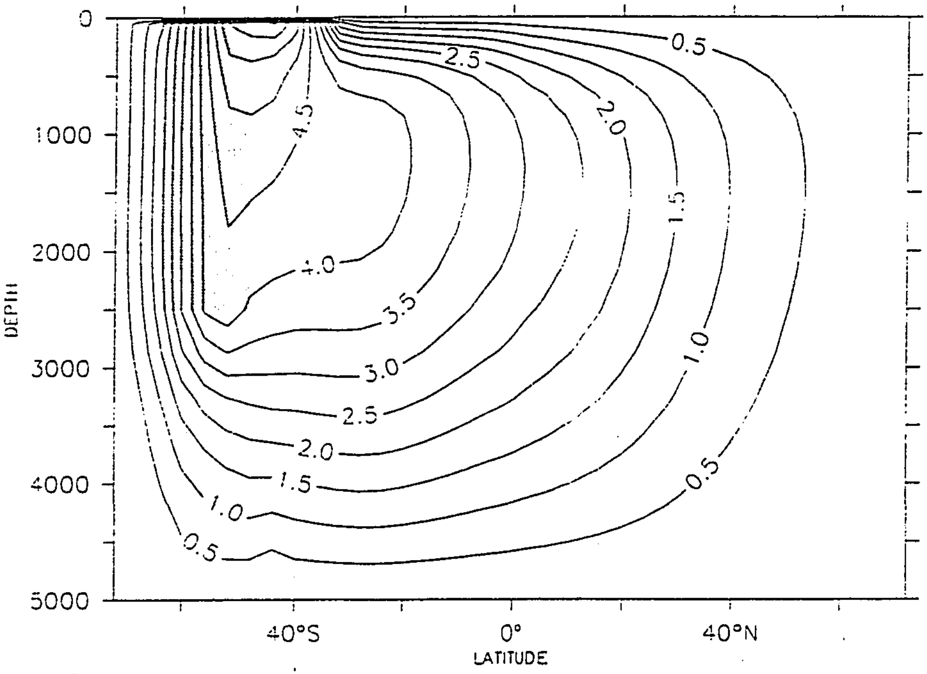

FIGURE 3.24 Overturning stream function for Experiment VII (switch-on transient case) a) after 40days, b) after7 years, and c) after 50 years. Shaded areas indicate location of reentrant channel.

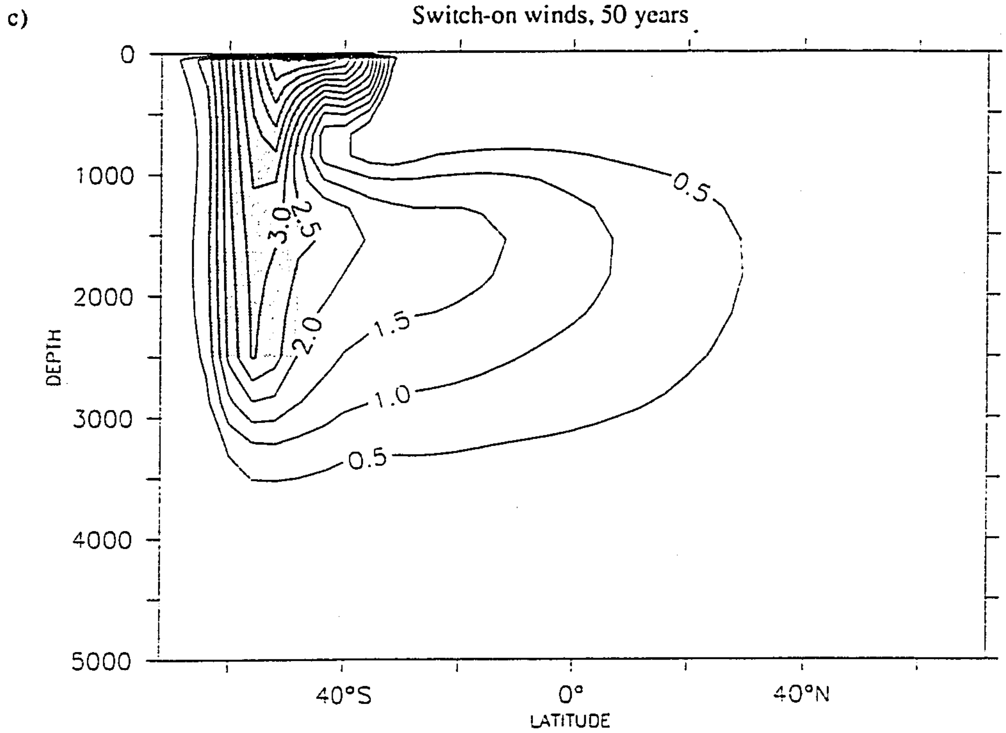

FIGURE 3.24 Overturning stream function for Experiment VII (switch-on transient case) a) after 40days, b) after7 years, and c) after 50 years. Shaded areas indicate location of reentrant channel.

3.5.1.2 Two-Basin

The basic procedures used in Experiment VII are repeated for a two basin case in Experiment IX. The ocean is initialized at rest and uniformly stratified. Winds are applied only in the region of the southern hemisphere where they were applied in Experiment VII. The near surface velocities after 400 and 800 days are shown in Figure 3.25.

The different responses of the two basins to changes in the wind stress allows further investigation into the link to the north. The signal seems stronger in the Atlantic than in the Pacific, and reaches north sooner. This can be partly attributed to the fact that the signal has to travel farther to cross the wider Pacific basin. It is subject to greater dissipation along this longer route, and the flow establishes more slowly. Insight into another

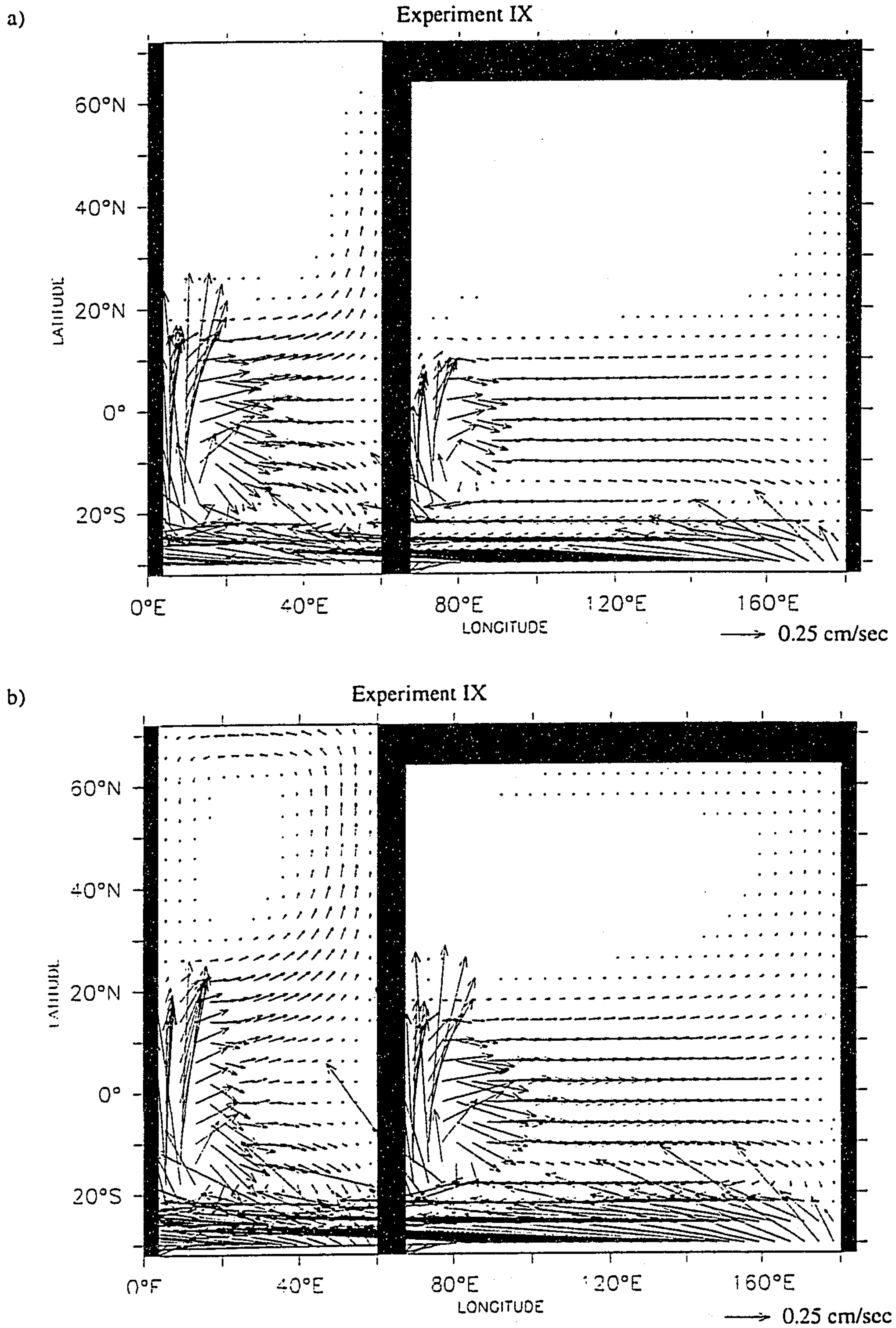

FIGURE 3.25 Horizontal velocities at 81m for Experiment IX after a) 400 days and b) 800 days.

interesting difference between the two basins can be seen in Figure 3.26. Meridional velocities at 14°S show that while the stratification was the same in the two basins, the signal projects different patterns onto the establishing western boundary currents. The different strengths at this latitude cannot be attributed to greater dissipation during a longer journey. The reason for the difference is geographical: the tip of South America extends further south than does the southern tip of Africa. The wind generated perturbation of the stratification is weaker and shallower where it intersects Africa than it is where it intersects South America. More of the flow continues westward south of Africa (like the Aghulas leak) rather than turn north when it intersects that continent.

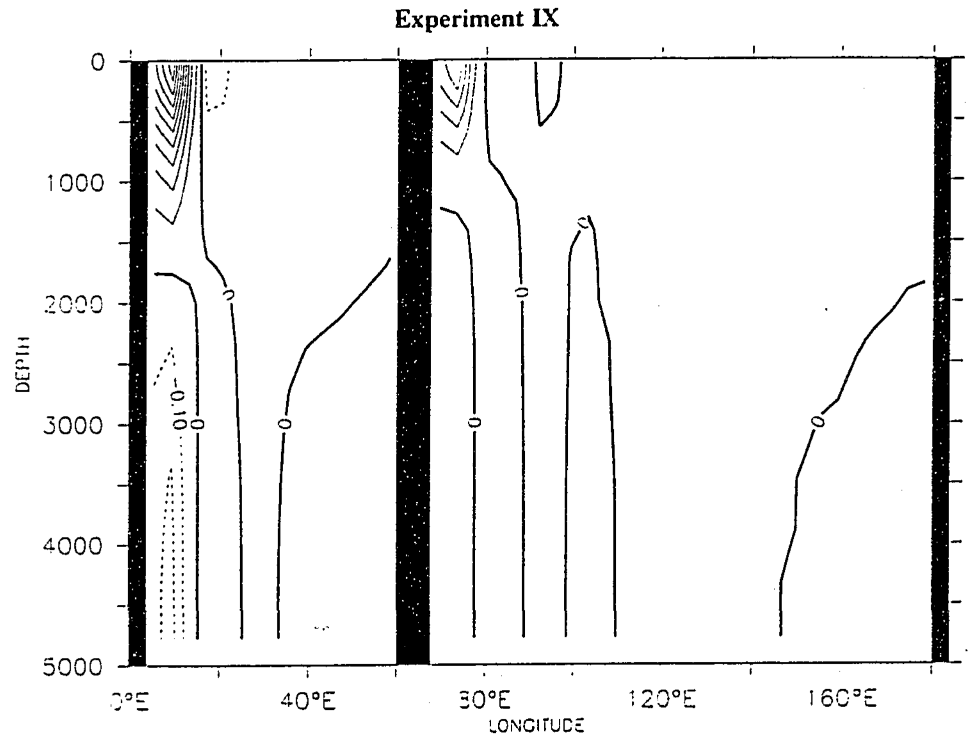

FIGURE 3.26 Meridional velocity for Experiment IX at 14°S after 400 days. Contours are 0.1 cm/sec.

3.5.2 Transient Responses to an Increase in Wind Forcing

3.5.2.1 One-basin increase winds

An additional transient experiment was conducted, Exp. VIII, in which the one-basin model was initialized at the equilibrium state achieved at the end of the weak winds case, Experiment III. In the analysis that follows, this is considered the basic state to which the anomalous velocities and tracer values are compared. The model was allowed to run for 10 years with unchanged forcing, but with synchronous time-stepping. The surface wind stress field was then changed to the strong winds (Experiment II) values, and the synchronous time-stepping was continued. All other boundary conditions remain the same - restoring in temperature and salinity.

An examination of the anomalous flow (Figure 3.27) shows a development very similar to the first transient experiment presented. The signal travels north along the western boundary to the equator, where it crosses to the east. There, a similar partition of the disturbance to northward propagating boundary modes and westward propagating Rossby modes occurs. Once this signal reaches the northern convecting region, however, the flows can no longer be so directly compared. The downwelling mode advances by depressing isopycnals along its route. Vigorous convection in the sinking region vertically homogenizes the water column, so the mode cannot continue its propagation by depressing the isopycnals. The signal effectively stalls in the northeast corner, and enhances the preexisting sinking there. The anomalous flow uses the established sinking region to connect the northward surface flow and southward deep flow. The established flow anoma-

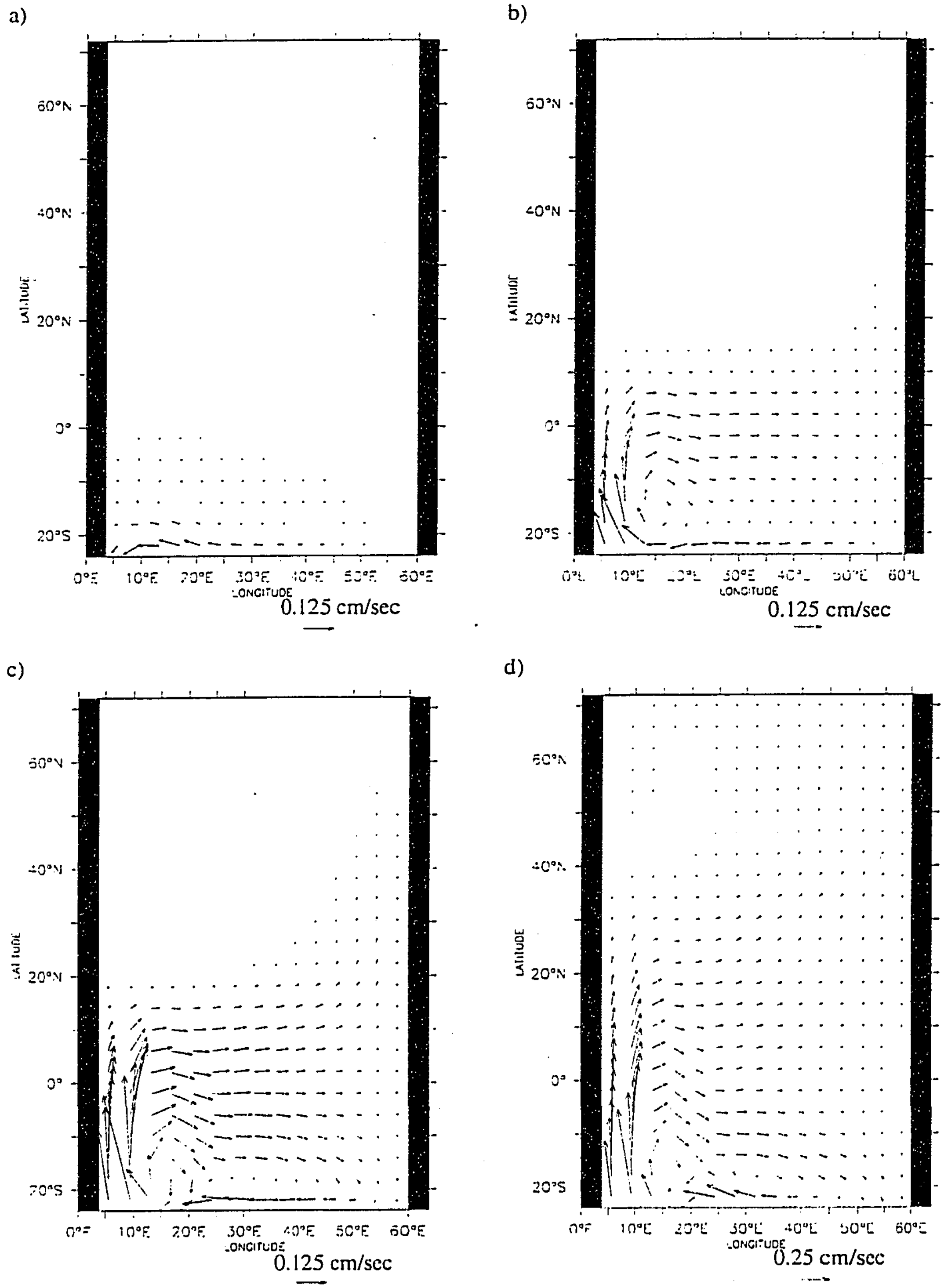

FIGURE 3.27 Horizontal velocity anomalies at 81m for Experiment VIII -Experiment III, after a) 40 days, b)200 days, c)400 days, d)4 years, e)6 years, and f)50 years. Note vector lengths.

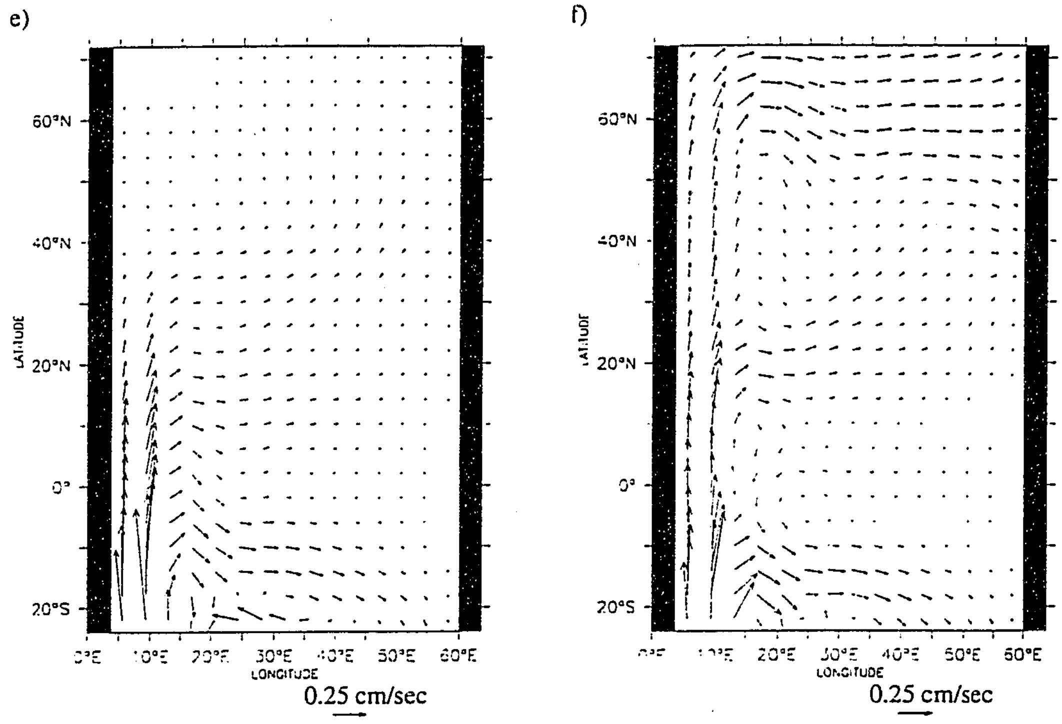

FIGURE 3.27 (Continued)

lies, similar to Figure 3.4a and Figure 3.4b, concentrate in the western boundary currents. The change in vertical motion (Experiment VIII- Experiment III) in the north of the basin is shown in Figure 3.28 after 50 years.

The change in the overturning stream function in response to the increased winds is shown in Figure 3.29. These can be compared to the similar figures for the switch-on winds case shown in Figure 3.24. The initial responses (Figure 3.24a and Figure 3.29a) are almost identical. The magnitude of the anomalous wind forcing is smaller than the wind forcing in the switch-on wind case, but the location of its application is the same. By the time 50 years have passed (Figure 3.24c and Figure 3.29c), the difference in the responses is readily apparent. Figure 3.29c is qualitatively very similar to the steady state

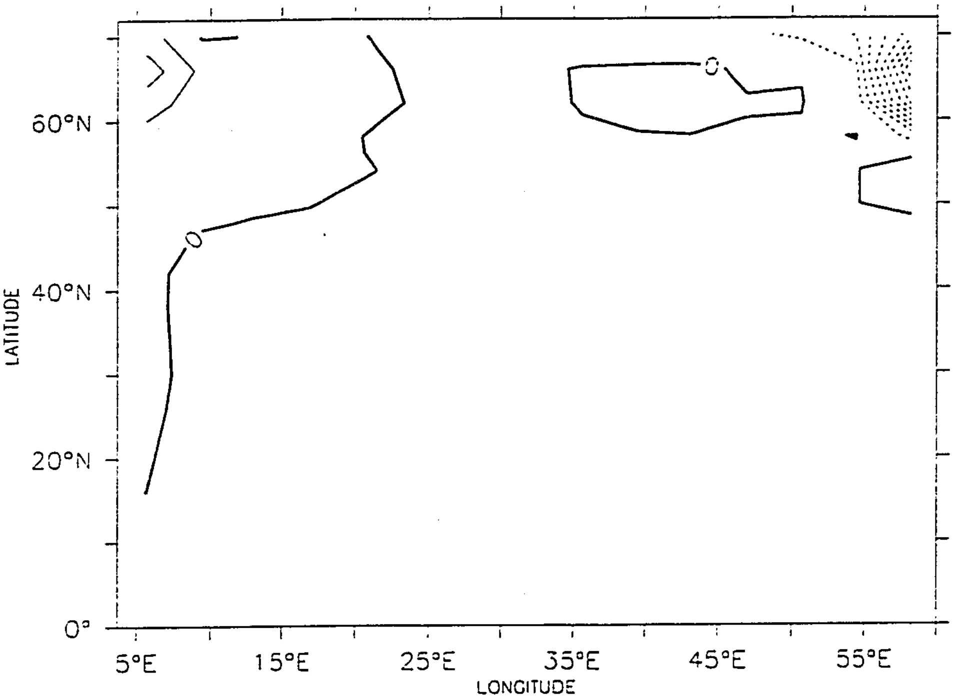

FIGURE 3.28 Vertical velocity anomaly at 1420m for Experiment VIII - Experiment III after 50 years. Contour interval is 20 m/yr.

difference in stream functions (Experiment II - Experiment III), with part of the change occurring locally and part occurring in the northern sinking region. The change in the maximum overturning at 60°N is shown in Figure 3.29d for the first 200 years. Note that the equilibrium overturning difference (Experiment II -Experiment III) is 1.8 Sv, and that approximately 80% of this change is has occurred in the first 200 years.

The changes in the circulation bring with them a shift towards northward flow in the upper ocean and southward flow below, resulting in increased northward heat transport. Figure 3.30 shows the anomalous northward heat transports for the developing flow. Also shown is the difference between the heat transports in Experiment II and Experiment III. The transient solution should tend towards this line. The maximum

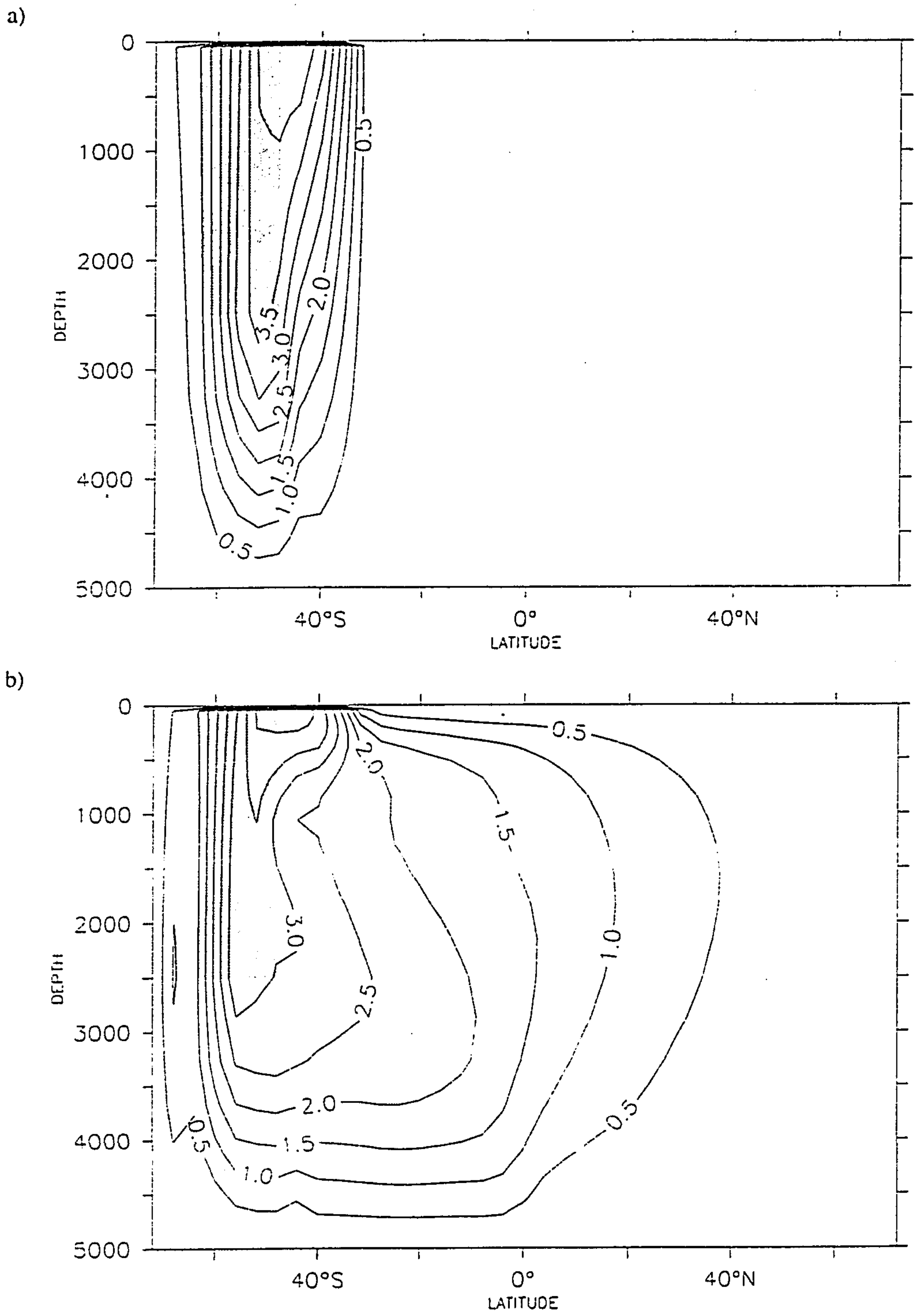

FIGURE 3.29 Anomalous overturning stream function, increased winds minus weak winds, after a) 40 days, b) 6 years, and c) 50 years. d) shows change in overturning stream function at 60° N as a function of time.

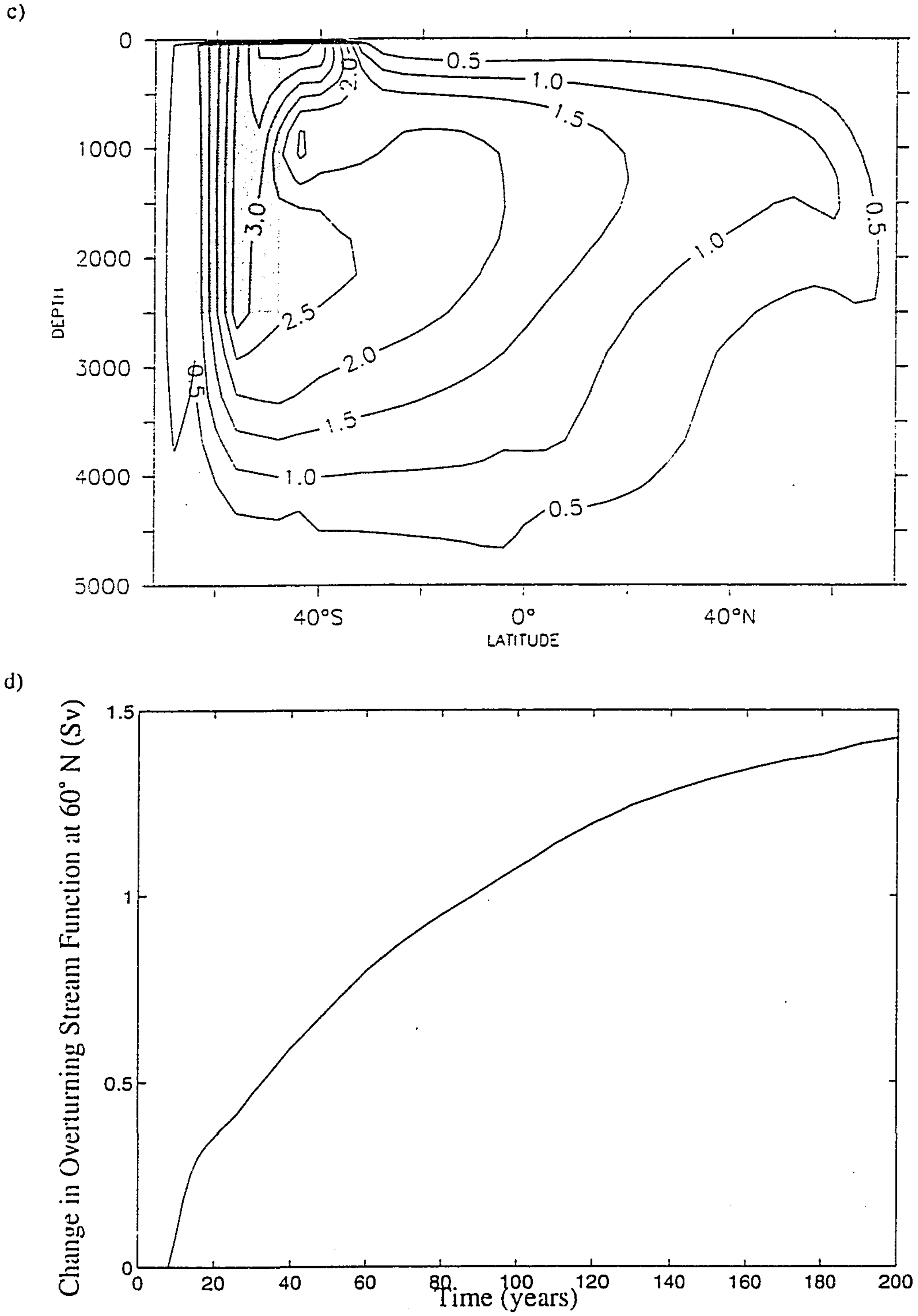

FIGURE 3.29 (Continued)

Northward heat transport is 17% stronger in Experiment II than it is in Experiment III. The magnitude of this change is kept small by the restoring boundary condition for temperature, which tends to bring the SST's to the same value for each run. Other parameterizations of the thermal boundary condition (i.e. Rahmstorf and Willebrand (1995)) might produce different changes in heat transport. The gradual reduction in the northward heat transport in the southern hemisphere occurs as NADW production gradually warms the deep southward flow.

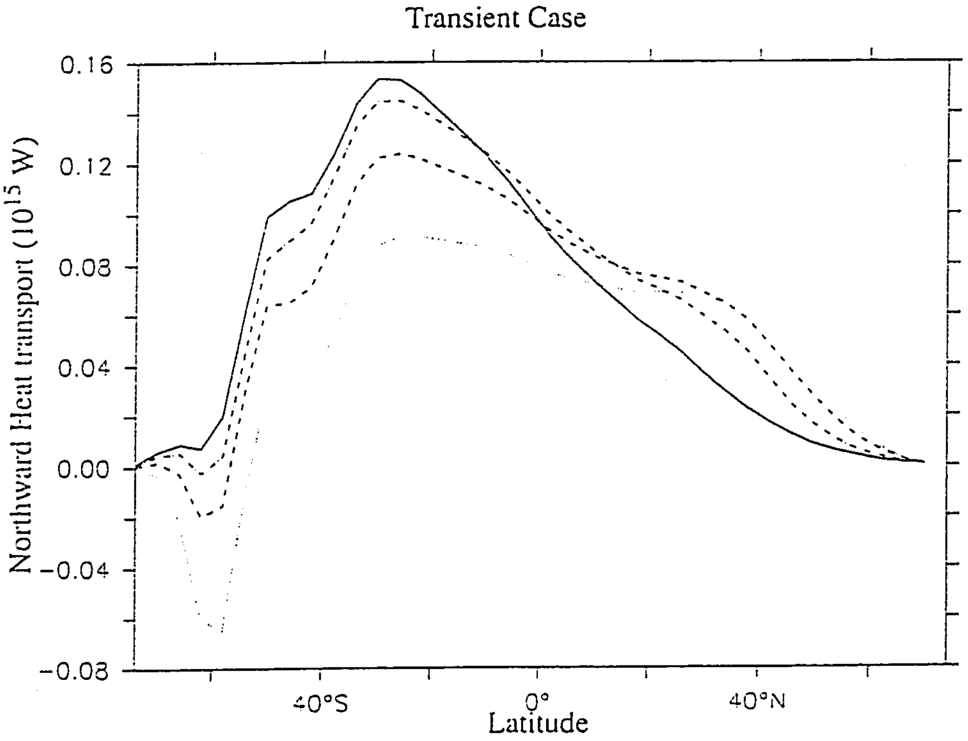

FIGURE 3.30 Change in northward heat transport (Exp.VIII - Exp.III) after two years (solid line), 30 years (dot-dashed line), and 110 years (dashed line) of increased winds. Dotted line is difference between steady-state strong-winds and weak-winds solutions, i.e. Experiment II - Experiment III. Units are 10^{15} watts.

3.5.2.2 Two-basin increase winds

The equilibrium solution from the two-basin, weak wind case (Exp. VI) was used as the starting point for Experiment X. The same procedures were followed for this case as were followed in the single basin experiment. The weak wind solution was switched to synchronous integration and allowed to run for ten years before the southern hemisphere westerlies were increased. The anomalous velocities near the surface are presented in Figure 3.31. As was the case in the single basin experiments, the development of the anomalous velocities closely parallels the development of the flow in the uniformly stratified switch-on case. In both basins, however, the signal takes longer to reach the northern boundary than it did in the switch-on case. The restoring boundary conditions here act to damp the advancing signal, and the non-uniform stratification further complicates the propagation of the modes.

It is interesting to note that the signal does behave differently upon reaching the north of the two basins. The flow in the Atlantic 'locks on' to the northeast corner once the baroclinic signal has reached that location, much as it did in the northeast of the one-basin ocean. The velocity anomalies produce a flow into the sinking region near the surface and away from it at depth. The path described by the anomalous velocities reaching the northeast corner progresses from a flow that crosses the basin at the equator and proceeds north along the eastern boundary to one that crosses the equator as a western boundary current and flows northeasterly across the interior. As the flow approaches equilibrium, the velocity differences approach those in Figure 3.10; the changes in velocity become concentrated in the western boundary currents and in the northern jet.

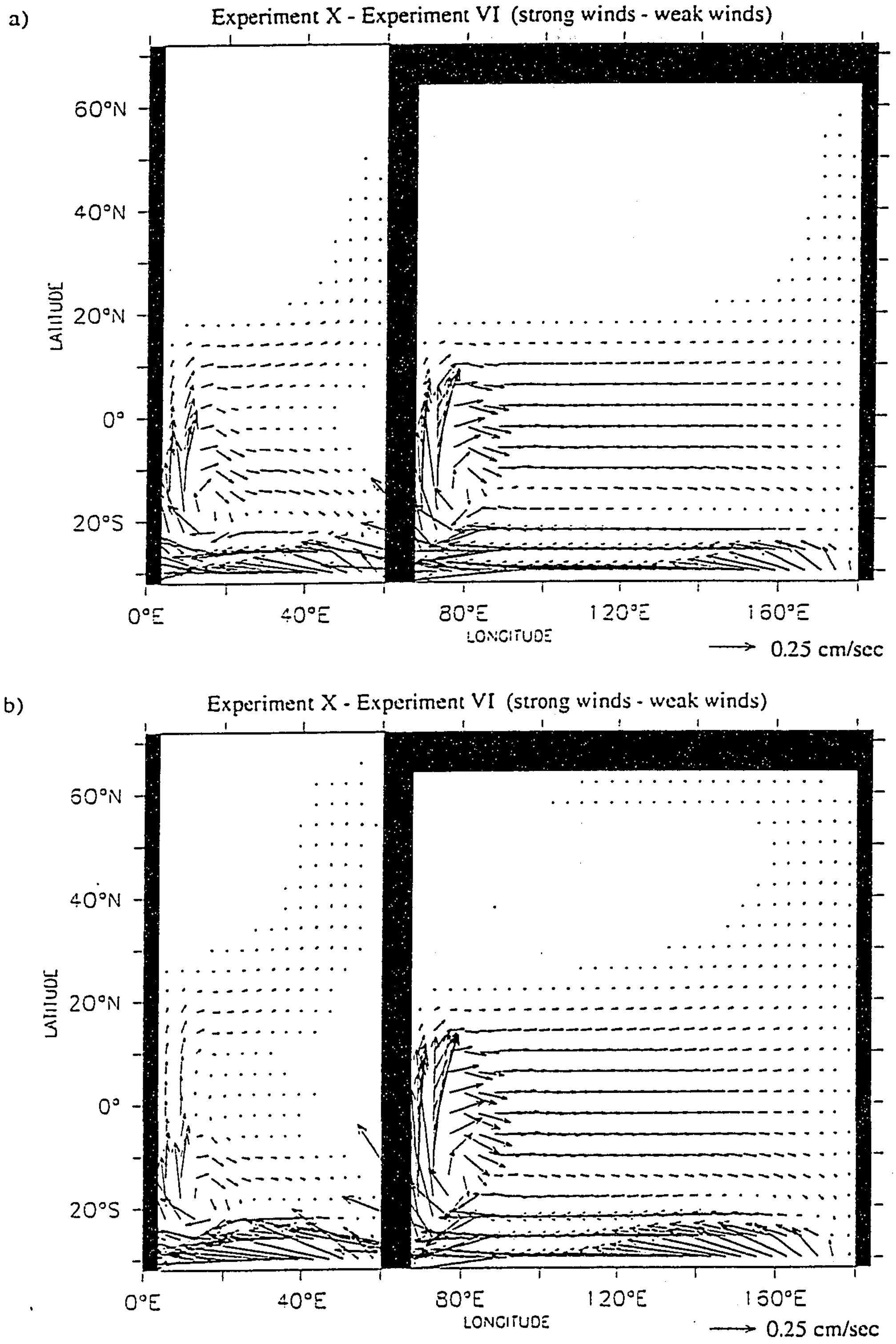

FIGURE 3.31 Velocity anomalies at 81m for Exp.X-Exp VI, after a) 400 days, and b) 800 days.

In the Pacific basin, however, the anomalous flow is not 'locked on' to the north-east corner, and the familiar recirculation of the signal along the northern wall is seen. This flow more closely resembles the flow in the switch-on case than does the flow in the Atlantic. In both basins the change in overturning reaches a peak within 30 years which exceeds the equilibrium change. As the frictional "leak" increases with the strengthening ACC, the change in the overturning at 30°S decreases slightly to its equilibrium value. In terms of change in the magnitude of the overturning, the equilibrium change is much larger in the Atlantic than in the Pacific, although the largest transient response occurs in the Pacific.

Chapter 4 Mixed Boundary Condition Experiments

4.1 Introduction

Rapid changes in air-temperature during the last glaciation, known as Dansgaard Oeschger events, have been inferred from $\delta^{18}O$ in the Greenland ice-core record (Dansgaard et al. 1993). Several hypotheses have been put forward to explain these rapid climate shifts. Broecker et al. (1990) and Broecker (1991) suggest a salt-oscillator mechanism, in which the net export of water vapor from the Atlantic basin drives oscillations in the North Atlantic overturning circulation. Broecker's idea includes the influx of glacial meltwater that would occur during the warm 'conveyor-on' circulation as additional support for a salt-oscillator driven primarily by the fresh water export from the Atlantic. Data from sediment records in the North Atlantic that show a correlation between NADW production and the temperature record from the Greenland ice core (Bond et al., 1993) have helped direct the focus of these proposals on processes regulating the rate of NADW production. Large inputs of glacial meltwater have been suggested as triggers for the transitions immediately following the so-called 'Heinrich events' (Broecker, 1994, Paillard and Labeyrie, 1994). Unfortunately, the timing of the meltwater pulses relative to the climate transitions has made incorporating them into a conceptual model of the transitions difficult. In addition, the Dansgaard-Oeschger events are not accompanied by meltwater pulses (Bond et al, 1993).

Winton (1993), Sarachik et al. (1996), and Winton (1996) suggest an internal ocean-only mode as a possible mechanism for the Dansgaard-Oeschger events. The ocean-only mode, identified as deep-decoupling oscillations, causes the thermohaline circulation to alternate between strong overturning and a collapsed state with only shallow overturning. During the collapsed state, heat diffuses into the interior at low latitudes, and a strong halocline maintains stable stratification in the high northern latitudes. As the interior warms, the increase in subsurface temperature eventually destabilizes the high northern latitudes, convection breaks out, and the strong overturning resumes. Large amounts of heat are released to the atmosphere during the overturning phase, allowing the ocean interior to cool. When the high northern latitudes cool sufficiently, the constant fresh water flux at the surface is able to suppress convection, returning the circulation to the collapsed state.

Winton (1993) produced this ocean-only mode, which he identified as a deep-decoupling oscillations, in a one-hemisphere sector model. Sarachik et al. (1996) showed similar deep-decoupling oscillations in a two-hemisphere sector model, while Winton (1996) produced the same oscillations in a two-dimensional, two-hemisphere ocean coupled to a simple energy-balance atmosphere model. The two-hemisphere models in which deep-decoupling oscillations have been produced, however, did not adequately allow for the formation of deep water in the southern hemisphere. Deep-decoupling oscillations occur because subsurface water in the high-northern latitudes becomes warm enough to destabilize the halocline there. Cold southern-source deep water in the North Atlantic could prevent that destabilization from occurring. Sediment records indicate that nutrient depleted water from the North Atlantic only reached intermediate depths at the last glacial maximum (Duplessey et al., 1988), suggesting that water of southern origin filled the deep ocean. For the deep-decoupling oscillations to be a possible explanation for Dansgaard-Oeschger events, the influence of the continued production of deep water in the southern ocean must be tested.

In many ocean models that are able to represent the production of deep water in both hemispheres, the response under steady, mixed boundary conditions is to have multiple equilibria. The behavior of the circulation in these cases includes the "halocline catastrophe" (F. Bryan, 1986, and Hughes and Weaver, 1994), multiple states of overturning circulation (Marotzke and Willebrand, 1991), and multiple conveyor-type circulations (Rahmstorf, 1994 and 1995, and Weaver and Hughes, 1994).

Transitions from one stable equilibrium solution to another are usually triggered by a transient forcing (e. g. meltwater pulse, stochastic forcing), with the circulation settling into a single stable mode under the applied steady forcing. Rahmstorf (1994) used a one-time pulse and returned to steady forcing, while Rahmstorf (1995) slowly varied the freshwater flux at the surface to observe the hysteresis response of the North Atlantic overturning circulation. Weaver and Hughes (1994) found a circulation that oscillated between two equilibria under stochastic forcing.

Variability occurs in some global ocean models under steady forcing. For example, Moore and Reason (1993) produced decadal-scale variability in their model, but only after removing all bottom topography. Drijfhout et al. (1996) produced internal oscillations on timescales ranging from 20 years to 1100 years in their ocean model. The modes of variability in the Drijfhout et al. model are all driven by changes in production of AABW and occur as a form of loop-oscillation involving the advection of salinity anomalies. In the millenial-scale mode, the salinity anomalies are advected though the northern sinking region. As these salinity anomalies pass through the North Atlantic, the rate of overturning is essentially unchanged, but the outflow from the Atlantic Basin is increased. Mikolajewicz and Maier-Reimer (1990) discussed similar advective oscillations in response to forcing by random freshwater flux anomalies.

In this chapter, deep-decoupling oscillations are reproduced in a one-hemisphere sector configuration of the GFDL Modular Ocean Model (MOM) model. Next, the same configuration and surface boundary conditions are used, but the deepest water is restored to a fixed density as an approximation of the influence of AABW. For the subsequent experiments, the basin is extended to include a southern ocean and then modified to include a reentrant channel. Three idealized salinity flux patterns are used: one with no AABW production, one that results in periodic production of AABW and one that results in continuous production of AABW. The behavior of the ocean circulation under all three flux patterns is described. Finally, the two-basin geometry of the previous chapter is employed in numerical modeling experiments forced by mixed boundary conditions. The salinity flux includes an inter-basin transport of fresh water from the Atlantic to the Pacific. The magnitude of the salinity flux is varied, and the changes in overturning circulation are reported. Only steady circulation results in the two-basin configuration until the restoring temperature at the surface is reduced. Under this cooler surface boundary condition, deep-decoupling oscillations are generated in the Atlantic when sufficient fresh water is transported from the Atlantic to the Pacific via the atmosphere.

4.2 Three-Dimensional Model Description

The model used is the MOM version of the GFDL ocean model described by Pacanowski et al. (1991). The one-hemisphere basin has been configured to resemble the closed basin used by Winton (1993). In the Winton (1993) model, however, the inertial terms in the momentum balance were eliminated. For comparability, mixing parameters have been set to values used by Winton (1993). Horizontal diffusivity has a value of 1.0 x 10^7 cm^2/sec, horizontal viscosity is 2.5×10^9 cm^2/sec, and vertical diffusivity and viscosity are 0.5 cm^2/sec. The one-hemisphere basin extends from 10°N to 70°N, and is 60° wide. The two-hemisphere basin extends from 70°S to 70°N, so that in the closed basin case the model is fully symmetric about the equator. The two-hemisphere basin is also configured with a reentrant channel similar to the one discussed in chapter 3, though its location is shifted north by 2° to maintain an Antarctic Peninsula that is two grid boxes in length (see section 3.2). Horizontal resolution is 3.75° in longitude and 4.0° in latitude. There are 16 levels in the vertical, defining a total depth of 5000m. The thickness of the levels increases from 50m in the top layer to 597m in the bottom layer. The one-hemisphere and two-hemisphere basins are shown in Figure 4.1. The two-basin experiments in section 4.5 use the two-basin configuration described in Chapter 3.

Surface boundary conditions for the one-hemisphere basin and the two-hemisphere basin are shown in Figure 4.2 and Figure 4.3, respectively. Temperature is

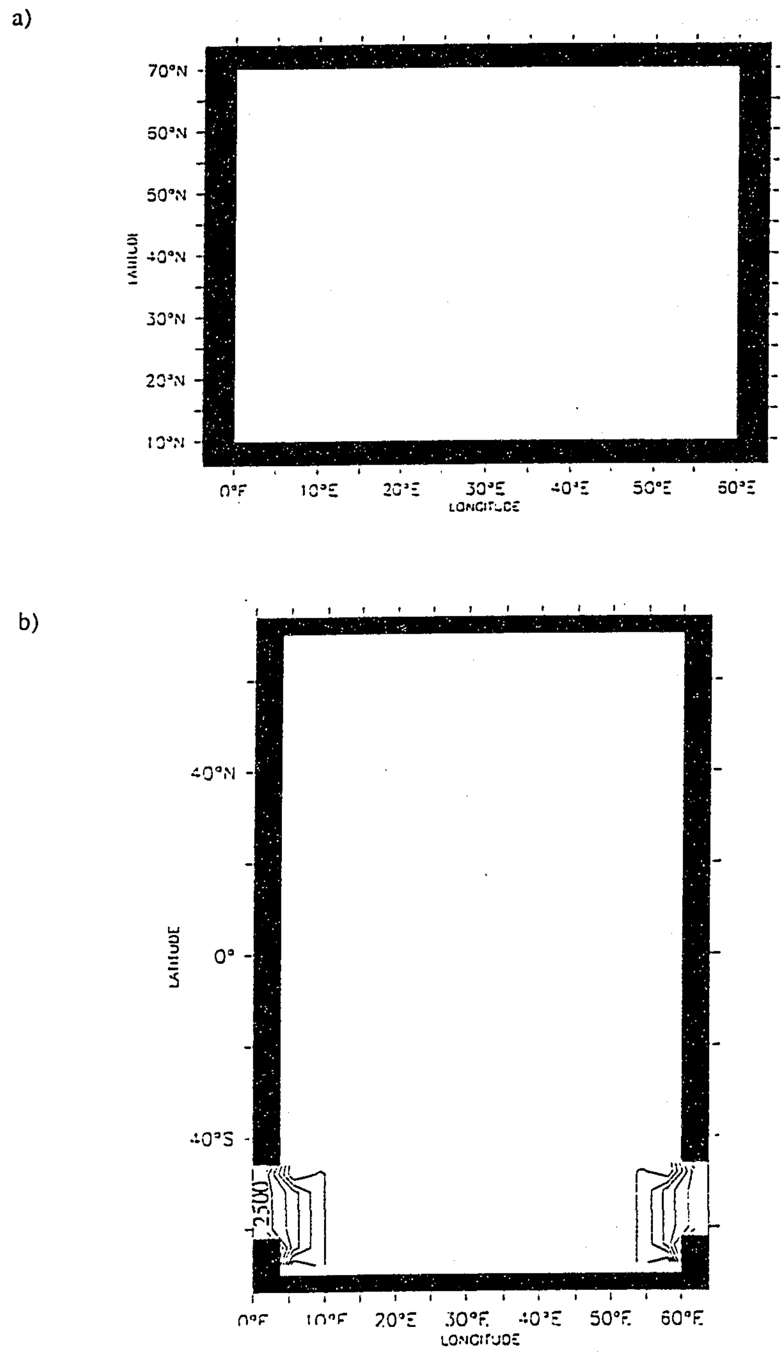

FIGURE 4.1 Basin geometries for Chapter 4. a) one-hemisphere basin, b) two-hemisphere basin. One-hemisphere basin is 5000m deep everywhere, topography in two-hemisphere basin is shown as contours with a sill depth of 2500m. Contour interval is 500m.

restored to prescribed values with a restoring time constant of 50 days. The temperature to which the top layer is restored is determined from the Levitus (1982) zonally and annually averaged values made symmetric about the equator by averaging Northern and Southern Hemisphere values. Only zonal wind stress is applied at the surface, with its value given by the analytical formula:

$$\begin{aligned} \tau_x(\phi) \;=\; & 0.32 + 0.68\sin\left(-5.7\left|\phi + 0.005\right|\right) \\ & -0.5\left(2. + \tanh\left(-7.3\left|\phi\right|\right)\right) \\ & -\tanh\left(10.\left(\frac{\pi}{2} - \left|\phi\right|\right)\right) \end{aligned} \qquad \text{(EQ 4.2.1)}$$

Where τ_x is the zonal component of the wind stress and ϕ is the latitude. The solution to EQ 4.2.1 is shown in Figure 4.2c and Figure 4.3d. A flux boundary condition is applied for salinity. Figure 4.2a shows the nominal flux pattern for the one-hemisphere basin, and Figure 4.3a shows the nominal flux pattern for the two-hemisphere basin. In the discussion that follows, 'salinity forcing', 'freshwater forcing', and 'hydrologic cycle' are equivalent when used in the context of the model.

The model runs are identified by the magnitude of salinity flux and by the basin configuration. The nominal profile is identified as 1x, twice the nominal forcing is identified as 2x, etc. Single hemisphere basin runs are identified as 1h, so a one hemisphere run with nominal salinity forcing would be run 1h_1x, a two-hemisphere run with half the nominal salinity forcing would be run 2h_0.5x, a two-basin run with nominal forcing would be 2b_1x, etc. Several one-hemisphere experiments with deep-restoring of the

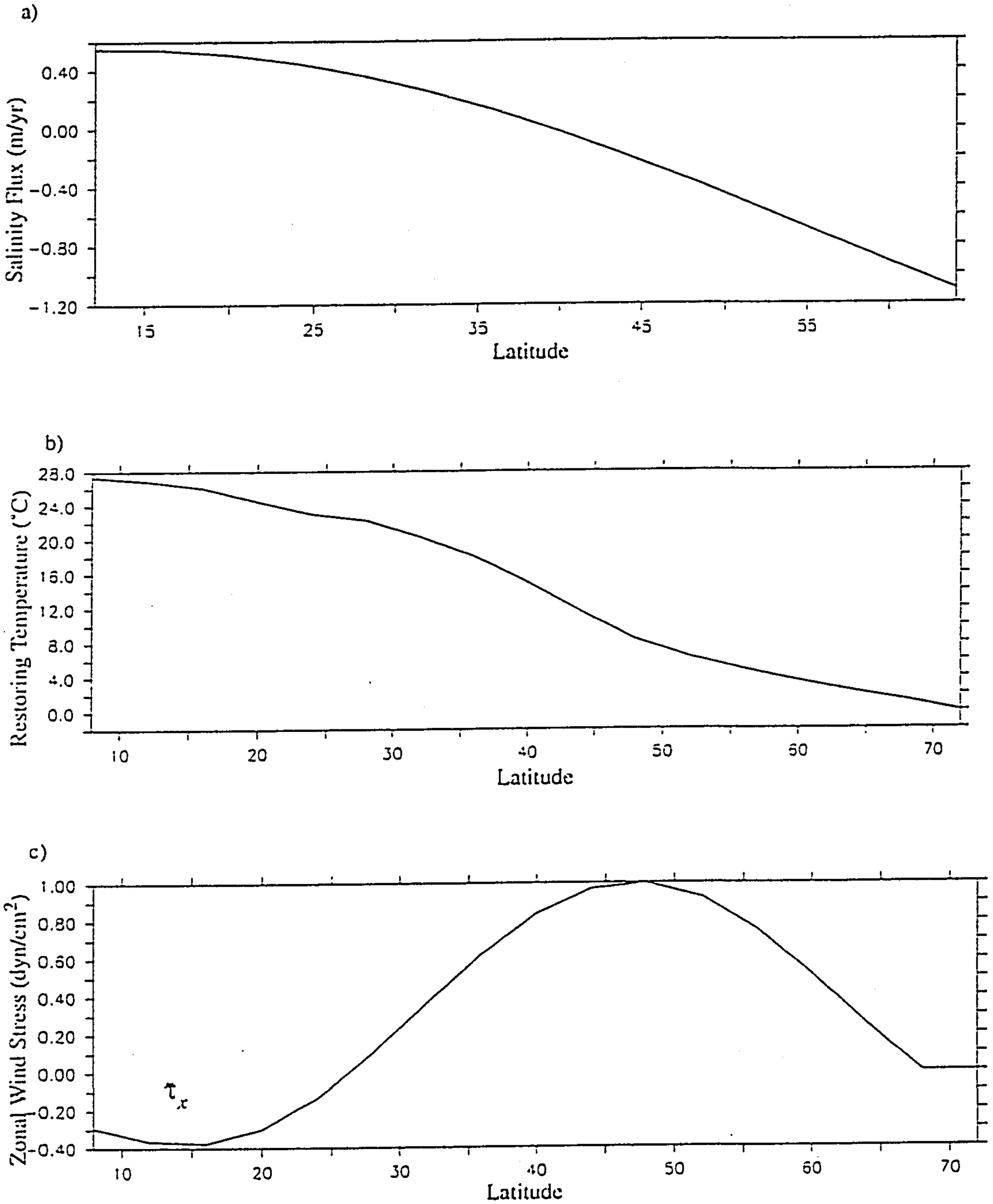

FIGURE 4.2 Forcing applied to one-hemisphere basin. a) nominal (1x) salinity flux, expressed in equivalent evaporation-precipitation (m/yr), b) restoring temperature (°C), c)zonal wind stress (dyn/cm^2)

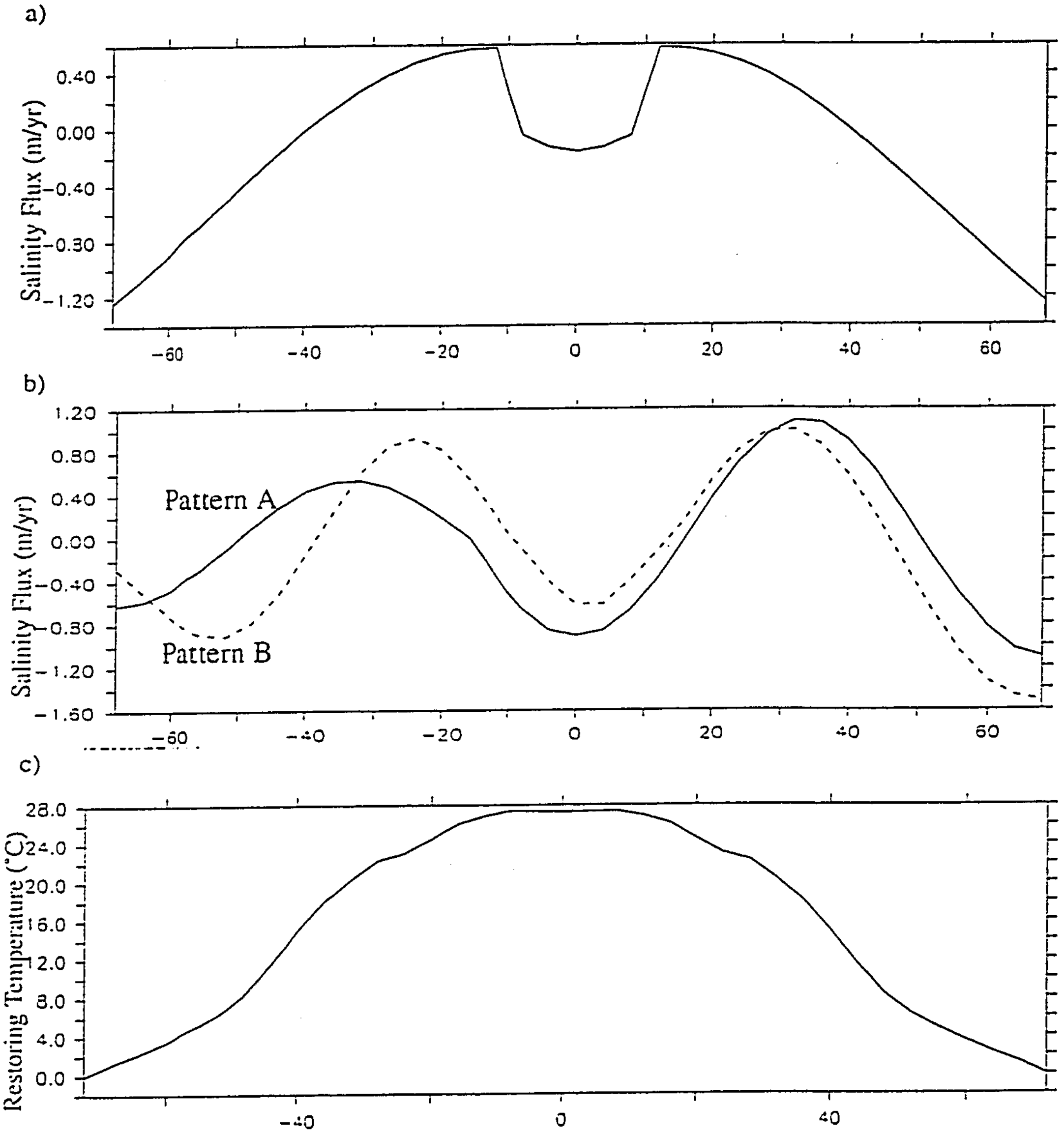

FIGURE 4.3 Surface boundary conditions for two-hemisphere basin runs. a)Symmetric salinity forcing, expressed in equivalent evaporation-precipitation (m/yr), b) Asymmetric salinity forcing (m/yr, solid line is pattern A, dashed line is pattern B), c) Restoring temperature (°C), d) Zonal wind stress (dyn/cm^2)

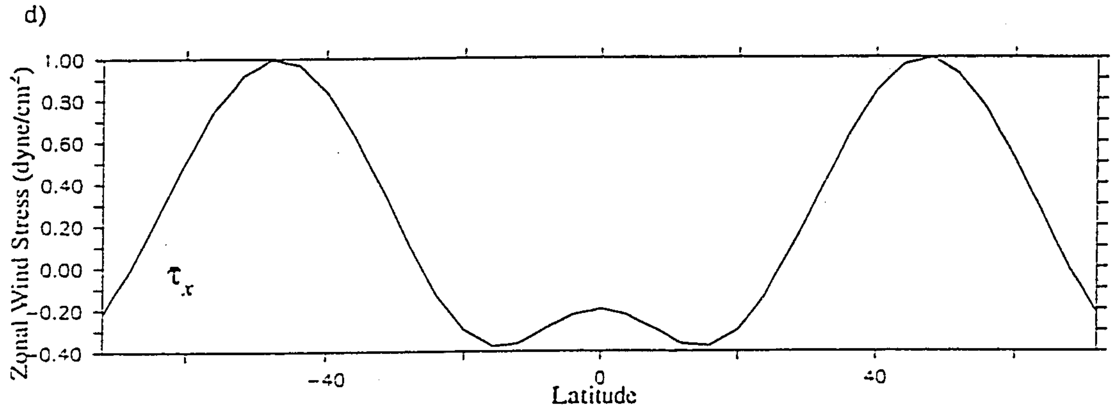

FIGURE 4.3 (Continued)

tracer values are presented, these receive an additional tag to identify the strength of the restoring. For example, a one-hemisphere run with one and a half times the nominal salinity forcing and the nominal deep restoring would be labeled 1h_1.5x_nom, and the same run with deep restoring reduced by 100 would be labeled 1h_1.5x_hun. A few two-hemisphere experiments are conducted in a closed basin, these are identified by the label 'closed'. A two-hemisphere experiment in a closed basin subjected to twice the nominal salinity flux would be identified as 2h_2x_closed.

The additional asymmetric salinity flux profiles shown in Figure 4.3b are identified by the labels with 'fluxA' or 'fluxB'. An experiment forced with the nominal strength of pattern A would be identified as 1x_fluxA, etc. Note that flux patterns A and B are only used in the two-hemisphere model, so the '2h' is not required. Two-basin experiments are denoted by '2b'. The Drake Passage effect is investigated in the two-basin configuration by increasing the strength of the Southern Hemisphere westerlies by 50% in runs designated by an 's' (2b_1xs, 2b_1.5xs, etc.) Because of the large number of experiments conducted in this chapter, the experiments for each section are summarized in tables in the individual sections.

4.3 One-Hemisphere Mixed Boundary Condition Experiments

In this section, mixed boundary condition experiments in a one-hemisphere basin are presented. The results for a standard model are presented first, followed by the results for a one-hemisphere basin with temperature and salinity of the deep ocean restored to a prescribed value. The experiments of section 4.3 are summarized in Table 4.1. Salinity flux range refers to the factor multiplying the salinity flux shown in Figure 4.2a. Deep restoring forcing is explained in section 4.3.2.

TABLE 4.1 Summary of one-hemisphere experiments.

Experiment Label	Salinity Flux Range	Deep Restoring Forcing	Salinity Flux Range - Behavior of Overturning
1h_(0.5-6)x	0.5x - 6x	None	0.5-1.0 steady 1.5-6.0 oscillatory
1h_1.0x_nom | 1h_2.0x_nom	1.0, 1.5, 2.0	Nominal	1.0 steady 1.5 oscillatory 2.0 steady
1h_1.0x_ten | 1h_3.0x_ten	1.0, 1.4, 1.5, 1.55, 1.6, 2.0, 3.0	Tenth	< 1.5 steady 1.5 oscillatory >1.5 steady
1h_1.0x_hun | 1h_2.0x_hun	1.0, 1.35, 1.4, 1.5, 1.6, 1.65, 1.75, 1.8, 2.0	Hundredth	< 1.4 steady 1.4-1.75 oscillatory >1.8 steady
1h_1.0x_thou | 1h_3.0x_thou	1.0, 1.5, 1.6, 2.0, 3.0	Thousandth	<1.5 steady ≥ 1.5 oscillatory

Notes for Table 4.1:

Salinity Flux Range: Factors by which salinity flux was multiplied for experiments.

Deep Restoring Forcing: Nominal deep restoring described by EQ 4.3.1 and Figure 4.7. Tenth, Hundredth, and Thousandth refer to fraction of nominal restoring.

Salinity Flux Range-Behavior of Overturning: Gives range of salinity flux resulting in steady or oscillatory overturning.

4.3.1 Experiments in the Standard Model

The purpose of this series of experiments is to produce deep-decoupling oscillations that can serve as a point of comparison with subsequent model runs. The basin averaged temperatures for a series of experiments with salinity forcing ranging from 0.5x to 6x are shown in Figure 4.4. Deep-decoupling oscillations occur in the one-hemisphere basin with timescales set by the strength of the salinity forcing as in Winton (1993). The overturning stream function for the 1h_0.5x experiment is shown in Figure 4.5a and for Experiment 1h_1x in Figure 4.5b. These steady northern sinking solutions are thermally dominated; the high-latitude freshening is insufficient to induce oscillations. As the fresh water forcing is increased, the halocline strengthens, and a steady production of deep water occurs at the southern edge of the halocline. These two experiments illustrate the fact that fresh water forcing sufficient to create a halocline is not necessarily sufficient to induce deep decoupling oscillations. The model can produce thermally dominant over-

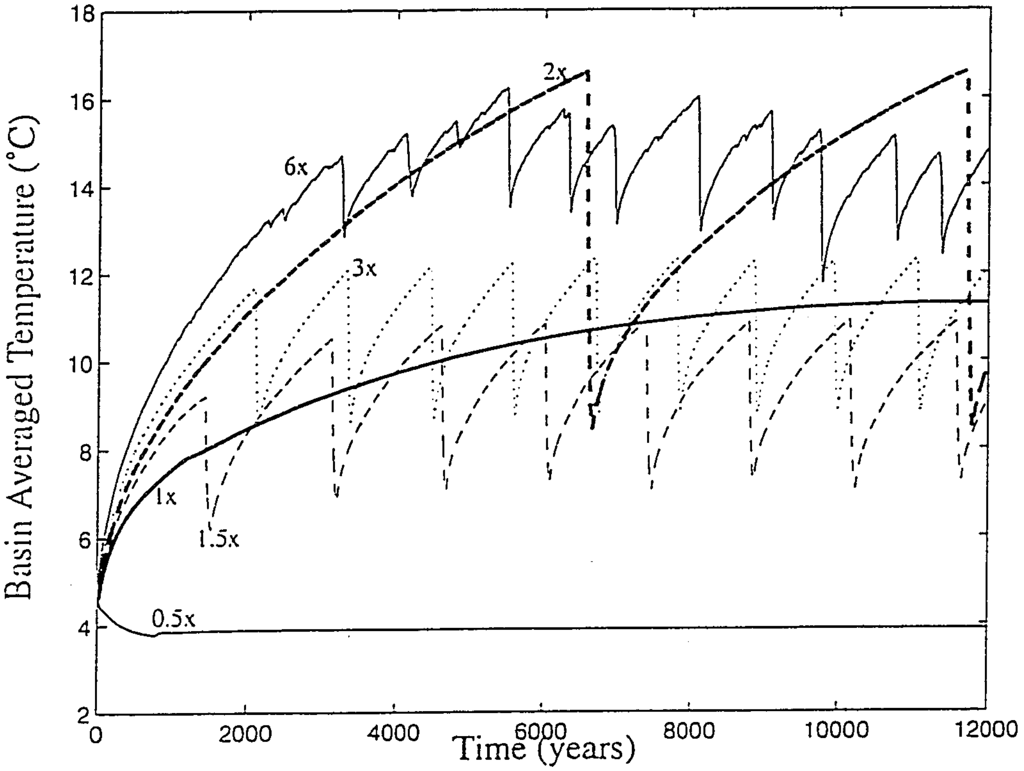

FIGURE 4.4 Basin averaged temperature for the standard one-hemisphere configuration under a range of salinity forcings. Heavy solid line is 1h_1x (nominal) forcing, lower light solid line is 1h_0.5x, light dashed line is 1h_1.5x, heavy dashed line is 1h_2x, dotted line is 1h_3x, and upper light solid line is 1h_6x salinity forcing.

turning solutions with a halocline present. As fresh water forcing in this model strengthens, the sinking region shifts southward and the temperature warms.

Increasing the salinity forcing to 1.5x produces deep-decoupling oscillations. A strong halocline forms in the north of the basin that prevents deep water formation. During this 'decoupled' phase, intermediate water is formed in the mid-latitudes, while in the low-latitudes heat diffuses downward to warm the ocean's interior. Eventually, the water beneath the halocline warms sufficiently to destabilize the water column, convection breaks out, and the deep-coupled phase of the cycle is resumed. The deep-coupled phase

a) 1h _0.5x Experiment

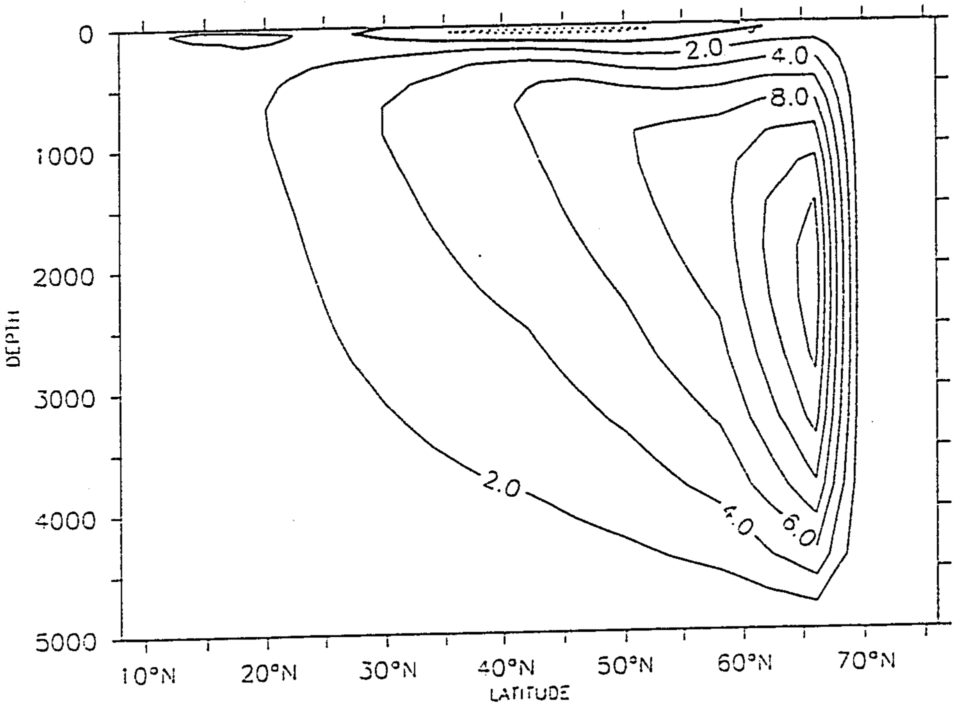

b) 1h _1.0x Experiment

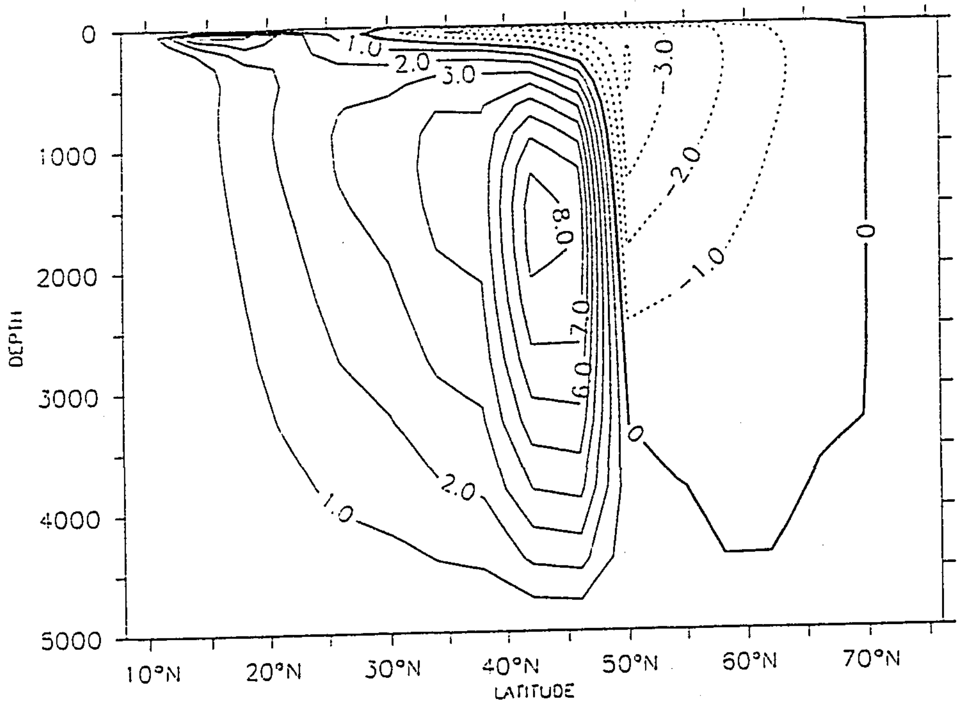

FIGURE 4.5 Overturning stream function for a) 1h_0.5x experiment, and b) 1h_1.0x experiment. Units are $10^6 m^3/sec$ (Sv), contours are 2Sv for a) and 1Sv for b).

is characterized by deep convection in the North accompanied by strong meridional overturning. During the deep-coupled phase large amounts of heat are released from the deep ocean to the atmosphere. The heat flux out of the high latitudes (42°N to 70°N) for experiment 1h_1.5x is plotted in Figure 4.6. As the deep ocean cools, the heat flux from the surface diminishes. When the density decrease caused by surface freshening exceeds the density increase caused by cooling, the halocline forms anew.

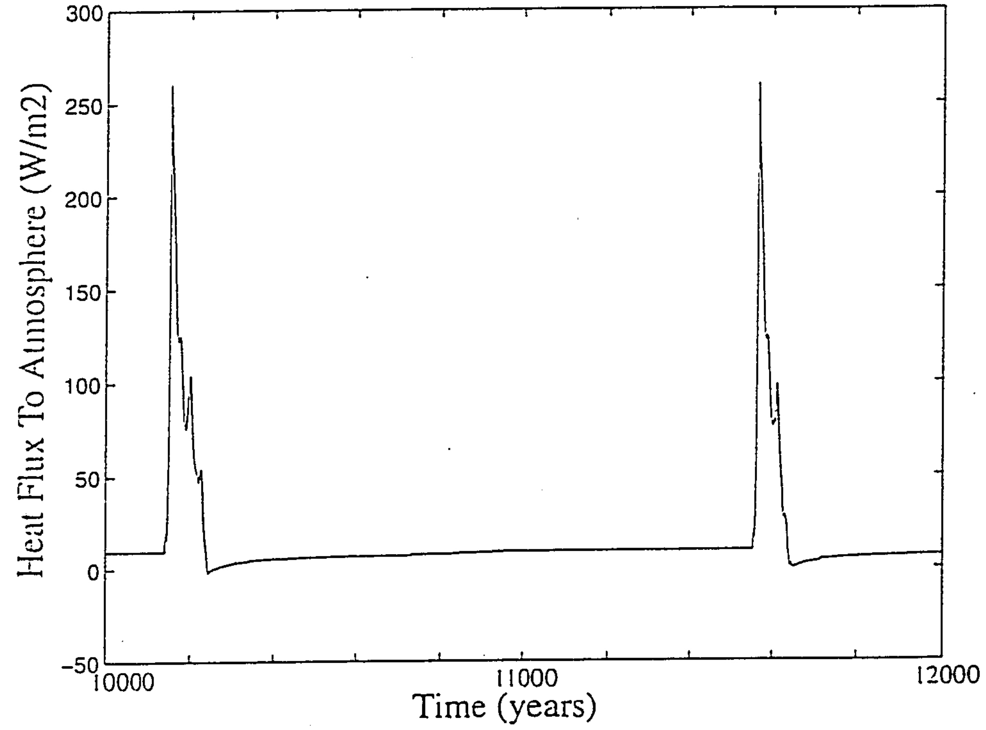

FIGURE 4.6 Heat flux from the ocean to atmosphere (W/m^2) from 42°N to 70°N for 1h_1.5x

The behavior under 1.5x forcing is typical of the deep-decoupling oscillations described by Winton (1993). Deep-decoupling oscillations occurred in all simulations with salinity forcings greater than 1.5x tested, up to a maximum of 6x. While some characteristic of the oscillations varied as the strength of the salinity forcing increased, the nature of the cycles remained unchanged.

4.3.2 Experiments with Deep Restoring

Deep-decoupling oscillations depend upon a gradual warming of the deep ocean to destabilize the sinking region. In a one-hemisphere sector model, this warming occurs when there is no deep water production in the north. Sediment records suggest that the collapse of the North Atlantic thermohaline circulation during the 'decoupled' phase of these oscillations does not exclude the continued production of deep water in the southern hemisphere (Charles and Fairbanks 1992). Continued production of cold deep or bottom water by a southern source could slow and/or reduce the deep warming that eventually allows the northern overturning to resume.

To test the sensitivity of deep-decoupling oscillations to the influence of a second deep water source, the following experiments were conducted. The configuration and surface forcing were identical to the experiments described above, in which deep decoupling oscillations were observed. The deep ocean was subjected to a linear restoring term of the form

$$\text{temperature: } rest = \gamma(T - T^{*}) \exp\left((\phi_o - \phi) / (\Delta\phi) \right) . \qquad \text{(EQ 4.3.1)}$$

$$\text{salinity: } rest = \gamma(S - S^{*}) \exp\left((\phi_o - \phi) / (\Delta\phi) \right) \qquad \text{(EQ 4.3.2)}$$

where T is the observed temperature, S is the observed salinity, T^{*} is the target temperature or salinity, S^{*} is the target salinity, γ is a depth-dependent restoring time scale, ϕ is the latitude, ϕ_o is the latitude of the southernmost ocean gridpoints, and $\Delta\phi$ is the latitudinal grid spacing. The target temperature and salinity, T^* and S^*, are 1°C and 34.72 psu, respectively. The restoring time scale, γ, shown in Figure 4.7, varied from $(52\ \mathrm{yr})^{-1}$ at 2519m to $(1.7\ \mathrm{yr})^{-1}$ in the bottom layer. The time scales of the nominal profile (nom) were multiplied by factors of ten, 100 and 1000 (γ divided by 10, 100, and 1000) in the models runs labeled 'ten', 'hun', and 'thou' respectively. The strong latitudinal dependence of the restoring insured that its influence was concentrated at the southern wall.

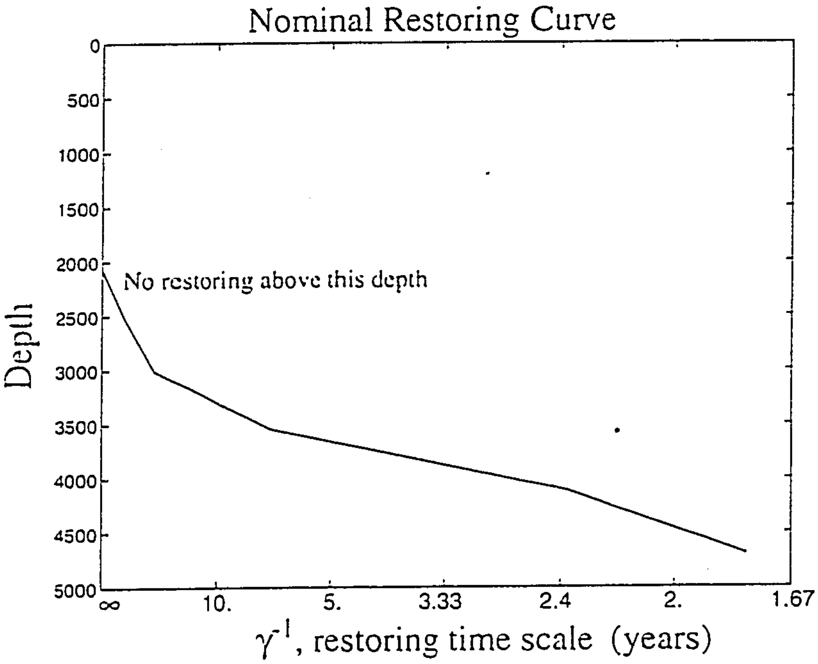

FIGURE 4.7 Depth dependence of restoring time scale for the deep ocean. The curve shown is for the strongest (nominal) restoring.

While restoring the deep ocean at the southern boundary is not the same as providing inflow of AABW, some insight can be gained by comparing the restoring with approximate inflow rates that would similarly influence the deep ocean. Consider the bottom level of the model, where γ^{-1} has a value of 1.7 yr. When the full latitudinal extent of the level is considered (60°), the southern restoring brings the entire level to T* with a time constant of about 26 yr. One Sverdrup of inflow (1 Sv=10^6 m^3/sec) yields a residence time within that lowest level of approximately 600 yr. As a rough approximation, the nominal restoring is similar to an exchange of 23 Sv across the southern wall with the properties T* and S* into the bottom layer. This very high value is reduced to 2.3 Sv for the 'ten' restoring cases, to 0.23 Sv for the 'hun' cases, and to 0.023 Sv for the 'thou' cases. Considering all of the restored levels, the equivalent rate of exchange across the southern wall is approximately 45 Sv for 'nom', 4.5 Sv for 'ten', 0.45 Sv for 'hun', and 0.045 Sv for 'thou'.

When deep restoring is applied to a one-hemisphere model, an overturning cell develops in the deep southern part of the basin, though its strength is the result of the more complex interaction of heating from the surface and the restoring that occurs along the bottom 2000m of the southern wall. This overturning cell is not the same as the presumed exchange in the above discussion, but its strength does vary as the strength of the restoring.

The results of these experiments for a constant salinity flux (1.5x) are shown in Figure 4.8. For weak, deep restoring at the southern wall (1h_1.5x_hun and 1h_1.5x_thou), oscillations continue with approximately the same period as the oscillations in the unrestored basin. As the strength of the restoring at the southern wall is increased, analogous to increased ventilation by AABW, the amplitude of the deep-decou-

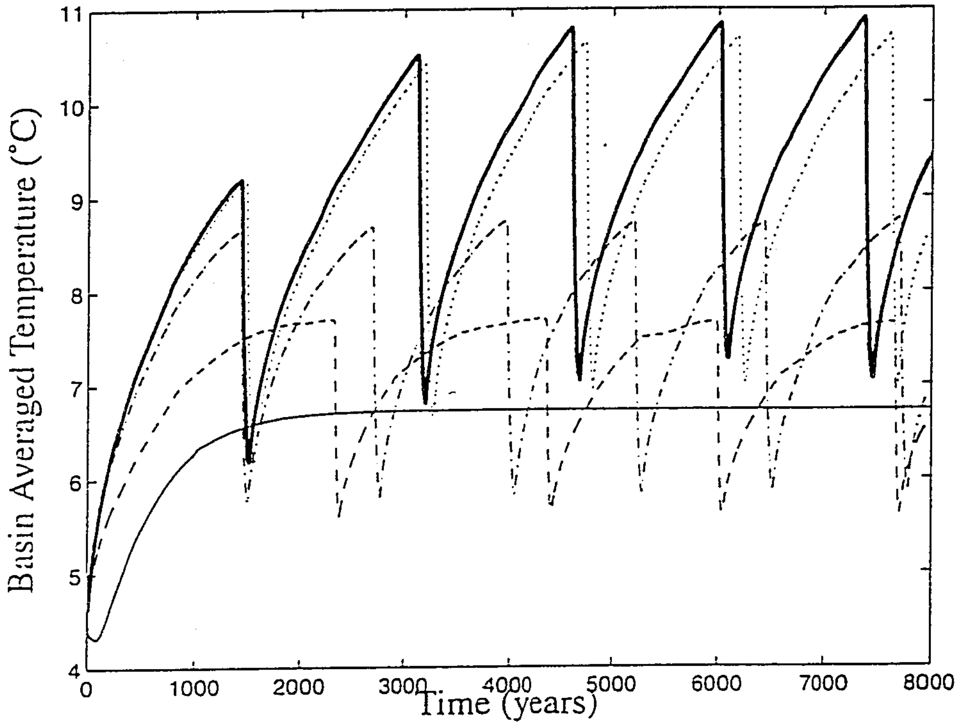

FIGURE 4.8 Basin averaged temperature for one-hemisphere basin under 1.5x salinity forcing. Heavy solid line is for the simulation without deep restoring, light solid line is nominal restoring (1h_1.5x_nom), dashed line is one-tenth restoring (1h_1.5x_ten), dot-dashed line is one-hundredth restoring (1h_1.5x_hun), and dotted line is for the one-thousandth restoring experiment (1h_1.5x_thou).

pling oscillations decreases. When the restoring at the deep southern wall is sufficiently strong (i.e 1h_1.5x_nom), a steady circulation is established (see Figure 4.9). This circulation produces some intermediate water at mid-latitudes, but the resulting subsurface warming never succeeds in destabilizing the higher latitudes. The cold bottom water created by restoring at the southern wall is the only source of deep water.

Next, the salinity forcing is varied to determine the range over which oscillations are found for the different restoring strengths. The 1.5x salinity flux cases were presented above because oscillations were seen to persist even under relatively strong deep restoring

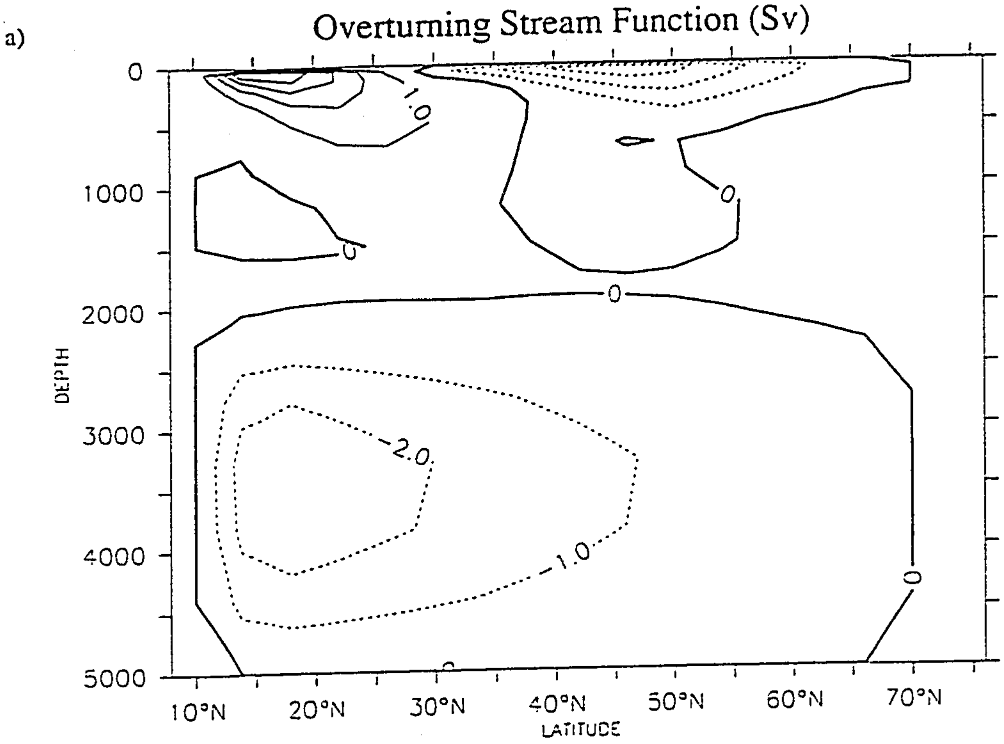

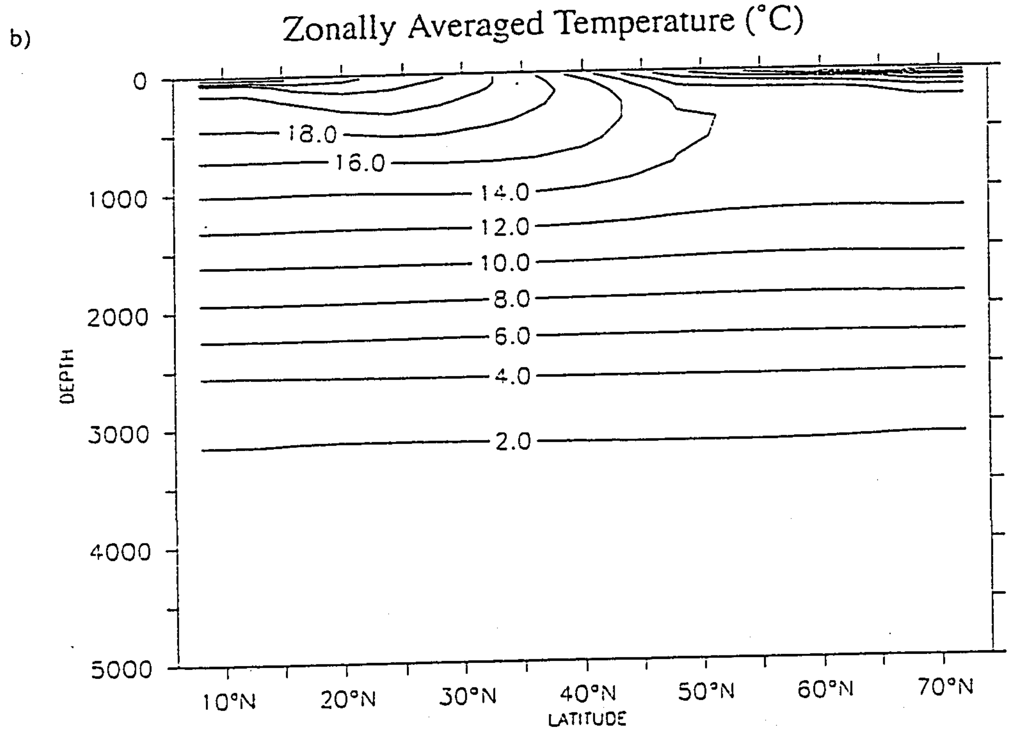

FIGURE 4.9 Steady state reached under 1.5x salinity forcing with full nominal deep restoring(1h_1.5x_nom) a) overturning stream function (Sv), and b) zonally averaged temperature (°C).

conditions. This was the lowest of the tested fresh water flux values for which the normal (no deep restoring) basin experienced deep-decoupling oscillations. As can be seen from the basin averaged temperatures presented in Figure 4.4, a fresh water forcing greater than 1.5x requires additional warming of the deep water before oscillations begin. The deep restoring precludes the higher temperatures required to destabilize the halocline that forms under the stronger salinity forcings.

In the one-hemisphere basin with no deep restoring, increases in the salinity forcing produced changes in the frequency of the oscillations, up to the maximum fresh water forcing attempted, 6x. In the cases with deep restoring, a stable circulation was found when the fresh water forcing was increased above a certain level. This circulation is similar to the decoupled phase of the oscillations, with the densest surface water found at relatively low latitudes. As an illustration, the basin-averaged temperatures for several of the model runs with deep restoring denoted by (hun) are presented together in Figure 4.10. For this strength of deep restoring, salinity forcing within the range of 1.4x to 1.6x produced deep-decoupling oscillations similar to those seen in the nominal cases above. However, when the salinity forcing is increased to 1.8x and greater, the model achieves a stable equilibrium circulation (see Figure 4.11). As heat is delivered to the intermediate depths at low latitudes, some of this heat acts to weaken the stratification in the high latitudes as in the 1h_1.5x case discussed above. The stronger halocline requires more heat to destabilize it. As the temperature in the intermediate depths increases, a stronger vertical temperature gradient in the deep ocean is established. The heat diffused to the deep ocean is removed by the deep restoring forcing, without delivering enough heat to the high latitudes to destabilize the halocline.

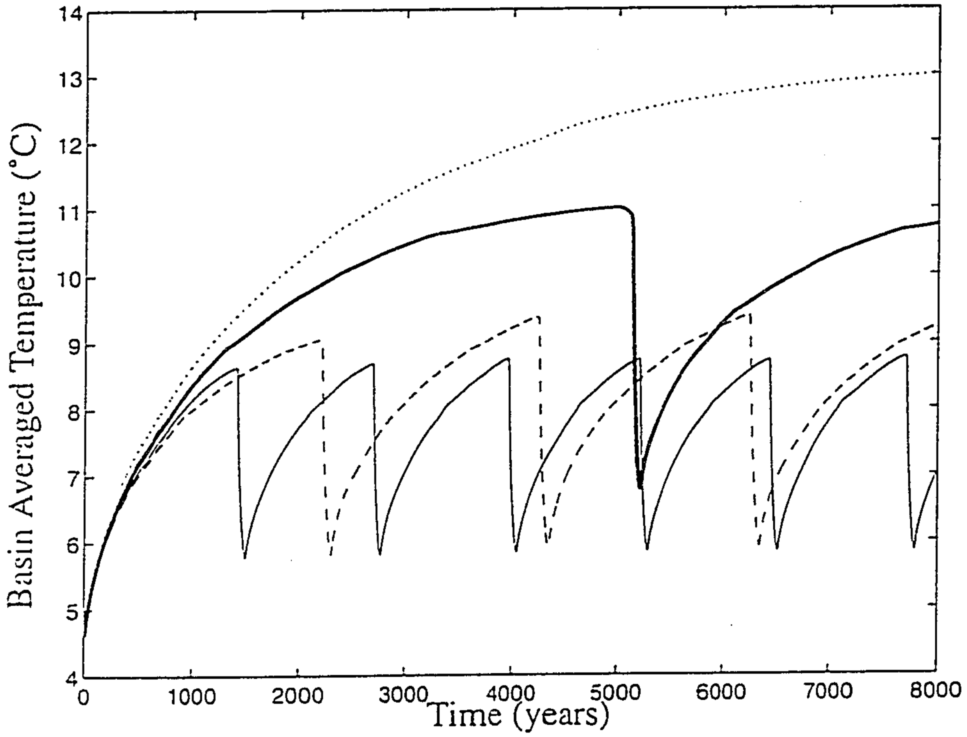

FIGURE 4.10 Basin averaged temperatures under a range of salinity forcings, with 'hun' deep restoring. Dashed line is 1h_1.4x_hun, thin solid line is 1h_1.5x_hun, heavy solid line is 1h_1.6x_hun, and dotted line is 1h_2x_hun salinity forcing.

When the restoring is reduced to one one-thousandth the nominal values (thou), the range over which oscillations can occur increases. Salinity forcing as high as 3x is seen to produce deep-decoupling oscillations. The rough estimates of the AABW inflow equivalents given above indicate that the 'thou' restoring can only be thought of as loosely representative of a situation where the presence of AABW moderates the deep temperatures. On the other hand, it is recognized that the vertical diffusivity used is considerably larger than the actual vertical diffusivity (Ledwell et al. 1993). Reducing the vertical dif-

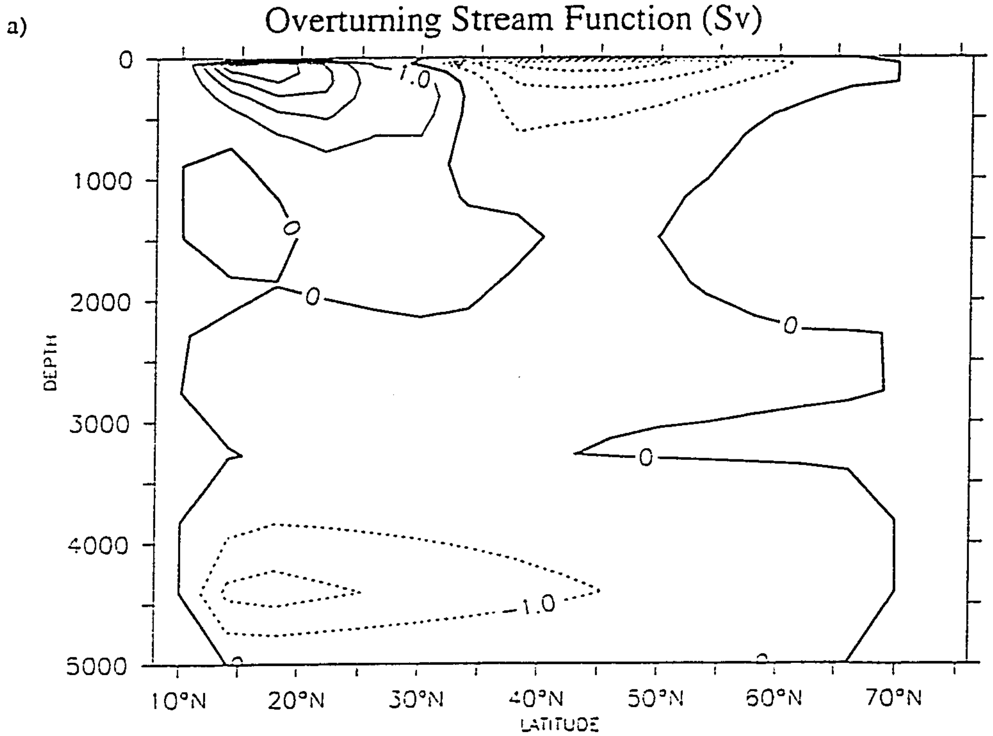

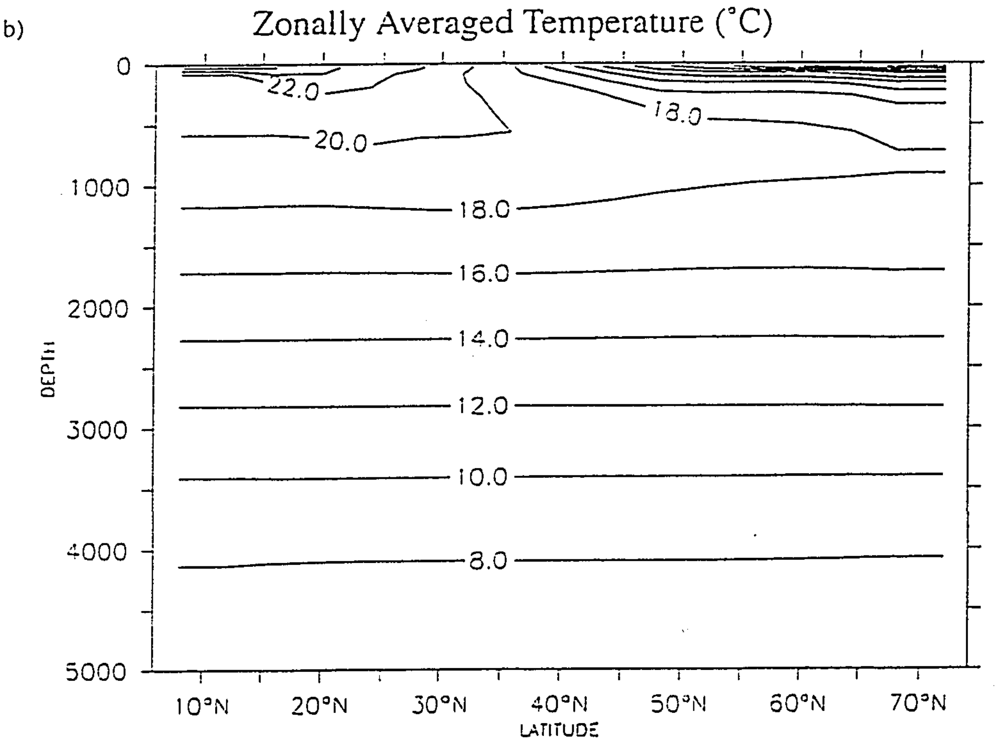

FIGURE 4.11 Steady state reached in experiment 1h_2x_hun a) Overturning stream function, units are 10^6 m^3/sec, and b) zonally averaged temperature, °C.

fusivity by an order of magnitude would allow the deepest waters to remain considerably colder, without precluding the subsurface warming necessary to destabilize the halocline. However, within the accuracy of this model, it can be seen that even a very moderate deep heat sink is sufficient to prevent deep-decoupling oscillations.

The above experiments illustrate the ability of a one-hemisphere basin model to produce deep-decoupling oscillations in the presence of a representation of bottom water, and they also illustrate the potential for AABW to prevent this type of variability. Implicit in this simplified representation of AABW is a supply of deep water with a highly adjustable capacity to extract heat from the upper ocean. This may not be a good assumption because of the dynamic constraints limiting the communication of the southern ocean south of Drake Passage with the upper ocean north of Drake Passage. To better simulate the influence of these dynamic constraints, a second set of experiments was conducted using a two-hemisphere basin.

4.4 Two-Hemisphere Mixed Boundary-Condition Experiments

In this section, numerical modeling experiments in a one-hemisphere basin are presented. The results for a closed two-hemisphere basin are presented first, followed by the results for a two-hemisphere basin with a reentrant channel. The results for the experiments of section 4.4 under steady forcing are summarized in Table 4.2. The response of the model under gradually increasing a decreasing salinity flux is described in section 4.4.2.3, and is not included in Table 4.2. A more complete description of the behavior of the model is available in the text. Salinity flux range refers to the factor multiplying the salinity flux shown in Figure 4.3a.

TABLE 4.2 Summary of steady two-hemisphere experiments.

Experiment Label	Salt Flux Pattern	Salinity Flux Range	Reentrant Channel?	Behavior of Circulation
2h_1.5x_closed 2h_2x_closed	Figure 4.3a	1.5, 2.0	No	Deep-decoupling oscillations, occurring first in one-hemisphere, then the next.
2h_0.5x | 2h_2x	Figure 4.3a	0.5, 1.0, 1.5, 2.0	Yes	0.5x Strong northern sinking 1.x-2.x Deep-decoupling oscillations in the North, no AABW production.
0.5x_fluxA | 2x_fluxA	Figure 4.3b Flux 'A'	0.5, 1.0, 2.0	Yes	0.5 Steady northern sinking 1x-2x Intermittent flushes in Antarctic region, with smaller northern flushes. No steady AABW production.
0.3x_fluxB | 1x_fluxB	Figure 4.3b Flux 'B'	0.3, 0.5, 0.75, 1.0	Yes	AABW production occurs in all experiments. 0.3 Strong northern sinking 0.5 Either Strong northern sinking or Subantarctic sinking 0.75 Subantarctic or weak northern sinking 1.0 Weak northern and weak Subantarctic sinking

4.4.1 Closed Basin Experiments

As a next step in improving the representation of AABW production in the basin model, the basin was expanded to extend from 70°S to 70°N. As in the one-hemisphere experiments, the temperature was restored using a 50-day restoring time constant to the Levitus(1982) zonally and annually averaged values. These temperature values were made symmetric about the equator by averaging Northern and Southern Hemisphere values. The same wind formula (EQ 4.2.1) used in the one-hemisphere experiments was applied, which generated a zonal wind stress that was symmetric about the equator. The salinity fluxes from 70°S to 10°S were the mirror image of those from 10°N to 70°N, so the extratropical regions are directly comparable to the one-hemisphere experiments. A small negative salinity flux (positive freshwater flux) was applied at the equator, which was increased to match the value at 10°N and S. The net salinity flux in the region between 10°S and 10°N was zero, as was the net salinity flux in each of the extra-tropical regions. This pattern of freshwater forcing results in no interhemispheric freshwater transport. The salinity flux for the whole basin is shown in Figure 4.3a.

When subjected to the 1.5x salinity forcing, the two-hemisphere configuration exhibited asymmetric oscillations. Separate flushes occurred in both the Northern and Southern Hemisphere. The basin averaged temperature is shown in Figure 4.12. The circulation was initially symmetric about the equator, and haloclines formed in both the North and South. The regions along the equatorward edges of the haloclines become convectively unstable, and as these instabilities interacted over approximately the first 800 years, the circulation became asymmetric about the equator. The first two declines in basin averaged temperature represent small, shallow flushes that occurred in the Southern Hemisphere. Following the second of these flushes, the Southern Hemisphere produced denser and deeper intermediate water, while the North remained stably stratified. During this time, the warm salty intermediate water produced in the Southern Hemisphere contributed to the subsurface warming. As the deep ocean warmed, the North also became unstable. The large temperature drop seen at about year 7000 in Figure 4.12 occurred when the North, where deep water had not been cooled as much by the earlier flushes, overturned to the bottom. A shorter decoupled phase was followed by a shallow southern flush, a return to the deeper intermediate water forming in the south, and the cycle continued.

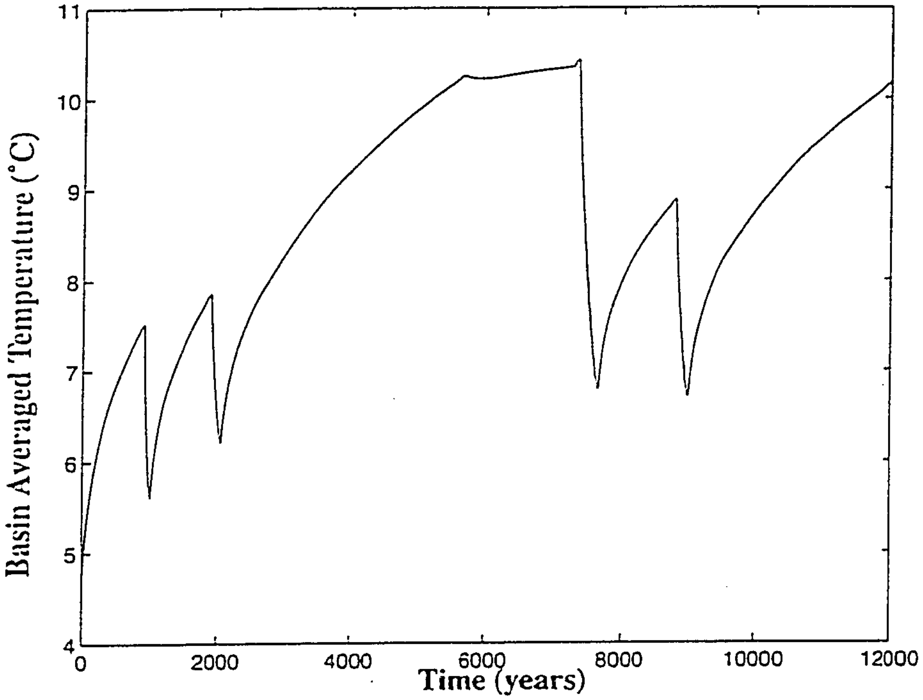

FIGURE 4.12 Basin averaged temperature for the closed two-hemisphere basin, experiment 2h_1.5x_closed. Units are °C.

In this configuration both hemispheres can and do serve as regions for a flush. Neither hemisphere was the preferred site for deep sinking, as evidenced by the fact that under 2x salt forcing (2h_2x_closed) a similar pattern of overturning occurred with the roles of the hemispheres reversed. Note that this configuration did not produce deep water between flushes.

4.4.2 Two-Hemisphere Basin Experiments with Reentrant Channel

The above example needed to be modified in order to better address the question of competing deep water sources in a more realistic ocean. A two-hemisphere basin with a reentrant channel was configured, as described in section 4.2. The basin with the reentrant channel was subjected to the same temperature and wind stress forcing as the symmetric two-hemisphere basin above. These results are discussed in section 4.4.2.1.

The freshwater flux profile used in section 4.4.2.1 was then altered to allow the production of AABW. This was attempted in two ways: first, by reducing the high latitude freshening in the southern hemisphere; and second, by shifting the freshening maximum northward. Both may be considered as an approximation to the role of brine rejection and northward ice drift, but they are primarily motivated by the desire to produce a continuous supply of AABW. The production of AABW requires salt to be advected southward across the ACC to compensate for the surface freshening. The rate of AABW production is limited by the supply of salt advected from lower latitudes. Toggweiler & Samuels (1995) suggest that an underrepresentation of the supply of NADW to the high southern latitudes is responsible for the chronic freshness of Antarctic surface waters in some coarse resolution models. In response to this shortcoming, some of these models enhance the Antarctic salinity (England, 1993, Toggweiler & Samuels, 1993b). Two salinity flux patterns, and the behavior of the model under those salinity forcings, are discussed in section 4.4.2.2 and section 4.4.2.3.

4.4.2.1 Equatorially Symmetric Forcing

The addition of a reentrant channel in the Southern Hemisphere, as a representation of Drake Passage, produces profound changes in the mixed boundary condition circulation. The dynamic constraint of no-net geostrophic flow above the sill across the latitude of Drake Passage, as discussed in Chapter 3 isolates the upper ocean south of Drake Passage from the more saline waters of the lower latitudes. The 1.5x salinity flux pattern that produced flushes in both hemispheres in the closed two-hemisphere basin could not produce flushes in the Southern Hemisphere once Drake Passage was added. The high southern latitudes were subject to a strong halocline that was isolated from the heat and salinity required to destabilize it. As a result, this region remained strongly capped and the model produced deep water only in the North. The 0.5x salinity flux supported no flushes and yielded steady deep water production. Oscillatory behavior was observed under salinity forcing greater than 0.5x (see Figure 4.13). Flushes occurred in the north only. Sediment records (e.g. Charles & Fairbanks 1992), however, indicate that high nutrient water from a southern source filled the deep oceans throughout the last glaciation. The above example illustrates the fact that deep-decoupling oscillations can occur in this configuration in the absence of AABW production. In order to test whether deep-decoupling oscillations could have been responsible for the climate variability seen in the ice core and sediment records, further modifications were required.

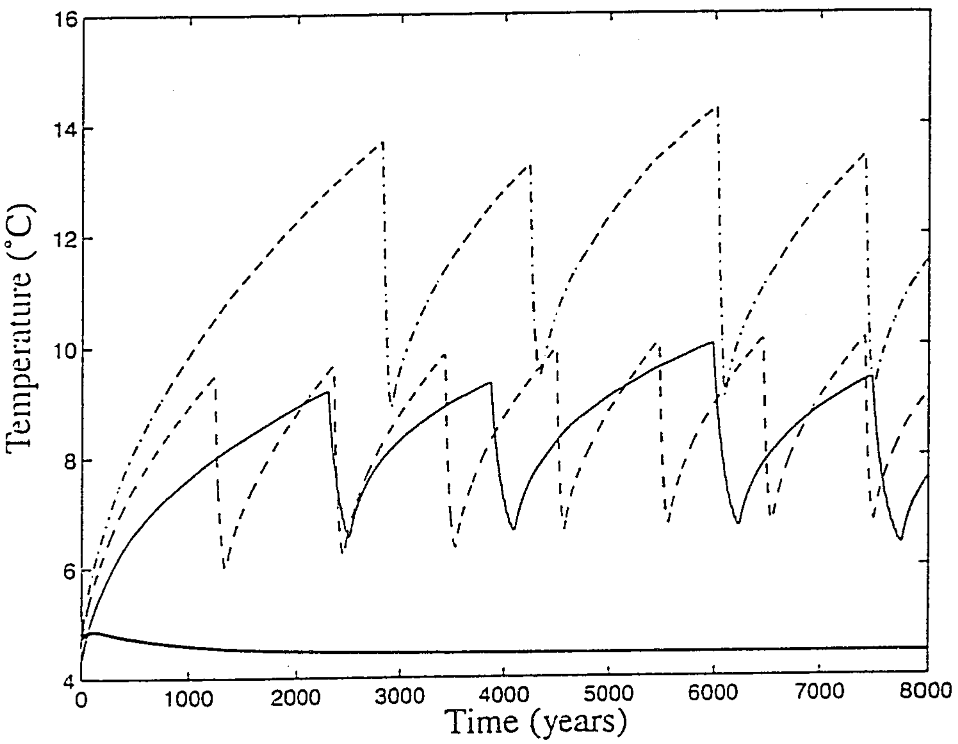

FIGURE 4.13 Basin averaged temperatures for two-hemisphere basin with reentrant channel, salinity forcing as in Figure 4.3a. Thin solid line is experiment 2h_1x, dashed line is experiment 2h_1.5x, dot-dashed line is experiment 2h_2x, and thick solid line is experiment 2h_0.5x.

4.4.2.2 Flux Pattern A

The first attempt to produce a continuous supply of southern-source deep water used the salt flux profile shown in Figure 4.3b as pattern A. This salt flux profile failed to produce continuous AABW production, but did result in oscillatory behavior with periodic southern deep water production. Beginning in the deep-decoupled phase (Figure 4.14a) the shallow intermediate water formation in the northern hemisphere gradually deepens (Figure 4.14b). As the Northern Hemisphere begins producing deep water that penetrates to the depth of the sill in Drake Passage, this deep water becomes available to supply the wind-driven upwelling south of the latitude of Drake Passage. The first

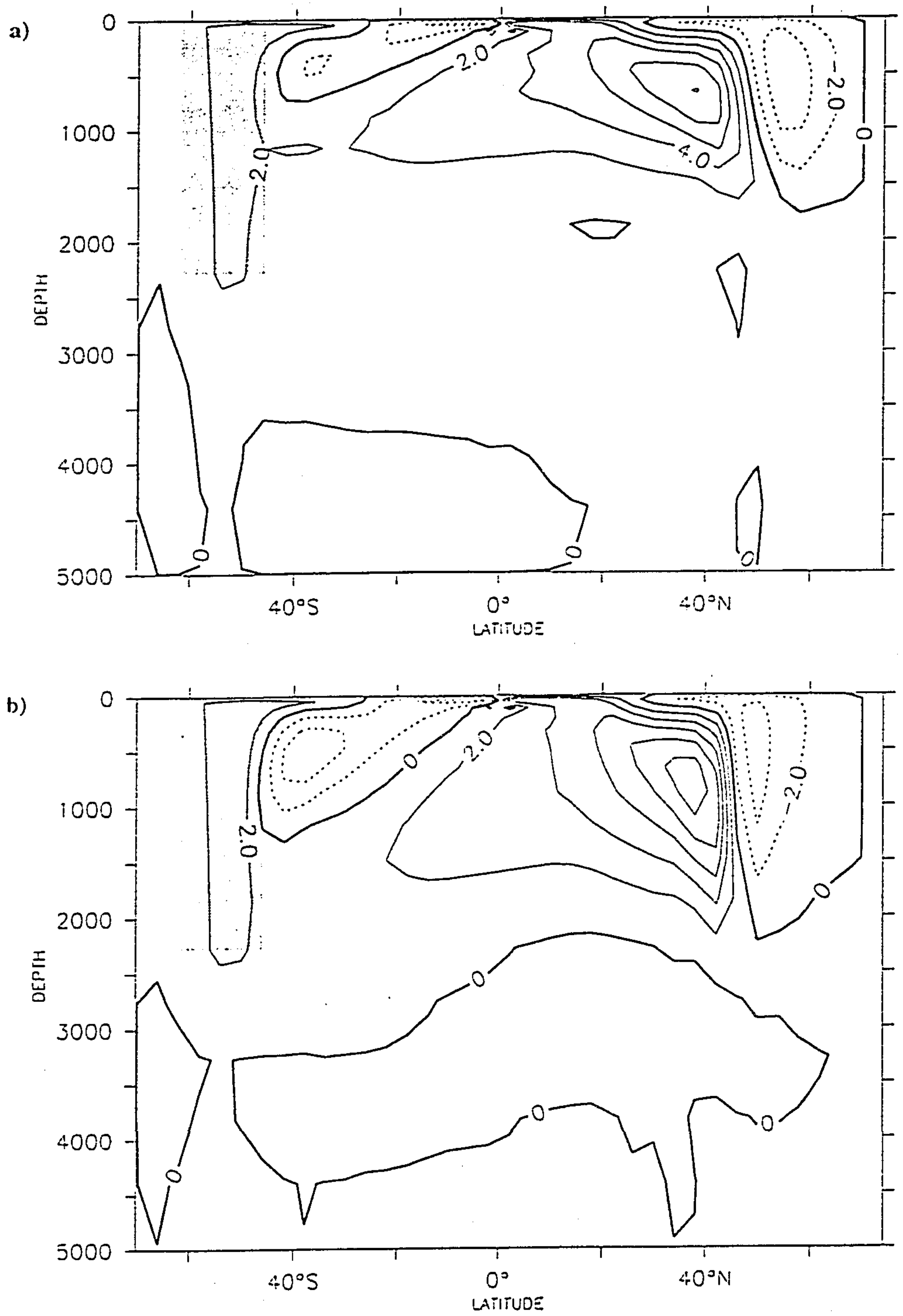

FIGURE 4.14 Overturning stream function during oscillations in Experiment 1x_fluxA. a) deep-decoupled phase (4300 yrs), b) gradual northern deepening (6500 yrs), c) beginning of flush (7550 yrs), and d) peak of flush (7700 yrs).

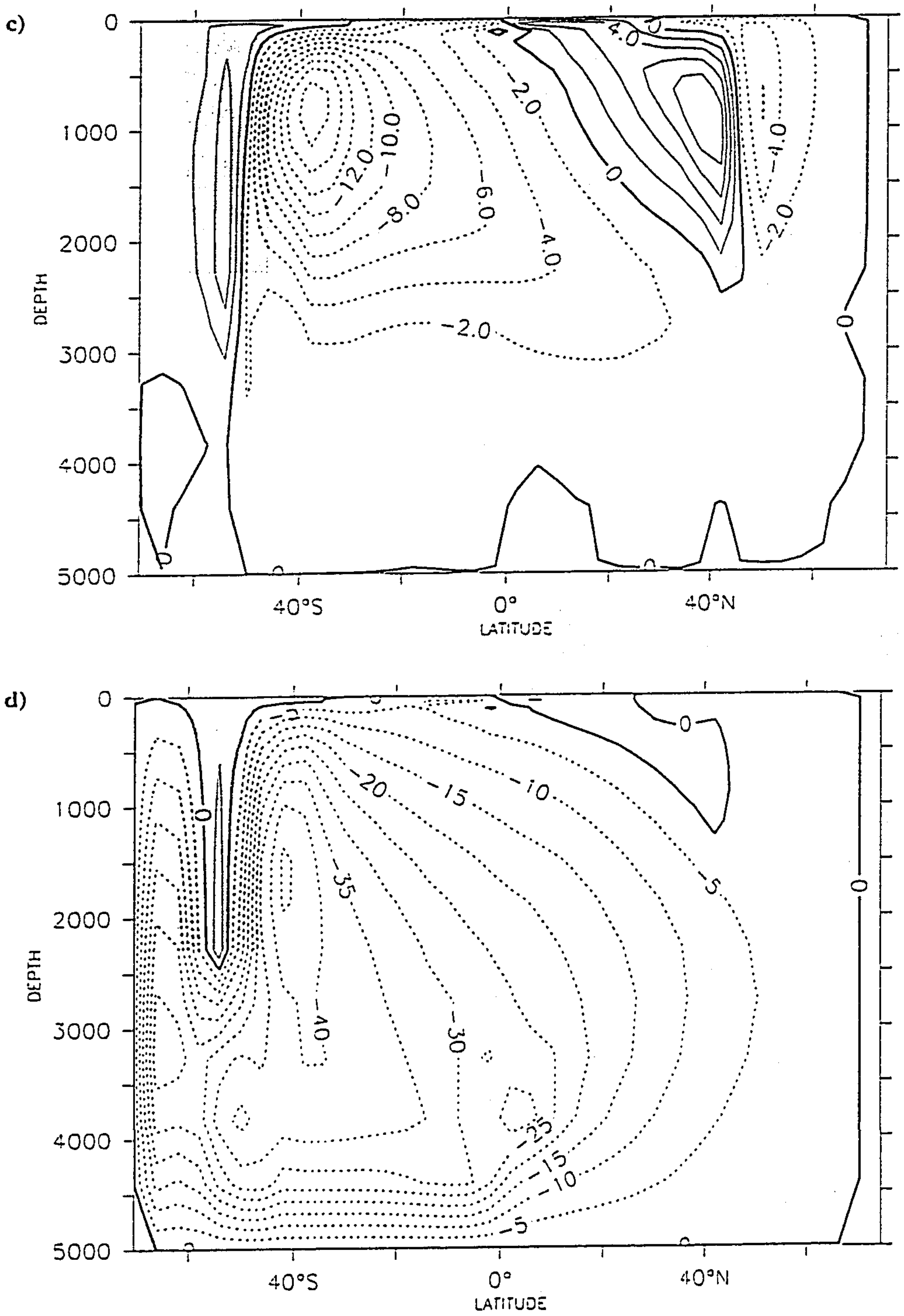

FIGURE 4.14 **(Continued)**

response is an increase in the sinking north of Drake Passage (Figure 4.14c), and eventually this eclipses the north as the source of deep water. As the Subantarctic deep water production increases, the southern halocline is eroded by the supply of relatively salty water, and a flush occurs in the Southern Hemisphere (Figure 4.14d). During peak AABW production, the northern sinking shoals. As AABW production ebbs and the southern halocline reforms, the mid-depths are ventilated by both Subantarctic and northern sources. Eventually, the northern source dominates this mid-depth ventilation again.

After a large flush like the one described above, the circulation begins a series of oscillations with smaller period and amplitude. These oscillations involve only flushes in the northern hemisphere; the southern halocline remains a permanent feature throughout the smaller flushes. The bottom water temperatures gradually warm throughout the cycle, while temperatures in the upper-deep ocean (~3000m) oscillate in temperature. The northern flush penetrates to the bottom, but in doing so it only slightly increases the area averaged density in the lowest layer. Over the course of several of these northern-flushing-only oscillations, the deep ocean gradually becomes less dense, and it is the reduction in the deep stratification that allows the southern flushes to proceed.

The model was also run with 0.5x_fluxA and 2x_fluxA forcing, and in none of these cases was AABW continuously produced. Run 0.5x_fluxA produced steady sinking in the North. Increasing the salinity flux to 2x_fluxA produced the same pattern of oscillations as the 1x_fluxA case: several smaller flushes in the north followed by a larger flush involving the southern sinking regions. The goal of this exercise was to examine the influence of a continuous supply of AABW on deep-decoupling oscillations, so a new flux pattern was sought.

4.4.2.3 Flux Pattern B

In order to produce a continuous supply of southern source deep water, the salt flux forcing was again modified. The next profile used is shown in Figure 4.3b as flux pattern B. The high southern latitudes now receive very little freshening, with the maximum freshening shifted northward away from the southern wall. This can be considered as either the effect of the northward export of ice and its subsequent melting in the ACC, or an artificial construct to obtain a continuous supply of AABW.

The model was forced by a range of salinity forcings, from 0.3x to 2x times the nominal value, but at no time were deep decoupling oscillations observed under steady forcing. Under some of the salinity forcings (0.4x-0.6x) the circulation did settle into different equilibria depending on the initial conditions, with both of the equilibria having continuous AABW production. To illustrate the behavior of the model under salinity forcing near this range, a hysteresis experiment similar to that of Rahmstorf (1995) was conducted. The model was initialized with weak salinity forcing (0.3x_fluxB), under which only a strong northern overturning equilibrium was found. The salinity forcing was increased step-wise to 0.4x_fluxB and the circulation was allowed to adjust for two thousand years. Thereafter, the salinity flux was increased by 0.05x and allowed to adjust every 1000 years, up to a salinity forcing of 1x_fluxB. The salinity flux was similarly stepped down to 0.35x_fluxB. As the salinity flux was reduced from 1x_fluxB, Subantarctic overturning was consistently stronger than northern overturning until 0.35x_fluxB, when strong northern sinking resumed. As can be seen in Figure 4.15, two equilibrium overturning solutions (weak northern and subantarctic) occur for the range of fluxes from 0.65x_fluxB to 1x_fluxB.

In addition, the salinity forcing was stepped down from the 0.65x_fluxB and 0.85x_fluxB values. When the salinity forcing was reduced after reaching only 0.65_fluxB and 0.85_fluxB, the overturning remained stronger in the Northern Hemisphere than in the Southern Hemisphere until about 0.55x_fluxB. Subantarctic overturning remained stronger than northern overturning as the salinity flux was further decreased, until 0.35x_fluxB, when strong northern overturning resumed. For a salinity forcing of 0.6x_fluxB, three overturning solutions are possible: strong-northern, weak-northern, and subantarctic.

The two equilibrium states produced by salinity forcing between 0.4x_fluxB and 0.6x_fluxB can be described as northern sinking and subantarctic sinking. An example of the overturning stream functions for the two equilibria is shown in Figure 4.16. Under salinity forcing weaker than 0.4x_fluxB, the solution approximated the northern sinking solution shown in Figure 4.16a. Under salinity forcing of between 0.4x_fluxB and 0.6x_fluxB, the subantarctic solution approximated the solution of Figure 4.16b. For the subantarctic sinking solution, as the salinity forcing increased from 0.4x_fluxB to 0.6x_fluxB, the subantarctic ventilation shoaled, and the ocean's interior was ventilated exclusively by AABW. In contrast, as the forcing increased from 0.4x_fluxB to

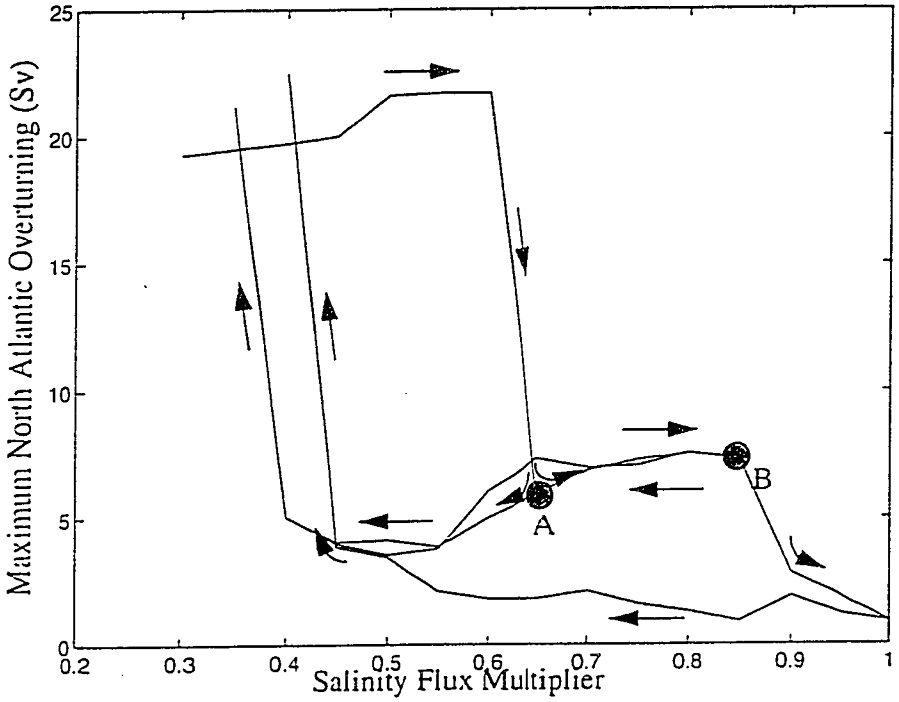

FIGURE 4.15 **Maximum North Atlantic overturning, hysteresis experiment. Model was initialized at 0.3x_fluxB, and the salinity forcing was gradually increased to 1x_fluxB. Decreases began at 0.65 ('A'), 0.85 ('B'), and 1x.**

0.6x_fluxB for the northern-sinking solution, the strength of the northern overturning remained relatively unchanged. As the salinity flux increased beyond 0.65x_fluxB, a weak northern sinking solution was seen, with the subantarctic sinking reduced to approximately 2 Sv.

The northern sinking case under 0.5x_fluxB is similar to today's THC, delivering large amounts of heat to the high northern latitudes (see Figure 4.17). The southern sinking case delivers the heat and salt of the low-latitude ocean to the Subantarctic where sinking occurs. Table 4.3 shows the advective transport of salt in the upper five levels (472m)

a) Northern Sinking Case

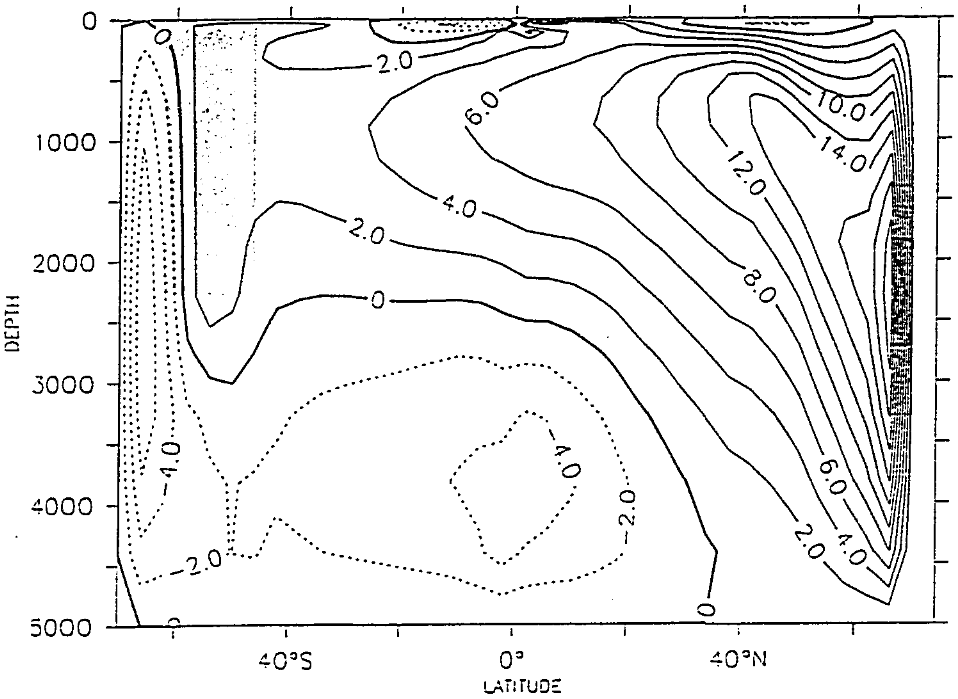

b) Subantarctic Sinking Case

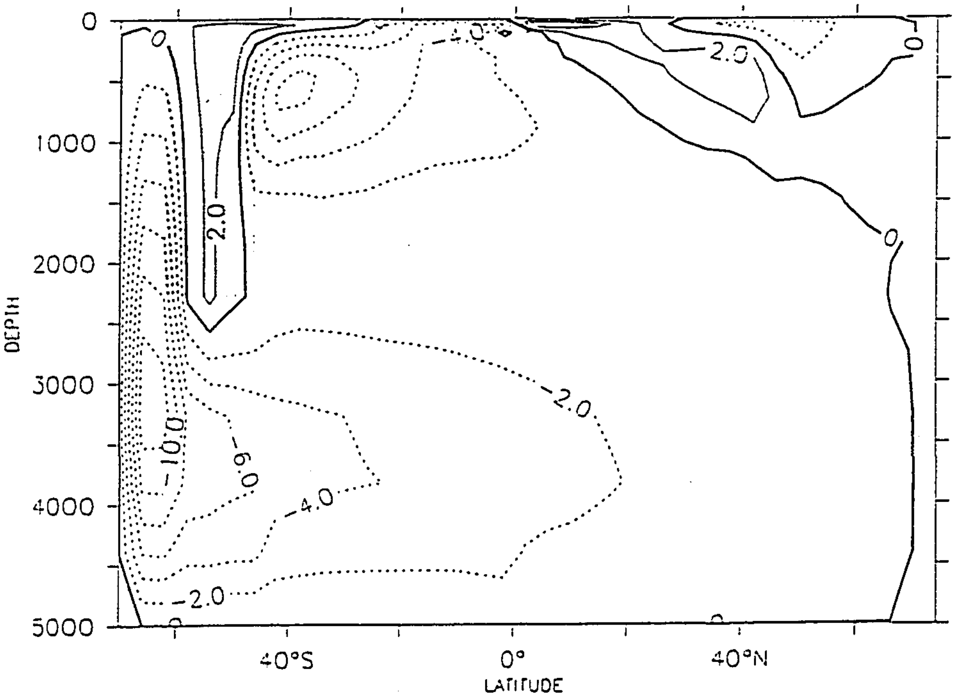

FIGURE 4.16 Overturning stream function for mixed boundary condition experiment 0.5x_fluxB. a) Northern sinking solution, and b) Subantarctic sinking solution.

of the ocean for the two equilibria. Note that in the northern sinking solution case there is *northward* transport of salt in the top 472m at 35°S.

TABLE 4.3 Advective transport of salt for the two equilibria seen in experiment 0.5x_fluxB.

	Northward Salt Transport in the top 472m at 35°S (10^8 kg/sec)	Northward Salt Transport in the top 472m at 35°N (10^8 kg/sec)
Northern Sinking Solution	0.80	4.22
Sub-Antarctic Sinking Solution	-2.99	1.20

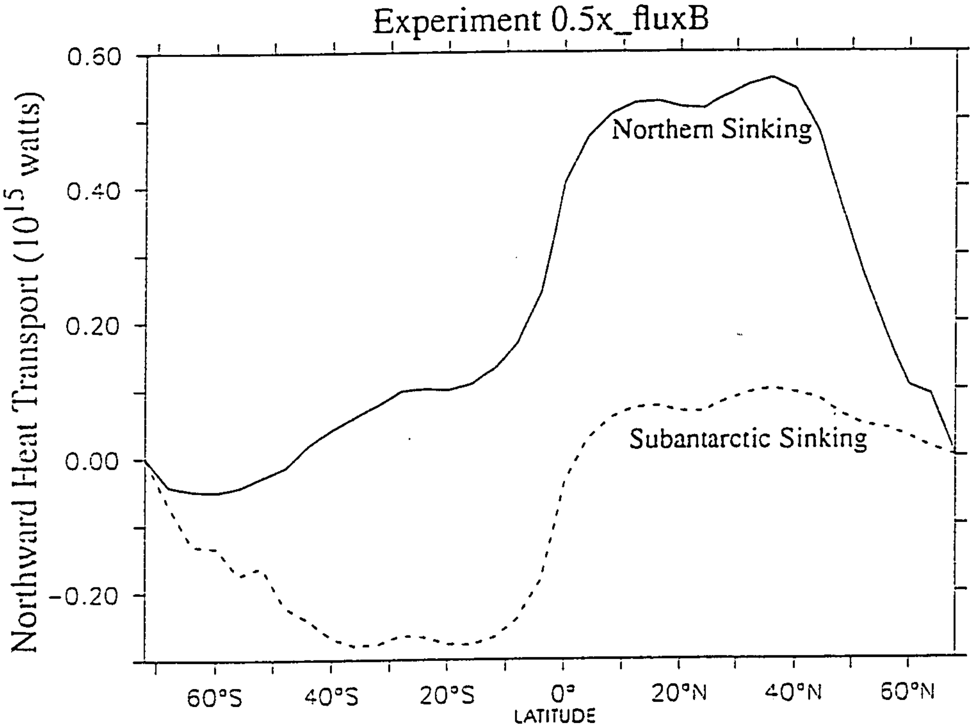

FIGURE 4.17 Northward transport of heat for the two equilibria of experiment 0.5x_fluxB. Solid line shows heat transport for northern sinking solution, dashed line shows heat transport for Subantarctic solution. Units are 10^{15} watts.

The hysteresis experiment illustrated the changes in the circulation in response to changes in the salinity forcing. In addition to the overturning circulations described above, different equilibria were found when the 0.75x_fluxB and 1x_fluxB salinity forcings were applied to an ocean basin initialized at rest. For both of these salinity forcings, an equilibrium was reached that approximated the subantarctic sinking case of 0.5x_fluxB. Under salinity forcing 0.75x_fluxB, 5.5 Sv of subantarctic overturning occurred to depths of up to 2000m, while less than 1 Sv of overturning to depths of approximately 1000m occurred in the North. Similarly, the 1x_fluxB forcing resulted in 3.6 Sv of subantarctic overturning, compared to 2 Sv on northern overturning. While neither of these constitute vigorous ventilation of the deep ocean, they are different overturning equilibria than were seen under the same forcing in the hysteresis experiment. In both equilibria, the deep ocean is ventilated from the antarctic sinking regions, and the stratification imposed by the presence of AABW prevents vigorous overturning from occurring elsewhere.

Although salinity forcings were found under which multiple equilibria were possible, no transitions between those equilibria occurred spontaneously. In Chapter 5, the behavior of deep-decoupling oscillations is examined in the context of simple box-models. A two-hemisphere box-model is used to more broadly explore the possible surface forcing to see if deep-decoupling oscillations can be generated.

4.5 Two-Basin Mixed Boundary Condition Experiments

In this section, mixed boundary conditions are applied to a two-basin model configuration. The results of a set of standard experiments are presented first, and then additional experiments are conducted to show that the Drake Passage effect is not diminished under mixed boundary conditions. AABW production continues under stronger fresh water forcing in the strong wind case than the nominal wind case. Finally, the restoring temperatures are adjusted downward to reflect a cooler climate, and the behavior of the circulation under a range of salinity forcings is noted. The cooler surface boundary conditions and sufficient inter-basin freshwater transport via the atmosphere combine to produce deep-decoupling oscillations in the presence of continued AABW formation. The results of the standard-climate experiments are summarized in Table 4.5, and those of the cold-climate experiments are summarized in Table 4.5.

4.5.1 Standard Forcing

The two-basin geometry of the experiments conducted in Chapter 3 was used for the experiments in this section. In light of the Drake Passage configuration experiments conducted in Section 3.4.2, the profile of Drake Passage was modified slightly. Below 2000m, the meridional width of the gap was reduced by raising the sill depth near the northern and southern boundaries of Drake Passage. These changes are apparent in the shaded area in Figure 4.20. Apart from the sill depth, no changes were made to the topography. The modified Drake Passage better represents the real bathymetry, and reduces the ACC transport to a more realistic value.

Temperatures at the surface are restored to the profile shown in Figure 4.18. North of 50°S, these temperatures are the same as those used in the two-hemisphere single basin experiments of section 4.4. The surface restoring temperatures south of 50°S are reduced to encourage AABW production. Unlike the two-basin experiments in Chapter 3, the same restoring temperature is used for both basins. The salinity flux, however, differs between the two basins. The salinity flux profile 'B' from the two-basin experiments is modified to produce three different patterns. The first, shown in Figure 4.19a and identified as pattern 'B1', produces an export of fresh water from the Atlantic basin of 0.29Sv. For comparison, Broecker (1991) estimates a fresh water export from the Atlantic basin of 0.35 ± 0.12 Sv. The second salinity flux pattern, shown in Figure 4.19b and identified as pattern 'B2', reduces the inter-basin fresh water transport to 0.22 Sv. Finally, salinity flux pattern 'B3', shown in figure Figure 4.19c, reduces the fresh water transport between basins to 0.11 Sv. Only the zonal component of the wind stress is applied, and the same values as those of section 4.4 are used (see Figure 4.3d).

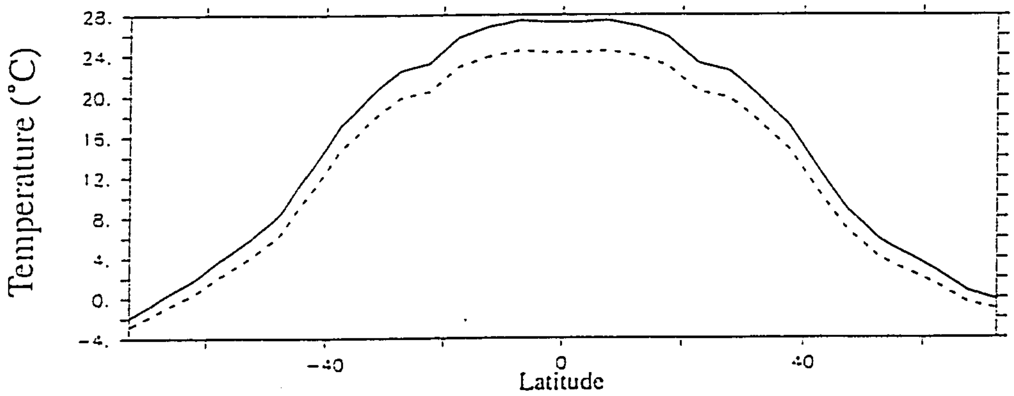

FIGURE 4.18 Restoring temperature for the two-basin mixed boundary condition experiments. Solid line is standard restoring temperature, dashed line is restoring temperature for cold-climate experiments.

Multiplying salinity flux pattern B1 by a factor ranging from 0.8 to 1.3 produces circulations that approximate the conveyor-type circulation of our current climate (see Figure 4.20). AABW is produced in the south and fills the deep ocean. NADW is formed in the north of the Atlantic and leaves the Atlantic basin between approximately 1500m and 3200m. The Pacific is characterized by broad upwelling, but unlike the fully restoring

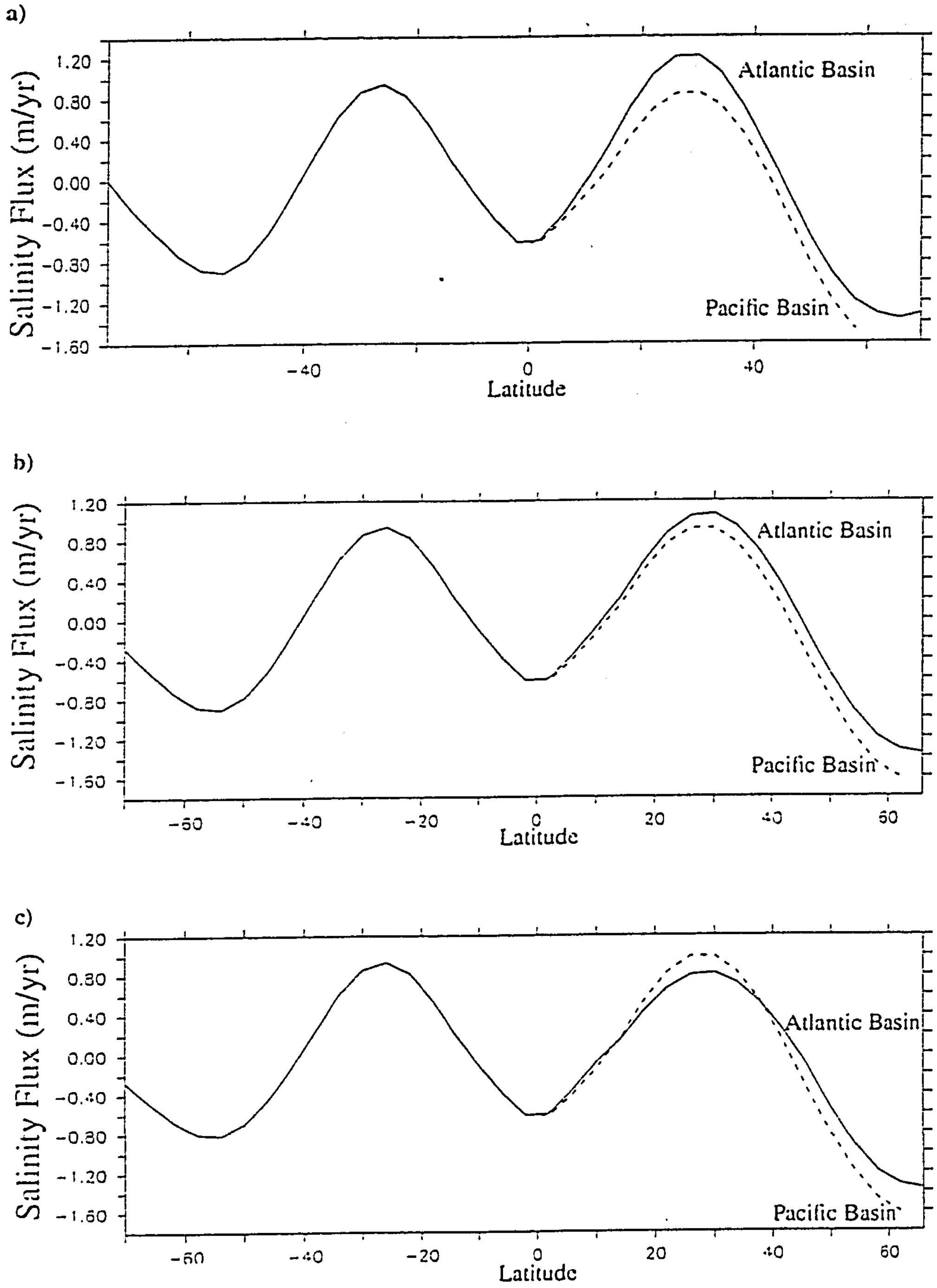

FIGURE 4.19 Salinity fluxes used in the two-basin mixed boundary condition experiments. a) salinity flux pattern B1, b) salinity flux pattern B2, c) salinity flux pattern B3. Fluxes are given in equivalent m/yr. In the North, the solid line represents the flux for the Atlantic basin, the dashed line for the Pacific basin.

experiments of Chapter 3, no intermediate water is formed in the North Pacific. A strong halocline caps the North Pacific instead.

Several descriptive measures of the circulations for these runs are given in Table 4.5. Note that as the magnitude of the salinity forcing is increased beyond 1x for salinity flux pattern B1, NADW production increases. Further increasing the fresh water flux to 1.4 times the standard forcing resulted in a shut-off of AABW production. This has implications for concerns about the stability of today's conveyor circulation. We expect that if the atmospheric temperature rises in response to anthropogenic greenhouse gas emissions, so will the amount of water vapor in the atmosphere. If the increase in atmospheric water vapor occurs without major changes in the basic patterns of atmospheric water vapor transport, the stronger freshwater export from the Atlantic that would result should act to enhance the existing NADW production. Note that this view takes into account only water vapor transport, and not temperature change or changes in atmospheric circulation or melt water boundary conditions. We are interested in looking at circulations with continued AABW production, so the fresh water flux was not increased beyond 1.4x. Creating a salinity flux pattern that freshens the region around Antarctica even less than this one does might prevent the Antarctic ventilation from shutting off before the North Atlantic overturning is eliminated. The steady solutions observed here, however, will allow us to examine the Drake Passage effect in a mixed boundary condition experiment.

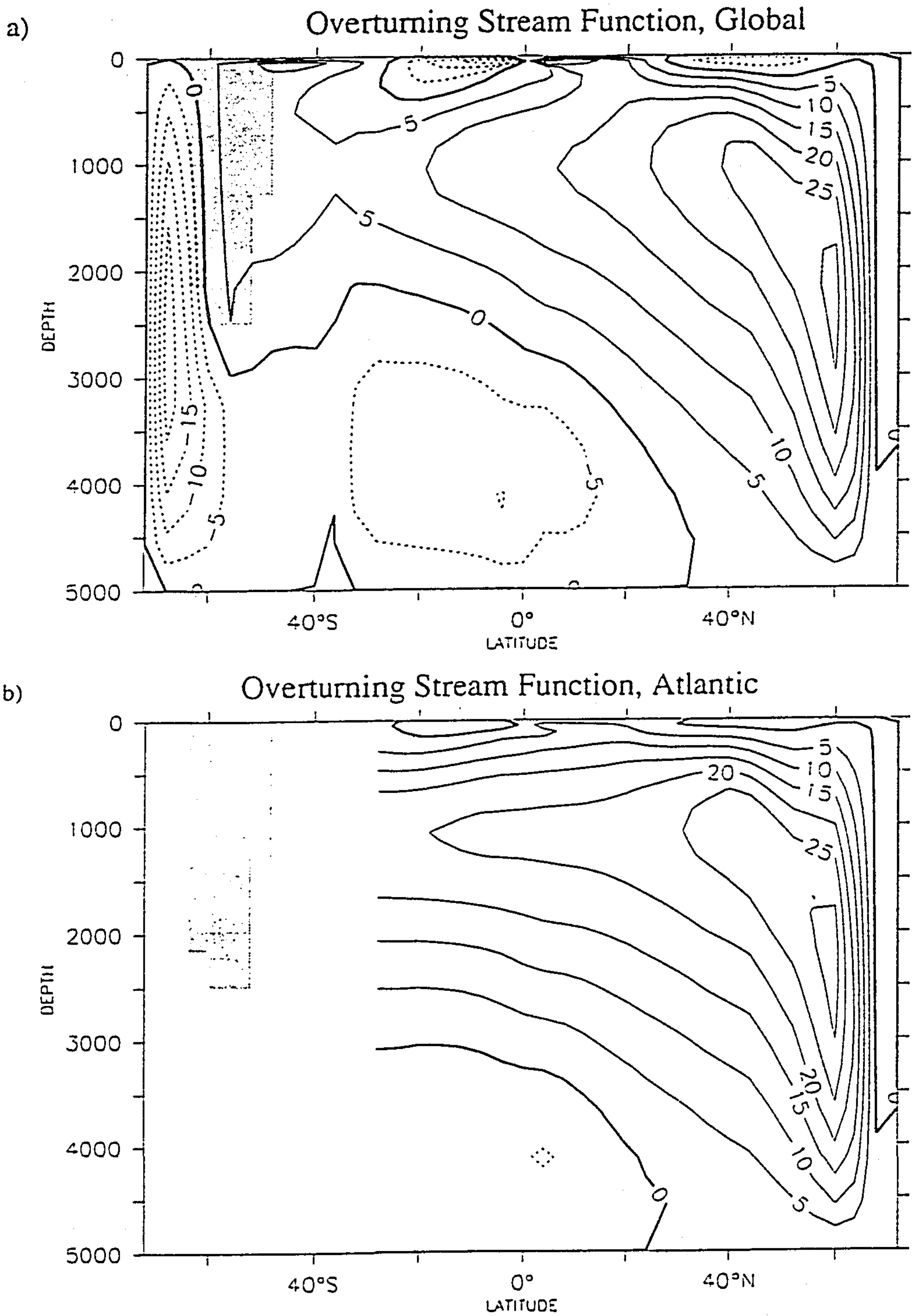

FIGURE 4.20 Equilibrium solution for standard salinity forcing, two-basin mixed-boundary condition experiment (exp. 1x_fluxB1). Overturning stream function a) global, b) Atlantic basin, and c) Pacific basin. Units are 10^6 m^3/sec (Sv), contour interval is 5 Sv. d) shows the zonally averaged salinity in the Atlantic basin. Units are psu, contours are 0.2 psu.

c) Overturning Stream Function, Pacific

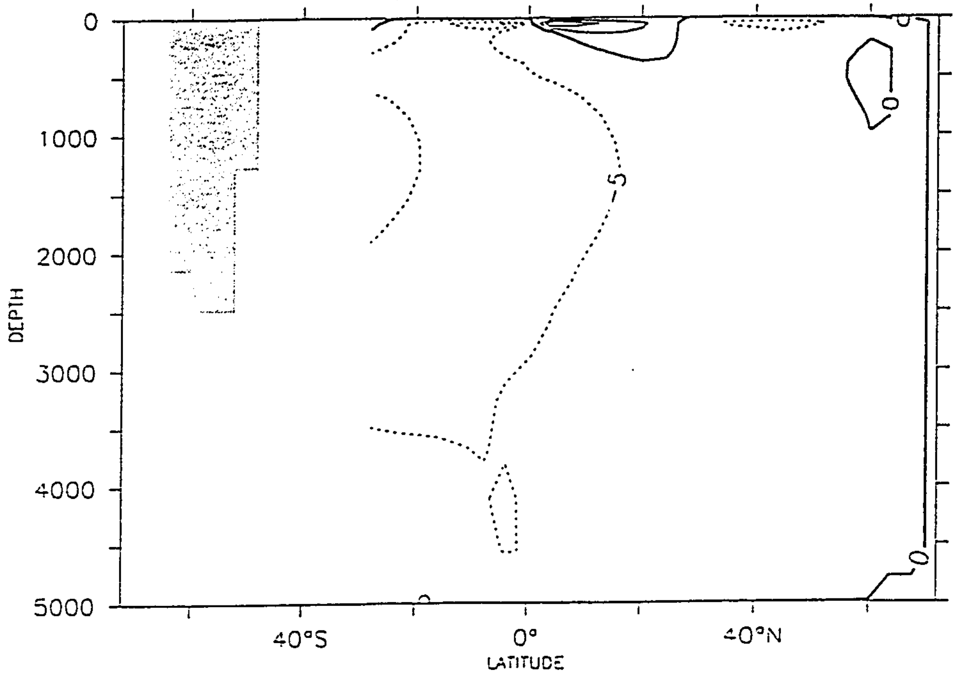

d) Zonally Averaged Salinity, Atlantic Basin

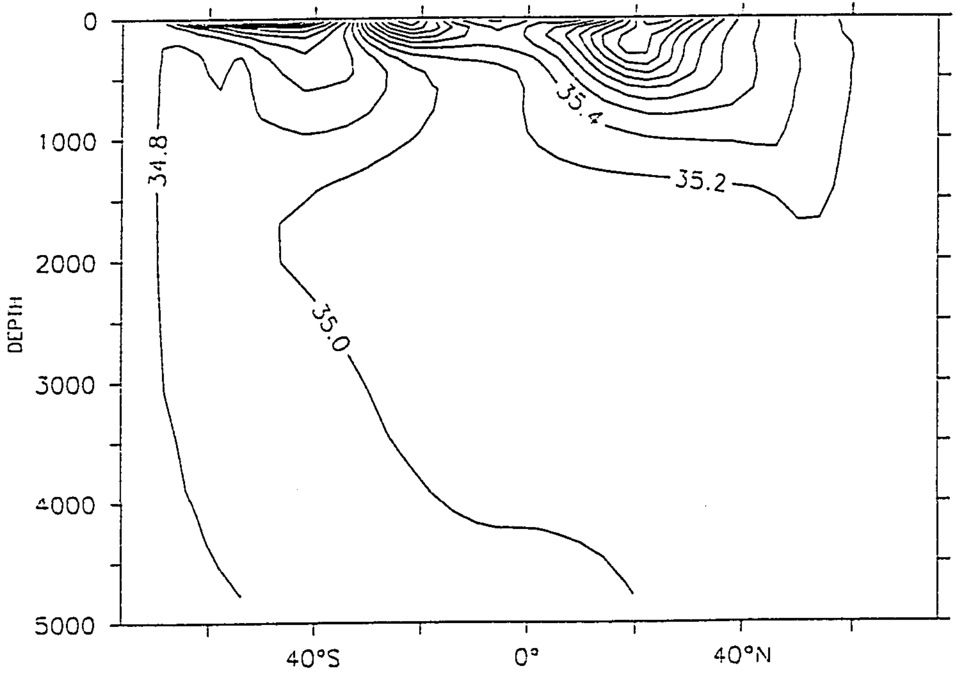

FIGURE 4.20 (Continued)

In addition, the steady mixed boundary condition solution created here will be revisited in Chapter 6, where a stochastic element will be added to the freshening in the North.

TABLE 4.4 Two-Basin Mixed-Boundary Condition Experiments, Standard Climate.

Experiment Label	Salinity Flux Multiplier	Atlantic Outflow (Sv)	AABW flow into Atlantic (Sv)	Heat Transport at 34°N (10^{15} W)	Maximum Northern Overturning (Sv)
0.8x_fluxB1	0.8	18.79	4.92	0.503	32.82
1.0x_fluxB1	1.0	18.90	4.71	0.523	31.59
1.2x_fluxB1	1.2	18.56	4.66	0.630	31.75
1.3x_fluxB1	1.3	18.72	4.31	0.639	32.19
1.4x_fluxB1	1.4	19.99	0.	0.645	30.42
Strong Southern Wind Experiments					
0.8xs_fluxB1	0.8	22.15	5.79	0.529	31.42
1.0xs_fluxB1	1.0	22.22	5.89	0.547	31.71
1.2xs_fluxB1	1.2	22.44	5.91	0.567	32.45
1.3xs_fluxB1	1.3	22.70	5.77	0.580	32.69
1.4xs_fluxB1	1.4	22.87	5.67	0.593	32.95
1.5xs_fluxB1	1.5	22.94	4.73	0.619	33.22
1.6xs_fluxB1	1.6	22.70	4.81	0.662	33.57
1.7xs_fluxB1	1.7	23.00	4.70	0.643	33.52

4.5.2 Drake Passage Effect Under Mixed Boundary Conditions

In order to examine the Drake Passage effect in a mixed boundary condition experiment, the Southern Hemisphere westerlies were increased by 50%. The model was allowed to come to equilibrium under both 80% (0.8xs_fluxB1) and 100% (1xs_fluxB1) of the standard salt flux. Then, starting from the equilibrium solution for experiment

1xs_fluxB1, the strength of the salinity forcing was stepped through the same progression of increases as the standard-wind case had been. As in the standard-wind case, the conveyor circulation was seen for surface forcing strengths ranging from 0.8 to 1.3 times the standard pattern. Unlike the standard-wind forcing case, the AABW production did not shut off when the salinity forcing was increased to 1.4 times its standard value; in fact, the circulation continued in the standard conveyor mode through 1.7xs, the maximum tested. The same measures of the circulation listed for the standard-wind forcing are listed for the strong-southern wind cases in Table 4.5.

The stronger Southern Hemisphere winds produce an increased Atlantic outflow, as they did in the restoring boundary condition experiments of Chapter 3. In the 1x_fluxB1and 1xs_fluxB1 salinity flux experiments, the Atlantic outflow increases by approximately 0.5 Sv for every additional 1 Sv of northward wind drift at the tip of South America. By comparison, in the two-basin restoring experiments in Chapter 3, the Atlantic outflow increases less than 0.25 Sv for every additional 1 Sv of northward wind drift at the northern boundary of Drake Passage. While the two sets of experiments differ in enough ways to make a direct comparison difficult, we see that the Drake Passage effect is not adversely affected by the switch to mixed boundary conditions.

The second interesting result from increasing the Southern Hemisphere westerlies in the mixed boundary condition experiments was ability of the model to form AABW under a stronger fresh water forcing. The strong winds act in two ways that encourage the continued production of AABW. First, and most directly, the northward wind drift tends to push surface water from the region of the strongest freshening away from Antarctica. Second, the increased Atlantic outflow delivers more high-salinity NADW to the deep circumpolar region, where it joins the water that is upwelled and transformed into AABW. The increase in the contribution of salty NADW at the expense of fresh Antarctic intermediate water in the circumpolar region allows the surface forcing to be increased considerably more than was possible in the normal-winds case.

The two-basin mixed boundary condition experiments are revisited in Chapter 6 with a stochastic element added to the northern freshening region. The strength of the Southern Hemisphere westerlies are increased in the stochastically forced case as well, to test how the Drake Passage effect influences the variability that is observed.

4.5.3 Mixed Boundary Condition Experiments in a Colder Climate

Winton (1996) found that as the average temperature of the atmosphere decreased, his model's overturning circulation increased Subantarctic deep water production at the expense of northern deep water production. In this set of experiments, the restoring temperatures are reduced, and steady salinity fluxes are applied. Because of the non-linearity of the equation of state, a particular salinity flux will have a larger impact on the buoyancy of a colder water mass than it would on a warmer mass of water. For this reason, we anticipate that the colder boundary condition will show a greater sensitivity to the high latitude freshening than occurred in the standard temperature experiments. The restoring temperatures were derived by reducing the standard two-basin temperatures by $3\cos(\varphi)$°C, where φ is the local latitude. The cold-climate restoring temperatures are shown in Figure 4.18. The model results from the cold-climate experiments are summarized in Table 4.5.

TABLE 4.5 Two-Basin Mixed Boundary Condition Experiments, Cold Climate.

Experiment Label	Salinity Flux Multiplier	Salinity Flux Pattern	Behavior of Circulation
1x_fluxB1_cold	1.0	B1	Oscillatory, alternating between strong North Atlantic overturning and weak N. Atl. overturning. AABW production continuous.
.8x_fluxB1_cold	0.8	B1	Steady strong NADW production.
1x_fluxB2_cold	1.0	B2	Steady circulation with only intermediate water formed in North Atlantic. Subantarctic ventilates deeper than North Atlantic.
1x_fluxB3_cold	1.0	B3	Steady circulation similar to 1x_fluxB2_cold.
Strong Southern Winds Experiments			
1xs_fluxB1_cold	1.0	B1	Oscillatory, similar to 1x_fluxB1_cold.
1xs_fluxB2_cold	1.0	B2	Steady circulation with Subantarctic ventilation of the deep ocean stronger than N. Atl. ventilation of deep.

The model was initialized at the steady equilibrium of the standard temperature 1x_fluxB1 experiment. When the colder restoring temperatures were applied, the overturning immediately began a series of century-scale oscillations. The circulation alternated between vigorous overturning in the North Atlantic (Figure 4.21a), and quiet periods of little or no overturning in the North Atlantic (Figure 4.21b). The heat flux out of the Atlantic basin north of 30°N is shown in Figure 4.22.

When the model was forced with 80% of the B1 pattern and the cold restoring temperatures (0.8x_fluxB1_cold) it reached a steady state with strong NADW formation. The conveyor circulation that resulted was similar to the circulation of the experiment 1x_fluxB1.

The oscillations observed in the cold-climate two-basin ocean model show a warming of the subsurface waters that contributes to the destabilization of the northern halocline. The water below the halocline also warmed in the one-basin, two-hemisphere experiments of section 4.4.2 in which AABW was produced continuously. In those experiments, however, a steady solution was found. One of the differences between the two cases is the removal of fresh water from the Atlantic basin in the two-basin configuration. This allows the Atlantic salinity to grow while the overturning is shut down. If it is the fresh water transport between basins that allows the oscillations to occur, the variability may fit the salt-oscillator description of Broecker (1991) better than it does the deep-decoupling oscillation description of Winton (1993). One way to test the importance of the fresh water transport is to reduce its magnitude.

Salinity flux pattern B2, shown in Figure 4.19b, reduces the fresh water transport out of the Atlantic from 0.29 Sv to 0.22 Sv. The majority of the reduction occurs in the Atlantic north of the Equator, where the fresh water export goes from 0.12 Sv to 0.05 Sv. When flux pattern B2 is applied, the circulation undergoes a couple of flushes, and settles

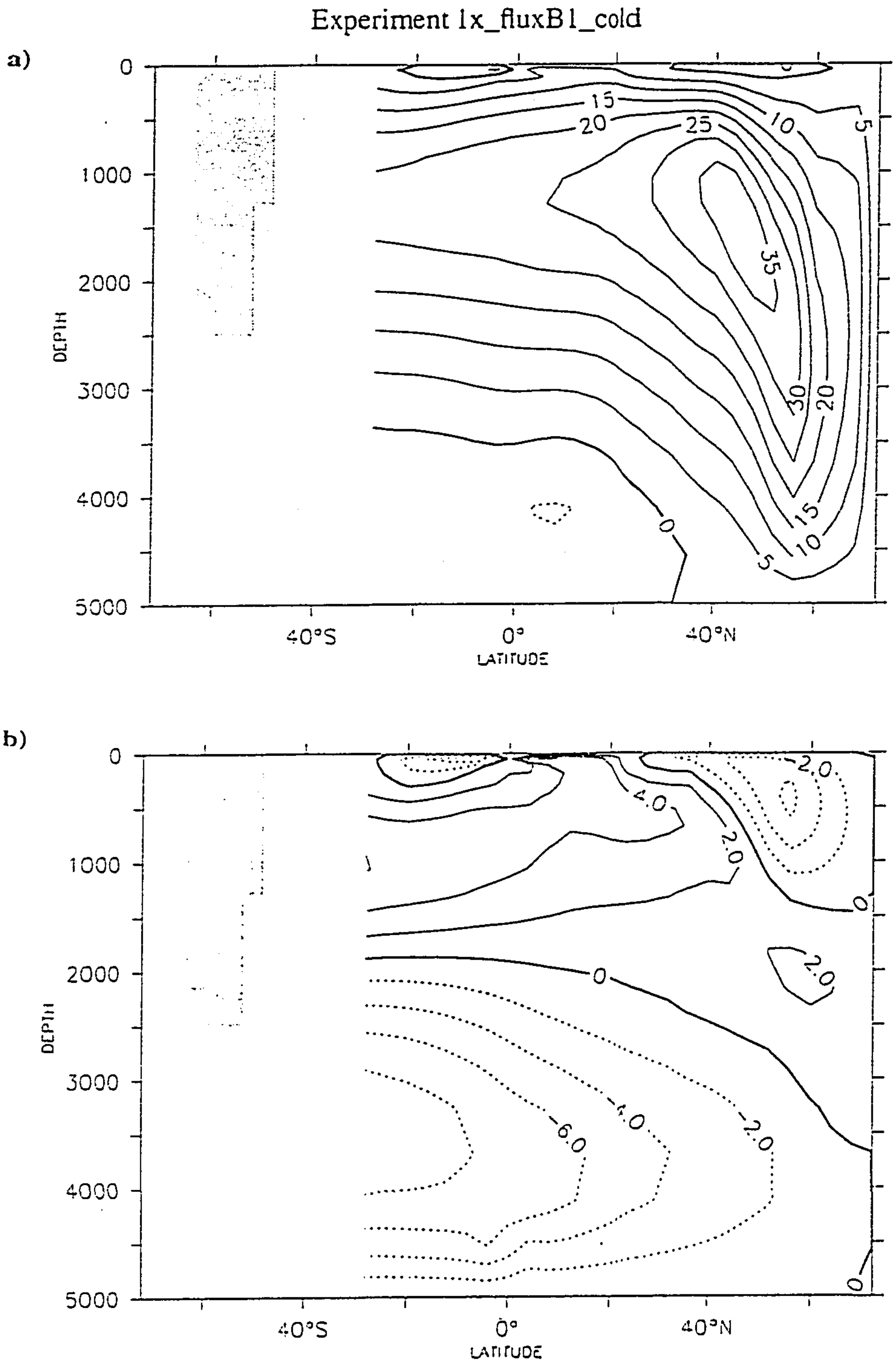

FIGURE 4.21 Overturning stream function, Atlantic basin, during oscillations in experiment 1x_fluxB1_cold. a) Strong overturning phase, and b) weak overturning phase. Shaded area indicates location of Drake Passage. Units are 10^6 m^3/sec (Sv). Contour interval for a) is 5 Sv, and for b) is 2 Sv.

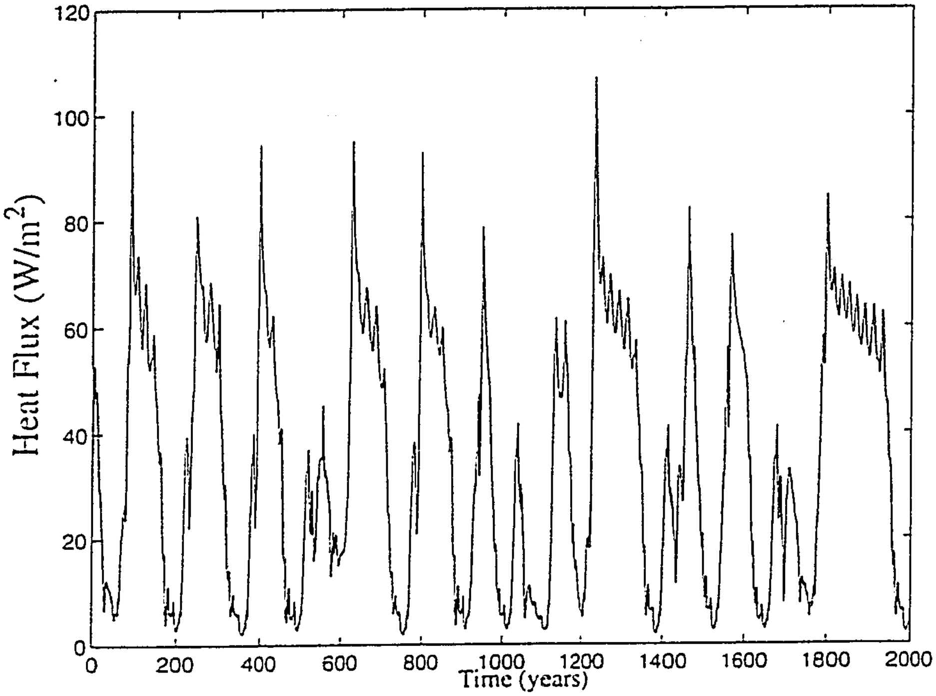

FIGURE 4.22 Average heat flux out of the Atlantic basin north of 30°N in experiment 1x_fluxB1_cold. Units are W/m^2.

into a steady overturning circulation. The global stream function for the steady 1x_fluxB2_cold experiment is shown in Figure 4.23a. Note that both the Subantarctic region and the North Atlantic produce only weak intermediate depth sinking. Salinity flux B2 resulted in steady strong NADW production in the warmer climate (not shown).

Salinity flux pattern B3, shown in Figure 4.19c, brings the freshwater transport out of the Atlantic Basin down from 0.29 Sv to 0.11 Sv (with 0.05 Sv north of the Equator). Under this salinity forcing, the ocean quickly settles into a steady Subantarctic sinking mode. The overturning stream function for experiment 1x_fluxB3_cold is shown in

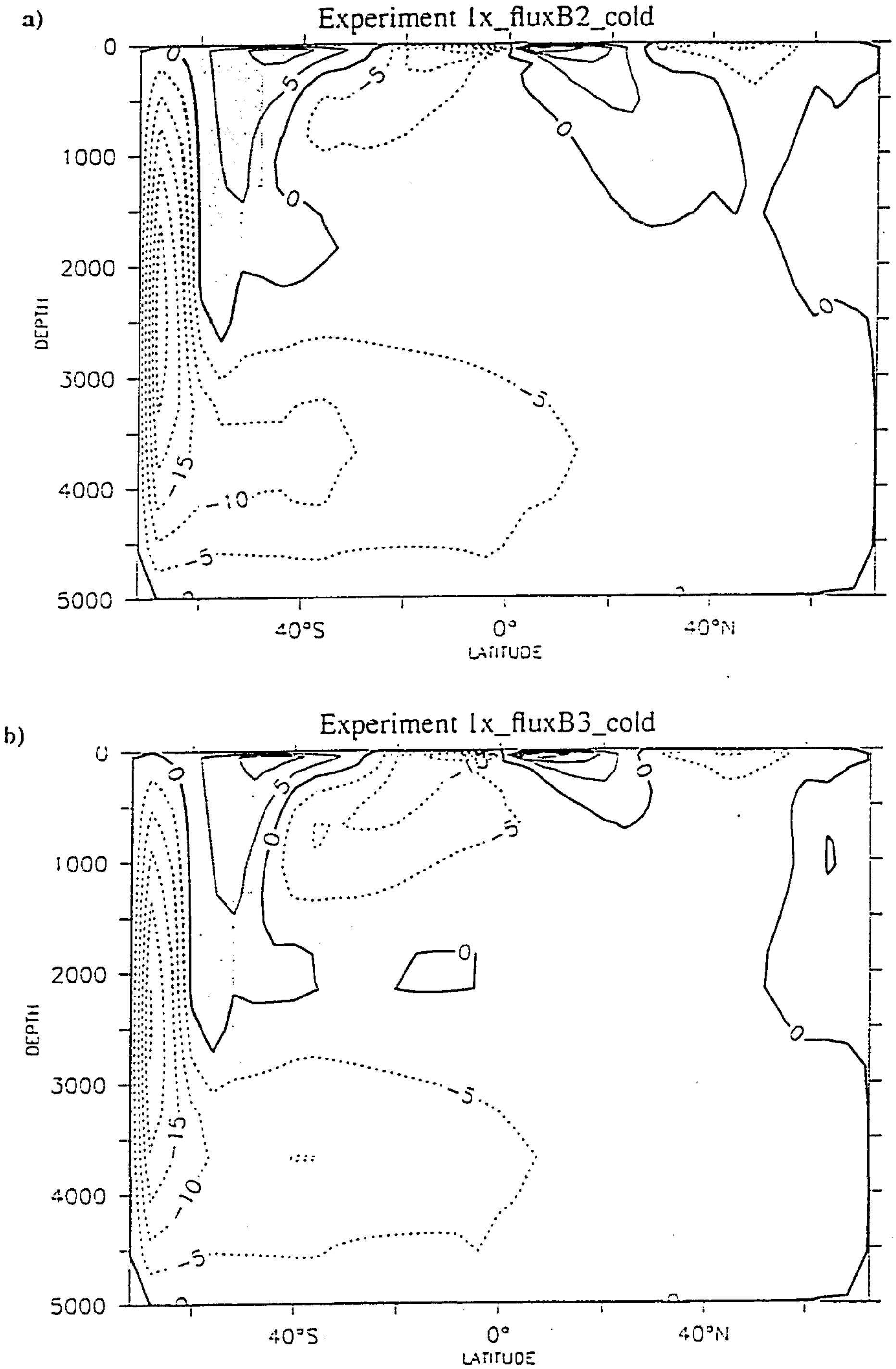

FIGURE 4.23 Overturning stream function, global ocean, a) for experiment 1x_fluxB2_cold, and b) for experiment 1x_fluxB3_cold. Shaded area indicates location of Drake Passage. Units are 10^6 m^3/sec (Sv).

Figure 4.23b. By comparison, the standard temperature equivalent (1x_fluxB3) produced steady strong NADW production (not shown).

Experiment 1x_fluxB1_cold was repeated with strong Southern Hemisphere westerlies, to see if the Drake Passage effect could produce either a steady northern-sinking solution or a bias towards the northern-sinking phase of the oscillations. Experiment 1xs_fluxB1_cold produced variability similar to that seen in the standard wind experiment. Strong Southern Hemisphere winds were also applied to an experiment forced under salinity flux B2 (1xs_fluxB2_cold). The stronger winds did not result in an increase or deepening of the northern sinking cell. Instead, the stronger winds increased the Subantarctic sinking and decreased the northern sinking. The global overturning stream function for experiment 1xs_fluxB2 is shown in Figure 4.24.

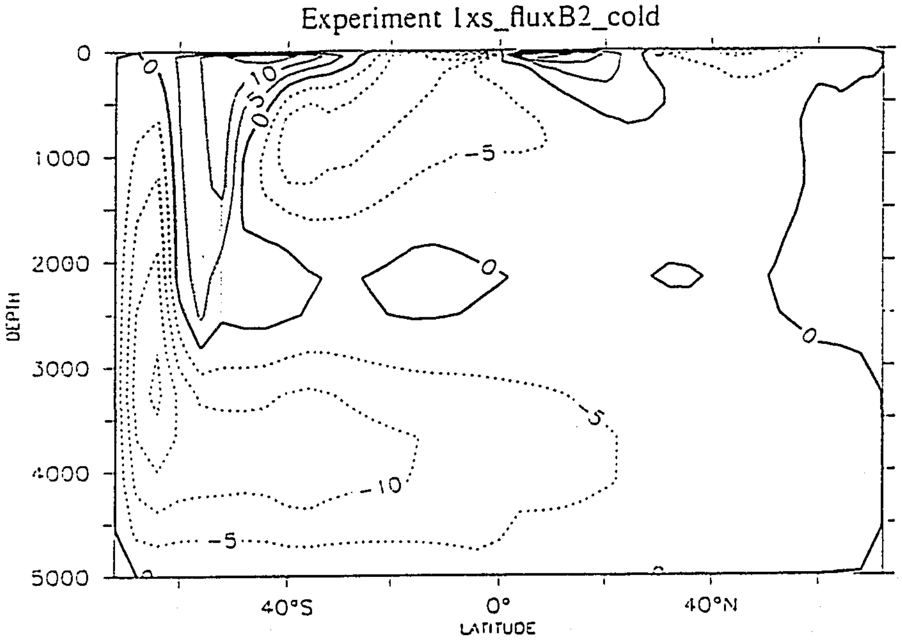

FIGURE 4.24 Overturning stream function, global ocean, for experiment 1xs_fluxB2_cold. Shaded area indicates location of Drake Passage. Units are 10^6 m^3/sec (Sv).

4.6 Summary

There is evidence that water of southern origin filled the deep North Atlantic at the last glacial maximum (Duplessy et al., 1988). The presence of cold AABW in the North Atlantic basin could have prevented the deep warming required to destabilize the northern sinking region. The deep-decoupling oscillations described by Winton (1993) occur precisely because subsurface warming destabilizes the North, so the continued production of AABW poses a challenge to this mechanism as a possible explanation for the rapid air-temperature changes known as Dansgaard-Oeschger events.

In this chapter, deep-decoupling oscillations were generated in a one-hemisphere basin. A restoring boundary condition was then applied to the deep ocean, concentrated at the southern boundary to simulate the effect of an influx of AABW. The range of surface forcing that generated deep-decoupling oscillations was greatly reduced by weak cooling of the deep ocean. Moderate cooling approximating an AABW inflow closer to the estimates of today's circulation (deep restoring 'ten') further restricted deep-decoupling oscillations, while stronger deep cooling prevented deep-decoupling oscillations entirely.

When the basin was expanded to include potential sinking regions in both the Northern and Southern Hemispheres, deep-decoupling oscillations occurred in the North only when no deep sinking occurred in the Southern Hemisphere. Two factors contributed to the stability of the no-northern sinking mode of overturning: First, cold AABW prevented unbounded warming of the deep ocean. Second, an overturning mode with deep sinking in the Subantarctic drew heat and salt from the low-latitudes towards the south.

The additional heat released in the south did not contribute to subsurface warming, and the northern halocline remained strong. In cases where the salinity forcing produced a strong halocline in the south, preventing deep sinking there, deep-decoupling oscillations in the north were possible.

In the two-basin experiments of this chapter, century-scale variability in NADW production proved possible even with continued production of AABW. When NADW production was shut off, subsurface warming in the Atlantic was observed. With relatively small exports of fresh water from the Atlantic to the Pacific via the atmosphere, however, the subsurface warming was unable to destabilize the high-latitude North Atlantic. In contrast, the larger inter-basin freshwater transport in experiment 1x_fluxB1_cold weakened the strength of the northern halocline. The subsurface warming proved to be sufficient to destabilize the high-latitude water column in this case, and vigorous overturning ensued. The cessation of the northern overturning occurred as in the one-basin experiments with deep-decoupling oscillations: as the temperature of the water column cooled, the equation of state of sea water caused the effects of salinity to become more important in determining density, and the surface freshening shut off convection. The oscillations combined aspects of both the salt-oscillator concept of Broecker (1991) and the thermally driven deep-decoupling oscillations of Winton (1993,1996).

Chapter 5 Box Model Experiments

5.1 Introduction

In this chapter, the behavior of a series of relatively simple box models is examined to gain insight into the sensitivity of the OGCMs deep-decoupling oscillation processes. Because the focus is on understanding the behavior of the OGCMs, only the behavior that relates to the three-dimensional model's behavior is investigated. For example, the possibility of a haline-dominant overturning exists for the box models. While the behavior of the box model in this regime may be mathematically interesting, it does not help elucidate deep-decoupling oscillations in the high latitudes.

A simple three-box model is described, and then modified to illustrate the response of the one-hemisphere sector model of section 4.3 to changes in restoring strength. A two-hemisphere twelve-box model is then presented, and used to illustrate the types of behavior seen in the two-hemisphere sector model of section 4.4. The advantages of using box models are two-fold. First, for very simple box models, analytical solutions can be calculated. Second, the extremely low computational expense of box models allows them to be used to explore the response under a wider range of boundary conditions and parameterizations than is practical in a GCM. Against these must be counted the disadvantage that some important features of the full three-dimensional circulation may be lost in the simplifications implicit in the box-model.

5.2 Three-Box Model

The simplified box model of Winton (1993) is used here to represent the processes in a single basin without dynamics or advective feedback. The model, shown in Figure 5.1, is designed to represent the competing effects on high-latitude stratification of the subsurface meridional heat transport (destratifying) and the atmospheric transport of water vapor (stratifying). The low and high latitude surface boxes have temperatures fixed at 15°C and 0°C, respectively. A fixed "atmospheric" salinity flux is applied to the upper boxes, transporting salinity from the high latitude to the low latitude box. There is horizontal mixing between the upper boxes, and vertical mixing with the deep box. When either the low or high latitude water columns becomes unstable, convective mixing is represented by increasing the vertical mixing parameter by a fixed factor. The equation of state is a quadratic fit to σ_θ between 0°C and 15°C.

The equations for this box model are given by:

$$\frac{dS_l}{dt} = \frac{2M_{ld}}{hL}(S_d - S_l) + \frac{2M_{lh}}{hL}(S_h - S_l) + \frac{F_s}{h} \tag{EQ 5.2.1}$$

$$\frac{dS_h}{dt} = \frac{2M_{hd}}{hL}(S_d - S_h) + \frac{2M_{lh}}{hL}(S_l - S_h) - \frac{F_s}{h} \tag{EQ 5.2.2}$$

$$\frac{dS_d}{dt} = \frac{M_{ld}}{HL}(S_l - S_d) + \frac{M_{hd}}{HL}(S_h - S_d) \tag{EQ 5.2.3}$$

$$\frac{dT_d}{dt} = \frac{M_{ld}}{HL}(T_l - T_d) + \frac{M_{hd}}{HL}(T_h - T_d) \tag{EQ 5.2.4}$$

$$M_{\{l,h\}d} = C_{\{l,h\}} M_v \tag{EQ 5.2.5}$$

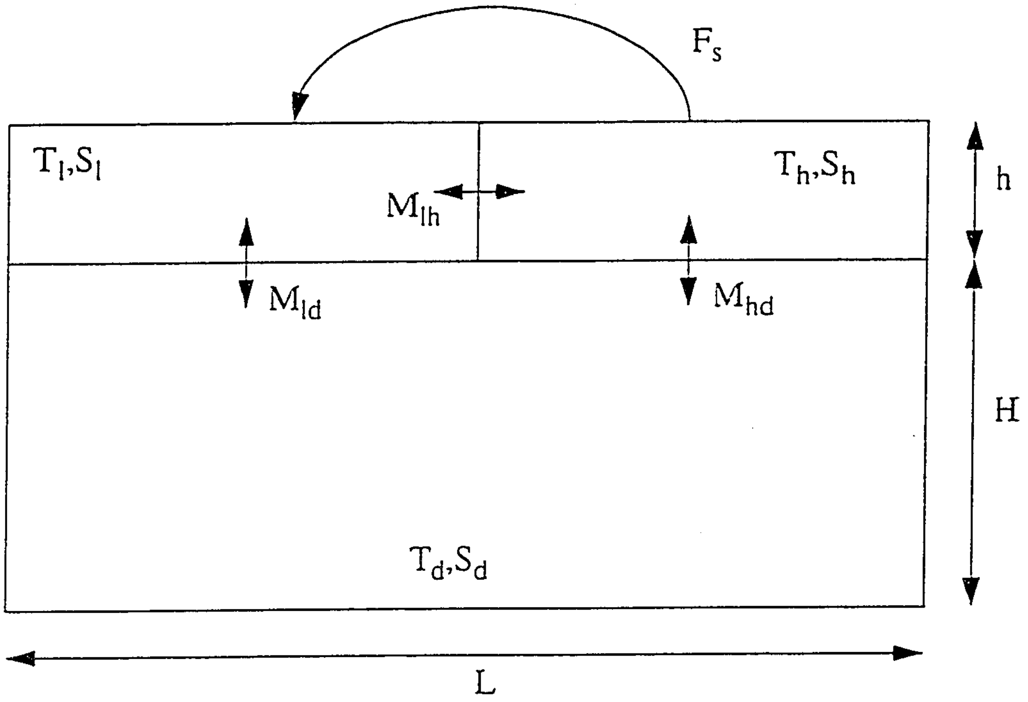

FIGURE 5.1 Simple three-box model (after Winton 1993)

$$\rho(T,S) = 0.79S - 0.0611T - 0.0055T^2 \qquad \text{(EQ 5.2.6)}$$

where T is temperature, S is salinity, ρ is density (expressed as σ_θ), M is mixing between boxes, F_s is the salt flux from the high-latitude to the low-latitude box via the atmosphere, and the subscripts l,h, and d refer to the low-latitude, high-latitude, and deep boxes, respectively. The convective parameter, C_{jd}, is defined as:

$$C_{jd} = \begin{cases} 1 & for \quad \rho_j > \rho_d \\ 10 & for \quad \rho_j \le \rho_d \end{cases} \qquad \text{(EQ 5.2.7)}$$

where $j = l$ or h and ρ is determined from EQ 5.2.6. The parameters have been selected to produce oscillations that are consistent with those generated in the one-basin model of

Winton(1993) and in the model that is presented in section 4.3. The geometry is given by h=50m corresponding to the thickness of the top grid layer in the three-dimensional model, H=500m as an approximation of the thickness of the warm plume that penetrates beneath the halocline during the decoupled phase of the oscillations, and L=6.37x10^6 m, the radius of the earth. The mixing parameters M_v and M_{lh} are based upon a vertical diffusive timescale and mixing by Ekman drift, respectively, from the three-dimensional model. The values are given by:

$$\frac{HL}{2M_v} = 200years \approx \frac{H^2}{k_v}$$

$$\frac{hL}{2M_{lh}} = 5years \approx \frac{Lhf}{\tau_x}$$

Steady solutions exist at either end of the range of F_s that produces deep decoupling oscillations, one a thermal-dominant and the other a halocline-capped solution. The thermal-dominant solution is characterized by deep convection in the cold, fresh high latitudes, while the halocline capped solution allows no deep convection in the cold and very fresh high latitudes. These can be determined: (i) for the thermal-dominant regime by finding the value of F_s that allows $\rho_h=\rho_d$ while convecting; and, (ii) for the halocline-capped regime by finding the value of F_s that allows $\rho_h=\rho_d$ with no convection. Analytically, these values are given by:

$$F_s = \frac{h\left(11\left(\frac{2M_{lh}}{hL}\right) + 10\left(\frac{2M_v}{hL}\right)\right)}{0.79}\left(0.0611T_d + 0.00511T_d^2\right) \qquad \text{(EQ 5.2.8)}$$

where

$$T_d = \frac{T_l + 10T_h}{11} = 1.36°C \qquad \text{(EQ 5.2.9)}$$

for the thermal-dominant solution, and by:

$$F_s = \frac{h\left(2\left(\frac{2M_{lh}}{hL}\right) + \left(\frac{2M_v}{hL}\right)\right)}{0.79}\left(0.0611T_d + 0.00511T_d^2\right) \qquad \text{(EQ 5.2.10)}$$

where

$$T_d = \frac{T_l + T_h}{2} = 7.51°C \qquad \text{(EQ 5.2.11)}$$

for the halocline-capped solution.

For the parameters selected above, $F_{s(thermal)}$ expressed in terms of the equivalent evaporation or precipitation is 45cm/year. $F_{s(capped)}$ is calculated to be 61 cm/year. Salinity fluxes within that range produce deep decoupling oscillations. Smaller fluxes (F_s<$F_{s(thermal)}$) produce a thermally dominant northern sinking solution, and stronger fluxes (F_s>$F_{s(capped)}$) produce a halocline-capped solution. The temperature of the deep box is shown in Figure 5.2 for the three-box model under a range of salinity fluxes. The upper and lower dashed lines show halocline-capped and thermally-dominant solutions, respectively. Note that if F_s is increased sufficiently beyond $F_{s(capped)}$, a haline-dominant solution is possible. A haline-dominant circulation would produce deep sinking in the

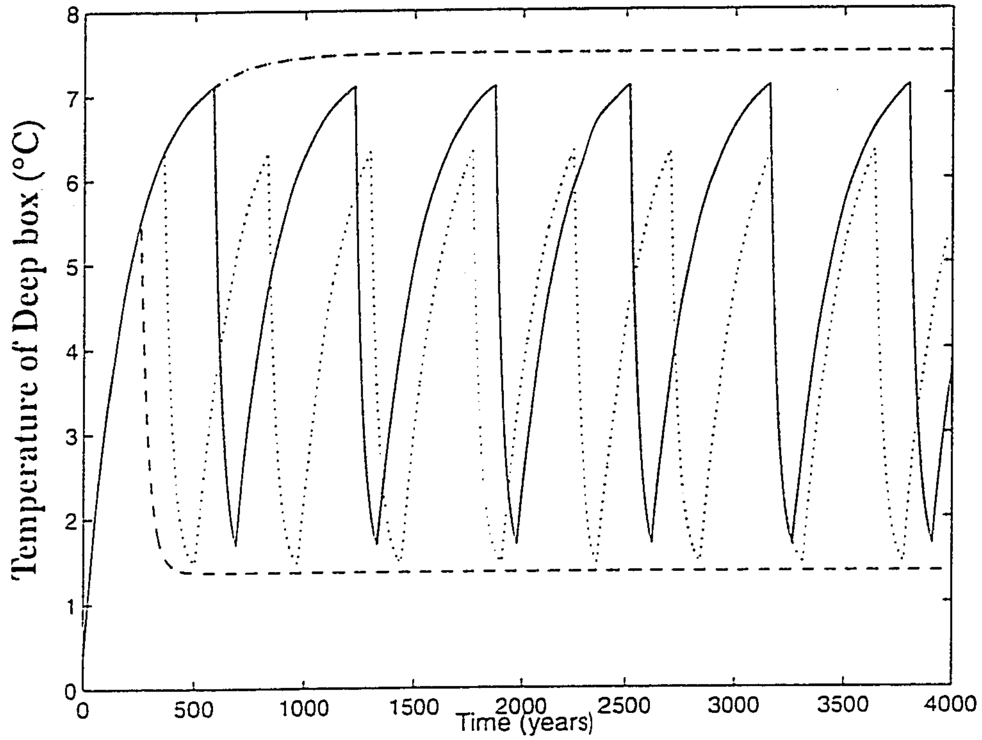

FIGURE 5.2 Temperature of the deep box in the three-box model under a range of salinity fluxes. Values for F_s are: 41cm/yr (lower dashed line), 49cm/yr (dotted line), 58 cm/yr (solid line), and 65 cm/yr (upper dashed line).

low-latitudes. This type of solution, with its very high freshwater fluxes and reversed overturning circulation, is not of interest to this study.

As can be seen from equation 5.2.8 and equation 5.2.10, the range of fluxes that will produce oscillations is independent of the choice of a representative depth H, except as it enters the selection of a characteristic vertical mixing parameter. Choosing a larger depth H will result in a longer vertical mixing timescale and hence a smaller value for the vertical mixing parameter. As an example, increasing the representative depth to 1000m yields $F_{s(thermal)} = 41$ cm/year and $F_{s(capped)} = 57$ cm/year, increasing the representative depth to 3000m yields $F_{s(thermal)} = 38$ cm/year and $F_{s(capped)} = 55$ cm/year.

5.3 Four-Box Model

The simple three box model presented above does not take into consideration the influence of the deep ocean on the subsurface layer. One way to represent the deep ocean is to add a fourth box below the subsurface box. The four box model shown in Figure 5.3 includes a layer of bottom water below the deep slab. The temperature and salinity of the bottom water were held constant. The time scale with which this influences the deep layer above it, $1/\gamma$, was taken as an unknown. The range of salinity fluxes for which deep-decoupling oscillations occur was sought as a function of γ.

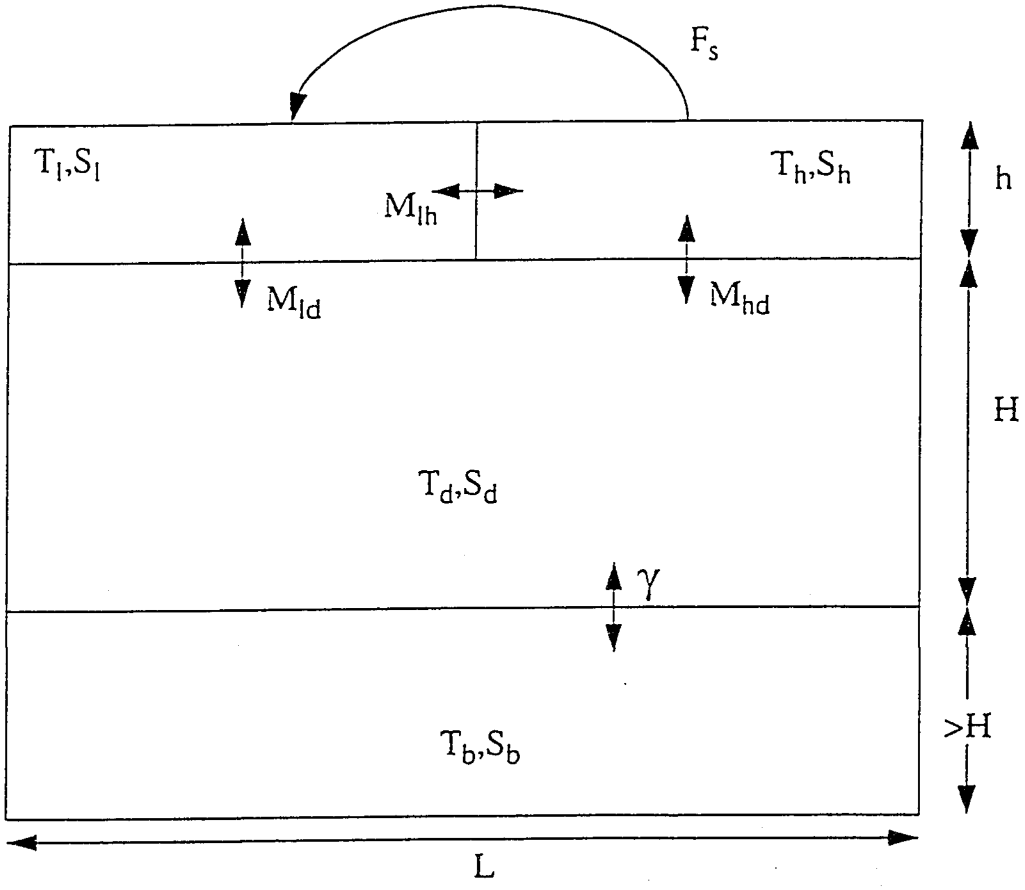

FIGURE 5.3 Four box model with a deep box representing AABW.

The equations for this four box model are given by replacing equation 5.2.3 and equation 5.2.4 by:

$$\frac{dS_d}{dt} = \frac{M_{ld}}{HL}(S_l - S_d) + \frac{M_{hd}}{HL}(S_h - S_d) + \gamma(S_b - S_d) \qquad \text{(EQ 5.3.1)}$$

$$\frac{dT_d}{dt} = \frac{M_{ld}}{HL}(T_l - T_d) + \frac{M_{hd}}{HL}(T_h - T_d) + \gamma(T_b - T_d) \qquad \text{(EQ 5.3.2)}$$

Where γ is the restoring constant described above, the subscript b refers to the bottom box, and all other variables are as defined in section 5.2. Temperatures and Salinities are restored toward the values given by T_b and S_b with a characteristic time scale of $1/\gamma$. Solving for the limits of the unsteady regime gives EQ 5.2.8 and EQ 5.2.10 as before, but the values for T_d are calculated differently in the four-box case:

$$T_d = \frac{\gamma T_b + \frac{M_v}{HL}T_l + \frac{M_v}{HL}T_h}{11\frac{M_v}{HL} + \gamma} \qquad \text{(EQ 5.3.3)}$$

for the thermal-dominant solution, and

$$T_d = \frac{\gamma T_b + \frac{M_v}{HL}T_l + \frac{M_v}{HL}T_h}{2\frac{M_v}{HL} + \gamma} \qquad \text{(EQ 5.3.4)}$$

for the halocline-capped solution.

In the limit of $\gamma \rightarrow 0$, these become equation 5.2.9 and equation 5.2.11. Figure 5.4 shows the range of fluxes, as a function of γ, that produce deep-decoupling oscillations with T_b=-1.0°C, S_b=35.0 psu. Parameters within the shaded area will produce deep-

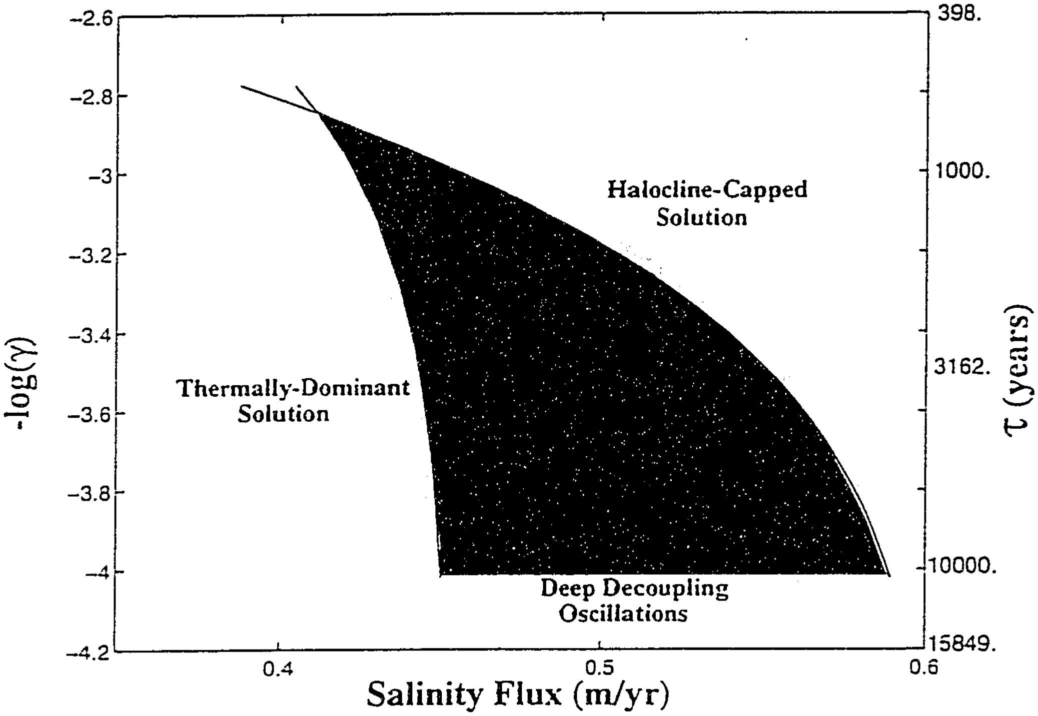

FIGURE 5.4 Parameter space in which oscillations are produced in the four box model. Shaded area indicates region in parameter space that will produce deep decoupling oscillations. Salinity flux is given in equivalent meters/year of fresh water evaporated or precipitated. As the restoring time τ gets long (-log(γ) goes to infinity) the limits approach those for the three-box model.

decoupling oscillations. The lower limit on the salinity flux that will produce deep-decoupling oscillations is seen to be less sensitive to the strength of γ than is the upper limit. The use of the fourth box as a deep restoring boundary condition is analogous to the deep restoring in the one-hemisphere experiments of section 4.3.2. The behavior in the four-box model is similar to that in the OGCM; for weaker restoring, deep-decoupling oscillations are seen over a wider range of forcings. The lower limit of fluxes that induce deep-decoupling oscillations in the three-dimensional model of section 4.3.2 also varies relatively little. In the competing influences on the stability of the high latitudes, the cold, deep ocean reduces the influence of subsurface warming in favor of the stabilizing effect of surface freshening.

5.4 Twelve-Box Model

5.4.1 Model Description

The four-box model illustrates the role that the deep ocean plays in maintaining the stability of the high latitudes. In order to more closely represent the behavior of the two-hemisphere sector models, an extension of the four-box model is required. The twelve-box model presented below illustrates the kind of circulations possible in the two-hemisphere sector model.

The function of the twelve-box model is very similar to that of the three- and four-box models, with the addition of advection. The geometry of the twelve-box model is shown in Figure 5.5. The system of equations can be summarized as follows:

$$\frac{dT_j}{dt} = \sum_{i = 1, 12} M_{i,j}(T_i - T_j) + \sum_{i = 1, 12} A_{i,j}T_i + \frac{F_{sj}}{h} \qquad \text{(EQ 5.4.1.1)}$$

where M is a 12 by 12 array of mixing parameters, A is an array of advective parameters, T is the tracer (temperature or salinity), and F_{sj} is the surface flux, applied to the top four boxes only. Throughout the discussion of this model, the following convention will be followed: $M_{i,j}$ refers to the influence of the tracers in box 'i' on the values of the tracer in

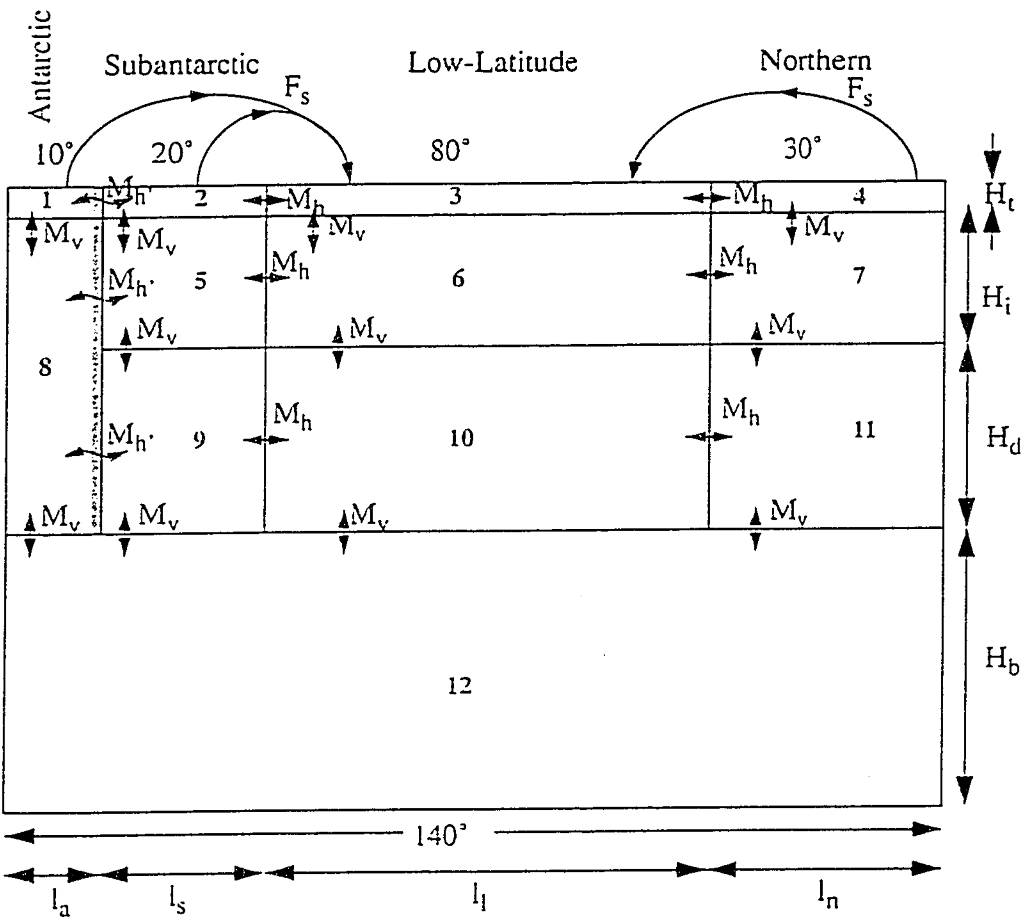

FIGURE 5.5 Twelve-box model. Salinity fluxes and mixing parameters are described in text. Shaded area indicates assumed Drake Passage, horizontal mixing across this area (grey arrows) is reduced.

box 'j'. Mixing between non-adjacent boxes is zero. The model is time integrated using a simple first-order differencing scheme.

Horizontal mixing between adjacent surface boxes is taken to occur on a 10 year time scale. This mixing time was made slightly longer than that in the three box model because it is used in conjuction with an advective parameterization described below. The horizontal mixing is adjusted to reflect the differences in the lengths of each region:

$$M_{3,2} = M_{3,4} = \frac{1}{10} year^{-1}, \qquad \text{(EQ 5.4.1.2)}$$

$$M_{2,3} = \frac{1}{10}\frac{l_s}{l_l} year^{-1}, \qquad \text{(EQ 5.4.1.3)}$$

$$M_{4,3} = \frac{1}{10}\frac{l_n}{l_l} year^{-1}. \qquad \text{(EQ 5.4.1.4)}$$

In the expressions for mixing and advective parameters, the subscripts for length l and depth h are assigned as follows: a, s, l, and n represent the Antarctic, Subantarctic, low-latitude, and northern locations; t, i, d, and b represent the top, intermediate, deep, and bottom layers. The horizontal mixing between the surface boxes of the Antarctic and Subantarctic, boxes 1 and 2, is described below. Horizontal mixing in the subsurface boxes is calculated as follows:

$$M_{s,l} = \frac{k_h}{l_l l_l} \qquad \text{(EQ 5.4.1.5)}$$

$$M_{l,s} = \frac{k_h}{l_l l_s} \qquad \text{(EQ 5.4.1.6)}$$

$$M_{n,l} = \frac{k_h}{l_l l_s} \qquad \text{(EQ 5.4.1.7)}$$

$$M_{l,n} = \frac{k_h}{l_l l_n} \qquad \text{(EQ 5.4.1.8)}$$

where k_h is the horizontal mixing parameter, l_s is the length of the Subantarctic box, l_l is the length of the low-latitude box, and l_n is the length of the northern box.

Horizontal mixing across the latitude of Drake Passage is slightly more complicated. The mixing between the surface boxes in the Antarctic and Subantarctic, boxes 1 and 2, is determined by:

$$M_{1,2} = \frac{k_h}{15 l_s l_s} \qquad \text{(EQ 5.4.1.9)}$$

$$M_{2,1} = \frac{k_h}{15 l_a l_s} \qquad \text{(EQ 5.4.1.10)}$$

where $k_h = 3 \times 10^7 \text{cm}^2/\text{sec}$ is the horizontal mixing parameter. These and all the mixing parameters linking Antarctic and Subantarctic boxes are reduced by a factor of fifteen to represent the weak mixing across the ACC. The surface boxes use the diffusively determined value rather than the wind mixing value ($1/10\ \text{yr}^{-1}$) because, in the absence of meridional boundaries, the surface water moving northward as Ekman drift cannot return southward at the surface in a western boundary current. The mixing between Antarctic and Subantarctic subsurface boxes (boxes 5 and 8) is reduced, as in equation 5.4.1.9 and equation 5.4.1.10, but the different thicknesses of the adjacent boxes are also taken into account:

$$M_{8,5} = \frac{k_h}{15 l_a l_s} \qquad \text{(EQ 5.4.1.11)}$$

$$M_{5,8} = \frac{k_h}{15 l_a l_a}\left(\frac{h_i}{h_i + h_d}\right) \qquad \text{(EQ 5.4.1.12)}$$

$$M_{8,9} = \frac{k_h}{15 l_s l_s}\left(\frac{h_d + h_i}{h_d}\right) \qquad \text{(EQ 5.4.1.13)}$$

$$M_{9,8} = \frac{k_h}{15 l_a l_s}. \qquad \text{(EQ 5.4.1.14)}$$

The adjustments for length and depth are selected to reflect an increase in the mixing across the latitude of Drake Passage with depth. This is an approximation of the increasing influence of topographic features that effectively narrow the latitudinal band without meridional barriers.

Density is determined by EQ 5.2.6, and the stability of the water column is used to determine a convective parameter as in the three and four-box models (EQ 5.2.7). In the Subantarctic, Low-latitudes, and North, vertical mixing between the top two levels is calculated by:

$$M_{v_{t,i}} = C_v \frac{k_v}{h_t h_i} \qquad \text{(EQ 5.4.1.15)}$$

and

$$M_{v_{i,t}} = C_v \frac{k_v}{h_t h_i} \qquad \text{(EQ 5.4.1.16)}$$

where $k_v = 0.5 \text{cm}^2/\text{sec}$ is the vertical diffusivity and C_v is the convective parameter as used in section 5.2. Mixing across the intermediate-deep interface in these regions is:

$$M_{v_{i,d}} = C_v \frac{k_v}{h_d h_d} \qquad \text{(EQ 5.4.1.17)}$$

and

$$M_{v d,i} = C_v \frac{k_v}{h_d h_i}. \qquad \text{(EQ 5.4.1.18)}$$

In the Antarctic, the surface box connects directly to a deep box, and vertical mixing is given by:

$$M_{v t,d} = C_v \frac{k_v}{(h_i + h_d)\,(h_i + h_d)} \qquad \text{(EQ 5.4.1.19)}$$

and

$$M_{v d,t} = C_v \frac{k_v}{(h_i + h_d)\,h_t}. \qquad \text{(EQ 5.4.1.20)}$$

Finally, the vertical mixing between the boxes of differing length are given explicitly:

$$M_{v 8,12} = C_v \frac{k_v}{h_b h_b} \frac{l_a}{l_b} \qquad \text{(EQ 5.4.1.21)}$$

$$M_{v 12,8} = C_v \frac{k_v}{(h_d + h_i)\,h_b} \qquad \text{(EQ 5.4.1.22)}$$

$$M_{v 9,12} = C_v \frac{k_v}{h_b h_b} \frac{l_s}{l_b} \qquad \text{(EQ 5.4.1.23)}$$

$$M_{v 10,12} = C_v \frac{k_v}{h_b h_b} \frac{l_l}{l_b} \qquad \text{(EQ 5.4.1.24)}$$

$$M_{v 11,12} = C_v \frac{k_v}{h_b h_b} \frac{l_n}{l_b} \qquad \text{(EQ 5.4.1.25)}$$

$$M_{v12,9} = M_{v12,10} = M_{v12,11} = C_v \frac{k_v}{h_d h_b} \qquad \text{(EQ 5.4.1.26)}$$

Surface advection is parameterized as overturning driven by horizontal density differences, as in Stommel (1961). The advection in each overturning loop is proportional to the difference in the densities of the two top boxes in that loop. The surface advection is defined as follows for the northern loop:

$$A_{m,n} = C_a M_{m,n} \frac{3 vol_m}{5000 vol_n} \qquad \text{(EQ 5.4.1.27)}$$

for m=3,4,7,and 6, and n = the downstream box (4, 7, 6, and 3). The convective parameter, C_a, is defined as:

$$C_a = \begin{cases} 1 \;\; for \; \rho_t > \rho_i \\ 100 \; for \; \rho_t \le \rho_i \end{cases} \qquad \text{(EQ 5.4.1.28)}$$

where *t* indicates the surface box, *i* indicates the intermediate depth box, *l* or *h* and ρ is determined from EQ 5.2.6. This is the equivalent of advecting 0.01 Sv for each σ_θ unit difference in the surface densities when convection is off, and 1. Sv for each σ_θ unit difference when convection is on. For the southern surface loop:

$$A_{m,n} = C_a M_{m,n} \frac{3 vol_m}{5000 vol_n} \qquad \text{(EQ 5.4.1.29)}$$

for m=3, 2, 5, and 6, n = the downstream box (2, 5, 6, and 3), and Ca is given by EQ 5.4.1.28. This is the equivalent of advecting 0.0067 Sv for each σ_θ unit difference in the surface densities when convection is off, and 0.67 Sv when convection is on. This choice of parameters leaves the surface wind mixing essentially unaltered when no convection is occurring. The large increase in advection when convection is occurring was motivated by changes in surface advection observed in the 0.5_fluxB experiments in section 4.4. The advection seen when convection is occurring is roughly equivalent to 10% of the wind mixing.

The subsurface advective loops are calculated similarly. The equivalent advective strength for both lower loops is 6 Sv for each σ_θ density difference in the intermediate boxes. The larger value is used to reflect the greater depth of the boxes, as well as the tendency for the density differences to be smaller at intermediate depths. The advection is increased by a factor of 5 if convection is occurring in a particular loop. For the density differences observed in the box model, this results in overturnings in the range of 15-20 Sv.

Surface boundary conditions are given in Table 5.1. As in the three- and four-box models, the surface temperatures are held fixed. The surface salinity flux pattern gives net evaporation in the low latitudes and net precipitation elsewhere. Note that the 46.3 cm/yr of freshening applied to the high latitudes in flux patterns 'A' and 'B' resulted in deep-

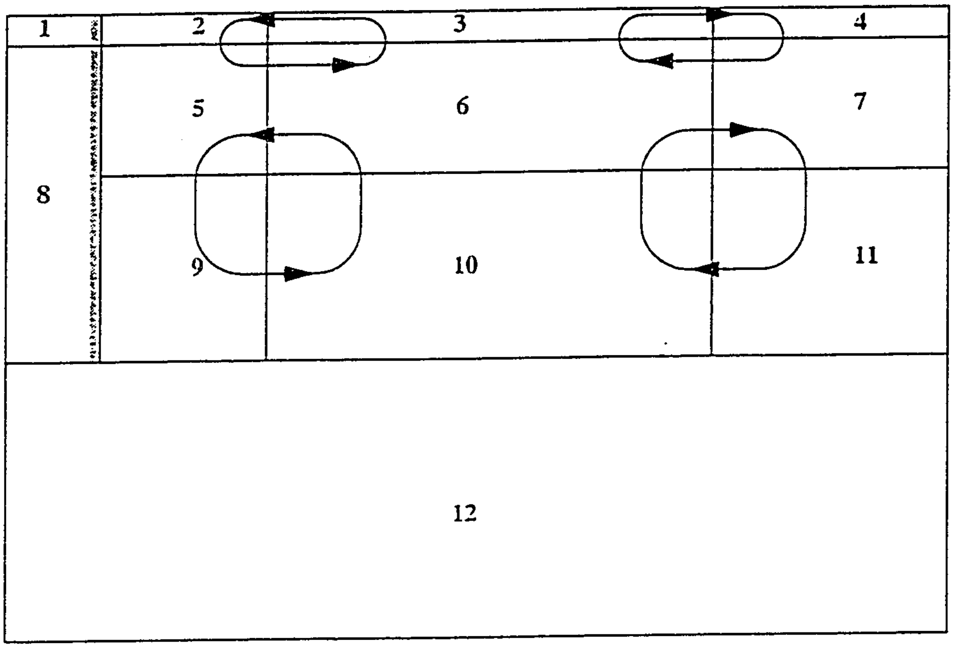

FIGURE 5.6 Diagram of advective loops used in the twelve-box model.

decoupling oscillations for the three-box model. The same freshening produced deep-decoupling oscillations over a broad range of γ in the four-box model as well.

TABLE 5.1 Surface boundary conditions for the twelve-box model. Temperatures are in °C, salinity flux is given in the equivalent evaporation-precipitation (m/yr).

	Temperature Pattern A (°C)	Freshwater Flux A (m/yr)	Temperature Pattern B (°C)	Freshwater Flux B (m/yr)
Antarctic	-1.8	-0.029	-1.8	-0.074
Subantarctic	3.0	-0.337	8.0	-0.337
Low-latitudes	18.	0.261	18.	0.267
Northern	0.0	-0.463	0.0	-0.463

5.4.2 Twelve-Box Model Results

The twelve-box model exhibits behavior very similar to that in the three-dimensional, two-hemisphere ocean general circulation sector model. The experiments conducted with the twelve-box model are summarized in Table 5.2. Using surface temperature pattern A and 0.6 times surface flux pattern A (0.6x_A, see Table 5.1), a stable equilibrium was found with convection in the Antarctic to the bottom, convection in the North to the deep box, and convection in the Subantarctic to the intermediate box. Increasing the salinity forcing to 0.8x_A produced two stable equilibria with convection to the bottom in the Antarctic, and a third with convection to the bottom in the Subantarctic. The three modes were produced as a result of three different initial conditions. In the first, the Subantarctic was initialized with a strong halocline, while the North and Antarctic were unstratified. Convection continued in the Antarctic and North to the bottom and deep boxes, respectively, and the Subantarctic remained stratified. In the second, initial conditions created a halocline in the North, convection to the deep in the Subantarctic, and convection to the bottom in the Antarctic. In the third, strong initial haloclines in both the North and Antarctic persisted, and convection to the bottom occurred in the Subantarctic. The solution without AABW production makes the point that as long as *any* region, in this case the Subantarctic, is capable of ventilating the deep ocean, deep-decoupling oscillations in the North are prevented.

For all stronger forcings, the North remained stratified. Increasing the salinity forcing to 1x_A and 1.2x_A resulted in solutions with convection to the bottom in the Antarctic, and to the deep in the Subantarctic. Finally, 1.4x_A produced only AABW, with the rest of the ocean stratified. Additional experiments were conducted for the 1x-, 1.2x-, and 1.4x_A salt flux patterns with strong initial haloclines in the Antarctic. In all three cases, the Antarctic halocline remained, a halocline formed in the North as well, and convection to the bottom occurred in the Subantarctic.

TABLE 5.2 Summary of twelve-box model experiments.

Surface Boundary Conditions	Salinity Flux Multiplier	Depth of Convection in Antarctic	Depth of Convection in Subantarctic	Depth of Convection in North
T_A, S_A	0.6x	Bottom	Intermediate	Deep
	0.8x	Bottom	-	Deep
		Bottom	Deep	-
		-	Bottom	-
	1.0x	Bottom	Deep	-
		-	Bottom	-
	1.2x	Bottom	Deep	-
		-	Bottom	-
	1.4x	Bottom	-	-
		-	Bottom	-
T_B, S_B	1x	-	-	Deep Decoupling Oscillations
T_B(Subantarctic=6°C) S_B	1x	-	Bottom	-
T_A, S_B	1x	-	Bottom	-

Notes for Table 5.2:

Surface Boundary Conditions: Temperature and salinity patterns A and B are listed in Table 5.1.

Salinity Flux Multiplier: Factor by which salinity flux was multiplied for experiments.

Depth of Convection: In each of the location, states deepest box reached by convection from the surface

An analysis of the salinity transports in the two 0.8x_A equilibria shows a pattern similar to that in the two equilibria of the three-dimensional model. For the Northern sinking case, advection and diffusion bring about four times as much salt into the top two Northern boxes as is delivered to the top two Subantarctic boxes. In the Subantarctic sinking case, slightly more salt is delivered to the upper Subantarctic boxes than is delivered to the top two Northern boxes. It is the supply of salt that determines which of the two stable modes develops.

The twelve-box model also shows the same response to increased fresh water flux as the two-hemisphere sector model. When the freshwater flux is sufficient to eliminate Northern sinking, the circulation first finds another location which, when supplied with the salt from the low-latitudes, can fill the deep ocean. Deprived of its supply of low-latitude salt, the North becomes very strongly stratified. When the salinity forcing is strong enough to shut off the Subantarctic sinking, a circulation with only Antarctic sinking was formed. Note that the fresh water flux in the twelve-box model for which Northern sinking could no longer be sustained was approximately the same as in the three-box model. In the twelve-box model, however, the cessation of Northern deep sinking was accompanied by a switch to deep sinking in the Subantarctic.

In order to form deep-decoupling oscillations in the twelve-box model, several modifications were required. First, a strong halocline was maintained in the Antarctic through an increase in the fresh water flux there. The possibility of the Subantarctic ventilating the deep ocean was eliminated by increasing the surface temperature to 8°C. The new surface boundary conditions are listed as temperature and salt flux 'B' in Table 5.1. Densities of the boxes in the Northern water column during deep-decoupling oscillations under salt flux 'B' is shown in Figure 5.7. In this example, the initial circulation includes deep sinking in the North. After approximately 6500 years, the fresh water flux creates a halocline, and convection ceases. The deep ocean warms until approximately year 14000, when convection between the intermediate and deep boxes breaks out. The ensuing overturning quickly destabilizes the surface, and deep convection resumes.

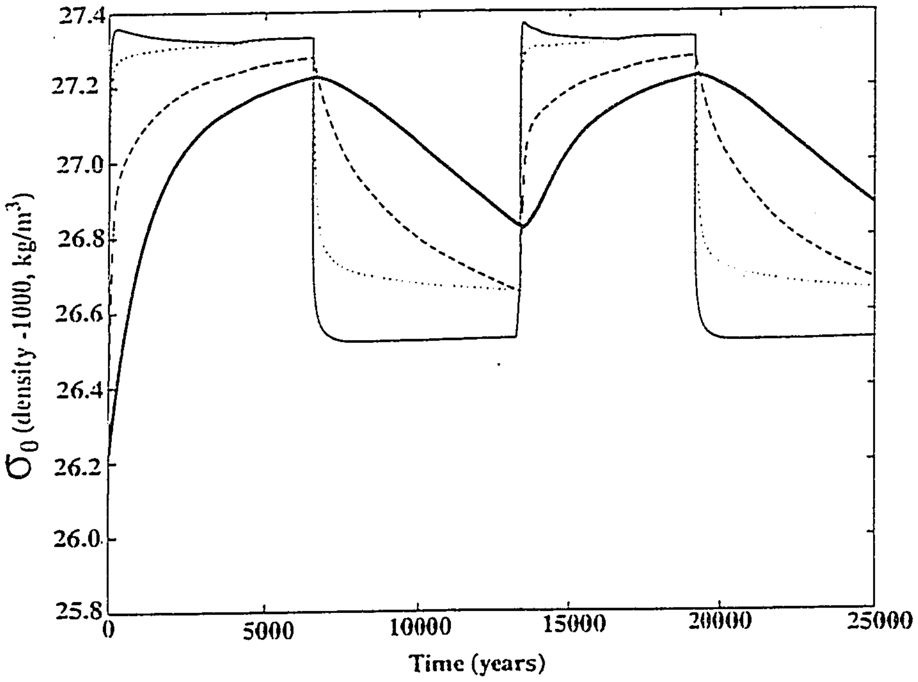

FIGURE 5.7 Density of boxes in the Northern water column during deep-decoupling oscillations in the twelve box model. Thin solid line is box 4 (top), dotted line is box 7 (intermediate), dashed line is box 11 (deep), and thick solid line is box 12 (bottom.) Densities are expressed as sigma-theta, units are kg/m^3

The deep-decoupling oscillations were the product of very specific surface forcing. Eliminating the convection in the Antarctic by itself proved insufficient to allow deep-decoupling oscillations. As long as the surface boundary conditions in the Subantarctic allowed, deep sinking occurred there. As an example, the combination of salt flux 'B' and temperature 'B' modified to include a 6°C Subantarctic temperature resulted in steady Subantarctic deep convection, regardless of initial conditions. Salt from the low-latitudes was advected to the Subantarctic sinking region, the North remained stratified, and no deep-decoupling oscillations were seen.

5.5 Summary

The viability of deep-decoupling oscillations as a mechanism to explain the rapid climate shifts known as Dansgaard-Oeschger events is posed a serious challenge by the stabilizing influence of AABW. The three- and four-box models presented in this chapter offer a simplified depiction of deep-decoupling oscillations. They illustrate how the continuous production of AABW which cools the deep ocean can suppress the oscillation by preventing the warming of the deep ocean by diffusive processes. The range of salt-flux forcing over which deep-decoupling oscillations occurred decreased as the influence of AABW increased. The reduced ability for deep-decoupling oscillations to occur agrees well with the behavior in the more complicated deep-restoring experiments of section 4.3.2, and offers improved insight into those experiments.

The more complicated twelve-box model presented in this chapter illustrates the second challenge to deep-decoupling oscillations; the ability of the Subantarctic to replace the North as the source of deep water. When the Subantarctic ventilates the deep ocean, advection in the upper ocean draws heat and salinity from the low-latitudes to the south.

The heat is released to the atmosphere in the Subantarctic, rather than contributing to the subsurface warming required to destabilize the North and allow deep-decoupling oscillations to occur. Likewise, advecting salt out of the low-latitude upper ocean makes less available to mix with the northern upper ocean, and the halocline in the North strengthens.

The twelve-box model was capable of producing all of the overturning modes seen in the two-hemisphere single basin experiments in Chapter 4. The success of the twelve-box model in representing the behavior of the three-dimensional model indicates that the relatively simple physics used captures the necessary elements of the circulation. The twelve-box model showed the same limits on deep-decoupling oscillations seen in the two-hemisphere single-basin experiments in Chapter 4. That is, no deep-decoupling oscillations could be generated as long as either the Antarctic or Subantarctic continued to convect to the bottom. The twelve-box model represented a single basin, and consequently could not include the inter-basin transport necessary to generate deep-decoupling oscillations in the two-basin experiments of section 4.4.2.3 that did include AABW production.

Chapter 6 Time-dependant Surface Forcing Experiments

6.1 Introduction

Deep-decoupling oscillations have been proposed as a mechanism to explain the rapid climate shifts known as Dansgaard-Oeschger events (Winton, 1993, 1996). In the two-basin experiments of Chapter 4, deep-decoupling oscillations occurred in a cold climate with large inter-basin fresh water transport via the atmosphere. When the interbasin transport was reduced, as it might have been in a cooler climate, a steady overturning circulation resulted. Transitions between the two steady overturning states in the two-hemisphere one-basin experiments described in section 4.4.2 do not appear to occur spontaneously.

The rapid timescale (decades) for the transition from cold (weak northern sinking) to warm (strong northern sinking) indicated by the ice core records agrees with an oceanic adjustment to convective instability in the water column, although the instability appears to require external forcing. Broecker et al. (1990) suggested a scenario to explain the oscillations in the North Atlantic that involves storage and release of fresh water in land ice. In this hypothesis for the oscillations, land ice is melted during the warm (conveyor-on) periods. When the melting freshens the surface sufficiently, the deep overturning is shut off, and the North Atlantic cools. Throughout the cool period, fresh water is exported from the Atlantic basin, and eventually the salinity increases to the point where deep overturning resumes. This theory runs into difficulty when the timing of the Heinrich events is considered (Bond et al. 1993); these large pulses of icebergs occur at the coldest part of the cycles, and are followed by rapid transitions to warmer temperatures.

Bond et al. proposed that the transition to the warm (conveyor-on) state following the Heinrich events occurs because of a retreat of the meltwater contribution from the ice sheet following the large melt pulses. Paillard and Labeyrie (1994) use a simple one-hemisphere box-model of the ocean linked to an ice sheet model to depict this process. A large increase in iceberg flux causes a collapse of the deep overturning. When basal freezing of the ice sheet halts the flux of icebergs, the deep overturning resumes, and the North Atlantic warms abruptly. This scenario presents a return to warm conditions that is consistent with the timing suggested by the sediment record. It does not, however, capture the fact that the transition to the cold (conveyor-off) climate appears to precede the Heinrich events.

In the experiments of section 4.5.3, oscillations were generated in a cold climate under steady mixed boundary conditions that included the removal of 0.29 Sv of freshwater from the Atlantic basin. These oscillations did not require episodic melt pulses to cause the transitions from one state to another. A weakness of these oscillations is that they are sensitive to the export of freshwater from the Atlantic basin. Reduced freshwater export results in a stronger halocline that the subsurface warming is unable to destabilize. In addition, the timescale of the oscillations is short compared to that of the Dansgaard-Oeschger events.

In this chapter, I explore some of the possibilities for transitions between overturning states. In section 6.2.1, I apply a variation of the melt pulse/ retreat idea to ocean circulations with different equilibrium states. In section 6.2.2 and section 6.3, I demonstrate that stochastic forcing applied to the high-latitude freshening region can also produces transitions between overturning states.

6.2 Two Hemisphere Experiments

6.2.1 Melt Pulse

In this section, we investigate the behavior of the two-hemisphere sector model when a melt pulse and retreat of glacial melt water is applied. The time scale of these pulses are short (years to decades) and the magnitudes are small (5-15% of the total flux). In choosing such small perturbations, I hope to represent changes that are smaller than those recorded as Heinrich events, thereby extending the scenario to Dangaard-Oeschger events as well. A number of equilibrium solutions from section 4.4.2 are used as initial conditions, to see how the equilibrium state of the circulation effects the response. The melt-pulse experiments of this section are summarized in Table 6.1.

For the first experiment, the equilibrium solution from experiment 0.5fluxB with Subantarctic deep sinking was used as an initial condition. The overturning circulation in this equilibrium solution produced overturning to the bottom in the Antarctic, weak, shallow overturning to approximately 1000m in the Northern Hemisphere, and moderate overturning to approximately 2000, in the Subantarctic (see Section 4.4.2.3, Figure 4.16b). To represent the addition of a meltwater pulse, the high-latitude freshening in the Northern

TABLE 6.1 Summary of melt-pulse experiments in two-hemisphere basin.

Surface Salinity Flux Pattern	Initial State of Overturning Circulation	Perturbation North of 40°N	Behavior of Circulation
0.5fluxB	Subantarctic sinking	5% increase in freshening for 30 years, 12% decrease for 8 years, return to steady forcing.	Transition to steady northern deep sinking.
	Northern deep-sinking	20% increase in freshening for 40 years, return to steady forcing.	Temporary shut-off of northern sinking, transition to weak and shallow northern sinking.
	Weak, shallow northern sinking	5-20% increase in freshening for up to 40 years, return to steady forcing.	Temporary cessation of northern sinking, return to weak and shallow northern sinking.
	Weak, shallow northern sinking.	5% increase in freshening for 30 years, decrease by 14% for 12 years, return to steady forcing.	Transition to steady northern deep sinking.
0.75fluxB	Subantarctic deep sinking.	5% increase for 30 years, 12% reduction for 8 years, return to steady forcing.	Transient period of strong northern deep sinking, followed by steady, weak, shallow northern sinking.

Notes for Table 6.1:

Surface Salinity Flux Pattern: Described in section 4.4 and Figure 4.19.

Initial State of Overturning Circulation: Described in section 4.4.

Perturbation north of 40°N: Increases in high-latitude freshening are represented by a zonally uniformly increase. Decreases are not zonally uniform; reduction in freshening is accompanied by a concentration of freshening near continental boundaries.

Hemisphere for this case was increased uniformly by 5% (from 0.1290 Sv to 0.1355 Sv) for thirty years. I then assume that after such a pulse, the total volume of meltwater experiences a reduction, and less of it reaches the central part of the high-latitude freshening region. For eight years, the freshening is reduced by 12% (to 0.1136 Sv), with the additional change that most of the freshening occurs near the lateral walls. At the end of the eight years, the salinity flux is returned to pattern 0.5fluxB everywhere. This represents a net increase of the high latitude freshening over the 38 years, yet at the end of this period the overturning has shifted to the steady northern deep-sinking state.

The perturbation described above acted to switch the overturning circulation from northern-sinking off to northern-sinking on. Figure 6.1 shows heat released from the basin north of 30°N as the transition is made. The heat flux increases very quickly as convection brings the warmer waters of the deep ocean in contact with the surface. As the overturning begins to approach its "northern-sinking-on" equilibrium state, the heat flux from the surface to the atmosphere decreases and approaches a steady state.

The transition from Northern deep sinking to Subantarctic deep sinking proves to require a much larger perturbation in the salinity flux. Several experiments were conducted in which the high-latitude freshening was increased by up to 20%, and applied to the steady Northern sinking solution for 0.5fluxB for up to 40years. All of the perturbations were sufficient to interrupt the strong Northern overturning. Upon returning to the steady 0.5fluxB, however, none of the models returned to the Subantarctic sinking mode. Rather, they all transitioned to a quasi-steady weak-northern overturning mode. This

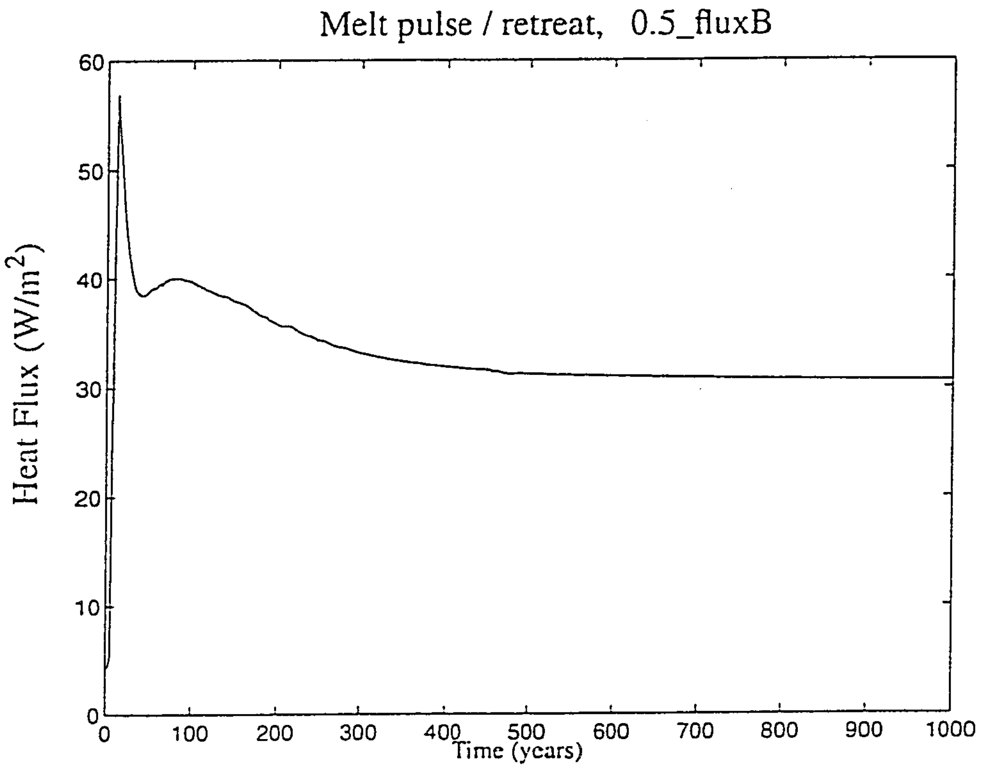

FIGURE 6.1 Heat flux from the ocean north of 30°N during transition from Subantarctic sinking to Northern sinking as a result of melt pulse/retreat cycle. Melt pulse ends at t=0, and an eight year retreat of glacial melt begins, represented by a reduction and redistribution of freshening at high latitudes. Salinity flux is returned to steady initial state for remainder of run. Units are W/m^2

solution was similar, but not identical, to the weak-northern overturning seen in the hysteresis experiment in section 4.4.2.3. The northern sinking was stronger than that found under 0.5fluxB during the hysteresis experiment, and a small-amplitude (3 Sv) oscillation was found in the Subantarctic, with a period of 25 years. The circulation is averaged over one period to give the stream function shown in Figure 6.2a, and its northward heat transport shown in Figure 6.2b.

Attempts to cause a transition from the weak, shallow northern overturning state to the Subantarctic sinking state as a result of similar melt pulses were unsuccessful. The

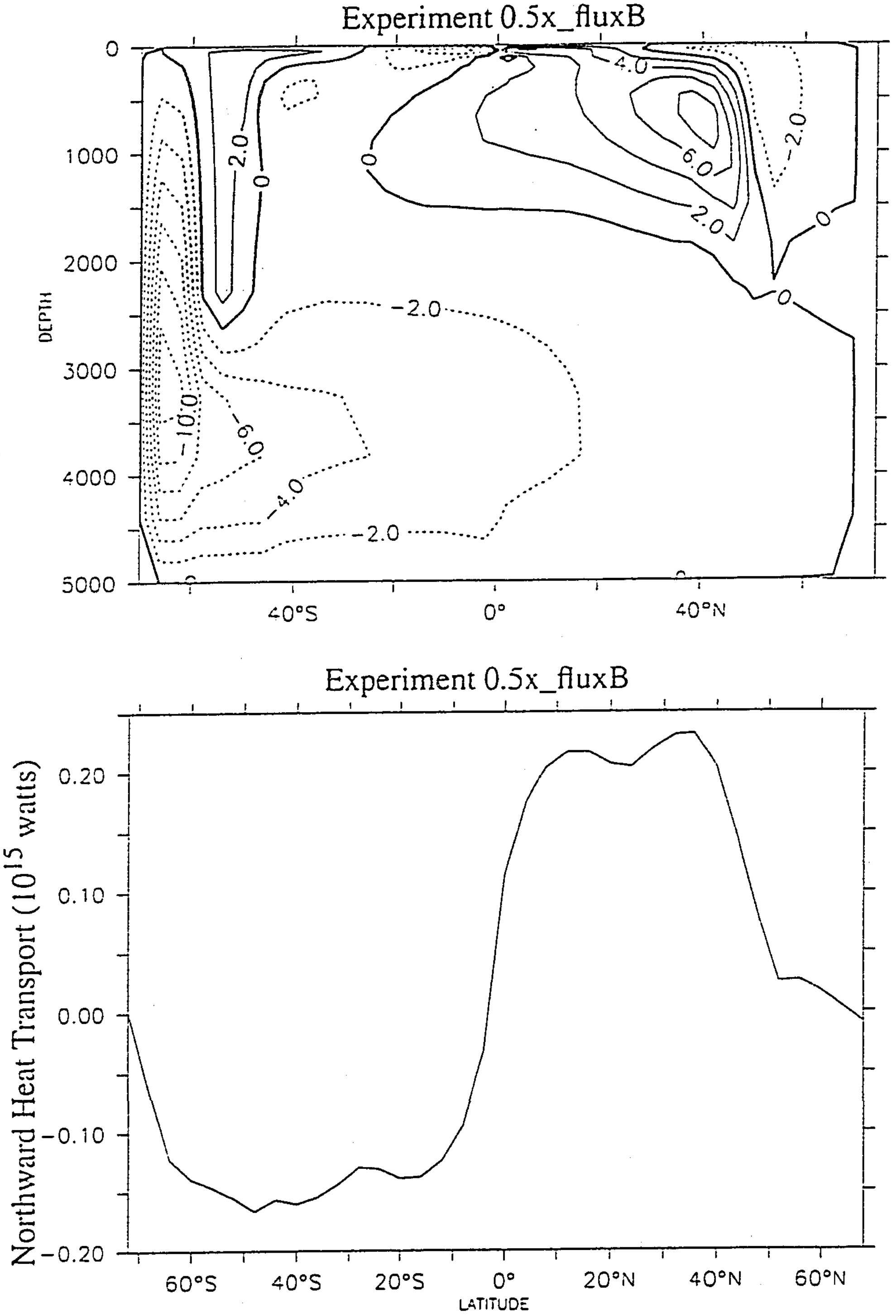

FIGURE 6.2 Weak northern overturning solution under 0.5x_fluxB salinity forcing. a) Overturning stream function (Sv), b) Northward heat transport (10^{15} Watts).

weak, shallow northern overturning circulation had a strong halocline throughout the northern freshening region. An additional melt pulse applied in the freshening region strengthened the existing halocline, but did not shut off the weak overturning. Such a transition appears to require a more substantial perturbation to overcome the existing transports. Thus changes in the surface boundary conditions elsewhere may be necessary to cause the circulation to shift to Subantarctic sinking. The reduced temperature experiment (experiment 1x_fluB2_cold) of section 4.5.3 provides an example of how a cooler climate could favor such a shift.

The halocline in the weak northern overturning state was susceptible to reductions in the fresh water flux that caused a transition back to the strong Northern overturning. As an example, the high latitude freshening in the North was subjected to a uniform 5% increase for thirty years. The freshening was then reduced by a total of 14% and rearranged so that all of the reduction occurred in the eastern-most 12° of the basin. After 12 years of this 'retreat' pattern, the flux was returned to the standard 0.5fluxB pattern. The circulation quickly transitioned to a steady strong Northern overturning. The heat flux out of the basin is shown in Figure 6.3.

The above examples occurred with a salinity flux pattern that was known to produce both a steady deep Northern sinking state and a Subantarctic sinking state, and in which an additional weak Northern sinking state had also been found. In the next example, I use a salinity flux that had not generated a steady deep Northern sinking state. Salinity flux 0.75fluxB is applied to the two-hemisphere basin, and allowed to come to a steady

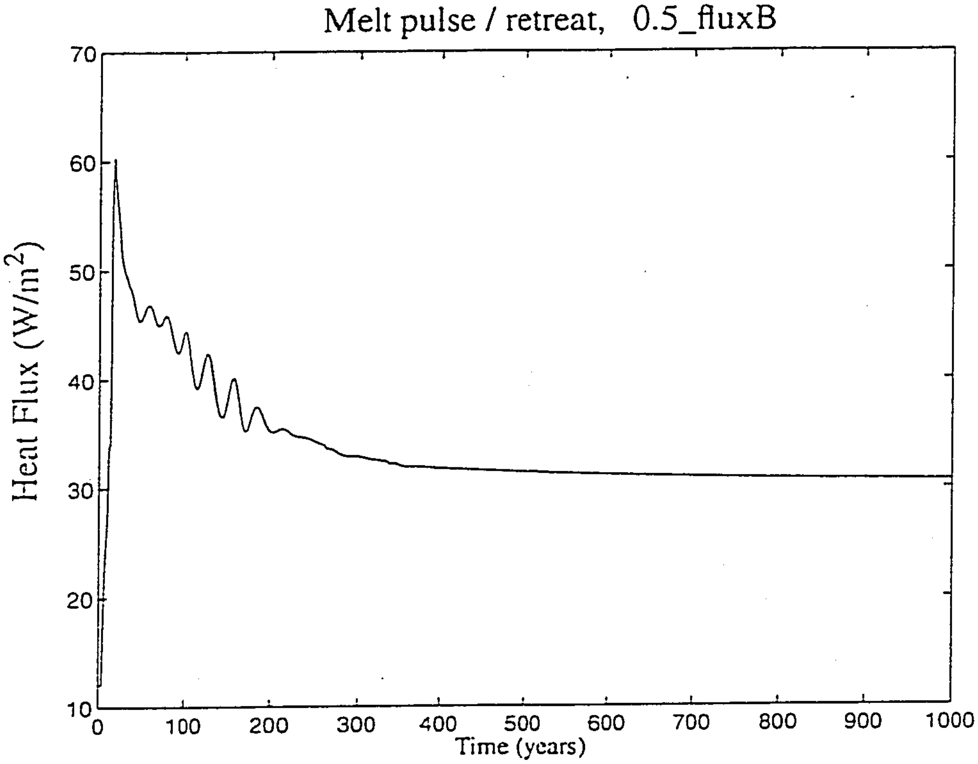

FIGURE 6.3 **Heat flux from the ocean north of 30°N during transition from weak Northern sinking to strong Northern sinking as a result of melt pulse/retreat cycle. Melt pulse ends at t=0, and a twelve year retreat of glacial melt begins, represented by a reduction and shift of freshening at high latitudes. Salinity flux is returned to steady initial state for remainder of run. Units are Watts/m^2**

Subantarctic sinking equilibrium. This served as the initial state for the perturbation experiment. The high latitude freshening was increased by 5% for 30 years. The 12% reduction and reorganization of the salinity flux used for the 0.5x_fluxB example was again applied for eight years, in this case yielding a net of 0.16 Sv freshwater equivalent in high latitudes. As before, the net anomaly is freshening. The salinity flux is then returned to 0.75fluxB and the circulation is allowed to adjust.

The salinity perturbation described above was sufficient to initiate deep water production in the Northern Hemisphere. This northern deep sinking solution continued after the salinity flux was returned to the initial pattern that had produced steady Subantarctic deep sinking. As the model is integrated forward, the northern sinking shoals, and a new equilibrium is reached. Figure 6.4a shows the overturning stream function before any salinity perturbation was applied. Figure 6.4b shows the overturning stream function in the middle of the flush in the Northern Hemisphere. Finally, Figure 6.4c shows the overturning stream function of the new weak Northern overturning solution 1000 years after the perturbation was applied. The heat released from the basin north of 30°N is plotted in Figure 6.5. In contrast to the results of the 0.5xfluxB pulse experiments, and the results of Paillard and Labyrie (1994), no pulse was required to turn off the deep Northern overturning.

The freshwater flux anomalies used to perturb the equilibria in the above examples to initiate northern sinking are not too large to rule out. MacAyeal (1993) estimates that a Heinrich event lasting approximately 250 years would result in a freshwater flux of 0.16 Sv. By comparison, the melt pulse used above was roughly 5% as large, and lasted only 30 years, while the retreat scenario reduced the freshening by approximately 12% of that value for eight and twelve years. While melt pulse/ retreat was presented in the context of the Heinrich events, the magnitudes of the perturbations are small enough that they could occur as a result of any number of smaller and less well recorded changes in the atmosphere, ocean, or cryosphere.

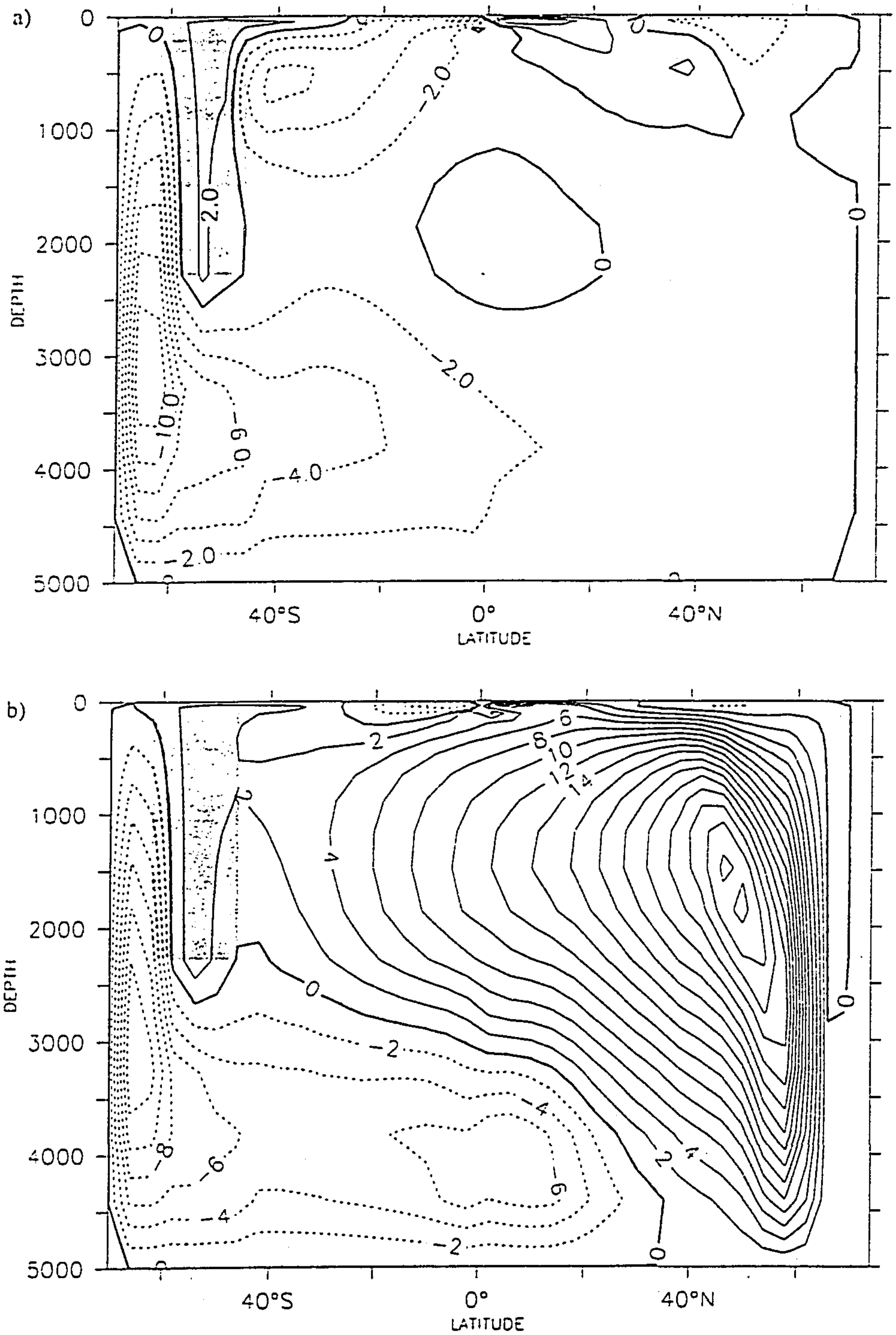

FIGURE 6.4 Overturning stream function for 0.75fluxB case. a) Prior to melt pulse/ retreat, b) during flush, 100years after beginning of retreat, and c) 1000 years after retreat. Units are 10^6 m^3/ sec (Sv), contour interval is 2 Sv.

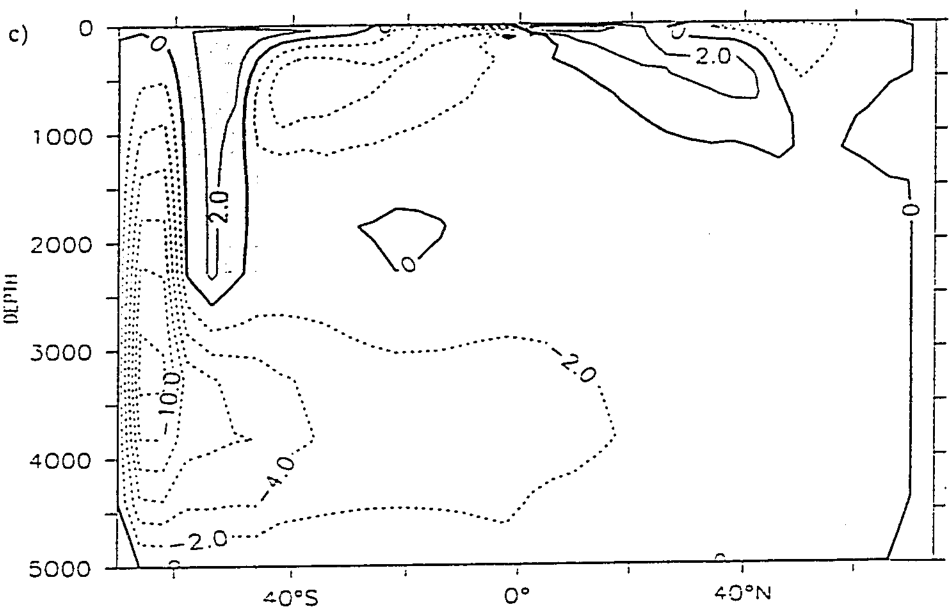

FIGURE 6.4 Overturning stream function for 0.75fluxB case. a) Prior to melt pulse/ retreat, b) during flush, 100years after begining of retreat, and c) 1000 years after retreat. Units are 10^6 m^3/ sec (Sv), contour interval is 2 Sv.

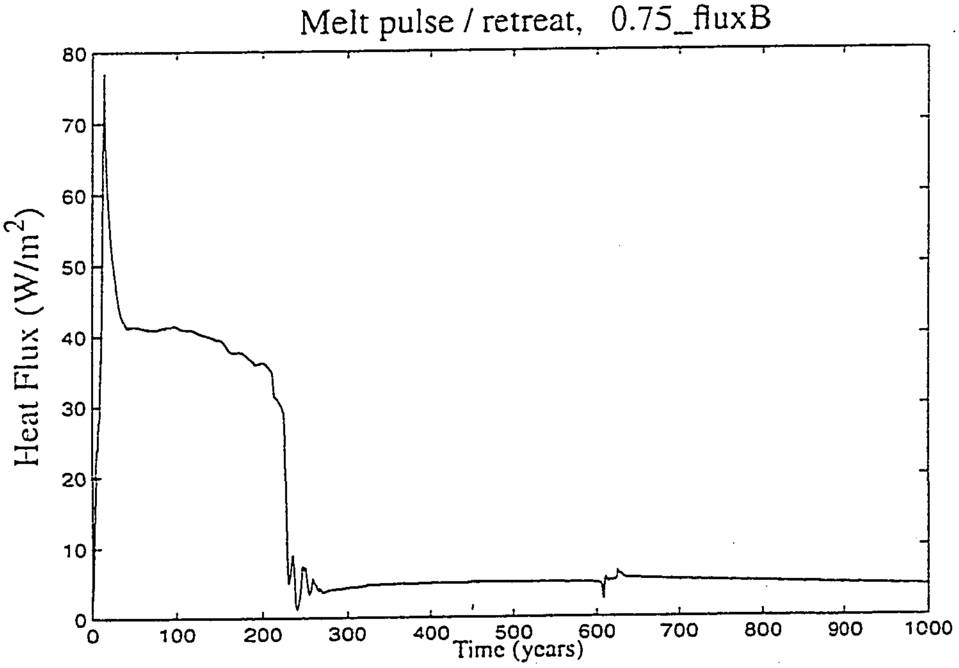

FIGURE 6.5 Heat flux from the ocean following melt pulse/retreat cycle with 0.75fluxB salinity forcing. Melt pulse ends at t=0, and an eight year retreat of glacial melt begins, represented by a reduction and shift of freshening at high latitudes. Salinity flux is returned to steady initial state for remainder of run. Units are Watts/m^2.

6.2.2 Stochastic Forcing

The meltwater pulse scenario was presented as a possible representation of the salinity forcing associated with a Heinrich event or other one time impulse of fresh water. In this section, another scenario is tested. A stochastic element is added to the freshening north of 42°N, in which the freshening is allowed to vary from its normal value. The salinity flux profiles and ranges of forcing are summarized in Table 6.2.

TABLE 6.2 Summary of two-hemisphere one-basin stochastic forcing experiments. Salinity flux pattern B is shown in Figure 4.3

Surface Salinity Flux Pattern	Range of Forcing North of 40°N	Initial State	Behavior of Circulation
0.5fluxB	0.8-1.2	Weak Northern	small departures from steady weak Northern sinking
	0.7-1.3		same
	0.8-1.2	Strong Northern	Small departures from steady strong Northern sinking
0.75fluxB	0.7-1.3	Subantarctic Sinking	One flush in the North, steady Weak Northern sinking
	0.6-1.4		Many distinct transitions between strong and weak Northern sinking, steady Weak Northern
	0.5-1.5		many transitions between strong and weak Northern sinking, no steady state
1x_fluxB	steady	Weak Subantarctic sinking, weaker Northern sinking	steady
	0.8-1.2		many distinct transitions between strong and no Northern sinking
	0.7-1.3		One shorter flush, transition to strong Northern sinking
	0.7-1.3	AABW only, no northern sinking	many distinct transitions between strong and no Northern sinking

Notes on Table 6.2:

Surface Salinity Flux Pattern: Salinity flux pattern 'B' is shown in Figure 4.3.

Range of Forcing North of 40°N: Numbers represent the stochastically determined range of values for a factor multiplying the surface salinity flux north of 40°N.

Initial State: See descriptions, Section 4.4.2.3.

The two steady solutions found under salt flux pattern 0.5fluxB in Section 4.4.2.3 were used as initial conditions for the first set of stochastic experiments. For both initial circulations, the salinity forcing north of 40°N was subjected to stochastic forcing. The stochastic forcing distribution was white, with a minimum period of one year. The forcing was applied as a zonally uniform multiplier of the existing high-latitude freshening. Under moderate stochastic forcing (up to a range of ± 30%) the circulation showed only small variations about it's initial state.

The steady Subantarctic sinking state of the 0.75fluxB forcing was then used as an initial condition (see Figure 6.4a). From this state, the stochastic forcing was able to disrupt the halocline and initiate vigorous overturning in the north, as the melt pulse had. Under moderate stochastic forcing (a range of 0.7-1.3) a single flush occurs in the north, and the model settles into a nearly steady state with weak northern overturning similar to the melt pulse experiment above. The weak-northern sinking equilibrium, as was the case with the 0.5fluxB melt-pulse derived weak-northern sinking, had not previously been observed as an equilibrium state. For both of these forcings, the weak-Northern overturning solution had been observed only as part of the hysteresis experiment. As a test, the stochastic element was eliminated from the fresh water forcing, and the integration was allowed to proceed under steady mixed boundary conditions. The weak Northern overturning continued as an equilibrium solution under steady forcing.

When the amplitude of the stochastic forcing is increased, the behavior becomes much more interesting. Beginning with the same 0.75fluxB initial condition, a range of freshening that is allowed to vary from 0.6 to 1.4 times its standard value produced a series of distinct century-scale flushes. During this period, the overturning was alternating between a strong- and weak-Northern overturning solution (see Figure 6.6). This behavior occurred only as a transient solution, however. The circulation eventually shifted to a steady weak Northern overturning. Note that the basin averaged temperature for the weak northern sinking state is roughly the same as the value for the initial Subantarctic sinking solution. In the weak northern overturning equilibrium, salt is delivered from the low-latitudes to the North; in the Subantarctic sinking solution more of this salt is delivered to the Subantarctic sinking region. Note also that the strong Northern overturning that was seen during the flushes acted to cool the deep ocean, and was not found as an equilibrium solution under steady forcing.

The salinity forcing was then increased to 1fluxB, and the equilibrium solution described in Section 4.4.2.3 was used as the initial condition for stochastic experiments. When the northern freshening region was subjected to stochastic forcing of ± 20%, the cir-

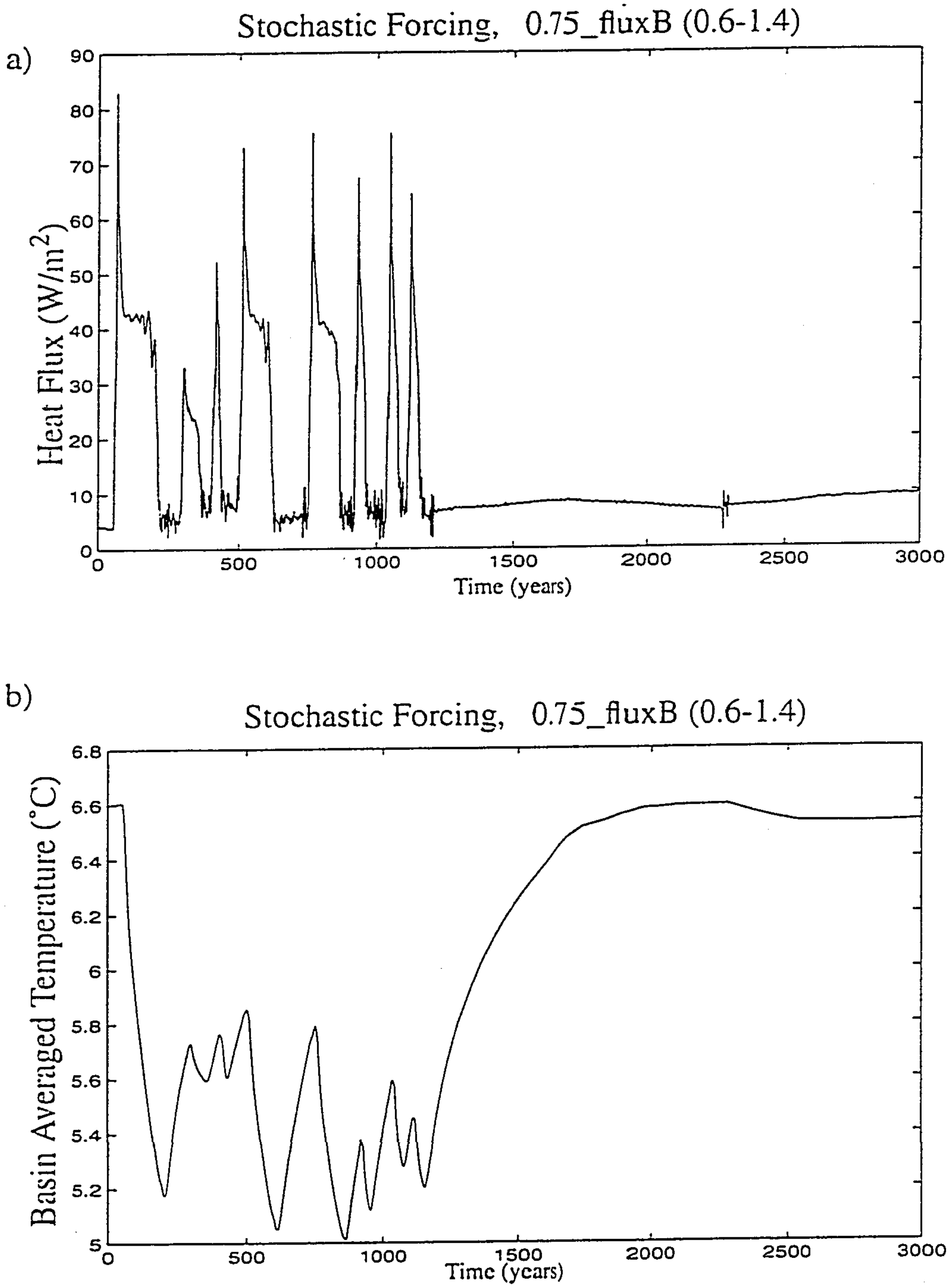

FIGURE 6.6 Response of the two-hemisphere model under 0.75fluxB salinity flux with stochastic forcing in the northern freshening region. Freshwater fluxes in the north ranged from 0.6 to 1.4 times their value given by steady 0.75fluxB forcing. a) **Heat flux from the basin north of 30°N (watts/m^2), and b) basin averaged temperature (°C).**

culation alternated between a state with strong Northern sinking and one in which only a little (approximately 2 Sv) intermediate water formed in both the North and Subantarctic. As was the case with the steady 1fluxB forcing, AABW production continued throughout.

Large amounts of heat are released from the Northern ocean as the flush proceeds, and the basin averaged temperature is seen to fall (Figure 6.7) As the deep ocean cools, the northern high latitudes become more susceptible to the variations in the freshwater flux at the surface, and the overturning 'shuts off' sooner under stochastic forcing than it would under the steady forcing. When the halocline forms after the collapse of the Northern overturning, it forms over a relatively cold water column. As the deep water warms and the water column becomes less well stratified, the same variations in freshwater flux at the surface allow convection to resume, and the Northern overturning is reinitiated. Thus applying a stochastic element to the freshwater flux in the northern sinking region allows modified deep-decoupling oscillations to occur with boundary conditions that would produce only deep water in the Southern ocean under steady forcing.

When the range of the stochastic forcing was increased to 0.7-1.3 times the 1fluxB forcing, the basin underwent a single flush in the North, and settled into a steady circulation with less than 4 Sv sinking to approximately 1100m in the North. Here initial conditions were found to be important. When the 0.7-1.3 times fluxB forcing was applied to the ocean initialized in the 'off' state of the oscillations in the stochastic forcing experiment above (0.8-1.2 times 1fluxB), and circulation went through oscillations similar to those found in the 0.8-1.2 times fluxB experiment. The heat flux from the basin north of 30°N

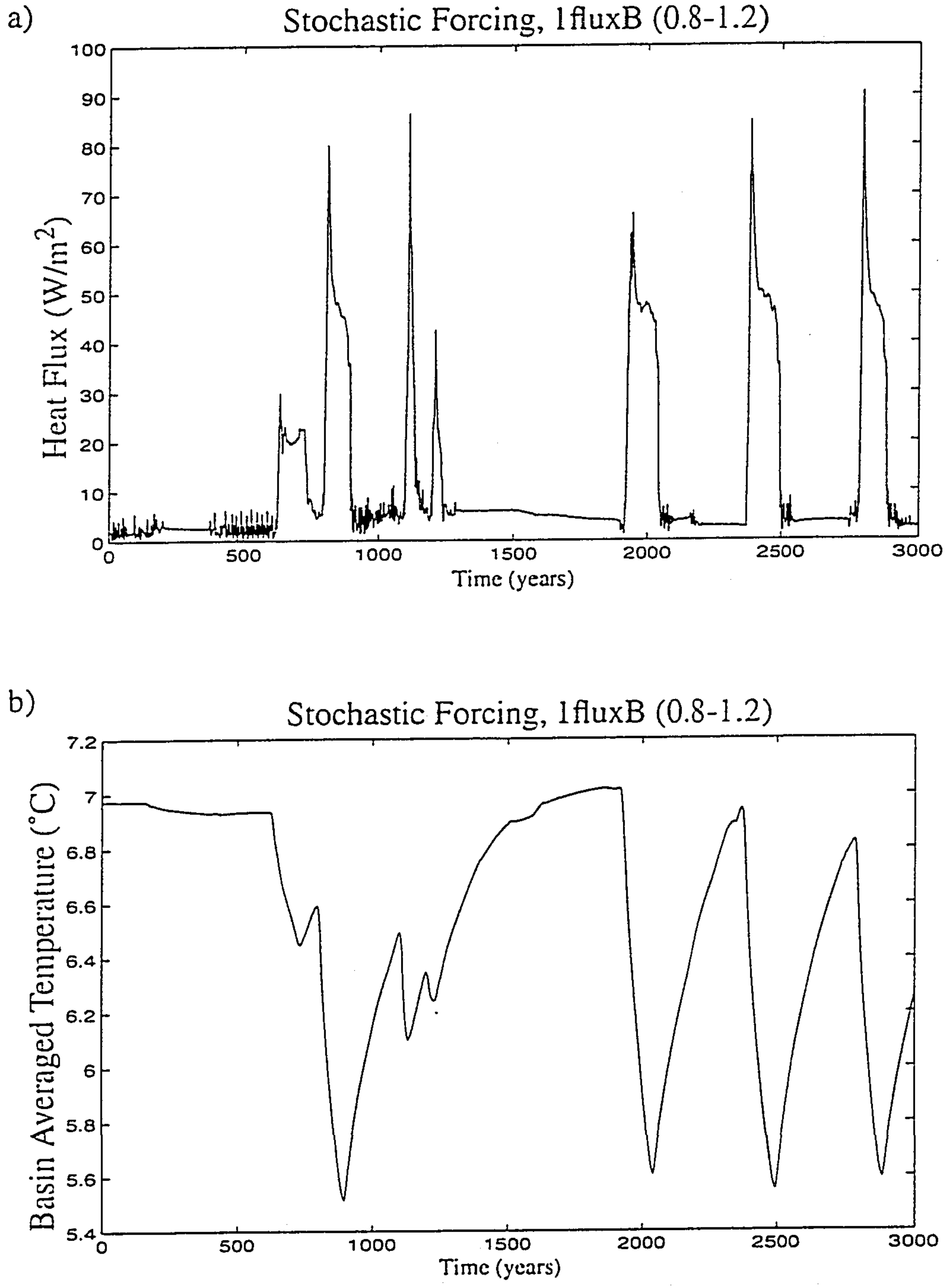

FIGURE 6.7 Response of the two-hemisphere model under 1fluxB salinity flux with stochastic forcing in the northern freshening region. Freshwater fluxes in the north ranged from 0.8 to 1.2 times their value given by steady 1fluxB forcing. a) Heat flux from the basin north of 30°N (watts/m2), and b) basin averaged temperature (°C).

for the oscillating 0.7-1.3 times 1fluxB experiment is shown in Figure 6.8. This gives us an example of surface boundary conditions that can give either steady Southern only sinking or oscillatory behavior, depending on the initial conditions.

The circulation under the weaker (0.8-1.2x) forcing settles into a state that produces much more regular oscillations with longer timescales than the stronger (0.7-1.3x) forcing produces. Two factors determine the timing of the oscillations. First, the subsurface must warm, and the speed with which the subsurface approaches its equilibrium temperature will help set the time scale. As the subsurface warming reduces the stability of the high latitudes, salinity flux perturbations of equal magnitude will become more likely to allow Northern deep sinking to resume. In these numerical model experiments, the subsurface temperature approaches its equilibrium value rather quickly, so the timing of the flushes is set by the amplitude of the stochastic forcing. The large amplitude forcing experiences perturbations sufficient to initiate a flush more often than does the smaller amplitude forcing.

6.3 Two-Basin Study

The timing of the oscillations in section 6.2 was determined, in part, by the warming of the deep ocean. The warming that occurs while Northern sinking is shut off, but AABW production continues might occur on a longer timescale when the Pacific basin must also be warmed. In this section, a stochastic element is added to the high latitude freshening applied to the two-basin configuration of section 4.5. The strength of the forcing is varied in order to generate the same type of oscillations seen in section 6.2.

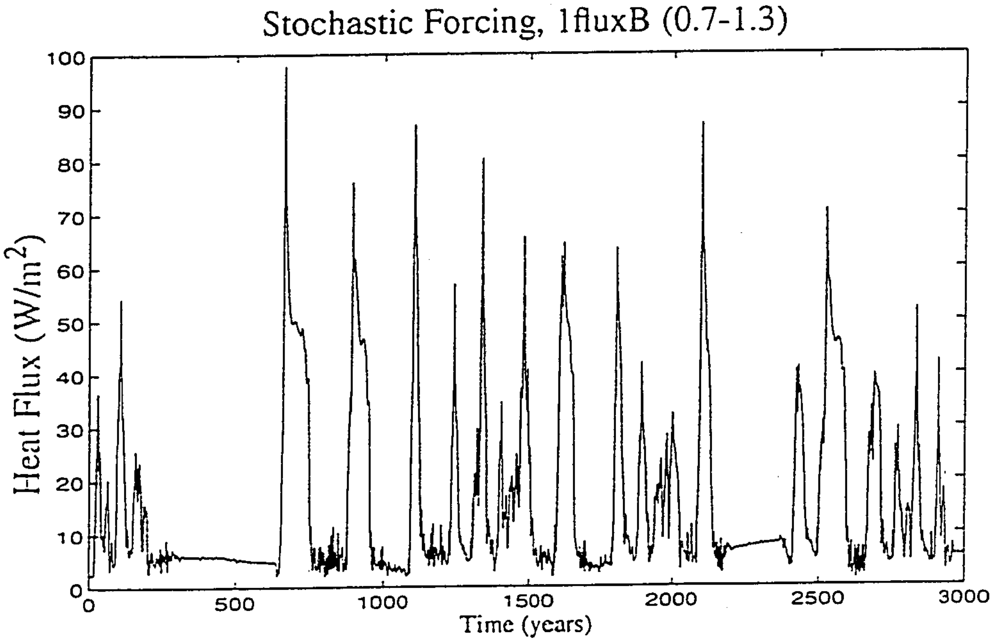

FIGURE 6.8 Heat flux from the basin north of 30°N in the two-hemisphere model under 1fluxB salinity flux. Stochastic forcing in the northern freshening region allowed freshwater fluxes in the north to range from 0.7 to 1.3 times their value given by steady 1fluxB forcing. Units are W/m^2.

The steady-state solutions for the 0.8x_fluxB1 and 1x_fluxB1 salinity flux experiments from section 4.5 are used as initial conditions for the stochastic experiments (see Figure 4.20). The salinity flux north of 40°N is subjected to stochastic forcing. When the freshening in the North is allowed to vary by ± 30%, the 0.8x salinity flux experiment continues its strong production of NADW.

When the same range (± 30%) is applied to the 1x salinity flux experiment, however, the model exhibits deep-decoupling oscillations. The heat flux from the ocean is shown in Figure 6.9. The overturning oscillates between a strong northern overturning and a weak northern overturning solution. The strong overturning solution is similar to the steady solution seen under steady 1x salinity flux, and the weak northern overturning solution is similar to the weak northern overturning state of the oscillations seen in the cold climate experiment of section 4.5. The weak northern overturning had not been seen in the two-basin experiments under steady forcing in the normal (warm) climate. In contrast, none of the stochastic experiments in section 6.2 that resulted in deep-decoupling oscillations had similar steady solutions (strong northern sinking). The stochastically forced warm-climate oscillations depicted in Figure 6.9 show a much stronger preference for the strong northern sinking state than do the oscillations in the cold-climate steady forcing experiment of section 4.5.

6.3.1 Strong Southern Winds

The numerical model experiments of section 4.5.2 demonstrated the operation of the Drake Passage effect under steady mixed boundary conditions. In this section, we can examine the influence of stronger Southern Hemisphere westerlies and the Drake Passage effect on the behavior of oscillations driven by stochastic foring. The equilibrium solution for the two-basin experiment 1xs_fluxB1 of section 4.5.2 was subjected to salinity forcing with a stochastic element added north of 40°N. The high northern latitude salinity flux was allowed to range ±30% of the standard 1x value, following the above example that produced oscillations.

When the strong Southern Hemisphere westerlies are applied to the two-basin model under salinity flux B1, the circulation goes through oscillations similar to those in the standard wind case. The heat flux out of the Atlantic basin north of 30°N is shown in

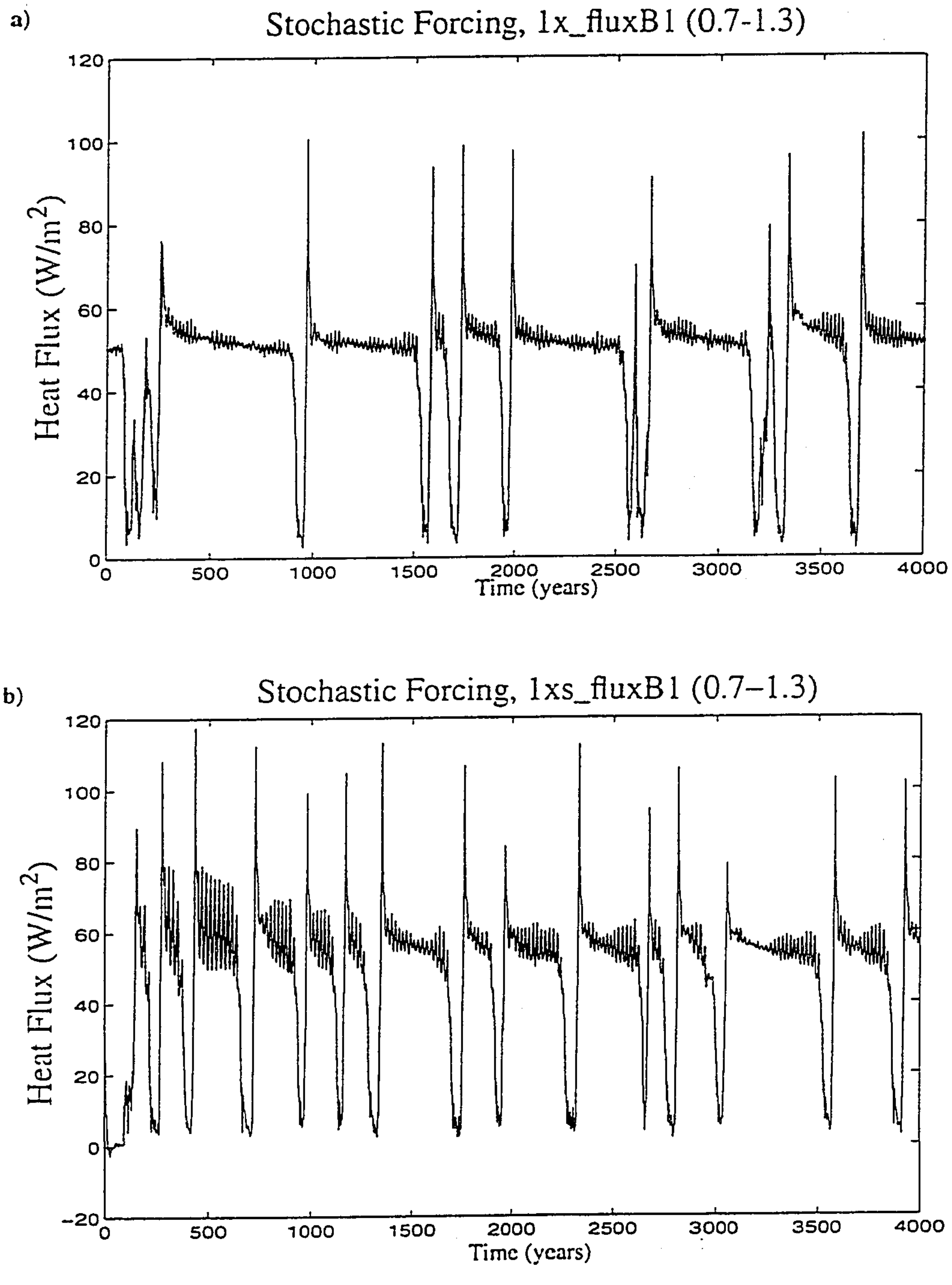

FIGURE 6.9 Heat flux from the Atlantic basin north of 30°N in the two-basin model under salinity flux 'B1'. a) experiment 1x_fluxB1 (0.7-1.3), and b) experiment 1xs_fluxB1 (0.7-1.3) (strong southern winds). Stochastic forcing in the northern freshening region allowed freshwater fluxes in the north to range from 0.7 to 1.3 times their value given by steady B1 forcing. Units are W/m^2.

Figure 6.9b. The circulation is seen to be more volatile than it was under standard wind forcing. The Drake Passage effect does not cause the overturning to be more stable in the strong-northern sinking state where the winds could be expected to enhance the NADW production. Rather, it enhances the overturning in the strong northern sinking state, which speeds the deep cooling and salt export that allow the North to become stratified again.

In the cold-climate experiments of section 4.5.3, reducing the restoring temperature for the two-basin experiment produced oscillations under steady application of salinity flux 'B1' (experiment 1x_fluxB1_cold; see Figure 4.22), and strong NADW production in experiment .8x_fluxB1_cold. When the freshening in the North is subjected to moderate stochastic forcing (± 30%), the circulation in experiment .8x_fluxB1_cold (0.7-1.3) develops regular oscillations. Note that the same range of stochastic forcing did not produce variability in the warmer .8x_fluxB1 (0.7-1.3) experiment.

6.4 Summary

Evidence of rapid transition between climate states has been inferred from $\delta^{18}O$ in the Greenland ice-core record (Dansgaard et al. 1993). Large glacial melting events have been proposed as possible mechanisms to trigger the transitions between cold and warm climate states (Bond et al., 1993, Paillard and Labeyrie, 1994). The deposition of ice-rafted debris in North Atlantic sediments known as Heinrich events have been interpreted as an indication of massive iceberg discharges. While this mechanism may be used to explain the rapid warming following the Heinrich events, most of the rapid transitions are not accompanied by a recorded melt-pulse.

In this chapter, much smaller perturbations in the hydrologic forcing are used to effect similar transitions in a OGCM. In a two-hemisphere single-basin ocean configuration, decadal scale perturbations are capable of inducing transitions from one mode of oceanic overturning to another. The magnitudes of the perturbations are approximately an order of magnitude smaller than estimates for the freshwater fluxes associated with Heinrich events (MacAyeal, 1993). Under surface forcing that allowed two stable northern sinking modes, the melt pulse/retreat perturbations caused transitions in both directions: from warm (strong northern overturning) to cold (weaker northern overturning) and from cold to warm. Under surface forcing that resulted in steady ventilation of the deep ocean from the Subantarctic, the melt pulse/ retreat pattern caused the transition from very weak northern sinking to strong northern sinking. In this case, no additional forcing was required; the cessation of the strong northern sinking occurred spontaneously.

Stochastic forcing of the high latitude freshening region also produces oscillation between overturning states of the thermohaline circulation. In both the one-basin and two-basin configurations used in this chapter, moderate variability in the fresh water forcing in the North generates rapid transitions between climate states. A particularly interesting result is produced in the cold-climate experiments of section 6.3. Stochastic forcing that had resulted in steady overturning in a warm climate resulted in variability in a cooler climate. The increased sensitivity to small variability in a cold climate may help explain why rapid climate transitions like the Dansgaard-Oeschger events are not seen during the warm interglacials (Keigwin et al., 1994, McManus et. al., 1994).

Chapter 7 Conclusions

The goal of this study has been to elucidate some of the connections between the southern and northern branches of the ocean's thermohaline circulation. Numerical models were employed to investigate several particular questions regarding the interaction of the two branches of overturning. Conclusions regarding the influence of southern hemisphere wind stress on northern overturning are discussed in section 7.1. In section 7.2, the ability of southern-source deep water to suppress variability in the northern sinking region is reviewed. Finally, the use of time-dependent surface forcing in the high-northern latitudes is discussed in section 7.3.

7.1 The Influence of Southern Hemisphere Winds on Northern Overturning

The rate of deep water production in the Northern Hemisphere is linked to the wind stress at the latitude of the tip of South America through a dynamical constraint called the Drake Passage effect. Conservation of mass requires that the northward surface Ekman drift at the latitude of Drake Passage be supplied by southward flow below the surface layer. Drake Passage creates a latitude band within which there can be no net zonal pressure gradient, limiting net geostrophically balanced southward flow to occurring below the heights of topographic features. Thus the southward flow that must upwell to supply the northward surface Ekman drift is either ageostrophic or occurs at a depth supplied by NADW formation.

The Drake Passage effect is demonstrated in an ocean general circulation model with very simplified geometry. Observing the transient response of the ocean to changes in the wind stress illustrates the mechanism through which the winds in the southern hemisphere influence the ocean circulation north of the equator. The dynamical constraint of no net geostrophic flow without an east-west pressure gradient isolates the upwelling and downwelling caused by the surface Ekman drift, allowing geostrophically balanced communication between the upwelling and downwelling only below the sill depth. The downwelling north of the gap spreads northward by exciting baroclinic modes that travel north as in the spin-up problem described by Kawase (1987).

In the absence of a preexisting sinking region in the north, the development of the flow very closely parallels the development of flow described by Kawase (1987) in a two-layer model with a prescribed source of deep water and cross-interfacial flow parameterized as a damping term in the continuity equation. In the experiments presented here, similar behavior is observed. The modeled forcing can be considered either a single source in the upper layer with downwelling through a thermocline, or a single sink in the lower layer with downwelling through the thermocline supplying it. The unstratified sinking region is analogous to a region of greatly increased damping in the continuity equation of the two-layer model of Kawase (1987).

Döscher et al. (1994) observed the transient response of higher resolution (1° and 1/3°) Community Modeling Effort (CME) Atlantic basin models to changes in the northern lateral thermohaline forcing. Their basins extended from 15°S to 65°N, and so did not include a second sinking region away from the source of their transient signals. Because of the different nature of the forcing, i.e. it is not dependent on the geostrophic constraint on the Drake Passage and is not linked to the thermal wind balance of the ACC, their results are primarily of interest as an example of baroclinic modes propagating in an OGCM. They observed a basin wide response to a spin up similar to that observed in simpler models. The signal originating from their northern boundary propagated similarly to the signal generated by changes in wind stress here. They did observe a vertical expansion of the NADW and contraction of AABW, though these changes occurred through interaction with the southern lateral boundary condition, not with a remote deep water source region. Their response also included changes in the barotropic stream function, through the JEBAR term of the vorticity equation.

In the presence of a sinking region in the north, the development of the flow is changed when it reaches that region. The sinking region offers a "path of least resistance" for the flow; an almost unstratified connection between the upper and lower ocean. The existing circulation and buoyancy forcing maintain this unstratified link between the upper and lower ocean. Deep water that had been broadly upwelling into the thermocline is diverted into the Ekman driven upwelling in the south. This shifts the thermal balance in the thermocline, and allows the thermocline to deepen. Depressing the thermocline north of the gap increases the horizontal density gradient across the latitude band of the gap. This increase in baroclinicity will establish, through the JEBAR term of the vorticity equation, the majority of the increase in the circumpolar current. Thus it is seen that the mechanism linking the wind stress in the south to the deep water production in the north is also responsible for establishing the new equilibrium density gradient for the ACC.

Communication between the winds in the Drake Passage latitudes and the northern sinking region in this model occurs on time scales on the order of years, although the maximum northern overturning approaches its equilibrium value on a time scale of order centuries. Because of the grid size dependence of the boundary mode propagation outlined in Appendix A, higher resolution models will also allow quicker communication between southern hemisphere winds and the northern overturning. As a result, higher resolution models might show greater sensitivity to shorter time scale variability in the winds. This is supported by the quicker response seen by Döscher et al. (1994) in their CME Atlantic. For coarse resolution models used for climate study, interannual variability in the wind stress over the southern ocean is unlikely to influence the rate of sinking in the north. Longer term changes in wind stress over the southern oceans, however, will play a role in modifying the thermohaline circulation of the ocean.

The Drake Passage effect is seen to be strongly dependent on the specified representation of Drake Passage. North of the latitude of Drake Passage, there are two significant sources of sub-thermocline water: the northern deep water formation region, and the AAIW formation region. In the zonal mean, water above the sill depth must either cross the latitude of Drake Passage ageostrophically or sink below the sill where it can cross southward geostrophically. The extent to which the equatorial Ekman drift at the tip of

South America influences the northern sinking is seen to depend on how easily the Subantarctic intermediate water can supply the upwelling region.

Moving the tip of South America poleward reduces the strength of the Atlantic outflow in part because the wind stress at the more southerly location is smaller, and in part because of the colder surface boundary condition at the more southerly location. The colder boundary condition reduces the stratification in the Subantarctic sinking region north of Drake Passage. The reduced stratification allows more Subantarctic water to reach sill depth, where it can supply the southward geostrophic flow beneath the sill. Because this more local supply is facilitated, less is demanded from the northern sinking source region. The response for the Atlantic outflow to changes in wind stress (Δ Atlantic outflow / Δ (τ_x/f)) is also reduced compared to the wide-Drake configuration.

Changing the depth of the sill produced similar results. A deeper sill depth reduced the ability of Subantarctic water to contribute to the geostrophic meridional flow below that depth, and the Atlantic outflow increased. This configuration showed greater sensitivity to wind stress changes than the nominal Drake Passage configuration did in section 3.3. A shallower sill depth made Subantarctic (local) return easier, and diminished the Atlantic outflow. In fact, simulations in this study produced a decrease in the Atlantic outflow with stronger southern hemisphere winds in the shallow sill experiments.

The dramatic reduction in the strength of the Drake Passage effect with decreases of sill depth indicates that particular care must be taken in representing the topography of the circumpolar region. Moreover, changes in the width and geometry of Drake Passage are similarly effective in altering the strength of the Drake Passage effect. Thus, while the Drake Passage effect appears to exert a noticeable influence on the rate of Northern sinking in these coarse resolution models, its importance in the real ocean is more difficult to predict.

The experiments with different sill depths also illustrated how the choice of sill depth influences the competition between AABW and NADW to fill the deep ocean. The dynamic constraint limiting geostrophically balanced meridional flow to below the tops of topographic features also applies to the southward supply of water to the AABW formation regions. A lower sill depth restricts the southward supply to the AABW formation, and AABW is reduced at the expense of increased NADW.

A note of caution about the importance of the Drake Passage effect can be derived from the mixed boundary condition experiments in this study. The wind stress at the latitude of the tip of South America did influence the rate of NADW production in experiments which contained steady northern deep sinking. However, the stronger southern winds did not result in NADW production under buoyancy forcing that would not produce NADW with weak Southern Hemisphere westerlies. Rather, the stronger winds resulted in more and deeper ventilation in the Subantarctic.

7.2 Steady Mixed Boundary Condition Experiments

There is paleoceanographic evidence suggesting that deep water in the North Atlantic during the LGM was of southern origin (Duplessy, et al. 1988). Winton (1996) found that as the average atmospheric temperature decreased, the overturning circulation gradually increased and deepened Subantarctic water production, while it diminished and shoaled Northern water production. The deep sinking shifted because, as the atmospheric temperatures decreased, the equation of state of sea water implied that the northern sinking region became increasingly sensitive to the salinity flux applied there. The possibility that deep water from the south is from a Subantarctic source rather than from enhanced AABW production is suggested by Michel et al. (1995). Their box-model study sought to explain the distribution of isotopic tracers in the sediment record from the LGM, but did not attempt to present a circulation based on actual surface forcing. Rather, transport between boxes was adjusted to produce a good isotopic 'fit' to observations. Michel et al. (1995) found that the $\Delta^{13}C$ record from the last glacial maximum is consistent with deep Subantarctic convection supplying the deep basins at that time.

The mechanism for deep decoupling oscillations proposed by Winton (1993) supposes that the heat acquired at low latitudes at the surface warms the sub-surface waters when northern sinking is interrupted. The results presented here for a mixed boundary condition sector model suggest that a combination of Subantarctic deep water and AABW fills the deep ocean when NADW production is reduced and/or shoaled. The Subantarctic serves as an alternate destination for low latitude surface waters, and enough of the heat can be delivered there to prevent the destabilization of the high northern latitudes. Subantarctic deep sinking with shallower northern sinking is found to be a stable mode of circulation, consistent with the theory of Michel et al (1995).

This study finds deep-decoupling oscillations in a two-hemisphere ocean basin under steady salinity forcing only if Subantarctic deep-water and AABW production are shut off. A study by Winton (1996) using a two-dimensional ocean coupled to an idealized atmosphere supports this idea. If the southern (Antarctic and Subantarctic) sinking mode is indeed a stable solution for the global overturning of the glacial ocean, some external forcing may be required to effect changes in the mode of overturning. It may be that a more complicated interaction between the ocean, atmosphere, and cryosphere is necessary to explain the Dansgaard-Oeschger oscillations.

One such possibility is presented in the two-basin experiments of this study. In the two-basin configuration, deep-decoupling oscillations occurred under very special circumstances: The climate was cooled, and the export of fresh water from the Atlantic basin is held at near current levels. If the freshwater export was reduced, the circulation settled into a steady state with no deep water production in the North Atlantic. This type of oscillation is something of a hybrid, incorporating elements of both the thermally driven deep-decoupling oscillations of Winton (1993, 1996) and the haline driven salt-oscillator of Broecker (1991).

Box models can be used to illustrate certain aspects of the response of ocean circulation to mixed boundary conditions. Obviously, there are limitations to using such simple models. For example, changes in the latitude of the sinking regions cannot be represented. Convection in the ocean occurs on much smaller scales, where local forcing can be significant. The advection of salt to the convecting regions occurs in circulations not well represented by the simplifications required in a box model. Nevertheless, the box models illustrate the conditions required to produce deep-decoupling oscillations. Note that the box-model configurations used were single basin, and could not include the interbasin freshwater transport necessary to produce deep-decoupling oscillations seen in the three-dimensional two-basin model.

In this set of box model experiments, the greatest impediment to deep-decoupling oscillations is the existence of an additional region that can serve as a viable deep water formation region. The alternate site serves to prevent warming of the ocean interior. It also removes salt from the low-latitude upper ocean, mixing it into the interior and making it unavailable to erode the halocline in the North. The transformation of the circulation that occurs when Northern sinking ceases is reminiscent of the so-called 'halocline catastrophe' of F. Bryan (1986). This type of transition is possible as long as an alternative deep water formation region is available. The findings of Michel et al. (1995) suggest that such an alternative circulation was available during the last glaciation.

A second impediment to deep-decoupling oscillations is the continued production of AABW. While no example of deep-decoupling oscillations in the presence of AABW was found in the twelve-box model, the possibility was raised by the four-box model where deep-decoupling oscillations persisted if the influence of the deep box was sufficiently weak. The sediment record indicates that deep water in the North Atlantic during the LGM was of southern origin (Duplessey et al 1988) and that production of AABW appears to be continuous throughout the last glaciation (Charles and Fairbanks 1992). It is difficult to determine, however, what the rates of AABW production were, and how much of the deep southern-source water was actually of Subantarctic origin.

7.3 Time-varying Mixed Boundary Condition Experiments

The simple perturbation experiments conducted in Chapter 6 illustrate several variations of transitions from one overturning mode to another. Under salinity forcing for which multiple equilibria exist, freshwater perturbations in the high latitudes can cause transitions from one steady mode to another. This type of transition has been seen by Rahmstorf (1994), although his study only illustrated how a freshwater pulse could cause a transition to a reduced overturning state. Here a melt pulse/retreat scenario is shown to be capable of causing a transition to a stronger overturning circulation as well.

Under salinity forcing for which no steady strong-northern overturning equilibrium existed, similar melt pulse/ retreat forcing was seen to produce a flush of rapid northern overturning. If Subantarctic deep water production was indeed favored during cold glacial periods, this case could illustrate a mechanism to explain the rapid temperature shifts known as Dansgaard-Oeschger events. The magnitudes of the perturbations used to produce the transitions between overturning states were considerably smaller than the melt pulses believed responsible for the Heinrich events recorded in the sediment record.

The stochastic forcing experiments illustrated another scenario which could explain the Dansgaard-Oeschger events in the climate record. Randomly applied variations in the strength of the freshening in the high northern latitudes produced deep-decoupling-like oscillations where none were possible under steady forcing. Subsurface warming reduces the stability of the Northern sinking region to such an extent that variability in the freshwater forcing can induce the onset of Northern overturning. The surface forcing selected did not produce a steady Northern sinking solution, so even with steady forcing the circulation would return to a steady southern sinking state. The stochastic forcing causes the shut-off of the Northern sinking to occur sooner, as the anomalies cap convection before the steady forcing would have been able to do so.

A colder climate increased the sensitivity of the northern sinking region to freshwater forcing. Not only is this true for steady salinity forcing, the same is true for time dependent anomalous forcing. Anomalies in the freshwater supplied to the sub-polar North Atlantic that do not prevent deep water formation in a warmer climate become more influential as the climate cools. Naturally occurring variability in the freshening that was relatively inconsequential in the warmer initial phases of the Dansgaard-Oeschger events could be sufficient to stop the overturning as the temperature falls. The cold northern halocline of the Subantarctic sinking state is similarly sensitive to perturbations in meltwater supply.

The following sequence of events is then proposed as a way of explaining the climate fluctuations seen as Dansgaard-Oeschger events. During the generally cooler glacial period, the circulations are assumed to start from an ocean circulation with reduced NADW production and enhanced Subantarctic deep water production. In this state, variations in the supply and distribution of meltwater and/or river runoff allow deep convection in the north to resume, and the circulation switches to the strong northern-sinking solution. Alternatively, the gradual increase in salinity due to the export of freshwater from the Atlantic basin, in the form of atmospheric water vapor transport, causes the switch to strong northern sinking. The halocline in the north allows the surface to be much cooler than the subsurface, which facilitates the transition to the northern-sinking-on state. The resumption of northern deep water production, however, requires an external 'push', either by steady (fresh water export) or transient (melt pulse, stochastic variability) forcing.

If the southern sinking overturning state is the steady solution, the transition from northern-sinking to southern-sinking can be accomplished with a steady surface freshwater flux. The addition of a stochastic element to the forcing facilitates the switching-off of the northern sinking in this case, but is not necessary. If the climate is capable of producing two steady states, then external forcing such as the stochastic freshening or meltwater pulse is necessary to cause the circulation to switch from northern-sinking to southern-sinking. This would be the case if the warmer 'conveyor-on' circulation resulted in increased interbasin freshwater transport, stabilizing the overturning in the northern-sinking mode.

References

Bond, G., W. Broecker, S. Johnsen, J. McManus, L. Labeyrie, J. Jouzel, and G. Bonani, 1993, Correlations between climate records from North Atlantic sediments and Greenland ice, *Nature*, **365**, 143-147.

Boyle, E. A., 1990, Quaternary deepwater paleoceanography, *Science*, **249**, 863-870.

Boyle, E. A., and L. D. Keigwin, 1987, North Atlantic thermohaline circulation during the past 20,000 years linked to high latitude surface temperature, *Nature*, **330**, 35-40.

Broccoli, A. J., and S. Manabe, 1987, The influence of continental ice, atmospheric CO_2, and land albedo on the climate of the last glacial maximum, *Clim. Dyn.*, **1**, 87-99.

Broecker, W. S., 1987, The biggest chill, *Nat. Hist. Mag.*, **97**, 74-82.

Broecker, W. S., G. Bond, M. Klas, G. Bonani, andW. Wolfli, 1990, A salt oscillator in the glacial Atlantic? I. The concept, *Paleoceanography*, **5**, 469-477.

Broecker, W. S., 1991, The great ocean conveyor, *Oceanography*, **4**, 79-89.

Bryan, F., 1986, High latitude salinity effects and inter-hemispheric thermohaline circulations, *Nature*, **323**, 301-304

Bryan, K., 1984, Accelerating the convergence to equilibrium of ocean-climate models, *J. Phys. Oceanogr.*, **14**, 666-673

Bryan, K., 1991, Ocean circulation models, *Strategies for Future Climate Research,* M. Latif, Ed., Max-Planck Institut für Meteorologie, 265-286.

Charles, C. D., and R. G. Fairbanks, 1992, Evidence from Southern Ocean sediments for the effect of North Atlantic deep-water flux on climate, *Nature*, **355**, 416-419

CLIMAP Project Members,1981, Seasonal reconstruction of the Earth's surface at the last glacial maximum, *Geol. Soc. of Am. Map and Chart Ser.*, **36**

Cox, M. D., 1989, An idealized model of the world ocean. Part I: The global-scale water masses, *J. Phys. Oceanogr.*, **19**, 1730-1752

Dansgaard, W., and S. J. Johnsen, H. B. Clausen, D. Dahl-Jensen, N. S. Gunndestrup, C. U. Hammer, C. S. Hvldberg, J. P. Steffensen, A. E. Svelnbjornsdottir, J. Jouzel, and G. Bond, 1993, Evidence for general instability of past climate from a 250-kyr ice-core record, *Nature*, **364**, 218-220

Deacon, G. E. R., 1937, The hydrology of the Southern Ocean, *Discovery Rep.*, **15**, 1-124, plates I-XLIV

Döös, K. and D. J. Webb, 1994, The Deacon cell and the other meridional cells of the Southern Ocean, *J. Phys. Oceanogr.*, **24**, 429-442.

Döscher, R., C. Böning, and P. Herrmann, 1994, Response of circulation and heat transport in the North Atlantic to changes in thermohaline forcing in northern latitudes: A model study, *J. Phys. Oceanogr.*, **24**, 2306-2320

Drijfhout, S., C. Heinze, M. Latif, and E. Maier-Reimer, 1996, Mean circulation and internal variability in an ocean primative equation model, *J. Phys. Oceanogr.*, in press

Duplessy, J. C., N. J. Shackelton, R. G. Fairbanks, L. Labeyrie, D. Oppo, and N. Kallel, 1988, Deepwater source variations during the last climatic cycle and their impact on the global deepwater circulation, *Paleoceanography*, **3**, 343-360

England, M. 1992 , *The global-scale circulation and water-mass formation in a World Ocean model*. Ph.D. dissertation, University of Sydney, 225pp.

Gill, A. E., and K. Bryan, 1971, Effects of geometry on the circulation of a three-dimensional southern-hemisphere ocean model, *Deep-Sea Res.*, **18**, 685-721

Gordon, A. L., 1986, Interocean exchange of thermocline water, *J. Geophys. Res.*, **91**, 5037-5046

Haney, R. L., 1971, Surface thermal boundary condition for ocean circulation models, *J. Phys. Oceanogr.*, **1**, 241-248

Hellerman, S., and M. Rosenstein, 1983, Normal monthly wind stress over the world ocean with error estimates, *J. Phys. Oceanogr.*, **13**, 1093-1104.

Hughes, T., and A. Weaver, 1994, Multiple equilibria of an asymmetric two-basin ocean model, *J. Phys. Oceanogr.*, **24**, 619-637

Johnson, S. J., H. B. Clausen, W. Dansgaard, K. Fuhrer, N. Gundestrup, C. U. Hammer, P. Iverson, J. Jouzel, B. Stauffer, and J. P. Steffensen, 1992, Irregular glacial interstadials recorded in a new Greenland ice core, *Nature*, **359**, 311-313

Kawase, M. 1987, Establishment of deep ocean circulation driven by deep-water production, *J. Phys. Oceanogr.*, **17**, 2294-2317.

Keigwin, L. D., W. B. Curry, S. J. Lehman, and S. Johnsen, The rold of the deep ocean in North Atlantic climate change between 70 and 130 kyr ago, *Nature*, **371**, 323-325.

Kutzbach, J. E., and P. J. Guetter, 1986, The influence of changing orbital parameters and surface boundary conditions on climate simulations for the past 18,000 years, *J. Atmos. Sci.*, **43**, 1726-1759

Lautenschlager, M. and K. Herterich, 1990, Atmospheric response to ice age conditions: climatology near the earth's surface, *J. Geophys. Res.*, **95**, 22547-22557

Ledwell, J. R., A. J. Watson, C. S. Law, 1993, Evidence for slow mixing across the pycnocline from an open-ocean tracer-release experiment, *Nature*, **365**, 701-703

Levitus, S., 1982, Climatological Atlas of the World Ocean, *NOAA Prof. Pap. 13*, U. S. Government Printing Office, Washington, D.C.

MacAyeal, D. R., 1993, Binge/purge oscillations of the Laurentide ice sheet as a couse of the North Atlantic's Heinrich events, *Paleoceanography*, **8**, 775-784

Manabe, S., and A. J. Broccoli, 1985a, A comparison of climate model sensitivity with data from the last glacial maximum, *J. Atmos. Sci.*, **42**, 2643-2651

Manabe, S., and A. J. Broccoli, 1985b, The influence of continental ice sheets on the climate of an ice age, *J.Geophys. Res.*, **90**, 2167-2190

Manabe, S., K. Bryan and M. J. Spelman, 1990, Transient response of a global ocean-atmosphere model to a doubling of atmospheric carbon dioxide, *J. Phys. Oceanogr.*, **20**, 722-749

Manabe, S., and R. J. Stouffer, 1988, Two stable equilibria of a coupled ocean-atmosphere model, *J. Climate*, **1**, 841-866

Manabe, S., R. J. Stouffer, M. J. Spelman and K. Bryan, 1991, Transient responses of a coupled ocean-atmosphere model to gradual changes of atmospheric CO_2. Part I: Annual mean response, *J. Climate*, **4**, 785-818

Marotzke, J., and J. Willebrand, 1991, Multiple equilibria of the global thermohaline circulation, *J. Phys. Oceanogr.*, **21**, 1372-1385

McDermott, D. A., 1996, The regulation of northern overturning by southern-hemisphere winds, *J. Phys. Oceanogr.*, in press.

McDermott, D. A., and E. Sarachik, 1996, Thermohaline circulations and variability in a two-hemisphere sector model of the Atlantic, In: The Natural Variability of the Climate System on Decande-to-Century Time Scales, D. G. Martinson, K. Bryan, M. Ghil, M. M. Hall, T. R. Karl, E. S. Sarachik, S. Sorooshian, and L. D. Talley, editors. National Academy Press, Washington D. C., in press.

McManus, J. F., G. C. Bone, W. S. Broecker, S. Johnsen, L. Labeyrie, and S. Higgins, High-resolution climate records from the North Atlantic during the last interglacial, *Nature*, **371**, 326-329.

Mertz, G. and D. G. Wright, 1992, Interpretations of the JEBAR term, *J.Phys. Oceanogr.*, **22**, 301-305.

Michel, E., L. D. Labeyrie, J. C. Duplessy, and N. Gorfti, 1995, Could deep Subantarctic convection feed the world deep basins during the last glacial maximum?, *Paleoceanography*, **10**, 927-942

Moore, A. M., and C. J. C. Reason, 1993, The response of a global ocean general circulation model to climatological surface boundary conditions for temperature and salinity, *J. Phys. Oceanogr.*, **23**, 300-328

Oppo, D. W., S. J. Lehman, 1995, Suborbital timescale variability of North Atlantic Deep Water during the past 200,000 years, *Paleoceanography*, **10**, 901-910

Pacanowski, R., K. Dixon, and A. Rosati, 1991, The GFDL Modular Ocean Model Users Guide, Version 1.0, GFDL Ocean Group Tech. Rep. No. 2, Geophysical Fluid Dynamics Laboratory/NOAA, Princeton University, Princeton, N.J. 08542

Paillard, D., and L. Labeyrie, 1994, Role of the thermohaline circulation in the abrupt warming after Heinrich events, *Nature*, **372**, 162-164

Petit, J.-R., M. Briat, and A. Royer, 1981, Ice age aerosol content from East Antarctic ice core samples and past wind strength, *Nature*, **293**, 391-394

Rahmstorf, S., 1994, Rapid climate transitions in a coupled ocean-atmosphere model, *Nature*, **372**, 82-85

Rahmstorf, S., 1995, Bifurcations of the Atlantic thermohaline circulation in response to changes in the hydrological cycle, *Nature*, **378**, 145-149

Rahmstorf, S., and J. Willebrand, 1995, The role of temperature feedback in stabilizing the thermohaline circulation, *J. Phys. Oceanogr.*, **25**, 787-805

Rind, D., 1987, Components of the ice age circulation, *J. Geophys. Res.*, **92**, 4241-4281

Sarachik, E. S., M. Winton, and F. L. Yin, 1996, Mechanisms for Decadal-to-Centennial Climate Variability, In Proceedings of a NATO Advanced Study Institute, Springer Verlag, in Press

Stommel, H., 1957, A survey of ocean current theory, *Deep-Sea Res.*, 4, 149-184

Stommel, H., 1958, The abyssal circulation, *Deep-Sea Res.*, **5**, 80-82.

Stommel, H., and A. B. Arons, 1960a, On the abyssal circulation of the world ocean - I. Stantionary planetary flow patterns on a sphere, *Deep-Sea Res.*, **6**, 140-154.

Stommel, H., and A. B. Arons, 1960b, On the abyssal circulation of the world ocean - II. An idealized model of the circulation pattern and amplitude in ocean basins. *Deep-Sea Res.*, **6**,217-233.

Toggweiler, J. R., K. Dixon, and K. Bryan, 1989, Simulations of Radiocarbon in a coarse-resolution world ocean model 1. Steady state prebomb distributions, *J. Geophys. Res.*, **94**, 8217-8242

Toggweiler, J. R., and B. Samuels, 1993a, Is the magnitude of the deep outflow from the Atlantic Ocean actually governed by southern hemisphere winds?, In: *The Global Carbon Cycle*, M. Heimann, ed., NATO ASI Series, Springer-Verlag, Berlin, pp. 303-331

Toggweiler, J. R., and B. Samuels, 1993b, New radiocarbon constraints on the upwelling of abyssal water to the ocean's surface, In: *The Global Carbon Cycle*, M. Heimann, ed., NATO ASI Series, Springer-Verlag, Berlin, pp. 333-366

Toggweiler, J. R., and B. Samuels, 1995, Effect of Drake Passage on the Global Thermohaline Circulation, *Deep-Sea Res.*, **42**, 477-500

Warren, B. A., 1990, Suppression of deep oxygen concentrations by Drake Passage, *Deep-Sea Res.*, **37**, 1899-1907

Weaver, A. J., J. Marotzke, P. F. Cummins, and E. S. Sarachik, 1993, Stability and variability of the thermohaline circulation, *J. Phys. Oceanogr.*, **22**, 39-60

Weaver, A. J., and T. M. C. Hughes, 1994, Rapid interglacial climate fluctuations driven by North Atlantic Ocean circulation, *Nature*, **367**, 447-450

Weaver, A. J., and E. S. Sarachik, 1991, The role of mixed boundary conditions in numerical models of the ocean's climate, *J. Phys. Oceanogr.*, **21**, 1470-93

Whitworth, T., W. D. Nowlin, Jr., and S. J. Worley, 1982, The net transport of the Antarctic circumpolar current through Drake Passage, *J. Phys. Oceanogr.*, **12**, 960-971

Winton, M., 1993, *Numerical investigations of steady and oscillating thermohaline circulations.* Ph.D. dissertation, University of Washington, 155pp.

Winton, M., and E. S. Sarachik, 1993, Thermohaline oscillations induced by strong steady salinity forcing of ocean general circulation models, *J. Phys. Oceanogr.*, **23**, 1389-1410

Yin, F. L., and E. S. Sarachik, 1995, Interdecadal thermohaline oscillations in a sector ocean general circulation model: Advective and convective processes, *J. Phys. Oceanogr.*, **25**, 2465-2484

Appendix A. Numerical Boundary Wave Speed

The speed of the Kelvin boundary waves in a coarse resolution model such the GFDL MOM model can be approximated (e.g. Winton(1993)). To examine a wave propagating along the eastern boundary in the northern hemisphere, consider a linearized shallow water model for a particular baroclinic mode. No-slip conditions at the boundary sets u=v=0 at x=0, while the onshore flow at x=-ΔX is approximately geostrophic. We see, then:

$$u = -\frac{g}{f}h_y \text{ and } h_t = -Hu_x = -\frac{Hu}{\Delta x} = \frac{g'H}{f\Delta x}h_y \qquad \text{(EQ A.1)}$$

where g' is the reduced gravity and $(g'H)^{1/2} = c$ is the gravity wave speed for the baroclinic mode. In this case, the equation describes a mode propagating northward at a speed of $(g'H)/(f\Delta x)$ with the coast to the right. The mode advances in latitude (ϕ), then, as:

$$R_e\frac{d\phi}{dt} = \frac{c^2}{f\Delta x} = \frac{c^2}{2\Omega\sin\phi\left(3.75^\circ\right)\left(\pi/180^\circ\right)R_e\cos\phi} \qquad \text{(EQ A.2)}$$

where R_e is the radius of the earth, and Ω is the rotational frequency of the earth.

Solving for ϕ as a function of time:

$$\phi = \operatorname{asin}\left(\frac{c^2}{\Omega\left(3.75^\circ\right)\left(\pi/180^\circ\right)R_e^2}(t-t_\circ) + (\sin\phi_\circ)^2\right)^{1/2} \qquad \text{(EQ A.3)}$$

This time dependent solution is shown as the dashed line in Figure 3.21.

Appendix B. JEBAR and the ACC

It has been widely noted that the so-called JEBAR (joint effect of baroclinicity and relief) term of the depth-averaged vorticity equation can be responsible for a significant depth-averaged current. A discussion of some of the interpretations of the JEBAR term, along with references to many other papers discussing its significance, can be found in Mertz and Wright (1992). A derivation of the depth-averaged vorticity equations follows for time-dependent flow, driven by wind and buoyancy forces, with the hydrostatic, rigid lid, and Boussinesq approximations imposed.

The linearized momentum equations for the horizontal velocities u, v are

$$u_t - fv = -\frac{1}{\rho_o}p_x + \frac{1}{\rho_o}\frac{\partial}{\partial z}\tau^{(x)} \qquad \text{(EQ B.4)}$$

$$v_t + fu = -\frac{1}{\rho_o}p_y + \frac{1}{\rho_o}\frac{\partial}{\partial z}\tau^{(y)} \qquad \text{(EQ B.5)}$$

where f is the Coriolis parameter, p is the pressure, ρ_o a reference density, and $\tau^{(x)}$, $\tau^{(y)}$ are the x,y components of the frictional stresses. The continuity equation is given by

$$u_x + v_y + w_z = 0 \qquad \text{(EQ B.6)}$$

where w is the vertical velocity.

The velocity is now separated into a component driven by the pressure gradient (u_p, v_p) and a component driven by the frictional stress (u_E, v_E) and depth average the inviscid versions of (B.4) and (B.5) and then cross differentiate to eliminate the pressure terms. Allowing overbars to denote the vertical average, this gives the equation

$$\hat{\xi}_t + H\bar{\mathbf{u}}_p \cdot \nabla\frac{f}{H} + \frac{f}{H}\nabla \cdot (H\bar{\mathbf{u}}_p) = J(\chi, H^{-1}) \qquad \text{(EQ B.7)}$$

where

$$\chi = \frac{g}{\rho_o}\int_{-H}^{0} z\rho\, dz \qquad \text{(EQ B.8)}$$

and the following definitions hold: the vorticity of the depth averaged flow is defined $\hat{\xi} \equiv (\bar{v}_p)_x - (\bar{u}_p)_y$, and the Jacobian is given by $J(A,B) \equiv A_x B_y - B_x A_y$. The expression $J(\chi, H^{-1})$ is the JEBAR term. Readers interested in a more complete discussion and additional formulations are referred to Mertz and Wright (1992).

In Section 3.3 is was noted that the changes in wind stress over the southern ocean produce large changes in stratification that are in turn responsible for the changes in transport within the ACC. As an illustration, the spun-up solution from the one-basin nominal winds case was subjected to strong and weak wind forcing, but the temperature and salinity fields were held fixed at the nominal wind equilibrium values. This should illustrate only that portion of the barotropic response that does not depend on the internal density structure of the ocean.

The range of flow through Drake Passage was greatly reduced. When the density structure was allowed to respond to changes in wind forcing, the transport ranged from

155 Sv for weak winds to 193 Sv for strong winds. With the density structure fixed at the nominal wind equilibrium structure, the range was reduced to 176.5 Sv for strong winds to 173.1 Sv for weak winds. In fact, with no wind forcing the transport only dropped to 171.4 Sv in the fixed density structure case.

To further illustrate the point, three runs were completed with a homogenous ocean. In a homogenous ocean χ would be horizontally uniform, and the JEBAR term would go to zero. The barotropic stream function for each run is almost identical to the barotropic stream function for the equivalent run with buoyancy forcing away from the ACC, but is very different in the region of the ACC. In a homogenous ocean, in which no baroclinicity can contribute (through JEBAR) to the barotropic flow, the transport through Drake Passage is greatly reduced. With a magnitude of only 5 Sv for strong wind forcing, it is clear that it is not the wind forcing alone that determines the strength of the ACC. Rather, the density structure of the ocean, determined by both the buoyancy forcing and the wind forcing, sets the strength of the ACC. The experiments illustrating the influence of JEBAR on the ACC are summarized in Table B1.

TABLE B1. Response of the ACC to changes in wind forcing. The experiments in the first column were allowed to adjust freely to the changes in wind forcing, those in the second and third columns had their density structures held constant.

	Antarctic Circumpolar Current (Sv)		
Wind Forcing	Nominal Experiments	fixed T,S	Homogenous Ocean
Weak	155.7	173.1	1.6
Nominal	174.8	174.8	3.3
Strong	193.5	176.5	5.0
No Wind	-	171.4	-

Appendix C. Level Thickness

Level thickness for the three-dimensional models used in this thesis. All model configurations in Chapter 3 had 20 levels. In Chapter 4 and Chapter 6, the one-basin configurations had 16 levels, while the two-basin configurations had 20 levels.

TABLE C1. Layer thickness for a) 16 level configurations, and b) 20 level configurations.

Level Number	a) Level thickness for 16-level configurations (m).	b) Level thickness for 20-level configurations (m).
1	50.0	50.0
2	67.5	62.0
3	89.5	76.0
4	116.5	92.0
5	148.8	110.5
6	185.7	131.0
7	228.0	153.5
8	274.0	178.0
9	323.5	204.5
10	374.5	232.5
11	424.5	260.5
12	473.0	289.0
13	515.5	317.5
14	552.5	345.0
15	579.5	370.5
16	597.0	393.5
17		413.5
18		429.5
19		442.0
20		449.0

VITA

David A. McDermott was born on December 27th, 1962. He received a B.S. from Rice University (Mechanical Engineering) in 1985. Prior to beginning graduate studies, he worked for Lockheed in Houston, TX, conducting engineering studies using a simulator of the Space Shuttle robot arm. He is married to Marian Allen McDermott, and has one daughter, Mara.